The Principles and Practice of the Xylophone Bar Magnetometer

A thesis submitted to the Faculty of SAgE in partial fulfilment of the requirements for admittance to the Degree of Doctor of Philosophy

By Harry T.D. Grigg MEng

School of Mechanical and Systems Engineering

Newcastle University

September 2013

Abstract

This thesis reports on work undertaken to analyse, design, optimise, and fabricate a high-Quality factor mechanical resonant magnetometer, based on a Xylophone Bar Resonator (XBR). The principle of operation is based on the use of nodal supports to mechanically isolate a transverse beam vibrating in its fundamental mode.

A control model is developed for the device, incorporating the effect of electromechanical parametric amplification. The device response and performance is shown to be strongly dependent on the Q factor of the sense element. The need for a quantitative model of XBR dynamics in order to design an optimal XBR is thus established. Using a Rayleigh-Ritz based approach, a model of the modal dynamics of an XBR is developed for the first time. In order to examine the efficacy of the nodal supports, a new model for support loss for resonators with two supports is developed and presented. Analytical models for other sources of dissipation are adapted for the first time to the XBR case. Combining these developments with a system level model allows for the development of a quantitative predictor of the fundamental and electronic noise limits on performance for an XBR.

The model is solved over the operational range of geometric parameters, yielding optimisation criteria for the geometry. Corresponding predictions for the force and magnetic field sensitivity are presented. Based on the results, an optimised XBR design is exhibited for a macroscopic metal flexural XBM to be fabricated via Wire EDM. The fabricated devices are characterised, constituting the first demonstration of a macroscopic flexural XBR. The resulting Q factors and sensitivities are shown to be in agreement with the predictions. Fruitful directions for further work are suggested throughout the thesis and summarised in the conclusions.

The original contribution to knowledge made by the thesis can be summarised as the development of an original and detailed theory of the principles of XBR optimisation for high Q, and demonstration of an operational macroscopic flexural XBM for the first time.

Acknowledgements

Firstly, I would like to give heartfelt thanks to my lead supervisor, Dr.B. J. Gallacher for his unwavering support, guidance, belief and inspiration throughout the eight years I have spent at this department. He is a true scientist and leads by example. I respect nobody more than Barry, and he is a true gentleman. I would like to thank John Hedley for always being there for me when I have needed to draw on his substantial experience and insight. The coruscations of Professor James Burdess' brilliance have consistently challenged and inspired my imagination throughout the work. Thanks to Richie Burnett, for his pure love of his profession and his willingness to give of his time to others who wish to share in it. Without the shop floor lads in Mechanical and Systems Engineering and in Electrical Engineering there would not be an XBM in Newcastle, so special thanks go to Brian Stoker, Steve Charlton, Mike Foster, Jack Noble, Malcolm Black, Chris Manning, Stuart Baker, Nicky Dafter and Jamie Hodgson. My colleagues and fellow postgraduate students in the school have been nothing but kind and supportive in all my experience here at Newcastle University, and I thank you all profoundly.

Without the foundation of emotional strength I derive from my close-knit group of family and friends, with whom I am privileged to be associated, it would not have been possible to complete this work. I have to thank my mother, Hazel Grigg, first and foremost, for being my rock for as long as I can remember. My aunt Ashlynn Middleton, my cousins Keeley Clarke and Verity Thompson, and my sisters Cherri Grigg Brookfield, Cathi Coston, and Brandi Mohler have all been there for me when it mattered. You mean more to me than words can express. At times, I have leaned heavily on my friends, and they have never let me fall. Scott Stevenson and Alexandra Peach, David Jeffs, Craig Gilbert and Jo Passe, Liam Redshaw, and Charlotte Duffy – I cannot thank you all enough. Thanks to Terry Kennedy for reminding me where my roots are. Thanks to Dan Cook for helping me look to the future. A special thank you to my friends Ben Shaw and Heather Moore for their tremendous assistance in proof reading and formatting the work. I love you all.

Table of Contents

Table of Tables

Table of Figures

Chapter 1: Introduction

This chapter sets the stage for the subsequent theoretical and experimental work by defining the goals of the project, introducing the principles of a resonant magnetometer and the fundamental mathematical and engineering concepts which will be assumed in the sequel, and assessing the current state of the art.

The first sections are dedicated to enunciating the goals of the body of work presented herein, including specific and objective goals for the thesis as a whole. We proceed to examine the particular case of interest, surveying the current literature on the topic, first quite generally and progressively adding detail, prioritising current designs, manufacture and performance. Comparison is made to other forms and types of magnetometer, both resonant and otherwise. Towards the end of the chapter, potential applications and the state of the art in terms of performance are reviewed and summarised. The aim of this section is to familiarise the reader with the context in which the research presented in later chapters arose, and to give a feel for the relevance and impact of the new knowledge derived in the work and presented in this thesis.

Symbols

T	Kinetic energy	$F_{LORENTZ}$	Lorentz force
V	Potential energy	I_{SENSE}	Sense current
C	Damping factor	B	Magnetic field
Q_{NC}	Nonconservative forces	h	Surface layer thickness
$x, \dot{x}$	Displacement, velocity	$\phi_{SURFACE}$	Surface loss factor
$F(t)$	Applied force	ϕ_{BULK}	Bulk loss factor
$\mathcal{L}$	Lagrangian	f	Forcing amplitude
R	Rayleigh dissipation function	K	Spring stiffness
$q, \dot{q}$	Generalised position, velocity	M	Mass
ω_F	Forcing frequency	ξ	Damping ratio
t	Time	A	Response amplitude

1.1 Thesis goals

The overarching aim of this thesis is to develop a sound theory of the design and performance of the *Xylophone Bar Magnetometer* (XBM) and the *Xylophone Bar Resonator* (XBR) on which it is based. The author seeks to explore the potential of this class of device in high-performance, compact magnetometer applications, including MEMS XBR magnetometers fabricated using micromachining techniques, mesoscale devices, and macroscopic XBMs; further, to explore the wider potential of the XBR in other high-Q resonator applications.

Particular goals for the work are specified by the following:

i. Assess the current state of the art in research resonant magnetometers and XBMs, and evaluate the theoretical potential and impact such devices are capable of achieving, with respect to specific application fields.

ii. Develop a sound theoretical understanding of the behaviour of the XBR and the performance of an XBM.

iii. Design and fabricate a macroscale flexural XBM prototype to operate under open-loop control for the first time as proof of the developed principles.

iv. Compare the theoretical and experimental results to extant devices, and draw conclusions as to the potential for the XBM and XBR in applications.

The style adopted herein is intended to present the findings in a form which allows the reader to readily employ the developed analyses and optimisation techniques to design an optimal XBM, and more broadly, to optimise resonant sensors for high performance. To this end, MATLAB code used to formulate and solve the models is available in full for free download online at https://dl.dropboxusercontent.com/u/28555534/Thesis%20XBR%20Models.zip. In the final chapter, the body of work contained in the thesis will be compared to and evaluated against these criteria.

1.2 Motivation

The research problem addressed by this thesis arose in the context of the study of MEMS inertial measurement units. A wide variety of application fields utilise sensors and actuators based on MEMS technologies; one important subclass important for navigation applications is termed an Inertial Measurement Unit (IMU). These integrated sensor-output systems are utilised as components of modern microelectronic devices such as mobile phones, tablets, motion-capture systems, handheld game controllers, and scientific field instruments. The basic function of these devices is straightforward: measure three orthogonal accelerations and three corresponding angular accelerations. These measurements can then be sampled and digitally integrated over time to give an estimate of relative position. With an initial position datum (such as could be supplied by GPS, for example), inertial orientation and navigation applications are available currently. Examples include AR applications such as Google Specs and Layar applications on ANDROID smartphones.

The accelerometers and gyroscopes in a MEMS 6 axis IMU are typically of the resonant type. They possess the attributes of low cost, low power consumption, and reasonable sensitivity and resolution of time-dependent signals in the presence of noise. However, the time scales over which inertial navigation using a MEMS IMU is viable

are seriously limited by the drift inaccuracy of the device and by the resolution of the sampling frequency. One technique that can be used with moderate-drift, high-bandwidth inertial measurement is to update the reference angular position coordinate with an angular datum supplied by Earth's magnetic field, using a Kalmann filter to combine the favourable long-time behaviour of the magnetic field (zero mean drift) with the favourable temporal resolution of the gyroscopes to dramatically improve navigation overall[1].

If field sensitivity corresponding to a precise measurement of Earth field such that the angle made with the IMU can be resolved to about 0.1 degrees can be achieved, then the frontiers of technology will be pushed back far enough to reveal an exciting new field of applications: precision portable IMUs. One compelling application entails indoor navigation for emergency services.

When first responders attend the scene of an accident or fire, the time taken to navigate an unfamiliar environment to locate survivors is a matter of life and death. Take the scenario of a smoke-filled, evacuated building on fire. Co-workers inform the first responders that a man is trapped by fire in the fourth floor executive suite. Now imagine a device, similar in form to night vision goggles but employing a precision MEMS IMU and AR technology as described, wirelessly connected to a central database storing the structural layout of the building.

Given a reference, such as could be obtained from a fixed landmark (the front door) to zero the initial position, it would be possible to arrange for a Heads Up Display to be superposed over the visual field, illustrating (via an arrow, for example) navigation directions in real time, irrespective of visibility or lighting conditions, which would allow the first responder to quickly and effectively navigate to a desired location as if they knew the building by experience. The effect would be similar to GPS navigation of a car, but with a much higher spatiotemporal resolution and no line-of-sight restrictions. The potential to save lives is manifest.

The same principles can be applied to underground navigation for cave rescue and mining purposes, consumer applications (QR codes in the entrance to a major supermarket; scan one, AR leads you to the offer!), tactical applications, and precision

UAV navigation, among others. A detailed survey of application fields is beyond the scope of this thesis, and indeed could form the basis of a substantial body of work in itself. However, it is intended that this brief sketch gives the reader a flavour of the breadth and depth of possible ends to which a MEMS 9 axis precision IMU could be put.

In order to bring this promise to fruition, a magnetometer with sensitivity approaching or better than $1nT/\sqrt{Hz}$ is required. The work presented here makes a contribution to the global ongoing research effort to develop the technological capabilities to achieve this level of performance.

1.3 Orientation

In this section, the landscape is outlined in terms of published research in particular technical niches pertaining to the research presented herein. An attempt is made at balance between the narrative flow of recent developments in the field and the bigger picture of driving socioeconomic trends and market development. The intent is that the unfamiliar reader should finish this section with a rudimentary feel for the current state of research and the direction and momentum of progress, across all the major areas touched on in the rest of the thesis.

1.3.1 Resonant sensors

Consider a resonant system, in which energy is cyclically exchanged between two storage forms, such as electric and magnetic, corresponding to resonant electrical circuits, or kinetic and elastic potential energy, in the case of mechanical resonators.

If the system parameters are known a priori at an initial time datum, and also are regarded as being influenced slowly in time by the environment of the system, then a mathematical model of the dependency of the properties of the resonator, coupled with a series of experimental measurements of its behaviour, can be used to infer environmental conditions. This is the principle of resonant sensing. This idea is now developed in a more concrete form.

If the energy in each storage reservoir is quadratic in the corresponding generalised coordinate, then the energy gradient, corresponding to the generalised force acting on

the coordinate, is linear in that coordinate. Such systems are termed linear resonators, the theory of which is old and very well known. An example is given below. We study the driven damped harmonic oscillator system composed of a single mass attached to ground by a Hookean spring and a viscous damper, as illustrated in Figure 1.1.

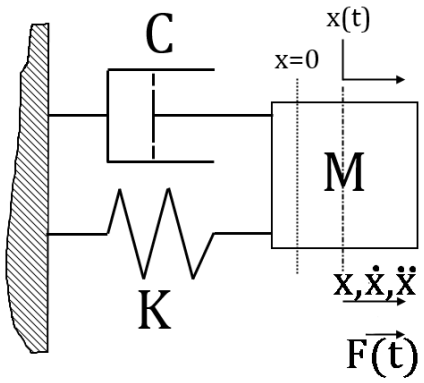

Figure 1.1 Forced, damped single mass-spring mechanical system.

The kinetic and potential energies, the Rayleigh dissipation function, and the nonconservative forcing are given respectively by

$$T = \frac{1}{2}M\dot{x}^2 \; ; V = \frac{1}{2}Kx^2; R = \frac{1}{2}C\dot{x}^2 \; ; Q_{NC} = F(t) \tag{1.1}$$

The equations of motion for such a system can be derived by means of the Euler-Lagrange equation (1.2):

$$\frac{\partial}{\partial t}\left(\frac{d\mathcal{L}}{d\dot{q}}\right) - \frac{d\mathcal{L}}{dq} = -\frac{dR}{d\dot{q}} + Q_{NC} \tag{1.2}$$

where $\mathcal{L} = T - V$ is the Lagrangian and q is the generalised coordinate, here identified with x. Substituting (1.1)into (1.2) yields the well-known equation of motion for the system:

$$M\ddot{x} + Kx + C\dot{x} = F(t) \tag{1.3}$$

It is expected that the response of such a system to a time harmonic forcing of the form $fe^{i(\omega_F t)}$ will be time harmonic. To test this hypothesis, we make the ansatz $x(t) = Ae^{i(\omega_F t + \phi)}$, where the parameter ϕ is to be determined. Thus, we obtain the classical result

$$A = \frac{f/M}{\left(\left(\frac{K}{M} - \omega_F^2\right) + i\omega_F \xi\right)} \tag{1.4}$$

Here, $\xi = \frac{C}{2\sqrt{MK}}$ is the nondimensional damping ratio. The response is seen to depend on the parameters f, K, M and C. For small C, it has a sharp peak in the vicinity of the undamped natural frequency of free vibration $\sqrt{\frac{K}{M}}$, when the first term in the denominator cancels. Additionally, the response amplitude is proportional to the forcing strength $|F|$.

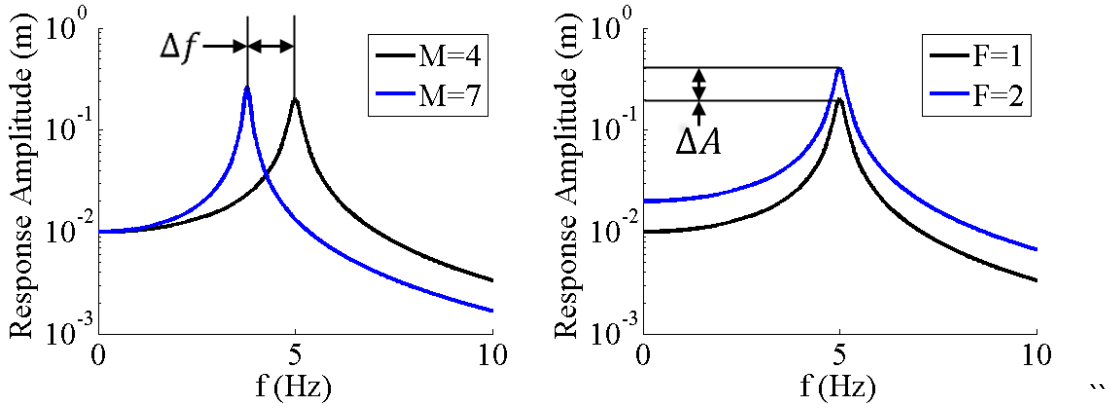

Figure 1.2 Changes in resonance behaviour of a damped, driven harmonic oscillator as the mass M and forcing strength F are respectively changed.

The curves plotted in Figure 1.2 represent typical operating mechanisms for resonant mass and force sensors, respectively. Resonant mass sensors work by configuring a system analogous to (1.3) so that the mass element has a chemical affinity for an analyte of interest in the environment, such as a particular protein or chemical species. Over time, the mass is then augmented by an amount related to the local concentration of the analyte, while the stiffness of the system is relatively unaffected. Then, by carefully monitoring the corresponding shift in resonant frequency observed experimentally over time and illustrated in the left axes of Figure 1.2, or by comparison to a control system, the added mass and hence the analyte concentration can be inferred.

On the other hand, resonant force sensors operate according to a different principle. Instead of having the intrinsic parameters of the resonant system influenced by the environment, the external forcing strength is connected to the field quantity of

interest, which may include an applied acceleration, rotation, or an electric or magnetic field, amongst other possibilities. While the resonant frequency is unaffected, the response amplitude (in the presence of damping) is directly proportional to the forcing strength. Thus, by experimentally observing the response amplitude, a mathematical model of the system may be used to infer the corresponding field quantity of interest. This is the fundamental operating principle of the resonant magnetometer, which constitute the object of study for this investigation.

There are many fields in which resonant sensors find application, including gravitational wave detection, industrial and automotive pressure sensors, medical technologies such as MRI, biological mass sensing, acceleration and angular acceleration, viscometry, etc. One of the first uses of an engineering sensor utilising modification of resonant properties of a sense element was in early pipe sensors, which use the influence of the viscosity of a fluid in a fluid-filled pipe on the resonant frequency of the device to infer the desired rheological properties from the measured natural frequency. These devices were first patented in the late 1960s and early 1970s. Other early resonant sensors included cylinder radial-deformation N=2 symmetric mode viscometers, resonant paddle viscometers, and other geometries. These early developments are reviewed well by Langdon in a 1985 paper[2].

From a MEMS perspective, some of the first prototypes were reported in the early 1980s by J.C.Greenwood[3], who reported fabrication of a membrane pressure sensor via anisotropic etching of silicon. The function was achieved via mounting the device support on a membrane pressure sensor, such that pressure-induced membrane deflection introduces axial prestress to the resonant element and hence a nonlinear frequency shift. Over the next decade or so, an burgeoning array of resonant microsensors, including accelerometers, viscometers, and pressure sensors were reported in the literature[4]. Today, a vast array of technologies utilise the principles of resonant sensing, from high-performance components in aerospace applications to the mass market for MEMS, which is now worth over $100bn globally[5].

1.3.2 High-Q Resonators

One application of high Q factor resonators is to resonant sensors. One application of particular fundamental interest, and a source of a great deal of knowledge about mechanical loss processes that is of relevance here, is the NSF-sponsored LIGO project[6] to detect gravitational waves and thus to provide further experimental proof of the predictions of general relativity. As a part of the 4km Michelson interferometer that constitutes the instrument, the mirrors are suspended under vacuum, initially using metal wires and in newer developments (Advanced LIGO[7]) fused silica suspensions. The thermal signal-to-noise in the supports and mirrors is related to their mechanical Q factor and loss sources by the fluctuation-dissipation theorem[8], [9], which relates dissipative forces to random, Gaussian fluctuations with white power spectral density. The connection will be explored further in the sequel.

In a series of papers coming from the development of Advanced LIGO suspension[10][11][12][13], the mechanical bulk and surface properties of fused silica were quantified. The lowest bulk loss factors in flame-polished, annealed fibres were found to be of the order $\phi_{BULK} = O(10^{-8})$, while the product of suface thickness and loss factor $h\phi_{SURFACE} = O(10^{-5})$. These properties, combined with favourable thermal properties from the perspective of thermoelastic loss, makes fused silica an appealing prospect for the fabrication of very high Q factor resonators. Indeed, there exists a whole literature on fused silica beams[14], disks, ribbons[15], fibres and other mechanical resonant structures, predating LIGO but influenced strongly in its development by it. Bulk mode resonators have been reported with Q factors exceeding 2×10^7 at room temperature[16]. There exists to the knowledge of the author no work in the literature, either experimental or theoretical in character, attempting to treat XBRs fabricated from fused silica or a similar low thermal loss material, on any length scale. A paper on nodally supported disks for measurement of loss factors in Fused Silica was published by Numata et al in Physics Letters A in 2000; the geometric impedance tuning principle employed in XBRs is applied from a different perspective therein. The potential of this material for use in microscale and macroscale XBRs is addressed for the first time in the literature in the present work.

1.3.3 Xylophone Bar Magnetometers

The concept of the XBM was first developed by Johns Hopkins University. The work was published in Applied Physics Letters[17], in 1996. Therein, Givens et al. describe a new magnetometer design, inspired by the resonant element of a musical xylophone, which consists of a wooden or metallic beam resonator, suspended at the nodepoints of its fundamental mode of resonance, when considered as a free beam.

The resonator had the form of a $39 \times 5.17 \times 0.9\, mm$ aluminium bar constituting mechanical resonator and henceforth referred to as the *sense beam*, supported at its nodes by copper wires $18mm$ long and out of the plane of vibration of the device, such that the wires were loaded only in torsion in the (ideal) resonator. An XBR with this type of out-of-plane, torsionally loaded support is termed a *torsional XBR*. Current was driven at AC frequencies through the wires so as to drive an axial current, termed the s*ense current* through the bar, and a controlled magnetic field was applied in the plane of the device and transverse to the beam.

The Lorentz force law, applied to an assumed uniform, perpendicular applied field of strength B and a sense current I_{SENSE}, yields a corresponding uniform force density $F_{LORENTZ}$ in phase with and proportional to the sense current, along the portion of the sense beam over which it flows. When the excitation frequency of the sense current was tuned using a phase-tracking scheme to the fundamental natural frequency of vibration of the sense beam and the response was observed via laser Doppler vibrometry (LDV), the response could be calibrated to the applied field strength. The relationship between the two is linear in the linear response regime of the resonator, and hence inference of the field strength variation from the measured responses is straightforwardly possible. This is the fundamental operating principle of the XBM. It can be classified as a force sensor of the type shown in the right-hand plot in Figure 1.2.

Givens et al. obtained a Q factor of 1220 for the first reported XBM. The corresponding field sensitivity was given as at least $1nT/\sqrt{Hz}$ by the author. The wide dynamic range of $80db$ was also reported in the study, which represents the ability in devices of this type to reduce the sense current in response to large field intensities

using a control implementation, allowing for almost arbitrarily large fields to be measured by the devices. No such levelling is possible with the common fluxgate magnetometers.

The next stages in the development of the XBM by the original research group was published as a technical report and a series of conference proceedings[18–22], leading up to the 2003 paper in Acta Astronautica[23]. A MEMS scale torsional XBR is presented in poly(Si), with sensitivity on the order of $100nT/\sqrt{Hz}$. Difficulties are encountered concerning deviations in the expected modal behaviour from the free-free ideal and medium quality factors around 1000 are reported as occurring due to the torsional effects of the supports, and a model comprising a torsional spring applied to an Euler-Bernoulli beam at the free-free nodepoints is presented, which is shown to account for the deviation. Meanwhile a research group from the University of Michigan Ann Arbour led by Nguyen, published a paper reporting the development of a torsional XBR with measured Q factors between 7500 and 8500, and compares the merits of Euler-Bernoulli and Timoshenko beam models for torsional XBR design.

In a 2010 paper[24], following on from a 2009 conference publication[25] another research group from Belgium, also coming from an aerospace background and in collaboration between several institutions, published plans for a PolySiGe torsional XBR, along with a dissipation model neglecting support loss and the effect of the supports. A few results are presented regarding the dependence of the damping on the atmospheric pressure and the beam width. The group published preliminary findings at the conference IEEE Sensors 2012[26], reporting a Q of 5000 and sensitivity to earth field, implying better sensitivity than $1000nT/\sqrt{Hz}$. They present and contrast microfabricated torsional and flexural XBRs in an array to provide resolution of the field components in three dimensions. They have yet to report in a journal article.

Lee and Lin published in 2008 a conference report[27] on modelling work undertaken on a double XBR microfabricated in polysilicon. The work presented was preliminary in nature.

The author has reported preliminary results of the modelling and experimental work on flexural XBRs, at the IMAPS 2011 DPC conference[28], detailing the first round of prototyping and early development of the analytical support loss model presented in Chapter 4; and also at the COMSOL conference 2011[29], reporting on Joule heating effects in XBRs.

To summarise the situation, the concept of a torsional XBR and associated XBM has been demonstrated by fabrication from macroscopic to microscopic scales. The resulting Q factors are high, and the field sensitivities exhibited by the devices are correspondingly very good. However, no cohesive treatment of the operating principles exists in the literature. No systematic study has been presented on the potential Q and performance limits to an XBR or XBM respectively. The work presented in this thesis attempts to fill this gap by developing a fairly general theory of the design and operating principles of an XBR and XBM. In addition, no macroscopic device using a flexural XBR has been reported on to date, and this thesis aims to be the first work to report on the development, principles, fabrication, and operation of such a device.

In order to drive a large sense current without incurring large losses or fluctuating feedthrough voltages on the sense beam, a high-conductivity material is required. On the microscale, this generally involves the use of heavily doped silicon. On the macroscale, metallic materials are attractive from an electrical perspective. The macroscopic XBRs fabricated in this project are all metallic. The consequences of this choice are explored in the thesis.

1.3.4 Resonant MEMS Magnetometers

One of the first publications on a Lorentz force resonant magnetometer, here using a ribbon type sense element, was made by Takeuchi[30] in 1984. Some of the first MEMS implementations were the Xylophone Bar Magnetometers discussed above. Other work has included clamped-clamped beam and folded-support beams[31] and frame resonators with interdigitated capacitive transduction and ensuing geometric complexity, as well as torsional paddle microresonators[32]. An adequate recent

review on the topic of resonant MEMS magnetometers is furnished by the 2009 publication by Herrera-May et al[33]. The number of papers indexed on SCOPUS containing the search term “MEMS Magnetometer” in their title has increased from six for the period 1995-2005 to 25 for the period 2006-present, which is an indication of the increased attention that micromachined magnetic field sensors have attracted, pursuant to the goal of a 9-DOF MEMS IMU.

1.4 Open Questions

From the brief review of the literature in Section 1.3, there are several areas in which current knowledge is incomplete and in which there is scope for research progress. Some of the open questions investigated in this thesis are summarised below.

- Is parametric amplification a useful technique to apply to XBMs? Can it be done?
- What are the limits of, and limiting factors on, the force sensitivity of XBRs and field sensitivity of XBMs? How do the associated sensitivities change as the parameters are varied? Are there general optimality conditions, or is it necessary to evaluate each material and geometric case separately? How do these effects vary with scale?
- How can we model these phenomena in an efficient, flexible way suited to design optimisation?
- In terms of mechanical engineering, is it possible to realise a flexural XBM using planar macromachining techniques, such as Wire EDM? If so, how can the resulting magnetometers be expected to perform?
- From a systems engineering perspective, how do the drive and sense processing electronics affect performance? What needs to be done in order to get the most from these ancillaries?

1.5 Impact

Part of the societal justification for the large sums of public money invested in scientific and engineering research is the positive economic and social effects derived from the research. It is therefore of interest to consider the potential impact, both within the narrow field of study and more broadly, when evaluating the outcomes of a research project.

The expected impact of the work presented herein as regards the MEMS design community can be summarised as:

- Development of new techniques to allow higher excursion, greater linearity and repeatability, and ultimately better resolution in MEMS sensors using the parametric control techniques developed in Chapter 2.
- Improvement in geometric design of XBRs and XBMs based on the XBR modal dynamics techniques presented in Chapter 3.
- Improved understanding of support losses in planar resonators more generally, as a result of the elastic wave modelling presented in Chapter 4.
- Improved performance of XBR systems via the more detailed systems level model developed in Chapter 5.

The expected impact in a broader societal context can be summarised as follows:

- Contribution towards developing a 9 axis precision MEMS IMU

1.6 References

[1] A. M. Sabatini, “Kalman-Filter-Based Orientation Determination Using Inertial/Magnetic Sensors: Observability Analysis and Performance Evaluation,” *Sensors*, vol. 11, no. 10, pp. 9182–9206, Sep. 2011.

[2] R. M. Langdon, “Resonator sensors - a review,” *Journal of Physics E: Scientific Instruments*, vol. 103, pp. 103–115, 1985.

[3] J. C. Greenwood, “Etched silicon vibrating sensort,” *Journal of Physics E: Scientific Instruments*, vol. 650, pp. 8–11, 1984.

[4] P. Hauptmann, “Resonant sensors and applications,” *Sensors and Actuators A: Physical*, vol. 26, no. 1–3, pp. 371–377, Mar. 1991.

[5] Yole Developpement, “MEMS for Cell Phones & Tablets,” 2012.

[6] P. Willems, “LIGO: The laser interferometer gravitational-wave observatory,” *2006 Conference on Lasers and Electro-Optics and 2006 Quantum Electronics and Laser Science Conference*, pp. 1–2, 2006.

[7] G. M. Harry, “Advanced LIGO: the next generation of gravitational wave detectors,” *Classical and Quantum Gravity*, vol. 27, no. 8, p. 084006, Apr. 2010.

[8] M. Devel, R. Bourquin, S. Ghosh, J. Imbaud, G. Cibiel, and F. Sthal, “Quartz crystal resonator noise and fluctuation-dissipation theorem considerations,” *2012 IEEE International Frequency Control Symposium Proceedings*, no. 1, pp. 1–5, May 2012.

[9] H. Sandberg, J.-C. Delvenne, and J. C. Doyle, “On Lossless Approximations, the Fluctuation- Dissipation Theorem, and Limitations of Measurements,” *IEEE Transactions on Automatic Control*, vol. 56, no. 2, pp. 293–308, Feb. 2011.

[10] A. V. Cumming, A. S. Bell, L. Barsotti, M. A. Barton, G. Cagnoli, D. Cook, L. Cunningham, M. Evans, G. D. Hammond, G. M. Harry, A. Heptonstall, J. Hough, R. Jones, R. Kumar, R. Mittleman, N. A. Robertson, S. Rowan, B. Shapiro, K. A. Strain, K. Tokmakov, C. Torrie, and A. A. van Veggel, “Design and development of the advanced LIGO monolithic fused silica suspension,” *Classical and Quantum Gravity*, vol. 29, no. 3, p. 035003, Feb. 2012.

[11] I. A. Bilenko and N. Y. Lyaskovskaya, “The investigation of thermal and non-thermal noises in fused silica fibers for Advanced LIGO suspension,” *Physics Letters A*, vol. 339, no. 3–5, pp. 181–187, May 2005.

[12] A. M. Gretarsson and G. M. Harry, “Dissipation of mechanical energy in fused silica fibers,” *Review of Scientific Instruments*, vol. 70, no. 10, p. 4081, 1999.

[13] S. D. Penn, A. Ageev, D. Busby, G. M. Harry, A. M. Gretarsson, K. Numata, and P. Willems, “Frequency and surface dependence of the mechanical loss in fused silica,” *Physics Letters A*, vol. 352, no. 1–2, pp. 3–6, Mar. 2006.

[14] R. Nawrodt, C. Schwarz, S. Kroker, and I. W. Martin, “Investigation of mechanical losses of thin silicon flexures at low temperatures,” *Classical and Quantum Gravity*, vol. 30, no. 11, pp. 1–12, 2010.

[15] A. Heptonstall, G. Cagnoli, J. Hough, and S. Rowan, “Characterisation of mechanical loss in synthetic fused silica ribbons,” *Physics Letters A*, vol. 354, no. 5–6, pp. 353–359, Jun. 2006.

[16] W. J. Startin, M. A. Beilby, and P. R. Saulson, “Mechanical quality factors of fused silica resonators,” *Review of Scientific Instruments*, vol. 69, no. 10, p. 3681, 1998.

[17] R. B. Givens, J. C. Murphy, R. Osiander, T. J. Kistenmacher, and D. K. Wickenden, “A high sensitivity, wide dynamic range magnetometer designed on a xylophone resonator,” *Applied Physics Letters*, vol. 69, no. 18, p. 2755, 1996.

[18] D. A. Oursler, D. K. Wickenden, L. J. Zanetti, and T. . Kistenmacher, “Development of the Johns Hopkins xylophone bar magnetometer,” *Johns Hopkins APL Technical Digest*, vol. 20, no. 2, pp. 181–189, 1999.

[19] D. K. Wickenden, J. L. Champion, R. B. Givens, T. J. Kistenmacher, J. L. I. Lamb, and R. Osiander, “Polysilicon Xylophone bar magnetometers,” in *PROC. SPIE3876, Micromachined Devices and Components V, 267*, 1999.

[20] D. K. Wickenden, R. B. Givens, R. Osiander, J. L. Champion, D. A. Oursler, and T. J. Kistenmacher, “MEMS-based resonating xylophone bar magnetometers,” in *PROC. SPIE3514, Micromachined Devices and Components IV, 350*, 1998.

[21] J. Miragliotta, R. Osiander, J. L. Champion, D. A. Oursler, and T. J. Kistenmacher, “Development of a MEMS xylophone bar magnetometer using optical interferometry for detection,” in *Materials Research Society Symposium - Proceedings*, 2000, pp. 217–222.

[22] L. J.L., D. K. Wickenden, J. L. Champion, R. B. Givens, R. Osiander, and T. J. Kistenmacher, “Micromachined polysilicon resonating xylophone bar magnetometer: resonance characteristics,” in *Materials Research Society Symposium - Proceedings*, 2000, pp. 211–216.

[23] D. Wickenden, “Micromachined polysilicon resonating xylophone bar magnetometer,” *Acta Astronautica*, vol. 52, no. 2–6, pp. 421–425, Mar. 2003.

[24] H. Lamy, I. Niyonzima, P. Rochus, and V. Rochus, “A xylophone bar magnetometer for micro/pico satellites,” *Acta Astronautica*, vol. 67, no. 7–8, pp. 793–809, Oct. 2010.

[25] H. Lamy, V. Rochust, I. Niyonzima, and P. Rochus, “A Xylophone Bar magnetometer for Micro/Pico Satellites,” in *60th International Astronautical Congress*, 2009, pp. 5853–5864.

[26] V. Rochus, R. Jansen, H. A. C. Tilmans, X. Rottenberg, and C. Chen, “Poly-SiGe-based MEMS Xylophone Bar Magnetometer,” no. 1, pp. 1–4, 2012.

[27] C.-J. Li and S.-K. Lin, “High-Q VHF micromechanical filters using free-free beam resonators,” *2008 IEEE International Conference on Electron Devices and Solid-State Circuits*, vol. 3, pp. 1–4, Dec. 2008.

[28] H. T. D. Grigg, “Towards a parametrically pumped Xylophone microbar magnetometer: Design optimisation of xylophone bar resonators,” in *IMAPS DPC*, 2011, pp. 160–165.

[29] H. T. D. Grigg and B. J. Gallacher, “Xylophone Bar Magnetometry and Inertial-grade MEMS Optimisation: a Multiphysics Approach,” in *Proceedings of the COMSOL Conference (Europe) 2011*, 2011.

[30] S. Takeuchi, “A resonant-type amorphous ribbon magnetometer driven by an operational amplifier,” *IEEE Transactions on Magnetics*, vol. 20, no. 5, pp. 1723–1725, 1984.

[31] H. Emmerich and M. Schofthaler, “Magnetic field measurements with a novel surface micromachined magnetic-field sensor,” *IEEE Transactions on Electron Devices*, vol. 47, no. 5, pp. 972–977, May 2000.

[32] Z. Kádár, A. Bossche, P. M. Sarro, and J. R. Mollinger, “Magnetic-field measurements using an integrated resonant magnetic-field sensor,” *Sensors and Actuators A: Physical*, vol. 70, no. 3, pp. 225–232, Oct. 1998.

[33] A. L. Herrera-May, L. A. Aguilera-Cortés, P. J. García-Ramírez, and E. Manjarrez, “Resonant Magnetic Field Sensors Based On MEMS Technology,” *Sensors*, vol. 9, no. 10, pp. 7785–7813, Sep. 2009.

Chapter 2. Control Model of an XBM

In this chapter, a series of analytical models for an XBM are developed, modelling different aspects of the system dynamics. First, a very simple free-free beam model is presented in Section 2.1, both as an introduction to the concepts and to provide intuitive insight into the behaviour and functional design of an XBR. A more sophisticated model based on extending the simple Euler-Bernoulli model to include electrostatic actuation in a general way is developed in Section 2.2 and used to derive an ODE approximation. The ODE is solved analytically in Section 2.3 for several cases using a multiple-scales singular perturbation method, and conclusions are drawn regarding the behaviour of the resonator under different operating conditions.

In order to analyse and develop a parametrically amplified XBR and hence gain fundamental insight into the behaviour of a parametric XBM, a dynamical model is required. Therefore, the aim of this chapter is to develop a model for the dynamics of an XBR, accounting for the time-dependent effects of variable capacitive actuation voltage. The problem is formulated using a variational approach via the Euler-Lagrange equations. Posing this problem leads to an ODE with inhomogeneous coefficients, causing classical solution ansatzes to fail. A multiple-scales singular perturbation analysis is employed to surmount this difficulty. Solutions to the model are examined for particular cases of the applied voltage, and the effect of parametric amplification is demonstrated. Next, the model is extended to consider the effects of mechanical and electrostatic nonlinearity. In a novel contribution to the literature, it is shown that if sufficient freedom is introduced in the form of independently-modulated frequency components of the capacitive actuation signal, then smooth nonlinearities for which a Taylor series expansion exists can be mitigated by a judicious choice of phases and amplitudes of the applied control voltages.

The use of parametric amplification in mechanical systems to enhance force response and effective Q factor was proposed in a 1991 paper in Physical Review Letters by Rugar and Grutter[1]. One way of capturing the essence of the concept is to consider the form of the damping force exerted on a single degree-of-freedom linear oscillator

with viscous damping and variable coefficients. Under the assumption of a harmonic response (valid for lightly damped systems), the force is a sinusoid in phase with the velocity and hence in quadrature with the displacement and restoring force. The application of an external force, opposing in sign and identical in form to the viscous force, would be expected to change the system response.

If the forcing were a classical arbitrary fixed amplitude harmonic term at the forcing frequency, then initially, mitigation of the damping force would lead to linear growth in the resonator amplitude. Assuming the external force is fixed, a new dynamic equilibrium would arise such that the excess of the damping force over the external force would exactly balance the classical forcing applied to the system, in a steady state. The equilibrium amplitude is then described by equating the work done over one cycle by the classical forcing to the *difference* between the work done by mitigating and damping forces.

If, instead of an external force, one contemplates the case where the mechanical parameters – i.e. force and inertia gradients, in the case of stiffness and mass modulation, respectively – are modulated at twice the frequency of forced vibration, then on each excursion, the quadrature component of total harmonic force is decreased in a *displacement-proportional* fashion such that for each excursion a certain fraction of the work done by the damping forces is mitigated (and not a fixed absolute quantity). Then, the change in equilibrium amplitudes is described by equality of the classical forcing work and the *quotient* of the normalised damping coefficient by a factor, termed the *parametric gain*, proportional to the modulation in the energy gradients relative to the fixed damping amplitude. Where the damping coefficient is already small, a relatively small modification of the system parameters in this fashion can thus be amplified by a large factor, theoretically infinite. Although the in-phase component of noise is also amplified[2], a factor of $\sqrt{2}$ can be gained by "squeezing" the quadrature component of noise power, termed *noise squeezing*[1]. Furthermore, the principle can be used to extract better SNRs and device performance in the presence of instrumental or environmental noise downstream of the resonator in the signal path[3]. However, in practice, above a threshold gain, such systems

become unstable and non-functional as sensors due to the intervention of nonlinearities or unaccounted-for second order effects.

The original paper by Rugar et al. achieved parametric gains around 15-20, demonstrating the dependence of the gain on phase, the analytical forms of the response using an ansatz method, and the utility of the method for achieving thermal noise floors in AFM cantilevers. Dâna et al. applied the method to GaAs microcantilevers in 1998[4], achieving a maximum gain around 10, as did Carr et al. in a torsional microresonator[5] two years later; both used ansatz methods to derive the analytical models. Optical modulation of the parameters was demonstrated for disk resonators supported by a central column by Zalalutdinov et al. in 2001[6], achieving stable gains up to 30. Ono et al. demonstrated a single-crystal silicon thermal sensor based on a cantilever resonator[7] under parametric amplification in 2005.

Application of parametric amplification to sensors utilising weak coupling between degenerate modes, such as rate and angle gyroscopes, has been explored in the literature quite extensively in the last decade[8–13], with stable gains up to and exceeding 100 reported. The analytical models formulated using a multiple scales method were found to yield good agreement with experiment until the onset of parametric instability. More recently, the technique has been applied to Lorentz force-based clamped-clamped resonant magnetometers by Thompson and Horseley[14][15], showing noise squeezing and parametric gains up to 65, with a resultant sensitivity of $87\ nT/\sqrt{Hz}$ from a device with a principal dimension of $500\mu m$.

Symbols		X	Mode shape
$\mathcal{L}_{\mathrm{E-B}}$	Euler-Bernoulli Lagrangian	$T,$	Generalised coordinate for beam model
ϱ	Material density	c	Flexural wave velocity
$\mathrm{A_x}$	Cross-sectional area	$\mathrm{Q_{NC}}$	Nonconservative force
$u(x,t)$	Transverse displacement of beam	q	Generalised coordinate in Euler-Lagrange equation
E	Young's Modulus	ω	Frequency
I	Second moment of area	β, β_n	Propagation factor, mode constant
x	Spatial coordinate of (sense) beam	s, s_n	Complex variable, n^{th} solution
ℓ	Length of (sense) beam	w	Out-of-plane depth
ε_0	Permittivity of free space	h_0	Capactive gap in reference configuration
$V(t)$	Time-dependent voltage	$u(x,t)$	Beam transverse displacement
$V_1(t)$	Top electrode voltage	$V_2(t)$	Bottom electrode voltage
$\mathbb{m}$	Electrode ratio: fraction of sense beam plated with electrode	dV_{CAP}	Elemental potential energy storage in capacitor
R	Rayleigh dissipation function	C_D	Damping coefficient
$T^*_{\mathrm{E-B}}$	Euler-Bernoulli cokinetic energy	$V_{\mathrm{E-B}}$	Euler-Bernoulli potential energy
V_{LINEAR}	Linearised potential energy storage	K_{q}	Quadratic nonlinear stiffness coefficient
K_{c}	Cubic nonlinear stiffness coefficient	$V_{\mathrm{NONLINEAR}}$	Fully nonlinear potential energy storage
ω_n	Natural frequency	λ	Mistuning parameter

$\overline{V_1}, \overline{V_2}$	Voltage scaling parameters for first, second electrode	$\boldsymbol{V}_1, \boldsymbol{V}_2$	Nondimensional time dependency of first, second electrode voltage
$\mathbb{V}_{1\mathrm{DC}}, \mathbb{V}_{2\mathrm{DC}}, \mathbb{V}$	DC bias voltages on first, second electrode, common bias voltage	ϕ	
A_m^n	n^{th} forward harmonic of i^{th} electrode	B_m^n	n^{th} backward harmonic of i^{th} electrode
ϕ	Phase offset	C_p	Parasitic capacitance
I_{FT}	Feedthrough current		
F	Forcing strength coefficient	P	Parametric pumping strength coefficient
α_{DC}	DC voltage coefficient	α_1	First frequency coefficient
α_2	Second frequency coefficient	$\mathbb{V}_{\frac{1}{2}}$	Half frequency voltage coefficient
$\mathbb{V}_2$	Double frequency voltage coefficient	δW_{NC}	Virtual work of nonconservative forces
F_{CAP}	Capacitive actuation force	$H(x)$	Heaviside step at x
M	Generalised mass	K_0	Linear generalised stiffness
ω_n^2	Modal natural frequency	w	Out-of-plane depth
$K_{E1\mathrm{i}}$	Electrostatic linear stiffness contribution from i^{th} electrode	ε_0	Permittivity of free space
K_{Ec1}	Cubic stiffness coefficient contribution from i^{th} electrode	K_{Eq1}	Quadratic stiffness coefficient contribution from i^{th} electrode
		ω_c^2	Cubic stiffness coeffiecient normalised by mass
ω_q^2	Quadratic stiffness coefficient normalised by mass	F_1	Electrostatic force from i^{th} electrode
F_2		ϵ	Small parameter; ratio of linear stiffness modulation to

			mechanical linear stiffness
R_1	Ratio of voltage scales between first and second electrodes	ϵq	See 2.45
ϵc	See 2.45	ϵv	See 2.45
ϵF	See 2.45	$X_{FF}^{(1)}, \beta_{(1)}$	Fundamental free-free mode of an Euler-Bernoulli beam; mode factor
$t, \hat{t}, \tilde{t}$	Time, fast time, slow time	$\hat{T}, \tilde{T}$	Fast, slow time coordinates
$\epsilon\lambda$	Mistuning of drive from natural frequency	$r(\tilde{t})$	Slow-time amplitude envelope modulation
$\theta(\tilde{t})$	Slow-time phase envelope modulation	r_s, θ_s	Steady-state response amplitude, phase
D_S	Slow time modulation equation denominator	Q, Q_{P}	Quality factor, Parametrically amplified equivalent quality factor
$\tilde{r}$	Amplitude deviation from critical point	$\tilde{r}_0$	Initial amplitude deviation
$\tilde{\theta}$	Phase deviation from critical point	$\tilde{\theta}_0$	Initial phase deviation
Λ		A, B, C, D	Arbitrary constants

2.1 A Free Beam

The intuitive justification for using an XBR as the sense element for a Lorentz magnetometer is to separate the main energy reservoir – the sense beam – from the support elements, such that the supports can be made as mechanically isolating as is feasible while the sense beam stores as much energy as possible, as described in Chapter 1. This implies that performance will be maximised by making the sense beam relatively large with respect to the supports. On this basis, it is reasonable to expect that in practical cases of interest, the important dynamics and the energy storage mechanisms in the resonator will be dominated by the sense beam, with a small perturbative contribution from the support beams. Then it is a sensible first approximation to consider the sense beam in isolation from its environment.

Figure 2.1 Fundamental flexural mode of vibration of a free beam, illustrated via Finite Element simulation in COMSOL Multiphysics®. The undeformed geometry is in solid outline; the deformed mode shape is in solid black. Note that the deformations are greatly exaggerated for clarity.

The simplest possible geometric model that forms a reasonable approximation to an XBR system is that of a slender cuboid in space representing the sense beam under no constraint at any of the boundaries. Provided that the assumptions of the Euler-Bernoulli theory are met, then such a body can be well approximated as a thin beam. The resulting mode shapes and natural frequencies following from such an analysis are well known. However, since this model forms the basis for subsequent analysis, the procedure is repeated here in some detail for context.

2.1.1 Euler-Bernoulli Lagrangian

First, the problem must be defined. The system is approximated here as a one-dimensional continuum of length ℓ. An appropriate model for the underlying physics is the Euler-Bernoulli Lagrangian density $d\mathcal{L}_{\mathrm{E-B}}$[16]:

$$d\mathcal{L}_{\mathrm{E-B}} = \left\{\frac{\varrho A}{2}(\dot{u}(x))^2 - \frac{EI}{2}(u''(x))^2\right\} dx \qquad (2.1)$$

The generalised Euler-Lagrange equations for a functional dependent on two variables can be shown to be[17]

$$\frac{\partial \mathcal{L}}{\partial q} - \left(\frac{\partial}{\partial t}\left(\frac{\partial \mathcal{L}}{\partial \dot{q}}\right) + \frac{\partial}{\partial x}\left(\frac{\partial \mathcal{L}}{\partial q'}\right)\right) + \left(\frac{\partial^2}{\partial t^2}\left(\frac{\partial \mathcal{L}}{\partial \ddot{q}}\right) + \frac{\partial^2}{\partial x^2}\left(\frac{\partial \mathcal{L}}{\partial q''}\right)\right) = \mathrm{Q_{NC}} \qquad (2.2)$$

where $\mathcal{L} \equiv \int_0^{\ell} d\mathcal{L}_{\mathrm{E-B}}\, dx$. and $\mathrm{Q_{NC}}$ is the nonconservative generalised force corresponding to the coordinate q. Applying (2.2) to (2.1) with $q = u$ and differentiating under the integral leads to the general equation of motion for the model:

$$\int_0^{\ell} \{\varrho A\ddot{u} - EIu''''\}\, dx = 0 \qquad (2.3)$$

For an elemental length, the integral can be dropped to give the equation of motion in PDE form:

$$\ddot{u} - \frac{EI}{\varrho A}u'''' = 0 \qquad (2.4)$$

2.1.2 Separation of Variables

By assuming a separable solution of the form

$$u(x,t) = X(x)T(t) \qquad (2.5)$$

one can pose (2.4) in the form

$$X(x)\ddot{T}(t) + c^2X''''^{(x)}T(t) = 0;\ c^2 = \frac{EI}{\varrho A_x} \qquad (2.6)$$

Which directly separates by a standard argument to give the coupled spatial and temporal ODEs

$$\frac{c^2}{X(x)}X''''(x) = -\frac{1}{T(t)}\ddot{T}(t) = \omega^2 \qquad (2.7)$$

Equations (2.7) are usually expressed in the standard form

$$X''''(x) - \beta^4 X(x) = 0;\ \beta^4 = \frac{\omega^2}{c^2} \tag{2.8}$$

$$\ddot{T}(t) + \omega^2 T(t) = 0 \tag{2.9}$$

The temporal equation (2.9) is that of a simple harmonic oscillator. Its general solution is well known to be given by

$$T(t) = Ae^{i\omega t} + Be^{-i\omega t} \tag{2.10}$$

Where A and B are arbitrary constants. The spatial equation (2.8) is a biharmonic equation. Its solutions are the mode shapes and mode factors for the system. From a mathematical perspective, the infinite dimensional Sobolev space of functions on the domain of definition with bounded differentials up to third order has a subspace which is invariant under the differential operator. Assuming a solution of the form $e^{s\omega x}$ and substituting into (2.8) leads to the eigenvalue equation

$$s^4 - \beta^4 = 0 \tag{2.11}$$

The four roots of this equation are given by

$$s_n i^n = \beta\ , n \in \{1,2,3,4\} \tag{2.12}$$

Hence, the general solution to (2.8) is given by

$$X(x) = Ae^{i\beta x} + Be^{-i\beta x} + Ce^{\beta x} + De^{-\beta x} \tag{2.13}$$

Where A, B, C, D are arbitrary constants to be determined by the application of boundary conditions. Finding these solutions reduces the original infinite dimensional differential PDE to an algebraic problem of dimension four for each particular value of β; hence the four arbitrary constants. This formulation gives a complete description of the possible continuum of (seperable) solutions to the PDE under rather general conditions. However, imposing particular finite boundary conditions constrains the possible values of β for which the solutions exist to a set of discrete points. Mathematically, the spectrum of the operator on a finite interval is discrete; physically, reflections at the boundaries are only coherent at particular frequencies. An arbitrary initial configuration will in general have energetic components in all of the coherent modes, each of which will oscillate at its corresponding frequency. These frequencies are what is meant by natural frequencies; the corresponding solutions are normal

modes of vibration. In Section 2.1.3, the natural frequencies and modes will be derived for the free beam. It will be convenient for this purpose to have the solution and its derivatives rearranged into the equivalent forms

$$\left.\begin{aligned} X(x) &= A\sin(\beta x) + B\cos(\beta x) + C\sinh(\beta x) + D\cosh(\beta x) \\ \beta X'^{(x)} &= A\cos(\beta x) - B\sin(\beta x) + C\cosh(\beta x) + D\sinh(\beta x) \\ \beta^2 X''^{(x)} &= -A\sin(\beta x) - B\cos(\beta x) + C\sinh(\beta x) + D\cosh(\beta x) \\ \beta^3 X'''^{(x)} &= -A\cos(\beta x) + B\sin(\beta x) + C\cosh(\beta x) + D\sinh(\beta x) \end{aligned}\right\} \quad (2.14)$$

2.1.3 Natural Frequencies and Mode Shapes

The arbitrary constants in (2.13) are determined by the application of boundary conditions. Algebraic considerations require exactly four boundary conditions for a determined system. The freedom of the ends from any forces or moments leads to the assertion that

$$EI\frac{\partial^3 X}{\partial x^3}\bigg|_{x=0} = EI\frac{\partial^2 X}{\partial x^2}\bigg|_{x=0} = EI\frac{\partial^3 X}{\partial x^3}\bigg|_{x=\ell} = EI\frac{\partial^2 X}{\partial x^2}\bigg|_{x=\ell} = 0 \quad (2.15)$$

Substitution of (2.15) into (2.14) and observing that the functions cos and cosh have value unity, while sin and sinh are zero, when their respective arguments are zero leads immediately to

$$C = A; \;\; B = D \quad (2.16)$$

The solution and its derivatives can then be written in the form

$$\left.\begin{aligned} X(x) &= A[\sin(\beta x) + \sinh(\beta x)] + B[\cos(\beta x) + \cosh(\beta x)] \\ X'(x) &= A[\cos(\beta x) + \cosh(\beta x)] + B[-\sin(\beta x) + \sinh(\beta x)] \\ X''(x) &= A[-\sin(\beta x) + \sinh(\beta x)] + B[-\cos(\beta x) + \cosh(\beta x)] \\ X'''(x) &= A[-\cos(\beta x) + \cosh(\beta x)] + B[\sin(\beta x) + \sinh(\beta x)] \end{aligned}\right\} \quad (2.17)$$

Substituting (2.17) into the third boundary condition (2.15) implies that

$$A\frac{[\sin(\beta\ell) - \sinh(\beta\ell)]}{[\cosh(\beta\ell) - \cos(\beta\ell)]} = B \quad (2.18)$$

The mode shapes are thus determined to within an arbitrary constant as

$$X(x) = A[\sin(\beta x) + \sinh(\beta x)] + \frac{[\sin(\beta\ell) - \sinh(\beta\ell)]}{[\cosh(\beta\ell) - \cos(\beta\ell)]}[\cos(\beta x) + \cosh(\beta x)] \tag{2.19}$$

Note that the third and fourth boundary conditions can be written in the form

$$\begin{bmatrix} -\sin(\beta x) + \sinh(\beta x) & -\cos(\beta x) + \cosh(\beta x) \\ -\cos(\beta x) + \cosh(\beta x) & \sin(\beta x) + \sinh(\beta x) \end{bmatrix} \begin{bmatrix} A \\ B \end{bmatrix} = \underline{0} \tag{2.20}$$

For a nontrivial solution, the rows and columns of the matrix must be linearly dependent. Expanding the determinant and equating to zero gives

$$([-\sin(\beta\ell) + \sinh(\beta\ell)] \times [\sin(\beta\ell) - \sinh(\beta\ell)]) - ([-\cos(\beta\ell) + \cosh(\beta\ell)] \times [-\cos(\beta\ell) - \cosh(\beta\ell)]) = 0 \tag{2.21}$$

Finally, after some tedious manipulation, we arrive at the spectral equation for the free-free beam:

$$\cot(\beta\ell)\cosh(\beta\ell) = \operatorname{cosec}(\beta\ell) \tag{2.22}$$

This transcendental equation has an infinite discrete set of solutions β_n, as is most clearly illuminated graphically.

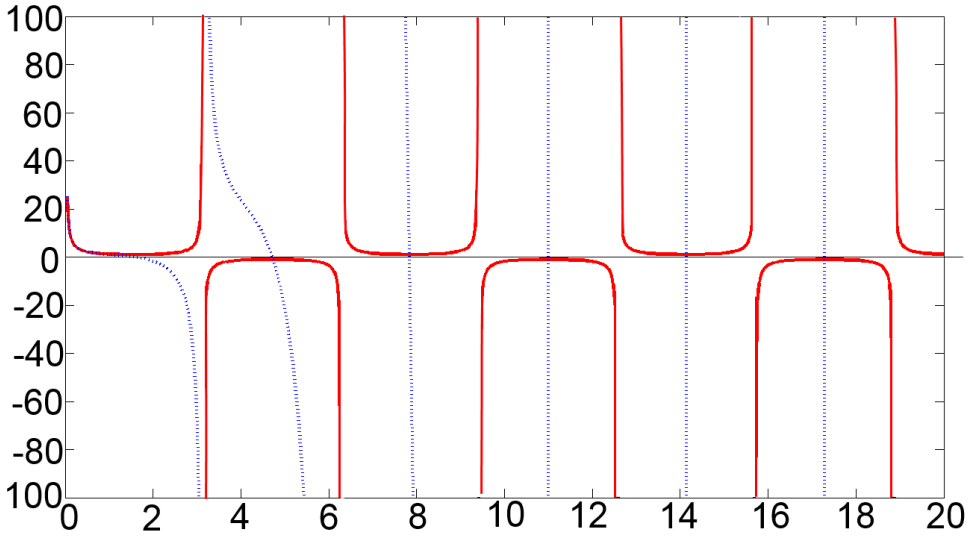

Figure 2.2 Frequency equation of a free-free beam, plotted against the argument βl. The blue dashed line is the left hand side of 2.22; the red solid line is the right hand side; their intersections are the discrete spectrum $\beta_n\ell$.

The first ten values of the solutions $\beta_n \ell$, $n \in \{1:10\}$ to (2.22) are collected below in Table 2.1, for convenient reference in the sequel.

	$\beta_n \ell$			
Mode Order(N)	Free-Free	Clamped-Clamped	Pinned-Pinned	Clamped-Free
1	4.7300	4.7300	π	1.8751
2	7.8532	7.8532	2π	4.6941
3	10.9956	10.9956	3π	7.8548
4	14.1372	14.1372	4π	10.9955
5	17.2788	17.2788	5π	14.1372
6	20.4204	20.4204	6π	17.2788
7	22.5619	22.5619	7π	20.4204
8	26.7035	26.7035	8π	22.5619
9	29.8451	29.8451	9π	26.7035
10	32.9867	32.9867	10π	29.8451

Table 2.1 Values of $\beta_n \ell$ for the first ten modes of a beam under selected boundary conditions commonly encountered in the sequel.

Once β_n is determined, rearranging (2.4) immediately delivers the corresponding natural frequencies

$$\omega_n = \sqrt{\frac{\varrho A \left(\beta_n \ell\right)^4}{EI \ell^4}} \tag{2.23}$$

2.2 Transduction Model

The simple model above is surprisingly efficient as a qualitative description of the unforced behaviour of an XBR. However, time-dependent conditions and resulting behaviour arising from signal transduction, forcing to maintain vibratory amplitude, field interaction (in the XBM extension), etc. are beyond its scope. The above model is modified in this section such as to capture some of these effects.

2.2.1 Modified Lagrangian density: Capacitive effect

In this subsection, a Lagrangian accounting for the physics of the coupled beam and electrostatic transducers system is formulated, beginning with the Lagrangian density from Section 2.1.1. The capacitive transducers can be modelled by adding a term to (2.1) in order to account for energy storage in the capacitors, which are modelled as approximately parallel plates. The energy storage density is then of the form:

$$\frac{\varepsilon_0 w}{2(h_0 - u(x,t))} V(t)^2 dx \tag{2.24}$$

where in (2.24), w is the out-of-plane depth, ε_0 is the permittivity of free space and the other terms are defined in Figure 2.3.

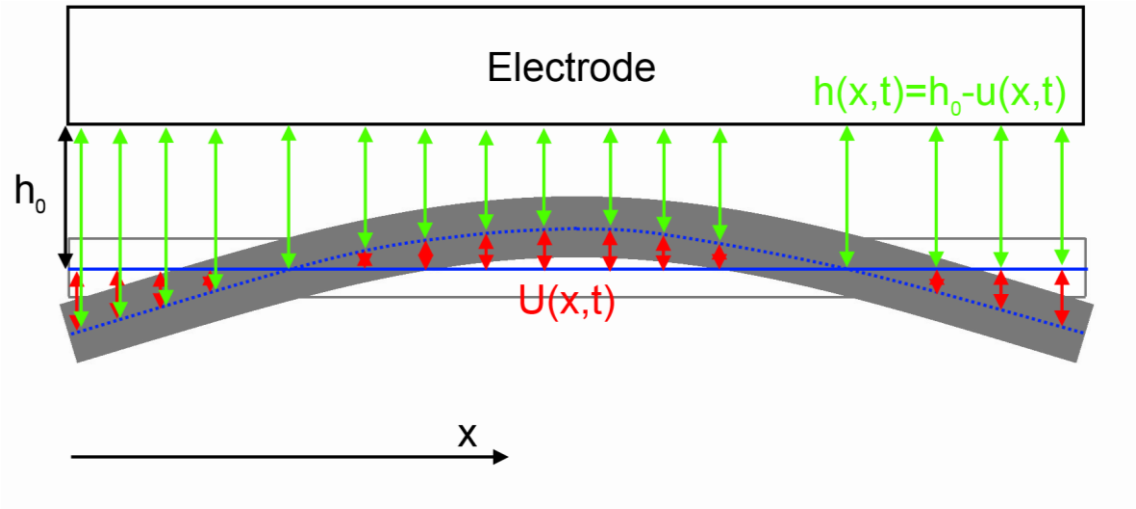

Figure 2.3 Illustration of the choice of variables for formulating the electrostatic dynamics. The sense is reversed for the same choice of sense beam displacement coordinate for a symmetric configuration, with a second electrode beneath the sense beam (omitted from the figure for clarity).

A *symmetric* arrangement of capacitors about the sense beam with identical functional characteristics will each possess an energy storage function of the form above, but

with opposing sense on u. Assuming separate time dependent voltages $V_1(t)^2$ and $V_2(t)^2$ are applied to the top and bottom plate electrode respectively, the energy storage in a differential element for a symmetric arrangement of electrodes can be written

$$\left[\frac{\varepsilon_0 w}{2(h_0-u)}V_1(t)^2+\frac{\varepsilon_0 w}{2(h_0+u)}V_2(t)^2\right]dx \tag{2.25}$$

One important detail of the capacitive effects has not yet been accounted for: the geometry of the device does not allow for the electrodes to easily span its entire length. In practical implementations, it is more straightforward to have electrodes symmetrically arranged about the internodal portion of the sense beam. If $\mathbb{m}$ is defined as the *electrode ratio* or the relative length of one of the two unplated regions of the sense beam distal to the centroid of the device to the total length ℓ of the sense beam, then it is possible to account for the spatially inhomogeneous plating configuration symbolically by taking the product of the capacitive energy storage term with appropriate Heaviside step functions. For the differential element, define dV_{CAP} as the stored potential energy in the capacitor, assuming the parallel plate approximation: $H(x)$ as the Heaviside step function, and write

$$dV_{\mathrm{CAP}}=[H(x-\ell\mathbb{m})-H(x-\ell(1-\mathbb{m}))]\left[\frac{\varepsilon_0 w}{2(h_0-u)}V_1(t)^2+\frac{\varepsilon_0 w}{2(h_0+u)}V_2(t)^2\right]dx \tag{2.26}$$

The idealised Hamiltonian system presented above fails to capture the effects of dissipation arising from such sources as thermoelastic effects, material damping, support loss, viscous damping by the atmosphere, acoustic radiation, and others. Since the interest lies in excitation at resonance, this is unacceptable. One simple approach is to include a Rayleigh dissipation function of the form

$$dR=\frac{C_D}{2}\dot{u}^2dx \tag{2.27}$$

Where C is an assumed damping coefficientThus modified, the Lagrangian density for the model can be written:

$$d\mathcal{L}_{\mathrm{E-B}}=dT^*_{\mathrm{E-B}}-dV_{\mathrm{E-B}}+dR \tag{2.28}$$

And the corresponding nonconservative capacitive force is

$$\frac{\partial}{\partial u} dV_{\mathrm{CAP}} \tag{2.29}$$

2.2.2 Modified Lagrangian density: Mechanical nonlinearity

The Euler-Bernoulli Lagrangian is derived on the basis of linear theory. In real systems, several sources of nonlinear mechanical restorative force can manifest. A typical problem in beam resonators clamped at both ends is midplane stretching. Since the supports of an XBR fit this description, it is desirable to be able to study the effect of introducing such a nonlinearity into the problem. Within the Lagrangian framework, this is achieved in a straightforward fashion by the inclusion of higher order contributions to the elastic potential energy. From Section 2.1, the linear form is

$$dV_{\mathrm{LINEAR}} = \frac{EI}{2}(u'')^2 \tag{2.30}$$

A general nonlinear elastic restorative force can be represented as a power series in u'', the first few terms of which can be written explicitly in the form

$$\frac{K_{\mathrm{q}}}{3}(u'')^3 + \frac{K_{\mathrm{c}}}{4}(u'')^4 + \cdots \tag{2.31}$$

Where the coefficients K_q and K_c represent the quadratic and cubic Taylor coefficients of the nonlinear restorative force respectively, dependent on the particulars of the nonlinearity. Then, the elastic potential energy stored in an infinitesimal beam element can be written as

$$dV_{\mathrm{NONLINEAR}} = \frac{EI}{2}(u'')^2 + \frac{K_q}{3}(u'')^3 + \frac{K_c}{4}(u'')^4 \tag{2.32}$$

2.2.3 Electrode Voltages

It will be necessary in what follows to specify the time dependence of the voltages explicitly. Assume that the imposed signal is piecewise smooth and periodic over an interval $\left(\frac{\omega_n+\lambda}{2}\right)$ where λ is a parameter describing the mistuning of the excitation from the natural frequency ω_n. Then each voltage can be expanded as a Fourier series without further loss of generality:

$$\left.\begin{aligned} V_1(t) = \bar{V}_1 \boldsymbol{V}_1(t) = \bar{V}_1 \left(\mathbb{V}_{1\mathrm{DC}} + \sum_{n=1}^{\infty} \begin{matrix} \mathrm{A}_1^n \mathrm{e}^{\pi n i\{(\omega_n+\lambda)t+\phi\}} \\ +B_1^n \mathrm{e}^{-\pi n i\{(\omega_n+\lambda)t-\phi\}} \end{matrix} \right) \\ V_2(t) = \bar{V}_2 \boldsymbol{V}_2(t) = \bar{V}_2 \left(\mathbb{V}_{2\mathrm{DC}} + \sum_{n=1}^{\infty} \begin{matrix} \mathrm{A}_2^n \mathrm{e}^{\pi n i\{(\omega_n+\lambda)t+\phi\}} \\ +B_2^n \mathrm{e}^{-\pi n i\{(\omega_n+\lambda)t-\phi\}} \end{matrix} \right) \end{aligned}\right\} \quad (2.33)$$

Where in (2.33), $\mathbb{V}_{1\mathrm{DC}}$ and $\mathbb{V}_{2\mathrm{DC}}$ are DC biases applied to the top and bottom electrode respectively, and the A_m^n and B_m^n.are the Fourier coefficients. To specify the voltages, it remains to choose the coefficients. The interest here lies in a parametrically pumped magnetometer, forced electrostatically at resonance. These considerations mandate the presence of harmonic content in the time-dependent terms at the natural frequency and at an integer multiple thereof. It is known[18] that the primary parametric resonance, which occurs for parametric modulation in the vicinity of twice the underlying natural frequency, is both stronger and more stable than the overtone parametric resonances. It is thus logical to excite primary parametric resonance and it is therefore desired to have independent modulation of the system at frequencies close to ω_n and $2\omega_n$.

However, there is a complication. Parasitic capacitances (primarily that from the forcing electrode to the sense electrode) lead to forcing signal feedthrough. If the forcing is chosen naively at ω_n, a situation can arise in which feedthrough is orders of magnitude larger than the signal generated by the vibrational response of the resonator.

A simple observation about the physics of forcing and feedthrough suggests a scheme to mitigate this problem. The quantity of sense interest is measured by a displacement current (Cf. Chapter 6). The feedthrough current is of the form

$$I_{FT} = C_p \frac{\partial V}{\partial t} \quad (2.34)$$

Where I_{FT}represents the feedthrough current signal, C_p the parasitic capacitance between the excitation and sense electrodes, and V the applied excitation voltage. For a time-harmonic signal, the derivative operator leads to a scaling and a phase shift, but no change in the harmonic content. On the other hand, the form of the corresponding forcing and parametric terms is:

$$F, P \propto \left(\frac{\varepsilon_0 w}{(h_0 - u)} V_2(t)^2 + \frac{\varepsilon_0 w}{(h_0 + u)} V_1(t)^2\right) \tag{2.35}$$

where F and P are understood here to be the forcing and parametric modulation contributions arising from the applied voltages. The manifestly quadratic dependency interacts with the harmonic content of the forcing voltage in an interesting and nontrivial way, as made plain by the identity:

$$\begin{aligned}
&\left(\alpha_{\mathrm{DC}} + \alpha_1\left[e^{i\omega_1 t} + e^{-i\omega_1 t}\right] + \alpha_2\left[e^{i\omega_2 t} + e^{-i\omega_2 t}\right]\right)^2 \\
&\equiv \alpha_1^2\left[e^{2i\omega_1 t} + e^{-2i\omega_1 t}\right] + \alpha_2^2\left[e^{2i\omega_2 t} + e^{-2i\omega_2 t}\right] \\
&+[\alpha_{\mathrm{DC}}^2 + 2\alpha_1^2 + 2\alpha_2^2] + 2\alpha_1\alpha_2\left[e^{i(\omega_1+\omega_2)t} + e^{-i(\omega_1+\omega_2)t}\right] \\
&+2\alpha_1\alpha_2\left[e^{i(\omega_1-\omega_2)t} + e^{-i(\omega_1-\omega_2)t}\right] + 2\alpha_{\mathrm{DC}}\alpha_1\left[e^{i\omega_1 t} + e^{-i\omega_1 t}\right] \\
&+ 2\alpha_{\mathrm{DC}}\alpha_2\left[e^{i\omega_2 t} + e^{-i\omega_2 t}\right]
\end{aligned} \tag{2.36}$$

That is, if we have harmonic content at two discrete frequencies present in a DC-biased signal, then squaring the signal introduces frequency domain components at the sum and difference of the frequencies and at twice the original frequencies, as well as the original frequencies and a DC component. The crucial point is that the physics relating applied capacitive voltages and the resulting forcing can be exploited to introduce spectral content to the forcing not present in, and incommensurate to, that present in the voltage signals themselves. This can be exploited to separate the feedthrough from the signal in the frequency domain.

To achieve the goals set out above, the applied voltage amplitudes are specified by Equations (2.37), leaving the phases of the harmonic components to be determined:

$$\begin{aligned}
\mathbb{V}_{1\mathrm{DC}} &= \mathbb{V}_{2\mathrm{DC}} = \mathbb{V}_{\mathrm{DC}} \\
|\mathrm{A}_1^1| &= \mathbb{V}_{\frac{1}{2}} \\
|\mathrm{A}_1^4| &= \mathbb{V}_2 \\
\left|\mathrm{A}_1^i\right| &= 0, i \neq 1,4 \\
\mathrm{B}_j^i &= \left(\mathrm{A}_j^i\right)^* \\
\left|\mathrm{A}_2^i\right| &= 0, \forall i \in \mathbb{Z}
\end{aligned} \tag{2.37}$$

Where in (2.37), $\mathbb{V}_{\mathrm{DC}}$ is a constant. The equations specify the harmonic content of the voltage on electrode 1, and hence of the feedthrough, to be in the vicinity of $\frac{\omega_n}{2}$ and $2\omega_n$. In particular, the feedthrough contains no components close to ω_n. Meanwhile, electrode 2 carries only a DC bias, equal in value to that of electrode 1, corresponding to its function as a capacitive pickoff.

The identity given above implies that the resultant forcing signal exerted on the resonator will carry harmonic content at DC, $\frac{\omega_n}{2}$, ω_n, $\frac{3\omega_n}{2}$, $2\omega_n$, $\frac{5\omega_n}{2}$,and $4\omega_n$. By using a lock-in amplifier or other notch-pass filter on the output signal to reject frequency components away from ω_n, this arrangement strongly reduces the feedthrough seen at the filter output, and thereby greatly mitigates one of the most persistent problems in designing practical microscale devices.

2.2.4 Method of Assumed Modes

The Lagrangian developed thus far in this section was derived by modification from that of a free-free beam, with the modifications coming from inhomogeneity of the coefficients in space and time, nonlinearity, and damping. The resulting equation of motion can be described as a nonlinear Hill equation[19]. The simple trial solution method of Section 2.1 fails, and the general solution of this problem is not analytically available. To gain some traction, again assume a separable solution defined to have the form

$$u(x,t) = \sum_{i=1}^{n} X_i(x) T_i(t) \tag{2.38}$$

This assumes that the forced response of the inhomogeneous, nonlinear system can be adequately described by a single generalised coordinate dictating the temporal behaviour of a corresponding modal displacement function. This is justified under the conditions that the nonlinearities and damping are small and hence can be treated as perturbations, while the harmonic content of the inhomogeneity is concentrated in the vicinity of the natural frequency of the fundamental mode (and an integer multiple thereof, which is not close to the second natural frequency).

To recap, the Lagrangian and nonconservative forces for the system are

$$\mathcal{L}(x,t) = \int_0^{\ell} d\mathcal{L}\, dx$$

$$= \int_0^{\ell} \left[\frac{\varrho A}{2}(\dot{u})^2 - \left(\frac{EI}{2}(u'')^2 + \frac{K_q}{3}(u'')^3 + \frac{K_c}{4}(u'')^4\right) + \frac{C}{2}\dot{u}^2\right] dx$$

$$Q_{\mathrm{NC}} = \frac{\partial}{\partial q_i}(\delta W_{\mathrm{NC}}) \tag{2.39}$$

Where δW_{NC} is the virtual work associated with the nonconservative electrostatics. The appropriate form of the Euler-Lagrange equation is given by (2.2). An explicit form remains to be derived for δW_{NC} and hence for Q_{nc}. Substituting the ansatz (2.38) into (2.2) yields the force acting on an infinitesimal beam element as

$$F_{\mathrm{CAP}} = \frac{\partial}{\partial T}(dV_{\mathrm{CAP}}) = \left[H(x - L\mathbb{m}) - H\big(x - L(1-\mathbb{m})\big)\right]$$

$$\times \frac{\varepsilon_0 w}{2h_0}\left(V_1{}^2\left[\frac{X}{h_0} + 2\frac{X^2T}{h_0^2} + 3\frac{X^3T^2}{h_0^3} + 4\frac{X^4T^3}{h_0^4} + \cdots\right] + V_2{}^2\left[-\frac{X}{h_0} + 2\frac{X^2T}{h_0^2} - 3\frac{X^3T^2}{h_0^3} + 4\frac{X^4T^3}{h_0^4} + \cdots\right]\right) \tag{2.40}$$

The method of assumed modes requires a choice of approximating shape functions X_i. A one-mode approximation is considered to elicit the qualitative features of the response and to simplify the analysis that follows; the extension to more approximating functions is considered in Chapter 3. The summation in (2.38) disappears; $u(x,t) = \sum_{i=1}^{n} X_i(x)T_i(t)$ becomes

$$u(x,t) = XT \tag{2.41}$$

The generalised force is given by the integral of the product of the force distribution and the mode shape X:

$$Q_{\mathrm{NC}} = \int_{\ell_{\mathbb{m}}}^{\ell(1-\mathbb{m})} \frac{\varepsilon_0 w}{2h_0}\left({V_1}^2\left[\frac{X^2}{h_0} + 2\frac{X^3T}{h_0^2} + 3\frac{X^4T^2}{h_0^3} + 4\frac{X^5T^3}{h_0^4}\right] + {V_2}^2\left[-\frac{X^2}{h_0} + 2\frac{X^3T}{h_0^2} - 3\frac{X^4T^2}{h_0^3} + 4\frac{X^5T^3}{h_0^4}\right]\right)dx$$

$$= \left\{\frac{\varepsilon_0 w\left({V_1}^2 - {V_2}^2\right)}{2h_0^2}\int_{\ell_{\mathbb{m}}}^{\ell(1-\mathbb{m})} X^2 dx\right\} + T\left\{\frac{\varepsilon_0 w\left({V_1}^2 + {V_2}^2\right)}{h_0^3}\int_{\ell_{\mathbb{m}}}^{\ell(1-\mathbb{m})} X^3 dx\right\}$$

$$+ T^2\left\{\frac{3\varepsilon_0 w\left({V_1}^2 - {V_2}^2\right)}{2h_0^4}\int_{\ell_{\mathbb{m}}}^{\ell(1-\mathbb{m})} X^4 dx\right\}$$

$$+ T^3\left\{\frac{2\varepsilon_0 w\left({V_1}^2 + {V_2}^2\right)}{h_0^5}\int_{\ell_{\mathbb{m}}}^{\ell(1-\mathbb{m})} X^5 dx\right\} \tag{2.42}$$

Combining (2.38), (2.39), (2.41) and (2.42), the equation of motion for the beam system is derived as

$$\int_0^{\ell}\left(\frac{\partial}{\partial t}\frac{\partial}{\partial \dot{T}}\left[\frac{\varrho A}{2}\left(X\dot{T}\right)^2\right]+\frac{\partial}{\partial T_i}\left[\frac{EI}{2}(X''T)^2+\frac{K_q}{3}(X''T)^3+\frac{K_c}{4}(X''T)^4\right]+\frac{\partial}{\partial \dot{T}_i}\frac{C}{2}\left(X\dot{T}\right)^2\right)dx$$

$$=\int_{\ell\mathbb{m}}^{\ell(1-\mathbb{m})}\frac{\partial}{\partial T_i}\left(\frac{\varepsilon_0 w}{h_0}\left[\left(V_1{}^2+V_2{}^2\right)\frac{XT}{h_0}+2\left(V_1{}^2-V_2{}^2\right)\frac{(XT)^2}{h_0^2}+3\left(V_1{}^2+V_2{}^2\right)\frac{(XT)^3}{h_0^3}+4\left(V_1{}^2-V_2{}^2\right)\frac{(XT)^4}{h_0^4}+\cdots\right]\right)dx \tag{2.43}$$

Collecting terms in powers of and derivatives of T yields

$$\int_0^{\ell}\left(\ddot{T}\left\{\varrho A\int_0^{\ell}X^2dx\right\}+\left[\left\{EI\int_0^{\ell}X''^2dx\right\}T+\left\{K_q\int_0^{\ell}X''^3dx\right\}T^2+\left\{K_c\int_0^{\ell}X''^4dx\right\}T^3\right]+\left\{C\int_0^{\ell}X^2dx\right\}\dot{T}\right)dx$$

$$=\left\{\frac{\varepsilon_0 w\left(V_1{}^2-V_2{}^2\right)}{2h_0^2}\int_{\ell\mathbb{m}}^{\ell(1-\mathbb{m})}X^2dx\right\}+T\left\{\frac{\varepsilon_0 w\left(V_1{}^2+V_2{}^2\right)}{h_0^3}\int_{\ell\mathbb{m}}^{\ell(1-\mathbb{m})}X^3dx\right\}$$

$$+T^2\left\{\frac{2\varepsilon_0 w\left(V_1{}^2-V_2{}^2\right)}{2h_0^4}\int_{\ell\mathbb{m}}^{\ell(1-\mathbb{m})}X^4dx\right\}$$

$$+T^3\left\{\frac{3\varepsilon_0 w\left(V_1{}^2+V_2{}^2\right)}{h_0^5}\int_{\ell\mathbb{m}}^{\ell(1-\mathbb{m})}X^5dx\right\} \tag{2.44}$$

The integral forms of the coefficients given above are somewhat unwieldy. To expedite the analysis, it serves to recast the equations into a simpler form. To wit, define the parameters

$$
\left.
\begin{gathered}
M = \left\{ \varrho A \int_0^{\ell} X^2 dx \right\} \quad 2\xi\omega_n = \left\{ i\omega_n C \int_0^{\ell} X\dot{X} dx \right\} \\
K_0 = \left\{ EI \int_0^{\ell} dx \right\} \quad \omega_n^2 = \frac{K_0}{M} \\
K_{E11} = \frac{\varepsilon_0 w \left(\overline{V_1^{\,2}}\right)}{h_0^3} \int_{\ell\mathbb{m}}^{\ell(1-\mathbb{m})} X^2 X'''' dx \quad K_{E12} = R_1 K_{E11} \\
K_{Eq1} = \left\{ \frac{3\varepsilon_0 w \left(\overline{V_1^{\,2}}\right)}{2h_0^4} \int_{\ell\mathbb{m}}^{\ell(1-\mathbb{m})} X^3 X'''' dx \right\} \quad K_{Eq2} = R_1 K_{Eq1} \\
K_{Ec1} = \left\{ \frac{2\varepsilon_0 w \left(\overline{V_1^{\,2}}\right)}{h_0^5} \int_{\ell\mathbb{m}}^{\ell(1-\mathbb{m})} X^4 X'''' dx \right\} \quad K_{Ec2} = R_1 K_{Ec1} \\
\omega_q^2 = \frac{K_q}{M} \\
\omega_c^2 = \frac{K_c}{M} \\
F_1 = \left\{ \frac{\varepsilon_0 w \left(\overline{V_1^{\,2}}\right)}{2h_0^2} \int_{\ell\mathbb{m}}^{\ell(1-\mathbb{m})} X^2 dx \right\} \quad F_2 = R_1 F_1 \\
\epsilon = \frac{K_{E11}}{K_0} \quad R_1 = \frac{\overline{V_2}^{\,2}}{\overline{V_1}^{\,2}} \quad \epsilon q = \frac{K_{Eq1}}{K_q} \quad \epsilon c = \frac{K_{Ec1}}{K_c} \\
\epsilon v = 2\xi = \frac{1}{Q} \quad \epsilon F = \frac{F_1}{M}
\end{gathered}
\right\} \quad (2.45)
$$

These parameters have physical significance. In particular, ω_n^2 is the Rayleigh's quotient of the assumed mode shape (Cf. Chapter 3) with no applied voltages on the electrodes, such that ω_n is a very good approximation to the fundamental mechanical resonance frequency of the system provided that $X(x)$ is a good approximation to the true mode shape; K_0 and M represent the generalised mechanical stiffness and mass respectively corresponding to the assumed mode shape; K_{Eij} is the electrostatic

generalised (stiffness) coefficient of the i^{th} power of T for the j^{th} electrode; F_i the component of displacement-independent classical generalised forcing corresponding to the ith electrode, and ε_i the quotient of the electrostatic softening coefficient arising from the ith electrode by the mechanical stiffness. The coefficients are normalised by the generalised mass to simplify analysis.

It remains to choose a suitable trial function X. The a priori design purpose of the XBR leads directly to the use of the fundamental free-free mode of the sense beam, which is denoted here as $X_{FF}^{(1)}$. It was derived in Section 2.1 as

$$X_{FF}^{(1)}(x) = A[\sin\left(\frac{\beta_{(1)}x}{\ell}\right) + \sinh\left(\frac{\beta_{(1)}x}{\ell}\right) + \alpha_{(1)}\left\{\cosh\left(\frac{\beta_{(1)}x}{\ell}\right) + \cos\left(\frac{\beta_{(1)}x}{\ell}\right)\right\} \quad (2.46)$$

where

$$\alpha_{(n)} = \frac{\sin(\beta_n\ell) - \sinh(\beta_n\ell)}{\cosh(\beta_n\ell) - \cos(\beta_n\ell)}$$

2.3 Multiple-Scales Singular Perturbation Analysis

The model developed in Section 2.2 not amenable to direct solution as an eigenvalue problem, for two reasons: it is nonautonomous and nonlinear. In its full generality, analytical solutions are not obtainable in closed form. Furthermore, the corresponding dynamics (amplitude dependence of the natural frequency, parametric resonance, etc.) are not exhibited in the linear, time invariant special case. That is to say, the perturbation introduced by these effects is singular, and a regular perturbation analysis will fail to capture them. On the other hand, these effects are typically expected to be unimportant on short time scales. By this heuristic argument, the application of a multiple-timescales singular perturbation analysis appears natural, and this approach is explored in this section.

2.3.1 Introduction of small parameter

Using the definitions of Section 2.2, we can rewrite 2.44 as

$$\ddot{T} + 2\epsilon v\omega_n\dot{T} + \omega_n^2(1 - \epsilon[\{\boldsymbol{V}_1^2\} + R\{\boldsymbol{V}_2^2\}])T + \epsilon\omega_{c1}^2(1 + \mathfrak{c}[\{\boldsymbol{V}_1^2\} - R\{\boldsymbol{V}_2^2\}])T^2 + \epsilon\omega_{q1}^2(1 - \mathfrak{q}[\{\boldsymbol{V}_1^2\} + R\{\boldsymbol{V}_2^2\}])T^3 + O(T^4) = \epsilon F(\{\boldsymbol{V}_1^2\} - R\{\boldsymbol{V}_2^2\}) \quad (2.47)$$

Notice that this equation reduces to an undamped harmonic oscillator in the limit $\epsilon \to 0$ as required.

2.3.2 Linear parametric case

Consider first the case where all nonlinearities are assumed negligible. Also, let the scaling voltages $\overline{V_1}$ and $\overline{V_2}$ be set equal to each other and unity. Then 2.47 reduces to

$$\ddot{T} + 2\epsilon v\omega_n\dot{T} + \omega_n^2(1 - \epsilon[\{\boldsymbol{V}_1^2\} + \{\boldsymbol{V}_2^2\}])T = \epsilon F(\{\boldsymbol{V}_1^2\} - \{\boldsymbol{V}_2^2\}) \quad (2.48)$$

This equation has the form of a damped, forced harmonic oscillator, with nonautonomous stiffness coefficient. Next, define slow and fast timescales and corresponding solutions:

$$\left.\begin{aligned} \hat{t} = t + O(\epsilon^2) \quad \tilde{t} = \epsilon t \\ T = \hat{T}(\hat{t}, \tilde{t}) + \epsilon\tilde{T}(\hat{t}, \tilde{t}) \end{aligned}\right\} (2.49)$$

Differentiation immediately yields

$$\left.\begin{aligned} \frac{\partial T}{\partial t} &= \left(\frac{\partial\hat{t}}{\partial t}\frac{\partial\hat{T}}{\partial\hat{t}} + \frac{\partial\tilde{t}}{\partial t}\frac{\partial\hat{T}}{\partial\tilde{t}}\right) + \epsilon\left(\frac{\partial\hat{t}}{\partial t}\frac{\partial\tilde{T}}{\partial\hat{t}} + \frac{\partial\tilde{t}}{\partial t}\frac{\partial\tilde{T}}{\partial\tilde{t}}\right) \\ &= \frac{\partial\hat{T}}{\partial\hat{t}} + \epsilon\left(\frac{\partial\hat{T}}{\partial\tilde{t}} + \frac{\partial\tilde{T}}{\partial\hat{t}}\right) + O(\epsilon^2) \\ \frac{\partial^2 T}{\partial t^2} &= \frac{\partial^2\hat{T}}{\partial\hat{t}^2} + \epsilon\left(2\frac{\partial^2\hat{T}}{\partial\hat{t}\partial\tilde{t}} + \frac{\partial^2\tilde{T}}{\partial\hat{t}^2}\right) + O(\epsilon^2) \end{aligned}\right\} (2.50)$$

Upon substitution of (2.50) into (2.48) and collecting terms of like order in the small parameter, we obtain the order-one and order-epsilon perturbation equations:

$$O(1): \quad \frac{\partial^2\hat{T}}{\partial\hat{t}^2} + \omega_n^2\hat{T} = 0$$

$$O(\epsilon)\colon \frac{\partial^2 \tilde{T}}{\partial \hat{t}^2} + \omega_n^2 \tilde{T}$$

$$= F(\{\boldsymbol{V}_1^2\} - \{\boldsymbol{V}_2^2\}) - 2\frac{\partial^2 \hat{T}}{\partial \hat{t} \partial \tilde{t}} - 2v\omega_n \frac{\partial \hat{T}}{\partial \hat{t}}$$

$$+ \omega_n^2(\{\boldsymbol{V}_1^2\} + \{\boldsymbol{V}_2^2\})\hat{T} \tag{2.51}$$

The $O(1)$ equation has the form of a simple harmonic oscillator equation in the fast-time dependent variable. The general solution can be written as

$$\hat{T} = \mathrm{B}_1 \mathrm{e}^{i\omega_n \hat{t}} + \mathrm{B}_2 \mathrm{e}^{-i\omega_n \hat{t}} \tag{2.52}$$

However, due to the assumed independence of the timescales, the complex amplitudes B_1 and B_2 can depend on slow time. By physical considerations the response should be a real quantity; the significance of a complex-valued $\hat{T}$ is not clear to the author, at least in the classical context. Making an ansatz for the time dependency of these variables in polar form as

$$\left.\begin{aligned} \mathrm{B}_1 &= \frac{r(\tilde{t})}{2} e^{i(\epsilon\lambda \hat{t} - \theta(\tilde{t}))} \\ \mathrm{B}_2 &= \frac{r(\tilde{t})}{2} e^{-i(\epsilon\lambda \hat{t} - \theta(\tilde{t}))} \end{aligned}\right\} \tag{2.53}$$

Where $\epsilon\lambda$ is a small parameter representing the mistuning of the forcing frequency from the linear natural frequency of the system in fast time, r is an amplitude and θ is a phase offset from the forcing frequency enforces this assumption and leads to

$$T = r(\tilde{t}) \frac{\mathrm{e}^{i(\omega_n \hat{t} + \lambda \tilde{t} - \theta)} + \mathrm{e}^{-i(\omega_n \hat{t} + \lambda \tilde{t} - \theta)}}{2} \equiv r\cos(\omega_n \hat{t} + \lambda \tilde{t} - \theta) \tag{2.54}$$

Basic calculus yields

$$\frac{\partial T}{\partial \hat{t}} = -r\omega_n \sin(\omega_n \hat{t} + \lambda \tilde{t} - \theta) \tag{2.55}$$

$$\frac{\partial^2 T}{\partial \hat{t} \partial \tilde{t}} = -\Big(\dot{r}\omega_n \sin(\omega_n \hat{t} + \lambda \tilde{t} - \theta)$$

$$+ r\big(\lambda - \dot{\theta}\big)\omega_n \cos(\omega_n \hat{t} + \lambda \tilde{t} - \theta)\Big) \tag{2.56}$$

From an intuitive standpoint, the analysis says that the basic form of the response for small nonzero epsilon is well approximated by a harmonic oscillation in real time, modulated "independently" over a long timescale compared to the period of oscillation. The envelope modulation encapsulates the effects of forcing, damping, nonlinearity, and parametric action. Observe that the form of the $O(\epsilon)$ equation (2.51) is again an undamped harmonic oscillator, this time with a nonzero forcing term. This approximation will grow in an unbounded fashion in time if any of the right-hand side terms have frequency-domain content at the resonant frequency. Since the interest lies in bounded solutions, physically interesting solutions correspond to the RHS of (2.51) being identically zero. Imposing this condition constrains the relationships between the forcing terms and the response. These constraints, or solubility conditions, must necessarily be met by any physical solution of the system, under the assumption of boundedness. They can also be manipulated to extract the amplitudes B_1 and B_2; hence, to obtain the total solution to first order.

The RHS of (2.51) can be written in terms of the applied voltages as

$$F(\{\boldsymbol{V}_1^2\} - \{\boldsymbol{V}_2^2\}) + \omega_n^2(\{\boldsymbol{V}_1^2\} + \{\boldsymbol{V}_2^2\})T - 2\frac{\partial^2 T}{\partial \hat{t}\partial \tilde{t}} - 2v\omega_n \frac{\partial T}{\partial \hat{t}} \tag{2.57}$$

Inserting the ansatz, (2.57) can be put as

$$\begin{aligned} F(\{\boldsymbol{V}_1^2\} - \{\boldsymbol{V}_2^2\}) + \omega_n^2(\{\boldsymbol{V}_1^2\} + \{\boldsymbol{V}_2^2\})T \\ + 2\left(\dot{r}\omega_n \sin(\omega_n \hat{t} + \lambda\tilde{t} - \theta) + r(\lambda - \dot{\theta})\omega_n \cos(\omega_n \hat{t} + \lambda\tilde{t} - \theta)\right) \\ + 2vr\omega_n^2 \sin(\omega_n \hat{t} + \lambda\tilde{t} - \theta) \end{aligned} \tag{2.58}$$

Making the time-dependence of the voltages explicit gives the following lengthy expression:

$$F\left\{\frac{\mathbb{V}_{\frac{1}{2}}^2+\mathbb{V}_2^2}{2}+\mathbb{V}_{\frac{1}{2}}^2\left(\frac{\cos(\omega_n\hat{t}+\lambda\tilde{t})}{2}\right)+\mathbb{V}_2^2\left(\frac{\cos\left(4(\omega_n\hat{t}+\lambda\tilde{t})\right)}{2}\right)\right.$$

$$+2\left(\mathbb{V}_{\mathrm{DC}}\mathbb{V}_{\frac{1}{2}}\cos\left(\frac{\omega_n\hat{t}+\lambda\tilde{t}}{2}\right)+\mathbb{V}_{DC}\mathbb{V}_2\cos\left(2(\omega_n\hat{t}+\lambda\tilde{t})\right)\right.$$

$$\left.\left.+\mathbb{V}_{\frac{1}{2}}\mathbb{V}_2\left(\frac{\cos\left(\frac{5(\omega_n\hat{t}+\lambda\tilde{t})}{2}\right)+\cos\left(\frac{3(\omega_n\hat{t}+\lambda\tilde{t})}{2}\right)}{2}\right)\right)\right\}$$

$$+r\omega_n^2\left\{\frac{4\mathbb{V}_{\mathrm{DC}}^2+\mathbb{V}_{\frac{1}{2}}^2+\mathbb{V}_2^2}{2}\left(\cos(\omega_n\hat{t}+\lambda\tilde{t}-\theta)\right)\right.$$

$$+\mathbb{V}_{\frac{1}{2}}^2\left(\frac{\cos(-\theta)+\left(\cos(2(\omega_n\hat{t}+\lambda\tilde{t})-\theta)\right)}{4}\right)$$

$$+\mathbb{V}_2^2\left(\frac{\left(\cos(3(\omega_n\hat{t}+\lambda\tilde{t})-\theta)\right)+\left(\cos(5(\omega_n\hat{t}+\lambda\tilde{t})-\theta)\right)}{4}\right)$$

$$+2\left(\mathbb{V}_{\mathrm{DC}}\mathbb{V}_{\frac{1}{2}}\left(\frac{\left(\cos\left(\frac{3(\omega_n\hat{t}+\lambda\tilde{t})}{2}-\theta\right)\right)+\left(\cos\left(\frac{(\omega_n\hat{t}+\lambda\tilde{t})}{2}-\theta\right)\right)}{2}\right)\right.$$

$$+\mathbb{V}_{\mathrm{DC}}\mathbb{V}_2\left(\frac{\left(\cos(3(\omega_n\hat{t}+\lambda\tilde{t})-\theta)\right)+\left(\cos(\omega_n\hat{t}+\lambda\tilde{t}-\theta)\right)}{2}\right)$$

$$+\mathbb{V}_{\frac{1}{2}}\mathbb{V}_2\left(\frac{\left(\cos\left(\frac{7(\omega_n\hat{t}+\lambda\tilde{t})}{2}-\theta\right)\right)+\left(\cos\left(\frac{3(\omega_n\hat{t}+\lambda\tilde{t})}{2}-\theta\right)\right)}{4}\right)$$

$$\left.+\mathbb{V}_{\frac{1}{2}}\mathbb{V}_2\left(\frac{\left(\cos\left(\frac{(\omega_n\hat{t}+\lambda\tilde{t})}{2}-\theta\right)\right)+\left(\cos\left(\frac{5(\omega_n\hat{t}+\lambda\tilde{t})}{2}-\theta\right)\right)}{4}\right)\right)\right\}$$

$$+2\left(\dot{r}\omega_n\sin(\omega_n\hat{t}+\lambda\tilde{t}-\theta)+r\left(\lambda-\dot{\theta}\right)\omega_n\cos(\omega_n\hat{t}+\lambda\tilde{t}-\theta)\right)$$

$$+2vr\omega_n^2\sin(\omega_n\hat{t}+\lambda\tilde{t}$$

$$-\theta) \qquad (2.59)$$

After applying the trigonometric identity

After applying the trigonometric identity

$$\cos(A+B) \equiv \cos(A)\cos(B) - \sin(A)\sin(B) \tag{2.60}$$

to (2.59), the mixed secular terms in (2.51) are revealed to be

$$\begin{aligned} F\mathbb{V}_{\frac{1}{2}}^2 \left(\frac{\cos(\omega_n \hat{t} + \lambda\tilde{t} - \theta)}{2}\cos(\theta) - \frac{\sin(\omega_n \hat{t} + \lambda\tilde{t} - \theta)}{2}\sin(\theta) \right) \\ + r\omega_n^2 \left\{ \frac{4\mathbb{V}_{DC}^2 + \mathbb{V}_{\frac{1}{2}}^2 + \mathbb{V}_2^2}{2} \left(\cos(\omega_n \hat{t} + \lambda\tilde{t} - \theta)\right) \right. \\ \left. + 4\mathbb{V}_{DC}\mathbb{V}_2 \left(\frac{\left(\cos(\omega_n \hat{t} + \lambda\tilde{t} - \theta)\right)}{2} \right) \right\} \\ + 2\left(\dot{r}\omega_n \sin(\omega_n \hat{t} + \lambda\tilde{t} - \theta) + r\left(\lambda - \dot{\theta}\right)\omega_n \cos(\omega_n \hat{t} + \lambda\tilde{t} - \theta) \right) \\ + 2vr\omega_n^2 \sin(\omega_n \hat{t} + \lambda\tilde{t} - \theta) \end{aligned} \tag{2.61}$$

The coefficients of $\sin(\omega_n \hat{t} + \lambda\tilde{t} - \theta)$ and $\cos(\omega_n \hat{t} + \lambda\tilde{t} - \theta)$ in (2.61) yield the solubility conditions as

$$\dot{r} + vr\omega_n = \frac{F\mathbb{V}_{\frac{1}{2}}^2}{4\omega_n}\sin(\theta) \tag{2.62}$$

$$r\dot{\theta} - r\lambda = \frac{F\mathbb{V}_{\frac{1}{2}}^2}{4\omega_n}\cos(\theta) + \frac{r\omega_n}{4}\left(4\mathbb{V}_{DC}^2 + \mathbb{V}_{\frac{1}{2}}^2 + \mathbb{V}_2^2 + 4\mathbb{V}_{DC}\mathbb{V}_2 \right) \tag{2.63}$$

The steady-state amplitude r_s and phase θ_s for this fundamental system can be seen by setting the derivatives to zero, reducing equations (2.62)-(2.63) to

$$r_s \frac{4v\omega_n^2}{F\mathbb{V}_{\frac{1}{2}}^2} = \sin(\theta_s) \tag{2.64}$$

$$r_s \left(\frac{4\omega_n\lambda + \omega_n^2\left(4\mathbb{V}_{DC}^2 + \mathbb{V}_{\frac{1}{2}}^2 + \mathbb{V}_2^2 + 4\mathbb{V}_{DC}\mathbb{V}_2 \right)}{-F\mathbb{V}_{\frac{1}{2}}^2} \right) = \cos(\theta_s) \tag{2.65}$$

And hence

$$r_s = \frac{F\mathbb{V}_{\frac{1}{2}}^2}{\omega_n^2\sqrt{(4v)^2 + \left(\frac{4\lambda}{\omega_n} + \left(4\mathbb{V}_{DC}^2 + \mathbb{V}_{\frac{1}{2}}^2 + \mathbb{V}_2^2 + 4\mathbb{V}_{DC}\mathbb{V}_2\right)\right)^2}} \tag{2.66}$$

Also

$$-\arctan\left(\frac{v}{\frac{\lambda}{\omega_n} + \left(\mathbb{V}_{DC}^2 + \frac{\mathbb{V}_{\frac{1}{2}}^2 + \mathbb{V}_2^2 + 2\mathbb{V}_{DC}\mathbb{V}_2}{4}\right)}\right) = \theta_s \tag{2.67}$$

These forms are represented graphically in Figure 2.4 below. For a given, fixed choice of the applied voltages and mechanical parameters, the behaviour captures to first order the expected frequency response amplitude and associated phase behaviour, correctly predicting a phase of $\frac{\pi}{2}$ at resonance.

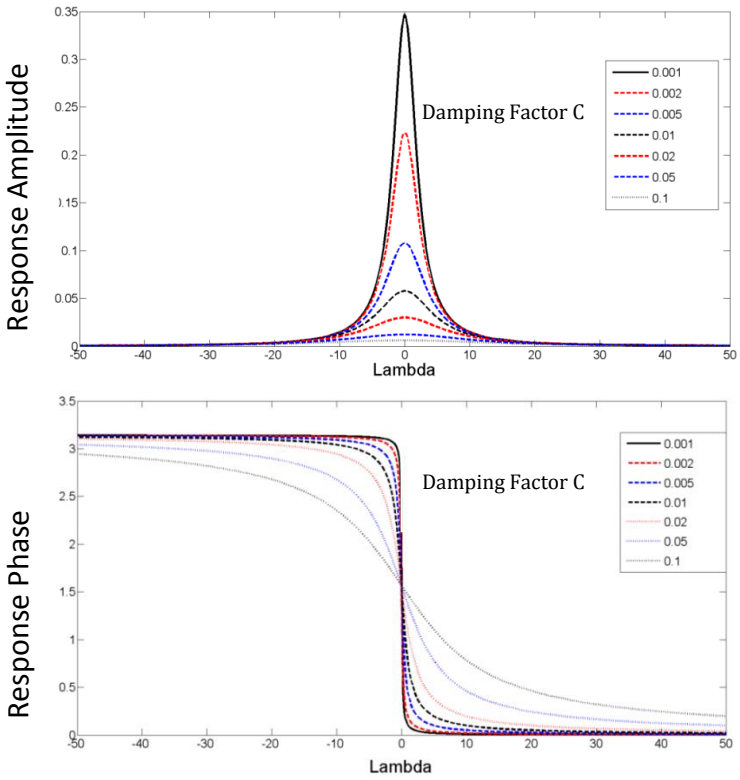

Figure 2.4 Top to bottom, predicted steady-state response and phase as a function of the mistuning parameter, plotted for several different values of the damping.

Choosing the phase of $\mathbb{V}_{\frac{1}{2}}$ to be zero as a datum, measuring the other phases in the system with respect to this "forcing", the steady state response has the form given by (2.66), with the numerator a real constant. Factoring out the real constant ω_n^2, the behaviour of the system at steady state is seen to be governed (to within linear dependence) by the denominator D_S :

$$D_s^2 = (4v)^2 + \left(\frac{4\lambda}{\omega_n} + \left(4\mathbb{V}_{DC}^2 + \mathbb{V}_{\frac{1}{2}}^2 + \mathbb{V}_2^2 + 4\mathbb{V}_{DC}\mathbb{V}_2\right)\right)^2 \qquad (2.68)$$

Considering the denominator as a complex-valued function of the complex applied voltage amplitudes, the response has a pole when $D_S = 0$. If the complex-valued voltage constants are chosen such that this condition is met, then the steady state response is infinite: this corresponds to parametric instability of the system. The classical result obtained by Gallacher et al. [8] imposes a restriction on the phase of the parametric term of the form $\text{Phase}(\mathbb{V}_2) = \pm\frac{\pi}{2}$ so that the arctan in (2.67) always evaluates as $\frac{\pi}{2}$, independent of the level of damping; this corresponds to making $\mathbb{V}_2$ purely imaginery in (2.68), reducing it to Gallacher's result.

Taking a step back, the overarching purpose of using a second harmonic parametric modulation term, as provided by $\mathbb{V}_2$, is to achieve parametric amplification.

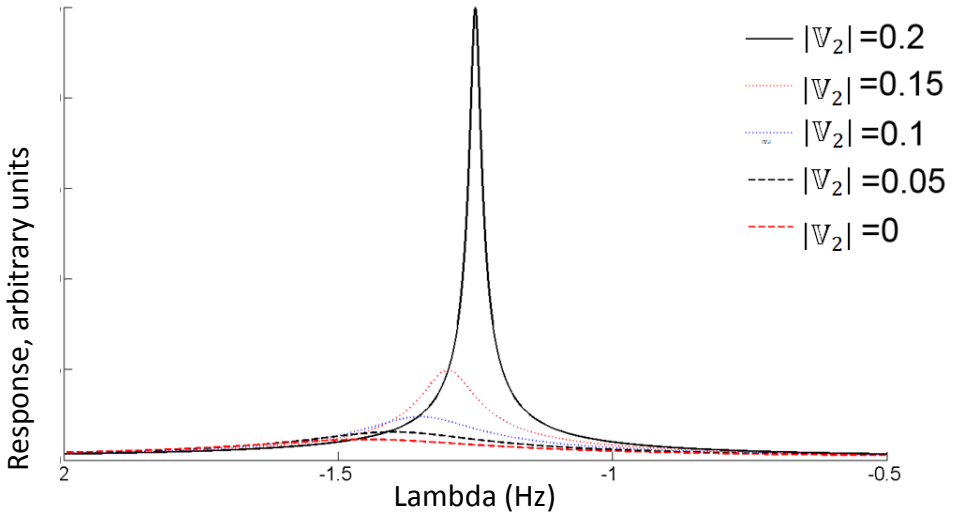

Figure 2.5 Parametric amplification of the response as $|\mathbb{V}_2|$ is varied at constant phase.

From the form of (2.68), it is clear that D_S contains a fixed real contribution from the damping summed with a term dependent on a quadratic term in the applied voltages. Fixing the phase of $\mathbb{V}_2$ at $\frac{\pi}{4}$ leads to a negative real contribution after the bracket is expanded. This term mitigates the damping, and as it is increased will push $Re(D_S)$ through 0. This can be seen as driving the effective damping to zero. In the absence of any DC bias, the product term $4\mathbb{V}_{DC}\mathbb{V}_2$ is zero, and straightforward parametric amplification can be observed, giving a family of curves identical to those shown in Figure 2.4. However, the electrical coupling between these variables introduces some additional complexity to the situation. In particular, any DC voltage component offsets the maximum of the frequency response curve, and the product term also couples this offset to the parametric voltage $\mathbb{V}_2$. This can be seen in Figure 2.5 to have the effect of shifting the location of the resonant peak and amplifying its size as the parametric voltage is varied.

Assuming an appropriate phase-tracking strategy is employed to mitigate mistuning, the steady state response of the mechanically linear system described in this subsection can be given in a concise form by combining equations (2.52), (2.56) and (2.64) to yield:

$$\hat{T} = \frac{F\mathbb{V}_{\frac{1}{2}}^2}{4\omega_n^2}\mathrm{Q}_P\cos(\omega_n\hat{t} + \Phi_P) \tag{2.69}$$

Where the quantity Q_P is termed the *parametric Q factor,* defined by

$$Q_{\mathrm{P}} = \frac{Q}{\sqrt{1 + Q^2\left(\mathbb{V}_{DC}^2 + \mathbb{V}_{DC}\mathbb{V}_2 + \frac{1}{4}\left(\mathbb{V}_{\frac{1}{2}}^2 + \mathbb{V}_2^2\right)\right)^2}}$$

Cf. Ref[14].

2.3.3 Mechanically nonlinear case

Expression (2.58) is inhomogeneous and nonautonomous but linear in the displacement. However, it is derived from more general nonlinear principles by making simplifying assumptions. These are subject to breakdown under particular sets of

operating conditions, excitations, and resonator geometries, under which it is possible for the dynamical system to exhibit phenomena qualitatively different from, and not predictable by means of, the linearised equations. It is therefore of considerable interest to have an understanding of the effect of introducing weak nonlinearity to the system.

Sources of nonlinearity are of course very numberous. The most apparent have already been implied earlier in this thesis: geometric nonlinearity inherent in continuum elasticity, and electrostatic nonlinearity deriving from Coulomb's force law and its inverse-square behaviour. Both can become important as the sense beam deflection becomes "large" in some sense, to be defined; both tend to zero in the limit of small deflections. Other nonlinear behaviours that may be of importance include various forms of nonlinear damping, which are however beyond the scope of the present work.

Since the geometric configuration is symmetric, any geometric nonlinearity can reasonably be assumed to be antisymmetric in the deflection. This implies that, expanding the nonlinearities as a power series, the odd order terms (cubic, quintic, etc.) are expected to dominate. Similarly, examining the form of the power series expansion for the electrostatic nonlinearity in Equation (2.40), it is seen that the even order (symmetric) terms are proportional to the voltage difference between the electrodes, while the odd order terms are proportional to the sum of the same voltages. Given the a priori information that the voltages will consist of a large DC bias and relatively small harmonic modulation, it is again reasonable to conclude that the odd order terms are dominant in this case also. This assumed form of approximation requires $R = 1$.

For simplicity and transparency of exposition, the first case under consideration is that in which geometric nonlinearity dominates electrostatic nonlinearity. This can be achieved by artificially setting

$$\epsilon c = O(\epsilon q) = O(\epsilon^2) \tag{2.70}$$

Of course, this statement is not mathematically true – no constants can be found such that the above relation holds, as was the case with assuming damping is of order ϵ.

However, this piece of algebraic sleight-of-hand yields valuable insight into the system behaviour in the presence of nonlinearity.

The equivalent to (2.47) for the nonlinear forced system can be written as

$$\ddot{T} + 2\xi\omega_n\dot{T} + \omega_n^2(1 - \epsilon[\{\boldsymbol{V}_1^2\} + \{\boldsymbol{V}_2^2\}])T + \epsilon\omega_c^2T^3 = \epsilon F(\{\boldsymbol{V}_1^2\} - \{\boldsymbol{V}_2^2\}) \quad (2.71)$$

Introducing small parameters and series forms for the solution and substituting into 2.70 by direct analogy to Section 2.2.1 leads to the modulation equations

$$O(1): \ \frac{\partial^2\hat{T}}{\partial\hat{t}^2} + \ \omega_n^2\hat{T} = 0 \quad (2.72)$$

$$O(\epsilon): \frac{\partial^2\tilde{T}}{\partial\hat{t}^2} + \omega_n^2\tilde{T} = F(\{\boldsymbol{V}_1^2\} - \{\boldsymbol{V}_2^2\}) - 2\frac{\partial^2\hat{T}}{\partial\hat{t}\partial\tilde{t}} - 2v\omega_n\frac{\partial\hat{T}}{\partial\hat{t}} + \omega_n^2(\{\boldsymbol{V}_1^2\} + \{\boldsymbol{V}_2^2\})\hat{T} + \omega_c^2T^3 \quad (2.73)$$

These have the same form as (2.51), with the additional term $\omega_{q1}^2T^3$ on the right hand side of the $O(\epsilon)$ equation. To expand the harmonic content, it is helpful to employ the basic trigonometric identity for $cos^3(x)$ to obtain

$$T^3 = \left(rcos(\omega_n\hat{t} + \lambda\tilde{t} - \theta)\right)^3 = r^3cos^3(\omega_n\hat{t} + \lambda\tilde{t} - \theta)$$

$$= r^3\left(\frac{3}{4}cos(\omega_n\hat{t} + \lambda\tilde{t} - \theta) + \frac{1}{4}cos\big(3(\omega_n\hat{t} + \lambda\tilde{t} - \theta)\big)\right) \quad (2.74)$$

The secular terms in the right-hand side of (2.73) are

$$\frac{F\mathbb{V}_{\frac{1}{2}}^2}{2}\big(\cos\big((\omega_n + \lambda)t - \theta\big)\cos\theta - \sin\big((\omega_n + \lambda)t - \theta\big)\cos\theta\big) + \omega_n^2\frac{4\mathbb{V}_{\mathrm{DC}}^2 + \mathbb{V}_{\frac{1}{2}}^2 + \mathbb{V}_2^2 + 4\mathbb{V}_{\mathrm{DC}}\mathbb{V}_2}{2}\cos\big((\omega_n + \lambda)t - \theta\big) + \frac{3\omega_c^2r^3}{4}\cos(\omega_n\hat{t} + \lambda\tilde{t} - \theta) + 2\left(\dot{r}\omega_n\sin(\omega_n\hat{t} + \lambda\tilde{t} - \theta) + r\big(\lambda + \dot{\theta}\big)\omega_n\cos(\omega_n\hat{t} + \lambda\tilde{t} - \theta)\right) + 2vr\omega_n^2\sin(\omega_n\hat{t} + \lambda\tilde{t} - \theta) \quad (2.75)$$

Collecting terms in $\cos((\omega_n + \lambda)t - \theta)$ and $\sin((\omega_n + \lambda)t - \theta)$leads to the simultaneous solubility conditions

$$\frac{4\omega_n}{F\mathbb{V}_{\frac{1}{2}}^2}(\dot{r} + vr\omega_n) = \sin(\theta) \tag{2.76}$$

$$\frac{4\omega_n}{F\mathbb{V}_{\frac{1}{2}}^2}\left(r\dot{\theta} - r\left(\left(\lambda - \frac{3\omega_c^2}{8\omega_n}r^2\right) + \frac{\omega_n}{4}\left(4\mathbb{V}_{DC}^2 + \mathbb{V}_{\frac{1}{2}}^2 + \mathbb{V}_2^2 + 4\mathbb{V}_{\mathrm{DC}}\mathbb{V}_2\right)\right)\right) = \cos(\theta) \tag{2.77}$$

For a qualitative insight, initially damping is neglected, and the time-derivatives are set to zero to search for critical points of the undamped system to obtain

$$\sin(\theta) = 0 \ \therefore \theta = 0, \pi \tag{2.78}$$

$$\frac{4\omega_n}{F\mathbb{V}_{\frac{1}{2}}^2}\left(-r\left(\left(\lambda - \frac{3\omega_c^2}{8\omega_n}r^2\right) + \frac{\omega_n}{4}\left(4\mathbb{V}_{DC}^2 + \mathbb{V}_{\frac{1}{2}}^2 + \mathbb{V}_2^2 + 4\mathbb{V}_{\mathrm{DC}}\mathbb{V}_2\right)\right)\right) = \cos(\theta) = \pm 1 \tag{2.79}$$

$$\left(\frac{\omega_n}{4}\left(4\mathbb{V}_{\mathrm{DC}}^2 + \mathbb{V}_{\frac{1}{2}}^2 + \mathbb{V}_2^2 + 4\mathbb{V}_{DC}\mathbb{V}_2\right) - \left(\lambda - \frac{3\omega_c^2}{8\omega_n}r^2\right)\right) = \pm\frac{F\mathbb{V}_{\frac{1}{2}}^2}{4r\omega_n} \tag{2.80}$$

The two choices of sign for the right-hand side of (2.90) correspond to two wholly separate solutions to the secularity conditions – i.e. two branches of solution to the original problem. Rearranging (2.80) into the form

$$\lambda = \frac{\omega_n}{4}\left(4\mathbb{V}_{\mathrm{DC}}^2 + \mathbb{V}_{\frac{1}{2}}^2 + \mathbb{V}_2^2 + 4\mathbb{V}_{\mathrm{DC}}\mathbb{V}_2\right) + \frac{3\omega_c^2}{8\omega_n}r^2 - \frac{F\mathbb{V}_{\frac{1}{2}}^2}{4r\omega_n} \tag{2.81a}$$

or

$$\lambda = \frac{\omega_n}{4}\left(4\mathbb{V}_{\mathrm{DC}}^2 + \mathbb{V}_{\frac{1}{2}}^2 + \mathbb{V}_2^2 + 4\mathbb{V}_{\mathrm{DC}}\mathbb{V}_2\right) + \frac{3\omega_c^2}{8\omega_n}r^2 + \frac{F\mathbb{V}_{\frac{1}{2}}^2}{4r\omega_n} \tag{2.81b}$$

It can clearly be seen from (2.80) and Figure 2.6 (below) that at steady-state for the undamped case considered, the mistuning from the linear natural frequency is dominated by a quadratic term $\frac{3\omega_c^2}{8\omega_n}r^2$ in the large-amplitude limit, while an inverse-

proportional term $\frac{F\mathbb{V}_{\frac{1}{2}}^2}{4r\omega_n}$ becomes large in the complementary limit of small displacements. This is the characteristic Duffing equation behaviour of amplitude-dependent "resonant" frequency.

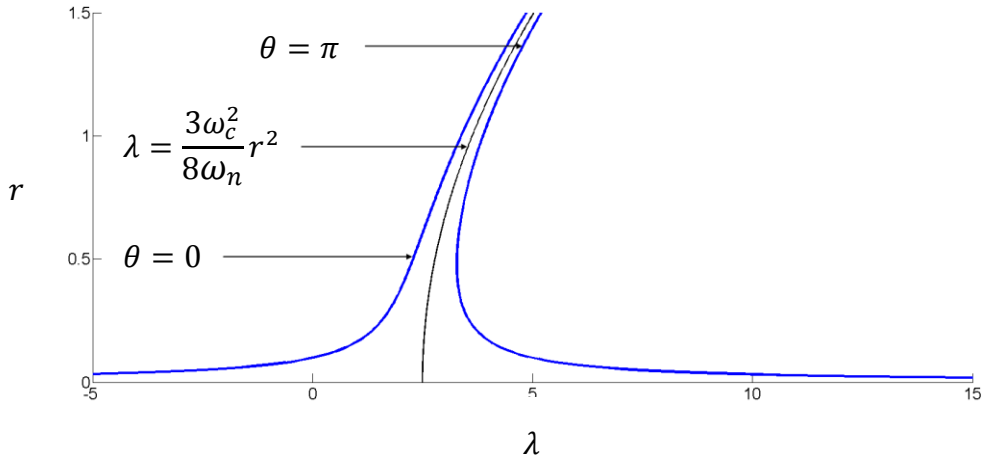

Figure 2.6 Undamped steady-state frequency response curve for the mechanically nonlinear case with parametric pumping of the linear stiffness. The quadratic form of lambda as a function of r is plotted explicitly, along with the two solution branches corresponding to $\theta = 0$and $\theta = \pi$.

The mechanical nonlinearity is usually of hardening type, meaning that the coefficient of T^3 in the governing equation is of the same sign as the liner stiffness coefficient. That is to say, as the displacement increases, the potential energy gradient becomes steeper and the spring effectively "hardens". This quality has the effect of bending the unperturbed linear resonance curve into the characteristic right-leaning form seen above. The degree of frequency modification with amplitude, and hence the curvature of the frequency response, is controlled directly by the cubic stiffness coefficient. A variety of possible hardening responses for different cubic stiffness coefficient values are displayed in Figure 2.7.

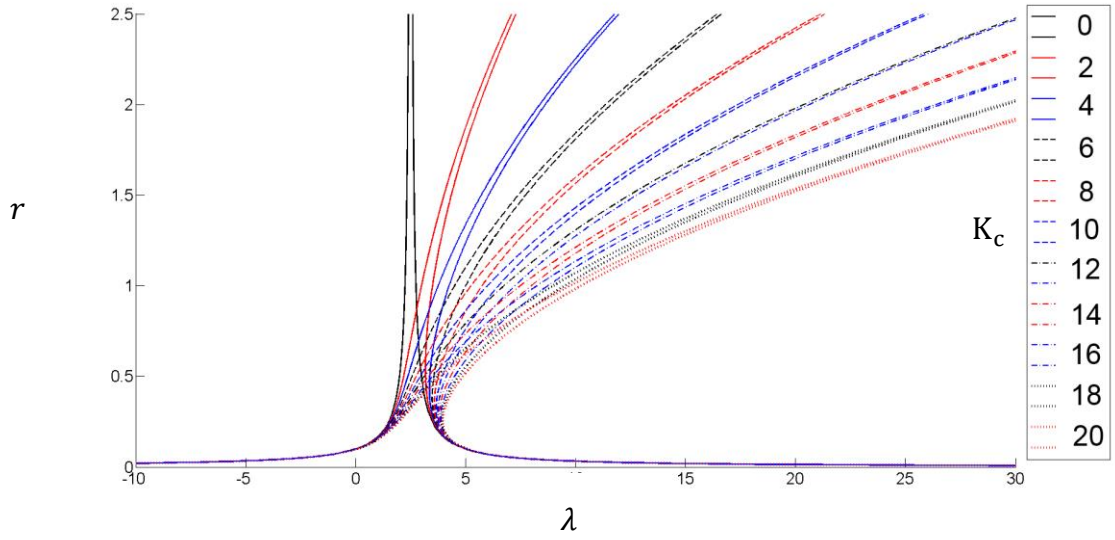

Figure 2.7 Change in the form of the frequency response for differing strengths of the mechanical nonlinearity K_c from 0 to 20. Note that for the former case, the form of the response reduces to the linear parametric case.

Note that only in the linear case $K_c = 0$ (solid black line in Figure 2.7) does the amplitude become unbounded at a particular frequency (the resonance frequency). The introduction of even the slightest nonlinearity, either hardening or softening, bounds the response amplitude if all other parameters including excitation frequency are fixed and finite. Thus, the resonance frequency is less well-defined in nonlinear systems.

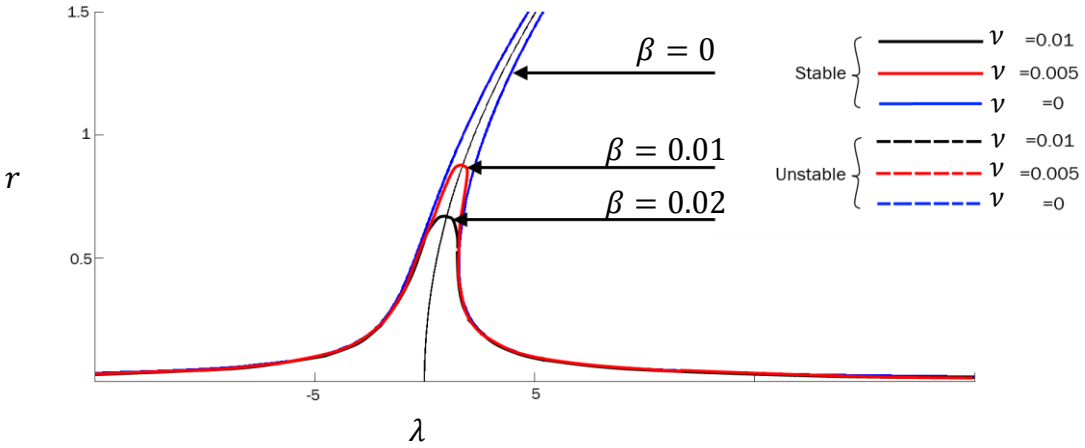

Figure 2.8 Frequency response for the mechanically nonlinear case with parametric pumping of the linear stiffness for different values of the damping coefficient. Note that the two separate branches are joined at finite λ by the damping. The phase varies smoothly along the new single curve.

The form of the response for all the nonlinear cases considered hitherto has been for the undamped case, obtained by setting $\nu = 0$ in equation (2.80). In this situation,

two branches of solution exist, due to the fact that (2.80) has two roots, constant regardless of the response amplitude r. This can be considered as the limit of the series of phase curves in Figure 2.4 as $\nu \to 0$. However, in any real system and the XBR in particular, dissipative processes exist (Cf. Chapter 5). This has the effect of bringing into existence a continuum of roots to (2.80) as the response amplitude is modulated. In other words, the phase no longer has two limiting values; instead, these are now asymptotes to a smoothly changing phase curve, as in the linear damped case. From the perspective of the frequency response graphs, this joins the two branches at a smooth finite peak amplitude depending on the strength of the damping, as seen in Figure 2.8.

Furthermore, there is a one-to-one correspondence between excitation frequency and response amplitude for given forcing, damping, etc. in the linear case; this is no longer true for nonlinear systems. At frequencies higher than the lower branch minimum the vertical projection of each excitation frequency intersects the response curve three times in the undamped case, and between 1 and 3 times in the damped case. Since the frequency response graphs show steady-state solutions to the solubility conditions, this represents multiple critical points of the dynamical system. This is another characteristic feature of nonlinear systems not observed in solutions to linear equations.

A question naturally arises from this analysis: which of these critical points are stable and which unstable? To attack this question, express the solution as a decomposition into the steady-state and a slow-time dependent error as

$$r(\tilde{t}) = r_s + \tilde{r}(\tilde{t});\ \theta(\tilde{t}) = \theta_s + \tilde{\theta}(\tilde{t}) \tag{2.82}$$

The stability of the critical points is determined by the linearised stability of the offset terms, since the (smooth) nonlinear flow is diffeomorphic to the linearised version in a deleted neighbourhood of the critical points [20]. Substituting (2.82) into (2.76) and linearising the trigonometric terms, one obtains

$$\frac{4\omega_n}{F\mathbb{V}_{\frac{1}{2}}^2}\left(r_s + \dot{\tilde{r}} + v(r_s + \tilde{r})\omega_n\right) = \left(\theta_s + \tilde{\theta}\right) \tag{2.83}$$

$$\frac{4\omega_n}{F\mathbb{V}_{\frac{1}{2}}^2}\Bigg((r_s+\tilde{r})\dot{\theta} - (r_s+\tilde{r})\Bigg(\left(\lambda-\frac{3\omega_c^2}{8\omega_n}(r_s+\tilde{r})^2\right) + \frac{\omega_n}{4}\left(4\mathbb{V}_{DC}^2+\mathbb{V}_{\frac{1}{2}}^2+\mathbb{V}_2^2+4\mathbb{V}_{DC}\mathbb{V}_2\right)\Bigg)\Bigg) = 1 \tag{2.84}$$

Recall that, at steady state,

$$\lambda = \frac{\omega_n}{4}\left(4\mathbb{V}_{DC}^2+\mathbb{V}_{\frac{1}{2}}^2+\mathbb{V}_2^2+4\mathbb{V}_{DC}\mathbb{V}_2\right)+\frac{3\omega_c^2}{8\omega_n}r_s^2+\frac{F\mathbb{V}_{\frac{1}{2}}^2}{4r_s\omega_n} \tag{2.85}$$

Removing the constant terms from (2.83) and setting the damping to zero, the dynamics near the right branch are governed by

$$\frac{4\omega_n}{F\mathbb{V}_{\frac{1}{2}}^2}\dot{\tilde{r}} = \tilde{\theta} \tag{2.86}$$

$$\frac{4\omega_n}{F\mathbb{V}_{\frac{1}{2}}^2}\left(r_s\dot{\theta}-\tilde{r}\lambda+\left(\frac{6\omega_c^2}{8\omega_n}r_s^2\tilde{r}\right)+\tilde{r}\frac{\omega_n}{4}\left(4\mathbb{V}_{DC}^2+\mathbb{V}_{\frac{1}{2}}^2+\mathbb{V}_2^2+4\mathbb{V}_{DC}\mathbb{V}_2\right)\right) = 0 \tag{2.87}$$

A stable solution corresponds to exponential decay of $\tilde{r}$ and $\tilde{\theta}$ at the same order with respect to time; hence, make an ansatz of the form

$$\tilde{r} = \tilde{r}_0 e^{\Lambda\tilde{t}};\ \tilde{\theta} = \tilde{\theta}_0 e^{\Lambda\tilde{t}} \tag{2.88}$$

Cancelling the time dependent terms, one obtains

$$\Lambda\tilde{r}_0 = \frac{F\mathbb{V}_{\frac{1}{2}}^2}{4\omega_n}\tilde{\theta}_0 \tag{2.89}$$

$$\tilde{\theta}_0 = \frac{\tilde{r}_0}{\Lambda}\left[\frac{F\mathbb{V}_{\frac{1}{2}}^2}{4r_s^2\omega_n}-\frac{3\omega_c^2}{4\omega_n}r_s\right] \tag{2.90}$$

Eliminating $\tilde{\theta}_0$ and solving for Λ gives the stability condition

$$\Lambda = \sqrt{\frac{F\mathbb{V}_{\frac{1}{2}}^2}{4\omega_n}\left[\frac{F\mathbb{V}_{\frac{1}{2}}^2}{4r_s^2\omega_n} - \frac{3\omega_c^2}{4\omega_n}r_s\right]} \tag{2.91}$$

For real $\mathbb{V}_{\frac{1}{2}}^2$,the term in brackets determines the stability of the right branch. When the term is positive, Λ is a pair of real numbers of opposing sign. Hence, from the ansatz, solutions in the vicinity of the branch in this region are repelled and the branch is unstable. At a particular point$\{r, \lambda\} \cong \{0.5,1\}$, indicated in red in Figure 2.9, the bracketed term is zero; the singularity is a saddle point in the phase space of the system. For values of r below the singularity, the bracketed term is negative and Λ takes values as complex-conjugate pairs. Hence, the branch is marginally stable. A transient solution in the vicinity of one of the marginally stable solution branches will oscillate in slow time.

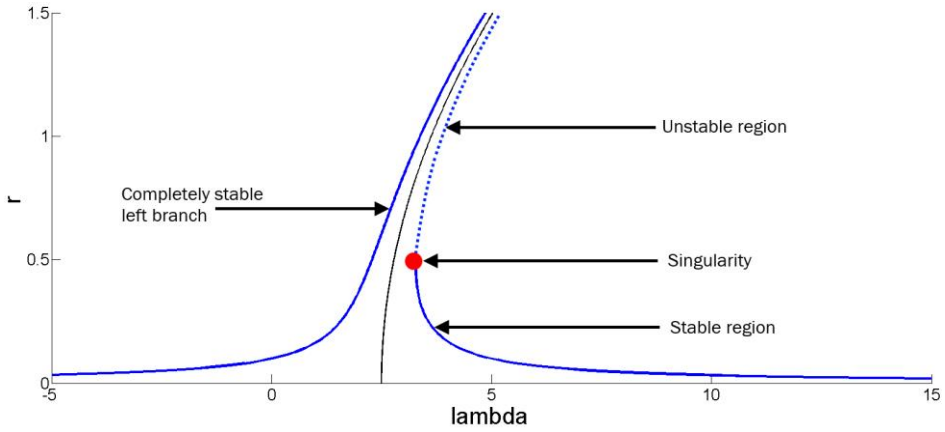

Figure 2.9 Plot of the nonlinear response showing stable and unstable solution branches.

The damped equivalent form of (2.91) is

$$\Lambda^2 + v\omega_n\Lambda + \frac{F\mathbb{V}_{\frac{1}{2}}^2}{4\omega_n}\left[\frac{3\omega_c^2}{4\omega_n}r_s - \frac{F\mathbb{V}_{\frac{1}{2}}^2}{4r_s^2\omega_n}\right] = 0 \tag{2.92}$$

Applying the quadratic formula yields

$$\Lambda = \frac{-v\omega_n}{2} \pm \sqrt{\frac{(v\omega_n)^2}{4} + \frac{F\mathbb{V}_{\frac{1}{2}}^2}{4\omega_n}\left[\frac{F\mathbb{V}_{\frac{1}{2}}^2}{4r_s^2\omega_n} - \frac{3\omega_c^2}{4\omega_n}r_s\right]} \tag{2.92}$$

Hence, damping shifts the singularity slightly by adding a small positive real constant to the radical, requiring the bracketed term overcome this positive bias before the argument switches sign and the solution stability. Damping also causes the transient response to die away and shifts the marginally-stable solutions to stability; in the presence of (positive) damping, solutions in the vicinity of the solid blue branches in Figure 2.9 tend towards the branch as time increases.

Another interesting behaviour exhibited in the presence of nonlinearity is the response to stronger or weaker forcing. It is clear from (2.90) that in the limit of vanishing forcing strength $F \to 0$, the solution tends to the quadratic form $\lambda = \frac{3\omega_c^2}{8\omega_n} r^2$ and that increasing F leads to amplification of the deviation of the branches from this ideal. The graphical representation Figure 2.10 shows this behaviour for a particular choice of parameters.

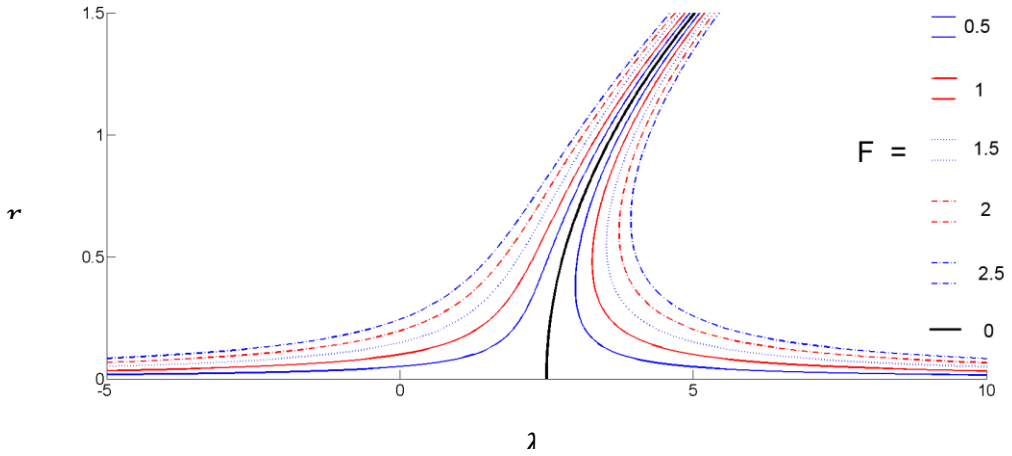

Figure 2.10 Undamped frequency response for different electrostatic coupling strengths F from 0 to 2.5. .

Recall from Section 2.2 that a "forcing" voltage $\mathbb{V}_{\frac{1}{2}}$ was chosen at half the linear natural frequency such as to introduce a classical forcing term at resonance. It might be naively expected that varying this term would have an analogous effect to artificially varying F. However, the coefficient in (2.92) of the parametric modulation also contains $\mathbb{V}_{\frac{1}{2}}$; changing this quantity therefore affects both the classical forcing and the parametric modulation term in a dependent fashion. The nature of the behaviour

is not immediately clear. Figure 2.11 shows what happens as $\mathbb{V}_{\frac{1}{2}}$ is varied in amplitude over a range of positive real values in the case under consideration.

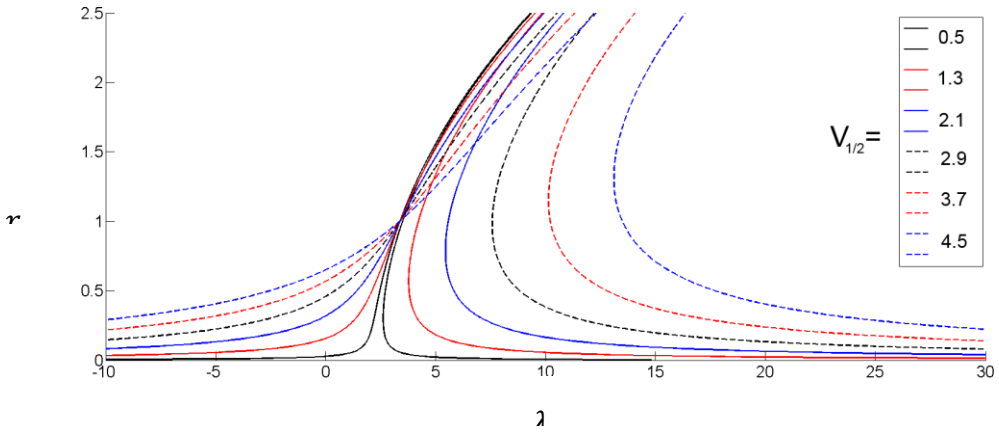

Figure 2.11 Undamped frequency response for different values of the half-frequency applied voltage waveform $\mathbb{V}_{\frac{1}{2}}$ from 0 to 2.5. The family of graphs now has a transversal self-intersection at a particular value of $\{r, \lambda\} \cong \{1.2\}$, and the behaviour of the curves is more complex than in Figure 2.10.

Summing up, in the presence of hardening mechanical nonlinearity, dynamical phenomena qualitatively differing from the linear case, including the coexistence of multiple stable solutions, amplitude-dependent "resonant" frequencies, and additional effects are present. If a sense control strategy based on the linear-parametric case is adopted in the presence of significant mechanical nonlinearity, then the results will be degraded, possibly to the point of irrelevance. Developing a nonlinear control system is possible but far more resource-intensive. Additionally, such a system would be capable of undergoing qualitative changes in response to small variations in the system parameters, greatly impeding mass production of devices based on the technology.

2.3.4 Fully nonlinear case

The behaviour of the reduced systems studied in Sections 2.3.1 and 2.3.2 under parametric excitation, with and without mechanical nonlinearity respectively, have been considered in this chapter in some detail. However, if the electrostatic nonlinearity is nontrivial, then the electrostatic component of the cubic stiffness is parametrically modulated with the same time-dependency as the electrostatic linear stiffness (and the forcing). New dynamics are introduced associated with the parametrically-pumped nonlinearity.

To examine the steady-state behaviour, augment the equation of motion with the derived cubic-parametric term to obtain

$$\ddot{T} + 2\epsilon v\omega_n\dot{T} + \omega_n^2(1 - \epsilon[\{\boldsymbol{V}_1^2\} + R\{\boldsymbol{V}_2^2\}])T + \epsilon\omega_c^2(1 - c[\{\boldsymbol{V}_1^2\} + R\{\boldsymbol{V}_2^2\}])T^3$$

$$= \epsilon F(\{\boldsymbol{V}_1^2\} - R\{\boldsymbol{V}_2^2\}) \tag{2.93}$$

Applying the approximation procedure as before yields the modulation equations as

$$O(1):\ \frac{\partial^2\hat{T}}{\partial\hat{t}^2} + \ \omega_n^2\hat{T} = 0 \tag{2.94}$$

$$O(\epsilon): \frac{\partial^2\tilde{T}}{\partial\hat{t}^2} + \omega_n^2\tilde{T}$$

$$= F(\{\boldsymbol{V}_1^2\} - \{\boldsymbol{V}_2^2\}) - 2\frac{\partial^2\hat{T}}{\partial\hat{t}\partial\tilde{t}} - 2v\omega_n\frac{\partial\hat{T}}{\partial\hat{t}} + \omega_c^2(1 + c\{\boldsymbol{V}_1^2 + \boldsymbol{V}_2^2\})\hat{T}^3$$

$$+\ \omega_n^2(\{\boldsymbol{V}_1^2\} + \{\boldsymbol{V}_2^2\})\hat{T} \tag{2.95}$$

The solubility conditions can be obtained as before, having the form

$$\dot{r} + vr\omega_n = \frac{F\mathbb{V}_{\frac{1}{2}}^2}{4\omega_n}\sin(\theta) \tag{2.96}$$

$$r\dot{\theta} - r\lambda = \frac{F\mathbb{V}_{\frac{1}{2}}^2}{4\omega_n}\cos(\theta) + \frac{r\omega_n}{4}\left(4\mathbb{V}_{DC}^2 + \mathbb{V}_{\frac{1}{2}}^2 + \mathbb{V}_2^2 + 4\mathbb{V}_{DC}\mathbb{V}_2\right)$$

$$+ cr^3\left(\frac{12\mathbb{V}_{\mathrm{DC}}^2 + 3\mathbb{V}_{\frac{1}{2}}^2 + 4\mathbb{V}_2^2 + 16\mathbb{V}_{DC}\mathbb{V}_2 - 3\frac{\omega_c^2}{\omega_n c}}{8}\right) \tag{2.97}$$

Following along the lines of Section 2.3.3, stationary solutions of the undamped system are sought by setting $\dot{r} = \dot{\theta} = 0$ and $v = 0$ to obtain

$$0 = \frac{F\mathbb{V}_{\frac{1}{2}}^2}{4\omega_n}\sin(\theta)\ \ \therefore\ \theta \in \{0, \pi\} \tag{2.98}$$

$$-r\left(\lambda+\frac{r\omega_n}{4}\left(4\mathbb{V}_{DC}^2+\mathbb{V}_{\frac{1}{2}}^2+\mathbb{V}_2^2+4\mathbb{V}_{DC}\mathbb{V}_2\right)\right.$$

$$\left.+cr^3\left(\frac{12\mathbb{V}_{\mathrm{DC}}^2+3\mathbb{V}_{\frac{1}{2}}^2+3\mathbb{V}_2^2+12\mathbb{V}_{DC}\mathbb{V}_2+\mathbb{V}_2^2+4\mathbb{V}_{DC}\mathbb{V}_2-3\frac{\omega_c^2}{\omega_n c}}{8}\right)\right)\frac{F\mathbb{V}_{\frac{1}{2}}^2}{4\omega_n}\mp\frac{F\mathbb{V}_{\frac{1}{2}}^2}{4\omega_n}$$

$$=0 \qquad (2.99)$$

This equation has the same form as for the previous case with the single exception being that the coefficient of r^3 depends on the applied voltages. This presents both opportunities and difficulties from a control perspective. On one hand, changing control parameters will directly influence the response nontrivially, generating behaviour that is not captured by the linear model and which must be accounted for in inferring sense quantities of interest for the application. On the other hand, the coupling of the applied voltage amplitudes and phases to the nonlinearity suggests the possibility of tuning or eliminating the nonlinearity by a careful manipulation of these parameters, such that the electrostatic softening cancels the mechanical hardening. This concept is illustrated in Figure 2.12, which shows plots of the frequency response of the system for various values of the pumping parameter. It can be seen that the stiffening nonlinearity is modified in an incremental fashion into a softening nonlinearity, passing through the linear case en route.

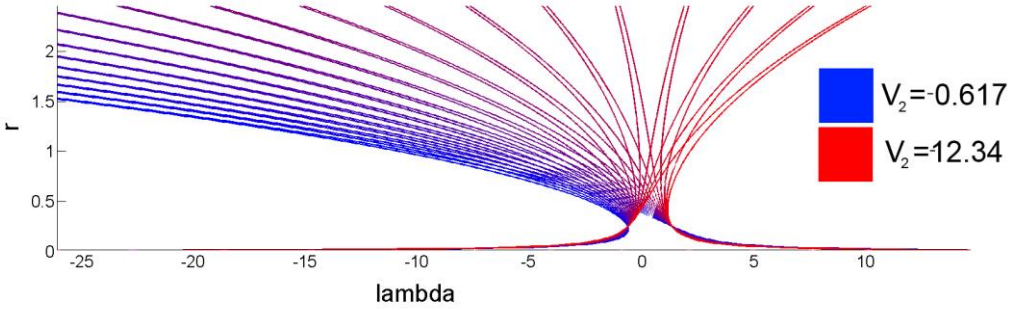

Figure 2.12 Frequency response obtained the parametric-nonlinear model, for differing values of the pumping parameter. The nonlinearity is modified from an effective stiffening to an effective softening behaviour, passing through a linear region.

This approach allows for mechanical nonlinearity to be cancelled by electrostatic nonlinearity, if the voltages are chosen such that

$$\frac{12\mathbb{V}_{\mathrm{DC}}^2 + 3\mathbb{V}_{\frac{1}{2}}^2 + 3\mathbb{V}_2^2 + 12\mathbb{V}_{DC}\mathbb{V}_2 + \mathbb{V}_2^2 + 4\mathbb{V}_{DC}\mathbb{V}_2}{8} = \frac{3}{8}\frac{\omega_c^2}{\omega_n c} \qquad (2.100)$$

2.4 Conclusions

A model has been developed from fundamental principles to model the behaviour and response of an XBR under parametric actuation and classical forcing, using a multiple-scales singular perturbation method. In the course of the investigation, new results have been developed generalising previous work of Gallacher et al.[8] regarding the response of a system to parametric modulation of arbitrary response and phase, with the result reducing to Gallacher's when the phase and amplitude are enforced to be stationary and independent parameters. It has been confirmed that parametric amplification is achievable in principle for a capacitively actuated XBR. It is shown that the effects of smooth polynomial nonlinearity of arbitrary finite degree can be mitigated by including a sufficient number of independent frequency components modulating the system parameters with frequencies commensurate to the natural frequency of the desired response. Furthermore, in an extension of ideas previously developed by Burnett[21]it has been shown to be possible by judicious selection of frequencies and utilisation of the feedthrough properties of capacitive actuation to offset the driving frequencies from the sensing frequency, mitigating the detrimental effects of feedthrough.

The dynamical model makes account only of the sense beam. In extending the modelling herein to a whole XBR, only the form of the integral quantities (generalised mass, stiffness, and forces) varies, once the mode shapes are established. This is done in Chapter 3 using a Rayleigh-Ritz approximation, similar in spirit to the single mode approximation here but with more modes and parametric freedom and a variational minimisation principle. Furthermore, damping is assumed; we defer study of the fundamental origins and quantitative modelling of dissipation until Chapter 5.

Continuations and extensions of value would include a formulation with spatially varying parametric amplification, leading to dynamic materials approaches and possibly further exploitable phenomena for vibration isolation, frequency and bandwidth modulation, and so forth. Also of interest would be a validation of the actuated mode shapes, i.e. a check on the applicability of the one-mode approximation. This could be achieved via numerical simulation or further analytical work. Finally, the extension to higher modes of vibration and more complex frame resonator geometries would allow generalisation of the conclusions of this chapter to a wider range of systems.

2.5 References

[1] D. Rugar and P. Grütter, "Mechanical parametric amplification and thermomechanical noise squeezing.," *Physical review letters*, vol. 67, no. 6. pp. 699–702, 05-Aug-1991.

[2] I. Bena, C. Van den Broeck, R. Kawai, M. Copelli, and K. Lindenberg, "Collective behavior of parametric oscillators," *Physical Review E*, vol. 65, no. 3, pp. 1–18, Feb. 2002.

[3] S. Forouzanfar, R. Mansour, and E. Abdel-Rahman, "Lorentz-force transduction for RF micromechanical filters," *Journal of Micromechanics and Microengineering*, vol. 22, no. 3, p. 035018, Mar. 2012.

[4] A. Dâna, F. Ho, and Y. Yamamoto, “Mechanical parametric amplification in piezoresistive gallium arsenide microcantilevers,” *Applied Physics Letters*, vol. 72, no. 10, p. 1152, 1998.

[5] D. W. Carr, S. Evoy, L. Sekaric, H. G. Craighead, and J. M. Parpia, “Parametric amplification in a torsional microresonator,” *Applied Physics Letters*, vol. 77, no. 10, p. 1545, 2000.

[6] M. Zalalutdinov, A. Olkhovets, A. Zehnder, B. Ilic, D. Czaplewski, H. G. Craighead, and J. M. Parpia, “Optically pumped parametric amplification for micromechanical oscillators,” *Applied Physics Letters*, vol. 78, no. 20, p. 3142, 2001.

[7] T. Ono, H. Wakamatsu, and M. Esashi, “Parametrically amplified thermal resonant sensor with pseudo-cooling effect,” *Journal of Micromechanics and Microengineering*, vol. 15, no. 12, pp. 2282–2288, Dec. 2005.

[8] B. J. Gallacher, J. S. Burdess, and K. M. Harish, “A control scheme for a MEMS electrostatic resonant gyroscope excited using combined parametric excitation and harmonic forcing,” *Journal of Micromechanics and Microengineering*, vol. 16, no. 2, pp. 320–331, Feb. 2006.

[9] K. M. Harish, B. J. Gallacher, J. S. Burdess, and J. A. Neasham, “Simple parametric resonance in an electrostatically actuated microelectromechanical gyroscope: theory and experiment,” *Proceedings of the Institution of Mechanical Engineers, Part C: Journal of Mechanical Engineering Science*, vol. 222, no. 1, pp. 43–52, Jan. 2008.

[10] K. M. Harish, B. J. Gallacher, J. S. Burdess, and J. a Neasham, “Experimental investigation of parametric and externally forced motion in resonant MEMS sensors,” *Journal of Micromechanics and Microengineering*, vol. 19, no. 1, p. 015021, Jan. 2009.

[11] Z. Hu, B. J. Gallacher, K. M. Harish, and J. S. Burdess, “An experimental study of high gain parametric amplification in MEMS,” *Sensors and Actuators A: Physical*, vol. 162, no. 2, pp. 145–154, Aug. 2010.

[12] B. J. Gallacher and J. S. Burdess, “Dynamic analysis of a microelectromechanical systems resonant gyroscope excited using combination parametric resonance,” *Proceedings of the Institution of Mechanical Engineers, Part C: Journal of Mechanical Engineering Science*, vol. 220, no. 9, pp. 1463–1479, Sep. 2006.

[13] M. Sharma, E. H. Sarraf, and E. Cretu, “Parametric Amplification / Damping in MEMS Gyroscopes,” *Quadrature*, pp. 617–620, 2011.

[14] M. J. Thompson and D. a. Horsley, “Parametrically amplified MEMS magnetometer,” *TRANSDUCERS 2009 - 2009 International Solid-State Sensors, Actuators and Microsystems Conference*, pp. 1194–1197, Jun. 2009.

[15] M. J. Thompson and D. A. Horsley, “Parametrically Amplified Z -Axis,” vol. 20, no. 3, pp. 702–710, 2011.

[16] L. Meirovitch, *Fundamentals of Vibration*, International Edition,. McGraw-Hill.

[17] R. Courant and D. Hilbert, *Methods of Mathematical Physics*. Wiley-VCH, 1989.

[18] R.A. Meyers, *Mathematics of Complexity and Dynamical Systems,* Springer, 2011

[19] G.M. Mahmoud, T. Bountis, and Sayed A. Ahmed, “Stability analysis for systems of nonlinear Hill’s equations”, Physica A, vol. 286, pp. 133-146, 2000

[20] J.J. Thomsen, *Vibrations and Stability:Advanced Theory, Analysis, and Tools,,* Springer, 2003

[21] R. Burnett et al., “Electronic detection strategies for a MEMS-based biosensor” *Journal of Microelectromechanical Systems*, vol. 22, no. 2, pp. 276–284, Apr. 2013

Chapter 3. Approximate models of an XBR

In this chapter, two approximate techniques for modal analysis of frame structures are introduced and applied the XBR case, with a view to optimising the resonator for the XBM application. The Rayleigh-Ritz-Meirovitch Substructure Synthesis Method (RRMSSM) splits up the domain of analysis into substructures, with the solution approximated on each substructure by a specially chosen quasicomparison trial function. The Finite Element Method is a well-established numerical approach, with several commercial packages available. COMSOL Multiphysics is used to model the resonator geometry in 3 dimensions. Both models are solved for a range of parameters, and the resulting mode shapes and natural frequencies are examined. Convergence and efficiency are examined and evaluated with respect to natural frequencies, mode shapes, and forces of constraint.

3.1 Introduction

The present chapter contains the development, comparison, and cross-validation of two methodologies for analysis of the mode shapes and natural frequencies of XBRs (and with some generalisation all resonant MEMS). The methods employed are a novel Rayleigh-Ritz based method, incorporating the enhancement of L. Meirovitch and adding a substructuring approach, and analysis via a commercial Finite Element code. The former is a novel model and approach developed herein; the second is intended to validate the first and extend its results.

The thrust of the work is to obtain a robust, efficient model for parametric optimisation of the XBR geometry with respect to the Q factor, natural frequency, compliance, and other properties of design interest. It was shown in Chapter2 that resonator Q factor plays a critical role in the performance of any resonant magnetometer, including the particular case of the XBM.

Symbols

A	Response amplitude	A_{x}	Cross-sectional area
$\mathbf{a}$	Weighting coefficient vector	$\mathbf{a_C}$	Constrained weighting coefficient vector
a_i , a_{ij}	ith, ijth component of $\mathbf{a}$	$\boldsymbol{b}$	Weighting vector of axial displacements
b	Support height	b_{ij}	ijth component of $\boldsymbol{b}$
$\mathbf{C}$	Constraint matrix	$\bar{\mathbf{C}}$	Nullspace matrix
E, E_i	Young's modulus, for ith substructure	$\mathcal{E}_i$	ith substructure
ϵ	Eigenvector perturbation	ϵ_i	Perturbation to ith coordinate
Φ	Gradient of displacement	Ψ	Curl of displacement
Υ_{N}	Normal dissipation factor	Υ_{T}	Transverse dissipation factor
$\mathbf{I}$	Identity matrix	I, I_i	Second moment, for ith substructure
K, K_i	Spring stiffness, of ith spring	$\mathbf{K}$	Stiffness matrix/operator
$\mathbf{K_G}$	Global Constrained stiffness matrix	$\mathbf{K_{GD}}$	Global Disjoint stiffness matrix
$\mathbf{K}_{iu}, \mathbf{K}_{iv}$	Transverse, axial stiffness submatrix for ith substructure	$\mathcal{K}$	Bulk modulus
λ	Eigenvalue	λ_i	ith eigenvalue
$\tilde{\lambda}_{\mathrm{i}}$	ith Ritz value	$\mathbf{\Lambda}$	Diagonal eigenvalue matrix
$\mathbf{L}$	System operator	ℓ	Total length
ℓ_i	Length of ith substructure	M_i	Mass of ith substructure
M, M_i	Lumped mass, of ith element	$\mathbf{M}$	Mass matrix/operator
$\mathbf{M_G}$	Global Constrained mass matrix		
$\mathbf{M_{GD}}$	Global Disjoint mass matrix	$\mathbf{M}_{iu}, \mathbf{M}_{iv}$	Transverse, axial mass submatrix for ith substructure

$\mathcal{N}$	Degrees of freedom per substructure	$\mathcal{M}$	Number of substructures
$\mathcal{O}$	Number of constraints	ρ	Material volume density
R	Rayleigh's Quotient	r	Ratio of longitudinal: transverse wave velocities in substrate
$\mathcal{S}$	Shear modulus	$\sigma_{\mathrm{N}}, \sigma_{\mathrm{T}}$	Normal, transverse average stress at support-substrate interface respectively
$\sigma_{ij}; i, j \in \{ x, y, z \}$	Stress parallel to *i*th axis on an infinitesimal plane with normal parallel to jth axis	t	Time
T	Kinetic energy	$\mathrm{T_L}$	Kinetic energy of lumped mass
T_{MAX}	Maximum kinetic energy	$\widetilde{U}, \overline{U}$	Trial space, invariant subspace
$\overline{\overline{U}}_{\mathrm{GD}}$	Global Disjoint trial space	u	Scalar Displacement
$\mathbf{u}$	Displacement vector	$\widetilde{\mathbf{u}}_{\mathrm{i}}$	ith Ritz vector
$\mathbf{u}^{\boldsymbol{p}}$	Perturbed eigenvector	$\mathbf{u}^{\boldsymbol{i}}$	ith Eigenvector
$\mathrm{u}_x, \mathrm{u}_y, \mathrm{u}_z$	Displacement of a substrate point parallel to x, y, z axes respectively	$\mathrm{u_N}$	Average normal displacement of support-substrate interface
$\mathrm{u_T}$	Average transverse displacement of interface	u_i	ith substructure transverse deflection
v_i	ith substructure axial deflection	V_{MAX}	Maximum Potential energy
ω	Frequency	ω_n	Natural frequency
ω_i	Natural frequency of ith mode	x, x_i	Axial coordinate, of ith substructure
$x, y, z,$	Substrate coordinate system		

Common Abbreviations

1QCF	RRMSSM model using one quasicomparison function per element	4QCF	RRMSSM model using four quasicomparison functions per element
NR	Ratio of ℓ_1: $(\ell_1 + \ell_2 + \ell_3)$	PP1	Rayleigh-Ritz model using one pinned-

			pinned admissible function per element
PP2	Rayleigh-Ritz model using two pinned-pinned admissible functions per element	PP4	Rayleigh-Ritz model using four pinned-pinned admissible functions per element
XBR	Xylophone Bar Resonator	XBM	Xylophone Bar Magnetometer
Notations			
$\dot{Z}$	First time derivative of Z	$\ddot{Z}$	Second time derivative of Z
Z'	First space derivative of Z	Z''	Second space derivative of Z
Z''''	Fourth space derivative of Z	$\mathbf{Z}^{\mathrm{T}}$	Transpose of Z

3.2 Rayleigh-Ritz-Meirovitch (RRM) method

The classical harmonic Rayleigh-Ritz method, in the context of modal analysis of linear mechanical systems, is a variational technique with a history spanning 100 years[1]. It is founded on the Rayleigh's quotient, which is a central object of study in mathematical field of functional analysis.

3.2.1 Rayleigh's Quotient for discrete systems

In his 1877 classical work[2], Rayleigh introduced a method of solution for free vibration problems that came to bear his name. The basis of Rayleigh's method is the insight that in an undamped linear resonant system, there exist two instants of time during the harmonic cycle at which the total system energy is in the form of kinetic energy, and likewise two instants during which all the energy is in the form of potential energy. Moreover, in a conservative system, energy is conserved and these quantities must be equal. As a first example, consider the classical single degree of freedom spring-mass system with mass M and spring stiffness K. The equation of motion is then given by

$$M\ddot{u} + Ku = 0 \tag{3.1}$$

Which has the well-known solution

$$u(t) = A\sin(\omega_n t + \varphi) \tag{3.2}$$

where φ is an arbitrary phase angle and $\omega_n = \sqrt{\frac{K}{M}}$. Taking Rayleigh's approach to the problem, the kinetic energy T and potential energy V have the values

$$T = \frac{1}{2}M\dot{u}^2 = \frac{1}{2}MA^2\omega_n^2\cos^2(\omega_n t + \varphi)\,;\;\; V = \frac{1}{2}Ku^2$$
$$= \frac{1}{2}KA^2\sin^2(\omega_n t + \varphi) \tag{3.3}$$

The instants when the energy is entirely kinetic or potential correspond to maxima of the trigonometric parts of (3), having unity value. Hence, it can be written that

$$V_{\mathrm{MAX}} = \frac{1}{2}KA^2;\quad T_{\mathrm{MAX}} = \frac{1}{2}MA^2\omega_n^2 \tag{3.4}$$

where V_{MAX} and T_{MAX} are respectively the maximum potential and kinetic energies over a harmonic cycle. Equating these quantities and solving for ω_n taking their quotient immediately yields

$$\frac{K}{M} = \omega_n^2 = R \tag{3.5}$$

where R is termed Rayleigh's quotient for the sytem. This procedure seems, at first sight, somewhat tautological, and indeed is in the case of a single degree of freedom system. One must solve the differential equation exactly in order to attack the approximation! The power of the method comes into play when multiple degrees of freedom are introduced. Consider next the coupled, asymmetric triple spring-mass system of Figure 3.1.

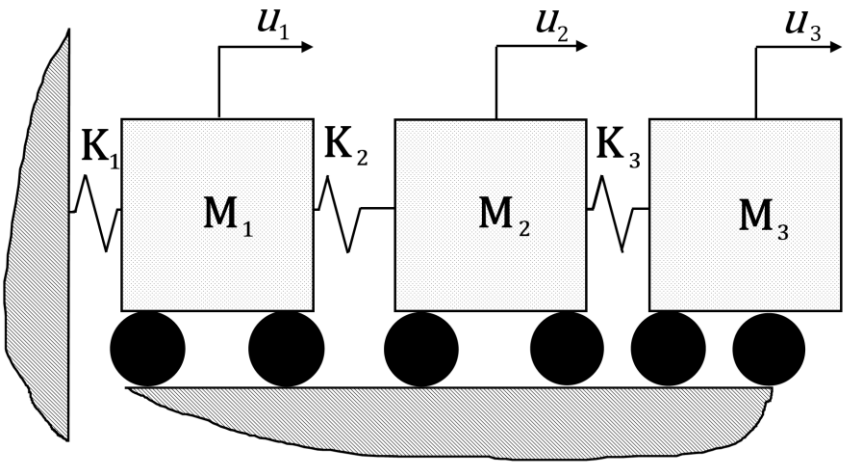

Figure 3.1 Three masses, coupled by springs. The coordinates $u_1 - u_3$ correspond to the displacement from equilibrium of the masses $M_1 - M_3$.

Parameter	Value	Description
$M_1[kg]$	1	First Mass
$M_2[kg]$	1	Second Mass
$M_3[kg]$	1	Third Mass
$K_1[n\,m^{-1}]$	20	First Spring Stiffness
$K_2[n\,m^{-1}]$	1	Second Spring Stiffness
$K_3[n\,m^{-1}]$	1	Third Spring Stiffness
$\mathbf{M}[kg]$	$\begin{bmatrix}1 & 0 & 0\\ 0 & 1 & 0\\ 0 & 0 & 1\end{bmatrix}$	Mass matrix
$\mathbf{K}[n\,m^{-1}]$	$\begin{bmatrix}-21 & 1 & 0\\ 1 & -2 & 1\\ 0 & 1 & -1\end{bmatrix}$	Stiffness matrix

Table 3.1. Lumped mass-spring model parameters

The equation of motion for the system specified by Figure 3.1 and Table 3.1 reads

$$\mathbf{M\ddot{u}} = \mathbf{Ku} \tag{3.6}$$

where $\mathbf{u}$ is the column vector $[u_1\ u_2\ u_3]^{\mathrm{T}}$ of displacements. The classical solution method assumes time harmonicity at an unknown frequency ω to obtain from (3.6) the algebraic generalised eigenvalue problem

$$\lambda\mathbf{Mu} = \mathbf{Ku} \tag{3.7}$$

where $\lambda = \omega^2$. The three eigenvalues define three natural frequencies $\omega_i; i \in \{1,2,3\}$. Since the operator $\mathbf{L} = \mathbf{M^{-1}K}$ is real symmetric and positive definite, the eigenvalues are all real and positive. The associated eigenvectors are the natural modes of vibration for the system. For a solution to (7) with nontrivial $\mathbf{u}$, the determinant of $\mathbf{L}$ must be zero.

Solution	Eigenvalue	Natural Frequency	Eigenvector
1	$\lambda_1 = 0.3684$	$\omega_1 = 0.6069$	$\mathbf{u}^1 = [0.0259 \quad 0.5339 \quad 0.8452]$
2	$\lambda_2 = 2.5790$	$\omega_2 = 1.6059$	$\mathbf{u}^2 = [-0.0458 \quad -0.8439 \quad 0.5345]$
3	$\lambda_3 = 21.0526$	$\omega_3 = 4.5883$	$\mathbf{u}^3 = [-0.9986 \quad 0.0526 \quad -0.0026]$

Table 3.2. Eigensolutions to the triple spring-mass system. Note that the first eigenvector contains only a small contribution from the first coordinate, due to the very high generalised stiffness associated with the large value of K_1.

The solutions given in Table 3.2 are accurate to the displayed precision. However, their direct calculation involves matrix operations of size n for a n -degree of freedom system. If n were large or even infinite, it would be of great value to obtain an accurate, reduced order approximation; this is precisely the value of Rayleigh's method.

To fix ideas, assume one wishes to obtain an estimate of the lowest eigenfrequency via Rayleigh's method. Rayleigh's quotient can be written in the form

$$R(\mathbf{u}) = \frac{T_{\mathrm{MAX}}}{V_{\mathrm{MAX}}} = \frac{\langle \mathbf{u}, \mathbf{K}\mathbf{u} \rangle}{\langle \mathbf{u}, \mathbf{M}\mathbf{u} \rangle} \tag{3.8}$$

where it has been implicitly assumed that the trial vector $\mathbf{u}$ comes from a Euclidean space, endowed with the Euclidean inner (dot) product $\langle \cdot, \cdot \rangle$. The value of Rayleigh's quotient when $\mathbf{u}$ is an eigenvector $\mathbf{u}^{\boldsymbol{i}}$ is the corresponding eigenvalue λ_i. Explicitly, for Solution 1 in Table 3.2, we have

$$R(\mathbf{u_1}) = \frac{\langle \mathbf{u^1}, \mathbf{K u^1} \rangle}{\langle \mathbf{u^1}, \mathbf{M u^1} \rangle}$$

$$= \frac{[0.0259 \quad 0.5339 \quad 0.8452] \begin{bmatrix} -21 & 1 & 0 \\ 1 & -2 & -1 \\ 0 & -1 & 1 \end{bmatrix} [0.0259 \quad 0.5339 \quad 0.8452]^{\mathrm{T}}}{[0.0259 \quad 0.5339 \quad 0.8452] \begin{bmatrix} 1 & 0 & 0 \\ 0 & 1 & 0 \\ 0 & 0 & 1 \end{bmatrix} [0.0259 \quad 0.5339 \quad 0.8452]^{\mathrm{T}}}$$

$$= 0.3684$$

$$= \lambda_1 \tag{3.9}$$

To see the behaviour of $R(\mathbf{u})$ in the vicinity of an eigenvector, work in coordinates defined by the eigenvectors ordered in an ascending fashion by corresponding eigenvalue by making a coordinate transform:

$$\mathbf{u} = \sum_{i=1}^{n} C_i \, \mathbf{u}^i = \mathbf{U}\mathbf{C} \tag{3.10}$$

Assume that the eigenvectors are normalised such as to satisfy

$$\mathbf{U}^{\mathrm{T}}\mathbf{M}\mathbf{U} = \mathbf{I}; \quad \mathbf{U}^{\mathrm{T}}\mathbf{K}\mathbf{U} = \mathbf{\Lambda} \tag{3.11}$$

and define a trial vector $\mathbf{u}^{\boldsymbol{p}}$ perturbed about the first eigenvector as:

$$\mathbf{u}^{\boldsymbol{p}} = [1 \ \epsilon_1 \ \epsilon_2 \ \epsilon_3 \ \ldots] \tag{3.12}$$

In the modal coordinate system

$$\mathbf{u^p} = 1\mathrm{e}_1 + \sum_{\boldsymbol{i=2}}^{\boldsymbol{n}} \epsilon_i \, \mathrm{e_i} \tag{3.13}$$

where $\mathrm{e_i}$ is the $\mathrm{i^{th}}$ orthonormal basis vector. The Rayleigh's Quotient can then be written

$$R(\mathbf{u^p}) = \frac{[1\mathrm{e}_1 + \sum_{\boldsymbol{i=2}}^{n} \epsilon_i \, \mathrm{e_i}][\boldsymbol{\Lambda}][1\mathrm{e}_1 + \sum_{\boldsymbol{i=2}}^{n} \epsilon_i \, \mathrm{e_i}]^{\mathrm{T}}}{[1 + \sum_{i=2}^{n} \epsilon_i^2]}$$

$$= \frac{[\lambda_1 + \sum_{i=2}^{n} \lambda_i \epsilon_i^2]}{[1 + \sum_{i=2}^{n} \epsilon_i^2]} \tag{3.14}$$

By expanding the denominator as a binomial series, one obtains

$$R(\mathbf{u^p}) \cong \lambda_1 + \sum_{i=2}^{n} (\lambda_i - \lambda_1)\epsilon_i^2 + O(\epsilon_i^4) \tag{3.15}$$

This important result highlights four properties of Rayleigh's quotient that have made it a foundation of modern functional analysis, as well as an invaluable tool in obtaining approximate natural frequencies in vibratory mechanics:

RI. R is stationary when $\mathbf{u}$ is an eigenvector, which can be expressed as $\frac{\partial R(\mathbf{u^p})}{\partial \epsilon}|_{\epsilon=0} = 0$

RII. R is minimal when $\mathbf{u}$ is the fundamental eigenvector: $\frac{\partial^2 R(\mathbf{u^1})}{\partial \epsilon^2}|_{\epsilon=0} > 0$

RIII. If the trial vector differs from an eigenvector by a quantity of order ϵ, then the Rayleigh's quotient will differ from the corresponding eigenvalue by a quantity of order ϵ^2.

RIV. If a parametric family of trial vectors exists and has members in the vicinity of an eigenvector, then the Rayleigh's quotient is stationary and minimised by the equivalence class of trial vectors which makes the smallest angle with the eigenvector in the state space of the system, as measured by the inner product.

Property **RIV** can be seen by again perturbing the trial vector in (3.15). One may observe that in the model system, since all the masses are equal but the first spring is

by far the stiffest in the system, the fundamental natural frequency is unlikely to greatly involve large displacements of the first mass. Furthermore, the ratio of the generalised stiffnesses associated to the second and third modal coordinates is $2:1$; given the quadratic dependency of the potential energy on the displacement, one might reasonably expect the fundamental mode to contain displacements in the vicinity of $[0\ \frac{1}{\sqrt{2}}\ 1]$, which would split the system energy equally between the second and third degrees of freedom and exclude their extremely stiff neighbour.

Inserting this expression as a numerical value for $\mathbf{u}^{\boldsymbol{p}}$ and evaluating the quotient, one obtains for the model system

$$R = \frac{[0\ \frac{1}{\sqrt{2}}\ 1]\begin{bmatrix} -21 & 1 & 0 \\ -1 & -2 & -1 \\ 0 & -1 & 1 \end{bmatrix}[0\ \frac{1}{\sqrt{2}}\ 1]^{\mathrm{T}}}{[0\ \frac{1}{\sqrt{2}}\ 1]\begin{bmatrix} 1 & 0 & 0 \\ 0 & 1 & 0 \\ 0 & 0 & 1 \end{bmatrix}[0\ \frac{1}{\sqrt{2}}\ 1]^{\mathrm{T}}} = 0.3905$$

$$= 1.0601\lambda_1 \qquad (3.16)$$

For such a rough estimate, the precision is remarkable, demonstrating the power of the quadratic convergence of the natural frequencies. It can also be seen that the error is positive and that the method overestimates λ_1, in accord with (3.15).

Attention turns now to interpreting the analytical results presented above in a geometric context. Consider first a two-DOF system with fundamental eigenvector $\mathbf{u}^1$ and second eigenvector $\mathbf{u}^2$:

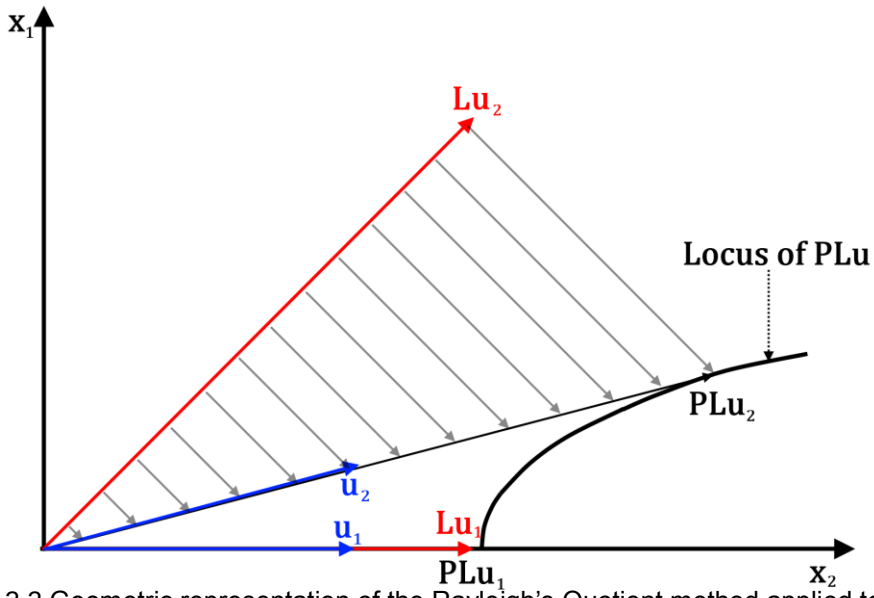

Figure 3.2 Geometric representation of the Rayleigh's Quotient method applied to a selfadjoint operator L defined on a 2D linear space. The system is described in terms of the coordinates x_1 and x_2, corresponding to the basis vectors $\mathbf{u}^2$ and $\mathbf{u}^1$ respectively. The operator $\boldsymbol{P}$ is the projection defined on the next page.

With reference to Figure 3.2, it is possible to obtain a qualitative understanding of the Rayleigh's quotient of a linear operator. For the case where a trial vector $\mathbf{u}^p = \mathbf{u}^1$, the system operator clearly does not change its direction, instead extending it to the vector $\mathbf{Lu}_1$, where the system operator is denoted by $\mathbf{L}$. Then, since $\mathbf{u}^1$ is a unit vector, the inner product of $\mathbf{u}^1$ and $\mathbf{Lu}^1$is simply the length of $\mathbf{Lu}^1$, the projection operation being trivial. For the case where the trial vector is not an eigenvector, as when $\mathbf{u}^p = \mathbf{u}^2$, the system operator will change its direction (unless the eigenvalues are degenerate); the inner product of $\mathbf{u}_2$ and $\mathbf{Lu}_2$ is equivalent to $\mathbf{PLu}_2$, the length of the projection of $\mathbf{Lu}_2$ onto $\mathbf{u}_2$, where the projection operator is denoted $\mathbf{P}$. The resulting locus of $\mathbf{PLu}^p$ as $\mathbf{u}^p$ is smoothly rotated at constant length in the vicinity of x_2, is shown in Figure 3.2. Equation (3.15) implies it is locally well approximated by a quadratic in the sine of the angle between $\mathbf{u}^p$ and $\mathbf{u}^1$.

Rayleigh's quotient can be written in the simpler form

$$R(\mathbf{L},\mathbf{u}) = \frac{\langle \mathbf{u}, \mathbf{Ku} \rangle}{\langle \mathbf{u}, \mathbf{Mu} \rangle} = \frac{\langle \mathbf{u}, \mathbf{Lu} \rangle}{\langle \mathbf{u}, \mathbf{u} \rangle} \tag{3.17}$$

With reference to Figure 3.2, we assume that the (orthogonal) eigenvectors $\mathbf{u}^2$ and $\mathbf{u}^1$are aligned with the axes $x_1$and x_2; furthermore, for simplicity, take the associated

eigenvalues to be 1 and some arbitrary value larger than 1 respectively. Under these conditions, (**17**) simplifies to

$$R = \langle \mathbf{u}, \mathbf{Lu} \rangle \tag{3.18}$$

This form admits a direct interpretation: let the operator $\mathbf{L}$ act on the trial vector $\mathbf{u}$ and then use the inner product to project the result back onto $\mathbf{u}$. The result is the Rayleigh's quotient R. The situation is illustrated geometrically for a simple two degree of freedom system in Figure 3.2; with a little effort, the properties **RI-RIV** follow intuitively.

3.2.2 The Rayleigh-Ritz method

One can argue from property **RIV** of the preceding section that, if the interest lies in finding the lowest eigenvalue and the corresponding shape of the fundamental mode, then Rayleigh's Quotient can be used to discern the superior of any two trial mode shapes, being that which yields the lower value of R. If one regards a smooth one-parameter family of trial solutions, then by imposing **RIV** a constructive procedure for finding the optimum member can be found.

The Rayleigh-Ritz (RR) method is exactly this procedure. It minimises the Rayleigh's quotient over a restriction of $\mathbf{u}^{\mathrm{p}}$ to a subspace $\widetilde{U}$, termed the trial space. **RIV** reads

$$\frac{\partial R(\mathbf{u}^{\boldsymbol{p}})}{\partial \epsilon} = 0 \tag{3.19}$$

Set $\mathbf{u}^{\boldsymbol{p}} = \sum_1^{\mathcal{N}} a_i \mathbf{u}^{\boldsymbol{i}}$ for a set of displacement vector candidates $\mathbf{u}^{\boldsymbol{i}}$, termed trial vectors. The a_i are then the weighting coefficients to be solved for. Thus, $\widetilde{U}$ is the span of the $\mathbf{u}^{\boldsymbol{i}}$, with each ray through the origin forming an equivalence class of solutions. By normalising the $\mathbf{u}^{\boldsymbol{i}}$ to unity, the problem is simplified without loss of generality. Imposing (3.19) leads directly to

$$\delta R = \sum_{i=1}^{\mathcal{N}} \frac{\partial R}{\partial a_i} \delta a_i = 0 \tag{3.20}$$

Notice that the variations of the coefficients δa_i are independent, so that for all i, $\frac{\partial R}{\partial a_i}$ must be identically zero.

The solution procedure can thus be expressed as

$$\forall i, \frac{1}{T_{\mathrm{MAX}}}\left(\frac{\partial V_{\mathrm{MAX}}}{\partial a_i} - \frac{V_{\mathrm{MAX}}}{T_{\mathrm{MAX}}}\frac{\partial T_{\mathrm{MAX}}}{\partial a_i}\right) = 0 \;\; \therefore \;\; \frac{\partial V_{\mathrm{MAX}}}{\partial a_i} - \lambda\frac{\partial T_{\mathrm{MAX}}}{\partial a_i} = 0 \quad (3.21)$$

Where $V_{\max}$ and T_{ref} are respectively the peak potential and reference kinetic energies of the system and λ is an eigenvalue[3]. The quantities $\frac{\partial V_{\max}}{\partial a_i}$ and $\frac{\partial T_{\mathrm{ref}}}{\partial a_i}$ are cast as matrices by the introduction of the series approximation, approximation rendering the problem algebraic and amenable to computational solution, once the necessary integral quantities have been evaluated. Substituting the series expression for u into (3.21), the resulting algebraic eigenvalue problem can be expressed as:

$$\mathbf{Ka} = \lambda\mathbf{Ma} \quad (3.22)$$

Where $\mathbf{K}$ and $\mathbf{M}$ are now the $\mathcal{N} \times \mathcal{N}$ mass and stiffness matrices resulting from the action of the operators in (3.17) on the series expansion, and $\mathbf{a}$ is the vector of weights. The solutions to this generalised eigenvalue problem are termed Ritz pairs: the eigenvectors are known as Ritz vectors $\tilde{\mathbf{u}}_{\mathrm{i}}$; the corresponding eigenvalues are Ritz values $\tilde{\lambda}_{\mathrm{i}}$.

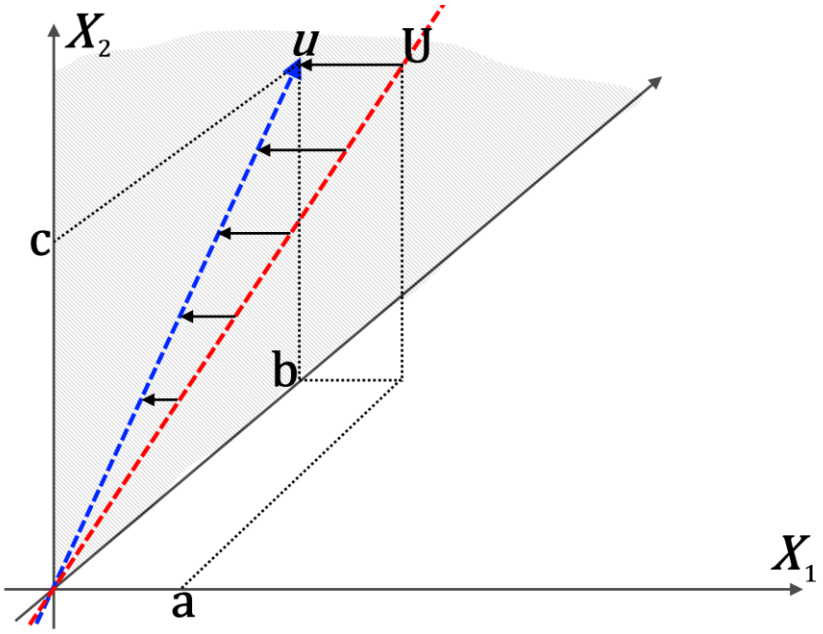

Figure 3.3 Geometric representation of the RR method operating on a selfadjoint operator on a 3D vector space, here represented by generalised coordinates $x_1, x_2,$, and x_3.

In Figure 3.3, an eigenvector of the system operator generates the red dashed invariant subspace $\overline{U}$. It is a one-dimensional linear space spanned by the vector $\mathrm{a}, \mathrm{b}, \mathrm{c}$ with respect to the chosen basis. A Rayleigh-Ritz approximation using $[0\ 0\ 1]$ and $[0\ 1\ 0]$ as trial vectors has the x_2x_3-plane as trial space $\widetilde{U}$, here hatched; the blue dashed Ritz vector ũ spans the orthogonal projection of $\overline{U}$ onto $\widetilde{U}$. The angle *from* $\overline{U}$ *to* $\widetilde{U}$ is the first principal angle between the subspaces $\overline{U}$ and $\widetilde{U}$. The sine of this angle is the subspace gap between the trial and invariant subspaces.

The situation differs from the pure Rayleigh's quotient, in that there is restriction in the argument, and an imposed minimisation constraint on the quotient itself. However, the quotient is used as the prime metric for the procedure, and some of its features are conferred. In particular, if $\widetilde{U}$ is close to an eigenvector (small subspace gap) then the lowest Ritz value is in error by a quantity of order of the product of the sine of the angle from the eigenvector to the subspace, termed the subspace gap (see Figure 3.3 and the references for more detail) and by the spectral norm of the system matrix[4].

3.2.3 Complete sets of trial functions

For the applications, a *minimising sequence* is initiated by taking $\mathcal{N} = 1$ and solving for the lowest Ritz value $\tilde{\lambda}_1$ and corresponding Ritz vector $\tilde{\mathbf{u}}_\mathbf{1}$. This amounts to the solution of the algebraic eigenvalue problem for the a_i. The process continues by incrementing $\mathcal{N}$ by adding another trial function, and iterating until desired convergence is achieved in the $\tilde{\lambda}_1$. Typically, although not essentially, the $\mathbf{u_i}$ are generated from a family of orthogonal functions. If the trial functions are drawn from a complete set, i.e. a Riesz basis of the Hilbert configuration space of the system, then the Minimax Theorem guarantees that in the limit $\mathcal{N} \to \infty$, convergence of the Ritz values is uniform, while convergence of the Ritz vectors (under good conditions – see eg.[5], [6]) is uniform *in the mean*.

3.2.4 Substructuring

A *substructure* is taken here to mean a simply connected subdomain of the domain of definition of the problem. In modal analysis of mechanical systems, substructuring methods involve partitioning the domain of the problem into $\mathcal{M}$ substructures,

introducing local approximations for each substructure with $\mathcal{N}$ local degrees of freedom, and requiring that geometric conditions of continuity are satisfied are called substructuring methods.

Henceforth, it is necessary to distinguish carefully between local quantities, relating to a substructure, and global quantities, relating to the whole structure. Additionally, distinction is made between global and global disjoint quantities, which refer respectively to the assembled (compatibility-constrained) structure and its substructures considered as distinct and independent.

The $\mathcal{N}\mathcal{M}$ −dimensional space $\widetilde{U}_{GD}$ formed by the Cartesian product of the state spaces of the local approximations is termed the *global disjoint trial space*. It is therefore spanned by the a_i; each point in $\widetilde{U}_{GD}$ corresponds to a choice of the a_i. The continuity conditions are imposed as a system of $\mathcal{O}$ constraints on the local approximations. Obtaining the constrained local approximation for all degrees of freedom in the approximation is equivalent to obtaining a *global* approximation to the original problem defined on the original domain, with each global degree of freedom consisting of one linear combination of the local degrees of freedom from each substructure. The global solution can be represented by a double sum of the form

$$\sum_{i=1}^{\mathcal{M}} \sum_{j=1}^{\mathcal{N}} a_{ij}\, \mathbf{u}_{ij} \tag{3.23}$$

The RR method as outlined applies to a problem with a single domain, on which all the trial functions are defined. For complex problems, however, a substructuring approach is far more flexible, splitting the original domain into subdomains with simpler geometry and able to be approximated by simpler trial functions. Each substructure is approximated by a trial space spanned by a finite set of substructure trial functions. A global trial space is then formed by the disjoint union of the substructure trial spaces, restricted by compatibility conditions between substructures, and the RR procedure is allowed to operate on this reduced system. In this approach, the global trial space for the problem is of dimension $\mathcal{N}\mathcal{M} - \mathcal{O}$.

3.2.5 Quasi-Comparison Trial Functions

In the RR method, the trial functions must be at least *admissible functions* – that is to say, they must satisfy the *geometric* boundary conditions of the problem, and be smooth enough for the Lagrangian to be well defined. It is desirable for simple problems for the functions to belong to a more rarefied class, namely *comparison functions*. These possess the additional property of satisfying the *natural* boundary conditions of the problem, as well as being admissible functions.

By the Minimax Theorem and the Riesz Representation theorem, when the degrees of freedom $\mathcal{N} \to \infty$, the use of comparison vs. admissible functions does not matter – they converge to the same limit. However, the convergence of the truncation is what is of importance for practical problems. Experience conforms to intuition in that comparison functions expedite convergence significantly when compared to general admissible functions. This can be seen as due to the possibility of a subspace gap existing between the trial space and the invariant subspace being present if admissible functions only are used, leading to slow convergence[7], Runge and Gibbs phenomena[8], etc. Hence, it is desirable to use comparison functions in the RR method whenever possible.

However, for complex boundary conditions such as those that arise in substructuring problems, a priori knowledge of the natural boundary conditions may be unavailable; even if this is not so, it may be difficult to choose functions that satisfy all the natural boundary conditions simultaneously.

One possible attack is the Quasi-Comparison Function (QCF) approach of Meirovitch[3]. Instead of trying to use a family of functions that are orthogonal and that satisfy the natural boundary conditions of the problem, the method proposes using trial functions consisting of an undetermined superposition of admissible functions, each of which satisfies a different simple natural boundary condition. If more families are used than natural boundary conditions are required to be satisfied, then it is always possible to choose the superposition to be a comparison function, and to leave one degree of freedom for the RR procedure to operate on. The cost is the introduction of additional degrees of freedom for each value of $\mathcal{N}$. However, the

subspace gap between $\overline{U}$ and $\widetilde{U}$ caused by the natural boundary conditions is thus eliminated. Practical experience shows that convergence is very often significantly expedited. The RR method with using QCF trial functions is referred to as the Rayleigh-Ritz-Meirovitch (RRM) method.

The RRM method is an established technique for modal analysis of complex structures. The first reference to the technique in the literature known to the author of this thesis was in 1980[3], which introduces the technique through a simple example, proves some basic results on convergence, and qualitatively discusses the method and its advantages in some detail. The same authors published several follow-up papers demonstrating and elucidating the substructuring approach with the Rayleigh-Ritz method[9–12]. A brief but interesting review of substructuring methods is presented by Sotiropoulos[13]. The convergence characteristics of the method are compared to classical FEA by Meirovitch and Kwak in a series of papers published in the early 1990s[14–16], which also prove the extension of the classical inclusion theorem to the substructured Rayleigh-Ritz approach when the natural boundary conditions are exactly satisfied.

The convergence of Rayleigh-Ritz substructuring methods are examined in some detail for various choices of structure, trial functions, and compatibility conditions for the beam case in a superb 1995 paper[17]. In particular the latter clearly presents the similarities and differences between the RRM approach (with and without substructuring), the classical FEM, and a modified approach presented within the paper.

Estimates of the asymptotic error and examination of the convergence behaviour of the RR method, with particular attention to convergence of the derivatives (cf. Sections 3.2.3 and 3.6) were presented in Chang's PhD thesis[7] in 1997.

3.3 Application to L-frame

In Section 3.2, the theory and intuition behind the Rayleigh-Ritz method, its extension to substructuring problems, and the use of the enhancement of Meirovitch and quasi-comparison functions was developed. In this section, the techniques are extended to frame structures.

3.3.1 Previous work

L-frames have been analysed extensively in the literature, both from the perspective of approximating real structures such as brackets, antennas and robot arms, and as an ideal test case for structural analysis methods and procedures capable of handling rigid body motion of the substructures. Morales applies his variation of the RRM method to this geometry in a series of recent papers[18], [19] that are relevant. Only flexural displacements are considered, using Clamped-Clamped and Clamped-Free modes to form the quasicomparison functions. Superior convergence is exhibited over the first five natural frequencies using a 12-DOF approximation relative to a 60-DOF FEA; comparison to these results is given in the sequel.

RRMSSM-based methods have been applied extensively to flexural vibrations of planar frame structures in the past. Beyond simple two-beam structures presented in the original paper from 1980 and its descendants[3], [9], [20], Morales presents the first fully-fledged RRMSSM frame structure application in a 2000 paper[21], developing a kinematical procedure and proving convergence for the multiply supported case and demonstrating superior convergence with respect to the FEM. In the aforementioned work, he details a kinematical procedure for multiply supported structures that is of direct relevance in what follows. He generalises his examples to more complex frames in a later work[22], again demonstrating expedited convergence, and extends the method to consider static Euler buckling in a 2007 paper.

3.3.2 Geometric configuration and substructures

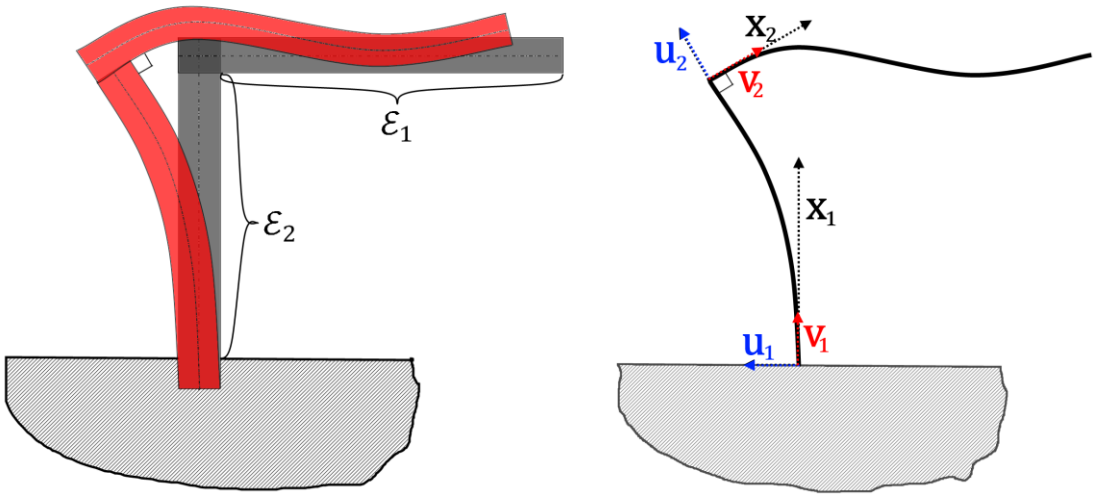

Figure 3.4 L-Frame structure: substructuring and coordinate systems.

The configuration considered in this section is illustrated in Figure 3.4. An L-shaped, one-dimensional structure in a two dimensional embedding space, composed of a single slender element with a right angle bend in general position along its interior, is viewed as two substructures, $\mathcal{E}_1$ and $\mathcal{E}_2$. Coordinates x_1 and x_2 are defined from the distal end and the common point for, $\mathcal{E}_1$ and $\mathcal{E}_2$ respectively; transverse and axial deflections are denoted by u_1 and v_1 for $\mathcal{E}_1$ and u_2 and v_2 for $\mathcal{E}_2$ respectively.

3.3.3 Physics

After substructuring, the components are modelled as 2-DOF 1-dimensional linear elastic fields: an Euler-Bernoulli flexural component $u(x)$ and a decoupled compressive elastic component $v(x)$, with the senses and sign conventions as shown in Figure 3.4. With this choice of physical field model, the Lagrangian density can be written as

$$\begin{aligned}\mathcal{L} &= T^* - V \\ &= \int_0^{\ell} \frac{\rho A_x}{2}(\dot{u}^2 + \dot{v}^2)\,\mathrm{d}x \\ &\quad - \int_0^{\ell} \frac{EI}{2}(u'')^2 + \frac{EA_x}{2}(v')^2\,\mathrm{d}x \end{aligned} \tag{3.24}$$

where $\mathcal{L}$ is the Lagrangian density, T^* is the cokinetic energy, V is the potential energy, ρA_x is the (potentially variable) mass density per unit length of the beam, EI is the flexural stiffness of the beam, while EA_x is the axial stiffness. This approach captures disjoint flexural and axial vibrations of each substructure; the coupling between the motions is achieved by constraining deflections and rotations fields at the common point to be commensurate:

$$v_1|_{\ell 1} = u_2|_0 \tag{3.25a}$$

$$u_1'|_{\ell 1} = u_2'|_0 \tag{3.25b}$$

However, to account for rigid body displacements of $\mathcal{E}_2$ arising from tip deflections and rotations, another approach is required. A lumped-parameter approximation is employed here for the purpose.

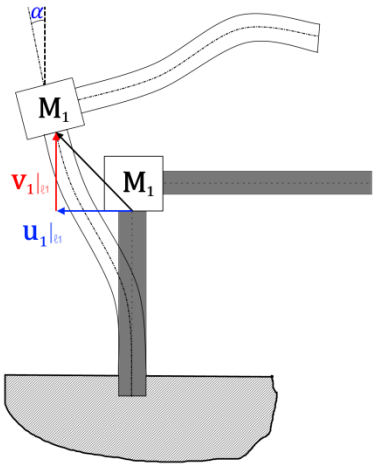

Figure 3.5 Effective lumped-mass configuration for the model. The transverse and axial tip displacements of $\mathcal{E}_1$are respectively $u_1|_{\ell 1}$ and $v_1|_{\ell 1}$; the rotational tip displacement is $\sin(\alpha)$.

The extra term in the system Lagrangian due to the addition of the lumped mass depicted in Figure 3.5 is given by

$$T_{\mathrm{L}}^{*} = \frac{M_2}{2}\left([u_1|_{\ell 1}]^2 + [v_1|_{\ell 1}]^2\right) \tag{3.26}$$

where T_{L}^{*} is the (co-)kinetic energy contribution due to the lumped mass $M_2 = \int_0^{\ell 2} \rho A_x dx_2$. Rayleigh's quotient for the system can be written explicitly as

$$R = \frac{\langle \mathbf{u}, \mathbf{K}\mathbf{u} \rangle}{\langle \mathbf{u}, \mathbf{M}\mathbf{u} \rangle}$$

$$= \frac{\int_0^{\ell_1} \frac{E_1 I_1}{2}(u_1'')^2 + \frac{E_1 A_{x1}}{2}(v_1')^2 \mathrm{d}x_1 + \int_0^{\ell_2} \frac{E_2 2}{2}(u_2'')^2 + \frac{E_2 A_{x2}}{2}(v_2')^2 \mathrm{d}x_1}{\int_0^{\ell_1} \frac{\rho_1 A_{x1}}{2}(\dot{u}_1^2 + \dot{v}_1^2)\,\mathrm{d}x_1 + \int_0^{\ell_2} \frac{\rho_2 A_{x2}}{2}(\dot{u}_2^2 + \dot{v}_2^2)\,\mathrm{d}x + \frac{M_2}{2}\left([u_1|_{\ell 1}]^2 + [v_1|_{\ell 1}]^2\right)} \tag{3.27}$$

3.3.4 Quasi-comparison functions

Having substructured the frame and imposed constraints and chosen the energy quadratic forms, it remains only to choose the trial functions before explicitly formulating the matrices. Quasi-comparison functions (Cf. Section 3.2.5) are employed for the purpose. Meirovitch defines quasicomparison functions as follows[23]:

- Each QCF must comprise a linear combination of at least two geometrically admissible functions;
- Each of the component admissible functions must be capable of satisfying the *complementary boundary conditions* (CBCs).

The CBCs are constraints of the form of inequalities with zero right hand side. They impose the requirement that the QCF possess the necessary algebraic freedom to satisfy the natural boundary conditions. In the geometric picture, the Hilbert space of solutions can be pictured as the limit of a series of corresponding finite-dimensional spaces of increasing dimensionality, where each basis vector corresponds to an element of a chosen set of orthogonal functions on the domain. For a beam and by extension beam superstructures such as planar frames, one natural candidate for the choice of basis function emerges: the modes under a particular set of boundary conditions. For example, take the case of a clamped-clamped beam, whose modes are well known [24].

In substructuring problems, nontrivial natural boundary conditions arise at points common to more than one substructure, such as joints and nodes. Continuity boundary conditions express the generally possible natural boundary conditions at a particular common boundary of two substructures with respect to kinematic relations. For example, $u_i|_{\ell i} \neq 0, u_i|_0 \neq 0$ and $v_i'|_0 \neq 0$ are all CBCs; the first represents freedom possessed by a structure to deflect at a boundary point $x_i = \ell_i$. To form QCFs, one must select from among some set of geometrically admissible trial function families, generated as the modes of the substructure fields under different boundary conditions, enough trial functions such that the resulting QCF contains enough freedom that *all* the CBCs can be satisfied. For the purpose of this analysis, Euler-Bernoulli beam modes generated from permutations of clamped, free, pinned and sliding boundary conditions will be employed to generate the u admissible families, while axial vibration modes of a rod with permutations of clamped and free ends will be used for the v admissible families. The admissible mode families and CBCs are displayed in Table 3.4, along with an indication of which admissible modes fulfil each CBC.

Requirement R1. The QCFs are formed by selecting the minimum number of families such that *all the CBCs are fulfilled*; that is to say, such that *at least* one entry from each row of Column 5 of Table 3.4 is chosen for each element and field.

Field	Boundary Condition	Shorthand notation
Flexural	$u = 0$ $u' = 0$	C; Clamped
Flexural	$u = 0$ $u'' = 0$	P; Pinned
Flexural	$u'' = 0$ $u''' = 0$	F; Free
Flexural	$u' = 0$ $u''' = 0$	S; Sliding
Axial	$v = 0$	C; Clamped
Axial	$v' = 0$	F; Free

Table 3.3 Boundary conditions used in analysis of flexural and axial vibration of slender members. An underbar denotes that the condition / mode family referred to are for axial displacements; its absence denotes reference to flexural displacements

In what follows, the flexural axial and transverse modes of a slender beam under different combinations of boundary conditions will be denoted by concatenating the shorthand notations introduced in Table 3.3 such that the first notation corresponds to the coordinate zero and the second to the coordinate maximum. For instance, CS will denote the clamped-sliding family of flexural modes, i.e. those that solve the BVP generated using the Euler-Bernoulli beam equations with the boundary conditions

$$u|_{x=0} = 0 \ (3.28a); \quad u'|_{x=0} = 0 \ \ (3.28b)$$

$$u'|_{x=\ell} = 0 \ (3.28c); \quad u'''|_{x=\ell} = 0 \ (3.28d)$$

Whereas CF denotes the Clamped-Free family of axial modes, i.e. those generated using the wave equation under the boundary conditions

$$v|_{x=0} = 0 \ (3.29a); \quad v'|_{x=\ell} = 0 \ (3.29b)$$

A numerical suffix denotes a particular member of the family. Zero denotes a rigid-body mode. For instance, FF0 is the Free-Free flexural rigid body mode (pure translation), CC2 is the first overtone of the Clamped-Clamped family, and so forth. Using this notation, Table 3.4 defines the admissible mode families for each substructure for the L-frame case.

Substructure	Field	Admissible mode families	CBC	Quasicomparison mode families
1	u_1	CC, CF, CS, CP	$u_1\|_{\ell 1} \neq 0$	CF, CS
			$u_1'\|_{\ell 1} \neq 0$	CF, CP
			$u_1''\|_{\ell 1} \neq 0$	CC, CS
			$u_1'''\|_{\ell 1} \neq 0$	CC,CP
1	v_1	CF, CC	$v_1\|_{\ell 1} \neq 0$	*CF*
			$v_1'\|_{\ell 1} \neq 0$	*CC*
2	u_2	CC, CF, CS, CP, PP, PC, PF, PS, FF, FP, FC, FS, SS, SP, SC, SF	$u_2\|_0 \neq 0$	FF, FP, FC, FS, SS, SP, SC, SF
			$u_2'\|_0 \neq 0$	PP, PC, PF, PS, FF, FP, FC, FS
			$u_2''\|_0 \neq 0$	SS, SP, SC, SF, CC, CF, CS, CP
			$u_2'''\|_0 \neq 0$	CC, CF, CS, CP, SS, SP, SC, SF

Table 3.4 Complementary boundary conditions for the L-frame structure and corresponding mode families admissible under each CBC. The letters C, F, S, and P refer to Clamped, Free, Sliding, and Pinned conditions respectively.

Any linear combination of functions satisfying **R1** and containing at least two complete families of simple modes will be termed an **R1**-QCF. All **R1**-QCFs satisfy the geometric boundary conditions automatically, and contain enough freedom to satisfy the natural boundary conditions. It is clearly possible to satisfy **R1** in several inequivalent ways; for example, for the field u_1, one could use a combination of C-P and C-S modes to form

the quasicomparison funtions, or alternately one could use C-F and C-C modes. Similar multiplicities apply for the other fields and elements. The above procedure generates families of QCFs indexed by a discrete parameter; the $\mathcal{M}$th QCF contains $2\mathcal{M}$ axial and $2\mathcal{M}$ flexural trial functions for a total of $4\mathcal{M}$ DOF. For elements where axial deflections can be neglected, only the $2\mathcal{M}$ axial DOF need be included.

The trial space for an element consists of the example presented in this section, the choices of **R1**-QCF are presented in Table 3.5.

Substructure	**Field**	**R1**-QCF1	**R1**-QCF2	**R1**-QCF3
1	u_1	a_{11}CF1 +a_{21} CC1	a_{11}CF1+a_{21} CF2 +a_{31}CC1+a_{41} CC2	a_{11}CF1+a_{21} CF2 +a_{31}CF3+a_{41} CC1 +a_{51}CC2+a_{61} CC3
1	v_1	b_{11}CF1 +b_{21} CC2	b_{11}CF1+b_{21} CF2 b_{21}CC1+b_{21} CC2	b_{11} CF1+b_{21} CF2 +bCF3+b_{41} CC1 +b_{51} CC2+b_{61} CC3
2	u_2	$a_{12}PF0$ $+a_{22}SF0$	$a_{12}PF0$ $+ a_{22}PF1$ $a_{32}SF0 + a_{42}SF1$	a_{12}PF0+a_{22} PF1 +a_{32}PF2+a_{42} SF0 +a_{52}SF1+a_{62} SF2

Table 3.5 Explicit forms for the first, second and third order quasicomparison functions R1-QCF1, R1-QCF2 and R1-QCF3 for the L-frame.

For each of the deflection fields u_i and v_i corresponding to the flexural and axial displacements in the ith substructure, the cokinetic and potential energies corresponding to the $\mathcal{M}$th order quasicomparison functions can be expressed as a $2\mathcal{M} \times 2\mathcal{M}$ matrix left- and right-multiplied by a column $2\mathcal{M} -$ vector. For example, the cokinetic energy of the $\mathcal{M}$th QCF for the ith element can be written as

$$\mathrm{T}^*{}_i = \mathbf{K_i a_i} = \begin{bmatrix} a_{1i} \\ \vdots \\ a_{Mi} \\ b_{M+1i} \\ \vdots \\ b_{2Mi} \end{bmatrix}^T \begin{bmatrix} \mathbf{K}_{1u} & \mathbf{0} \\ \mathbf{0} & \mathbf{K}_{1v} \end{bmatrix} \begin{bmatrix} a_{1i} \\ \vdots \\ a_{Mi} \\ b_{M+1i} \\ \vdots \\ b_{2Mi} \end{bmatrix} \tag{3.30}$$

The global disjoint trial space is identified with the span of the QCFs. The corresponding scalar entries in the global disjoint coefficient vector are the global disjoint degrees of freedom; prescribing them up to a multiplicative constant selects a unique element of the Hilbert space on which the original problem was defined, and inserting this choice into the Rayleigh's quotient yields a corresponding Ritz value, approximate to the corresponding natural frequency.

3.3.5 Explicit formulation

The simplest case will be worked through explicitly, both algebraically and numerically, in the following subsection. The more complex case of the XBR follows a precisely identical order of operations and procedure, save the added complexity of dealing with more substructures and constraints between them.

Substituting the order 1 quasicomparison function approximation from Table 3.5 into the expression for Rayleigh's Quotient gives

$$R = \frac{\begin{array}{c} \sum_{k=1}^{2} \int_0^{\ell_k} \frac{E_k A_{xk}}{2} \sum_{i=1}^{2m} b_{ik} \mathbf{v}'_{ik} \sum_{j=1}^{2m} b_{jk} \mathbf{v}'_{jk} \, \mathrm{d}x_k \\ + \sum_{k=1}^{2} \int_0^{\ell_k} \frac{E_k I_k}{2} \sum_{i=1}^{3n} a_{ik} \mathbf{u}''_{ik} \sum_{j=1}^{2n} a_{jk} \mathbf{u}''_{jk} \end{array}}{\begin{array}{c} \sum_{k=1}^{2} \int_0^{\ell_k} \frac{\rho_k A_{xk}}{2} \left(\sum_{i=1}^{3n} a_{ik} \dot{\mathbf{u}}_{ik} \sum_{i=1}^{3n} a_{jk} \dot{\mathbf{u}}_{jk} + \sum_{i=1}^{2m} b_{ik} \dot{\mathbf{v}}_{ik} \sum_{i=1}^{2m} b_{jk} \dot{\mathbf{v}}_{jk} \right) \mathrm{d}x_k \\ + \sum_{k=1}^{2} \frac{M_2}{2} \left(\sum_{i=1}^{3n} a_{ik} \mathbf{u}_{ik}|_{\ell 1} \sum_{j=1}^{3n} a_{jk} \mathbf{u}_{jk}|_{\ell 1} + \sum_{i=1}^{2m} b_{ik} \mathbf{v}_{ik}|_{\ell 1} \sum_{j=1}^{2m} b_{jk} \mathbf{v}_{jk}|_{\ell 1} \right) \end{array}} \tag{3.31}$$

The rather cumbersome expression (3.31) can be more elegantly expressed in matrix form. The numerator is cast as

$$\mathbf{a_i^T K_{GD} a_i} = [a_{11} \; a_{21} \; b_{11} \; b_{21} \; a_{12} \; a_{22}] \begin{bmatrix} \mathbf{K_{1u}} & \mathbf{0} & \mathbf{0} \\ \mathbf{0} & \mathbf{K_{1v}} & \mathbf{0} \\ \mathbf{0} & \mathbf{0} & \mathbf{K_{2u}} \end{bmatrix} \begin{bmatrix} a_{11} \\ a_{21} \\ b_{11} \\ b_{21} \\ a_{12} \\ a_{22} \end{bmatrix} \tag{3.32}$$

Where the global, disjoint stiffness matrix $\mathbf{K_{GD}}$ is composed of the 2x2 substructure block stiffness matrices as follows:

$$\mathbf{K_{1u}} = \frac{E_1 I_1}{2}\begin{bmatrix} \int_0^{\ell_1} (CF1'')^2 \mathrm{d}x_1 & \int_0^{\ell_1} CF1''CC1''\mathrm{d}x_1 \\ \int_0^{\ell_1} CF1''CC1''\mathrm{d}x_1 & \int_0^{\ell_1} (CC1'')^2 \mathrm{d}x_1 \end{bmatrix}$$

$$\mathbf{K_{1v}} = \frac{E_1 A_{x1}}{2}\begin{bmatrix} \int_0^{\ell_1} \left(\underline{CF}1'\right)^2 \mathrm{d}x_1 & \int_0^{\ell_1} \underline{CF}1'\underline{CC}1'\mathrm{d}x_1 \\ \int_0^{\ell_1} \underline{CF}1'\underline{CC}1'\mathrm{d}x_1 & \int_0^{\ell_1} \left(\underline{CC}1'\right)^2 \mathrm{d}x_1 \end{bmatrix}$$

$$\mathbf{K_{2u}} = \frac{E_2 I_2}{2}\begin{bmatrix} \int_0^{\ell_2} (PF1'')^2 \mathrm{d}x_2 & \int_0^{\ell_2} PF1''SF1''\mathrm{d}x_2 \\ \int_0^{\ell_2} PF1''SF1''\mathrm{d}x_2 & \int_0^{\ell_2} (SF1'')^2 \mathrm{d}x_2 \end{bmatrix}$$

$\mathbf{K_{1u}}$ and $\mathbf{K_{1v}}$ are respectively the stiffness matrices for flexural and axial displacements of the first substructure and $\mathbf{K_{2u}}$ is the stiffness matrix for flexural vibrations of the second substructure. Similarly, the denominator of (**31**) can be cast in matrix form as

$$\mathbf{a_i^T M_{GD} a_i} = [a_{11}\ a_{21}\ b_{11}\ b_{21}\ a_{12}\ a_{22}]\begin{bmatrix} \mathbf{M_{1u}} & 0 & 0 \\ 0 & \mathbf{M_{1v}} & 0 \\ 0 & 0 & \mathbf{M_{2u}} \end{bmatrix}\begin{bmatrix} a_{11} \\ a_{21} \\ b_{11} \\ b_{21} \\ a_{12} \\ a_{22} \end{bmatrix} \quad (3.33)$$

In the next subsection, application of the constraints will be considered explicitly.

3.3.6 Constraint

The procedure followed thus far has derived uncoupled mass and stiffness matrices for each substructure, but without accounting for the coupling at the common point of the substructures. Clearly, the forces and moments at the common point, by which the

substructures interact, plays a central role in determining the overall modal dynamics of the system. The forces are of course not known a priori; indeed, finding some of them is the very objective of the exercise, from a support loss perspective. The collective behaviour of the substructures as an overall system is examined by enforcing conditions of geometric compatibility between the substructures. This imposes constraint on the trial space, reducing its dimension by the number of geometric constraints.

So far, in the L-frame model, six degrees of freedom have been introduced, corresponding to one **R1**-QCF for each of Substructure 1 axial and flexural displacements and Substructure 2 flexural displacements. Two constraints, not automatically satisfied by the QCFs, must be imposed at the common point.

$$u_1'|_{x_1=\ell} = u_2'|_{x_2=0} \qquad (3.34a)$$

$$v_1|_{x_1=\ell} = u_2|_{x_2=0} \qquad (3.34b)$$

The first of these expresses the rigidity of the connection between the substructures, that is to say, that the angle between them remains a right angle; the second expresses continuity between axial compression of the first substructure and deflection of the end of the second substructure proximal to the common point. In terms of the QCFs and the associated degrees of freedom, (3.34a) and (3.34b) have the form

$$\mathbf{C} = \begin{bmatrix} CF1'|_{x_1=\ell} & 0 & 0 & 0 & -PF0'|_{x_2=0} & 0 \\ 0 & 0 & \underline{CF}1|_{x_1=\ell} & 0 & 0 & -SF0|_{x_2=0} \end{bmatrix} \begin{bmatrix} a_{11} \\ a_{21} \\ b_{11} \\ b_{21} \\ a_{12} \\ a_{22} \end{bmatrix} \qquad (3.35)$$

The approximate solution for the system is found by applying the Rayleigh-Ritz procedure as described in Section 3.2. It may be noted that, for this particular approximation, only one disjoint degree of freedom from each substructure contributes to each of the two constraints. The effect of constraint can be read off directly: the first line specifies that the coefficients a_{11} and a_{12} are proportionally

related, in the ratio $a_{12} = \frac{CF1'|_{x_1=\ell}}{PF0'|_{x_2=0}} a_{11}$; similarly, the second line specifies that b_{11} and a_{22} are related in the proportion $b_{11} = \frac{\underline{CF}1|_{x_1=\ell}}{SF0|_{x_2=0}}$. The approximation for the complete L-frame system is evaluated subject to this constraint. Numerically, this can be accomplished by generating a basis set for the nullspace of $\mathbf{C}$, which will be of dimension 4, and letting the global displacement be represented in terms of this basis.

For the L-frame constraint matrix (3.35), the basis can be chosen readily. The second and fourth degrees of freedom, here indexed by a_{21} and b_{21} have zero coefficient in both constraints, and can again be taken as orthogonal basis vectors. The first and sixth degrees of freedom a_{11} and a_{22}, and the third and fifth degrees of freedom b_{11} and a_{12}, are respectively coupled by the first and second constraint equations. Seeking the vector in the $a_{11} - a_{22}$ plane orthogonal to the constraint, we have

$$a_{12} = -\frac{PF0'|_{x_2=0}}{CF1'|_{x_1=\ell}} a_{11} \tag{3.36}$$

And hence a unit column vector orthogonal to the constraint and to the $a_{21} - b_{21}$ plane is given by

$$\frac{1}{\sqrt{1 + \left(\frac{PF0'|_{x_2=0}}{CF1'|_{x_1=\ell}}\right)^2}} \begin{bmatrix} 1 & 0 & 0 & 0 & -\frac{PF0'|_{x_2=0}}{CF1'|_{x_1=\ell}} & 0 \end{bmatrix} \tag{3.37}$$

Similarly, one obtains for a unit vector orthogonal to the zero set of the second constraint as

$$\frac{1}{\sqrt{1 + \left(\frac{SF0|_{x_2=0}}{\underline{CF}1|_{x_1=\ell}}\right)^2}} \begin{bmatrix} 0 & 0 & 1 & 0 & 0 & -\frac{SF0|_{x_2=0}}{\underline{CF}1|_{x_1=\ell}} \end{bmatrix} \tag{3.38}$$

Then the rows of $\bar{\mathbf{C}}$ are an orthonormal basis for the orthogonal complement of $\mathbf{C}$ in the trial space.

$$\bar{\mathbf{C}} = \begin{bmatrix} 0 & 1 & 0 & 0 & 0 & 0 \\ 0 & 0 & 0 & 1 & 0 & 0 \\ Q_1 & 0 & 0 & 0 & -Q_1 R_1 & 0 \\ 0 & 0 & Q_2 & 0 & 0 & -Q_2 R_2 \end{bmatrix} \tag{3.39}$$

where

$$Q_1 = \frac{1}{\sqrt{1 + \left(\frac{PF0'|_{x_2=0}}{CF1'|_{x_1=\ell}} \right)^2}} \quad , \quad Q_2 = \frac{1}{\sqrt{1 + \left(\frac{PF0'|_{x_2=0}}{CF1'|_{x_1=\ell}} \right)^2}}$$

$$R_1 = \frac{PF0'|_{x_2=0}}{CF1'|_{x_1=\ell}} \quad , \quad R_2 = \frac{SF0|_{x_2=0}}{\underline{CF}1|_{x_1=\ell}}$$

To apply the constraint to the problem, the global trial space must be reduced to such vectors as satisfy the constraints; that is, to the rowspace of $\bar{\mathbf{C}}$**.** This is accomplished by conjugation of $\mathbf{M_{GD}}$ and $\mathbf{K_{GD}}$ with $\bar{\mathbf{C}}$ to form global constrained mass and stiffness matrices $\mathbf{M_G}$ and $\mathbf{K_G}$:

$$\mathbf{M_G} = \bar{\mathbf{C}}\mathbf{M_{GD}}\bar{\mathbf{C}}^{\mathbf{T}} \quad , \quad \mathbf{K_G} = \bar{\mathbf{C}}\mathbf{K_{GD}}\bar{\mathbf{C}}^{\mathbf{T}} \tag{3.40}$$

3.3.7 Solution procedure

From this stage, solution is straightforward, and in complete concert with the discrete Rayleigh-Ritz method as presented in Section 3. Equation (3.21) can again be applied to cast the Rayleigh-Ritz minimisation as an algebraic eigenvalue problem:

$$\mathbf{K_G}\mathbf{a_C} = \lambda \mathbf{M_G}\mathbf{a_C} \tag{3.41}$$

Where $\mathbf{a_C}$ is understood to be a column vector of constrained degrees of freedom, i.e. weighting coefficients for the rows of $\bar{\mathbf{C}}$, which define global constrained trial functions. The full gamut of linear algebraic techniques for solution of generalised eigenvalue problems can be brought to bear on (3.41).

When the method is applied to Bang's test case[30], the results demonstrate rapid convergence, as can be seen from Table 3.6.

Mode	Present work-1 QCF, 4 DOF	Present work-2 QCFs, 10 DOF	Morales et al. 12 DOF RRMSSM	FEM 60 DOF	Analytical
1	0.2247	0.2247	0.2247	0.2247	0.2247
2	0.8302	0.7940	0.7940	0.7940	0.7940
3	7.7918	2.6815	2.6814	2.6814	2.6814

Table 3.6 Comparison of results from Morales et al [22]. with the present work for the analytical test case originally proposed by Bang et al. The rightmost three columns are excepted from the references[19] and [30].

3.4 Application to XBR

In this section, the Rayleigh-Ritz-Meirovitch method developed in Sections 3.2 and 3.3 is applied to the XBR case.

3.4.1 Geometry and substructures

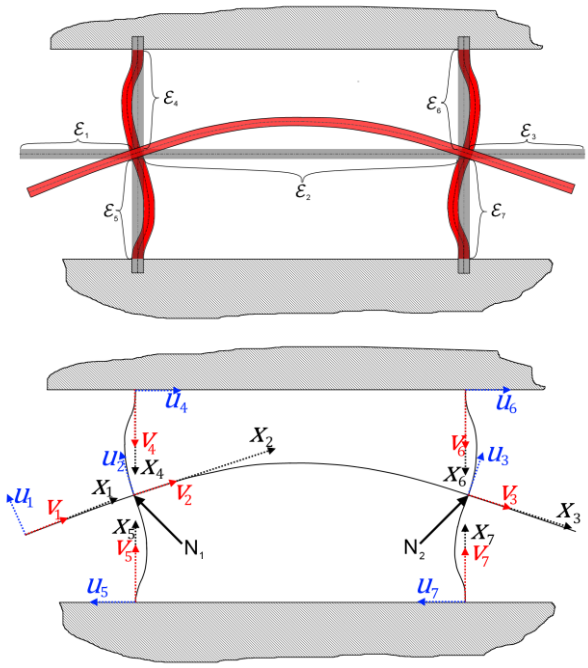

Figure 3.6 Diagram of an XBR, substructured into 7 elements, $\mathcal{E}_1 - \mathcal{E}_7$, for analysis. The hatched boundaries are mechanical ground, representing the connection to the substrate. The ith substructure ε_i has constant material density ρ_i and elastic modulus Y_i in- plane transverse height h_i and axial length ℓ_i. The local spatial coordinate for the ith substructure ε_i is denoted x_i; the corresponding transverse and axial deformations are denoted u_i and v_i respectively.

The XBR is configured, substructured, and labelled with coordinates as shown in Figure 3.6. Again, the structure is modelled as a collection of one-dimensional substructures in a two-dimensional embedding space. As for the L-frame analysed in Section 3.3, the right-angled joints are assumed fixed.

3.4.2 Physics

After substructuring, the deflections of the elements are represented by an Euler-Bernoulli flexural component $u(x)$ and a decoupled compressive elastic component $v(x)$ as denoted in Figure 3.6. The field Lagrangian is identical with the previous case, and is described by (3.24). As before, the deflections and rotations at N_1 and N_2 are constrained to be commensurate:

$$u_1|_{\ell 1} = u_2|_0 \ (3.42a) \qquad u_1'|_{\ell 1} = u_2'|_0 \ (3.42b)$$

$$u_1|_{\ell 1} = -v_4|_{\ell 4} \ (3.42c) \qquad u_1'|_{\ell 1} = u_4'|_{\ell 4} \ (3.42d)$$

$$u_1|_{\ell 1} = v_5|_{\ell 5} \ (3.42e) \qquad u_1'|_{\ell 1} = u_5'|_{\ell 5} \ (3.42f)$$

$$u_2|_{\ell 2} = u_3|_0 \ (3.42g) \qquad u_2'|_{\ell 2} = u_3'|_0 \ (3.42h)$$

$$u_2|_{\ell 2} = -v_6|_{\ell 6} \ (3.42i) \qquad u_2'|_{\ell 2} = u_6'|_{\ell 6} \ (3.42j)$$

$$u_2|_{\ell 2} = v_7|_{\ell 7} \ (3.42k) \qquad u_2'|_{\ell 2} = u_7'|_{\ell 7} \ (3.42l)$$

For the XBR, one of the quantities of interest relates to calculation of support loss (cf. Chapter 4), and hence the accurate resolution of the forces at the distal ends of $\mathcal{E}_4 - \mathcal{E}_7$ when the resonator vibrates in its fundamental symmetric flexural modes is required. The condition of zero displacement at N_1 and N_2 parallel to the axis of $\mathcal{E}_2$ in an undeformed configuration was imposed on the problem based on this consideration, to improve efficiency. Given this, no axial freedom in deflection is required at the nodes for $\mathcal{E}_1 - \mathcal{E}_3$ no rigid body DOF and lumped masses need be included to account for rigid translation of these elements in a swaying motion, and no translatory freedom is needed from the QCFs for $\mathcal{E}_4 - \mathcal{E}_7$. This set of assumptions is equivalent to neglecting the swaying modes of the XBR. However, axial effects are included in $\mathcal{E}_4 - \mathcal{E}_7$. via the inclusion of axial quasicomparison functions, transverse

freedom at the nodes in the QCFs for $\mathcal{E}_1 - \mathcal{E}_3$, and a corresponding lumped-mass term in the mass matrix.

3.4.3 Quasi-comparison Trial Functions

Following the approach of Section 3.3.4, it is necessary to examine the CBCs to determine valid sets of QCFs. At the nodes N_1 and N_2, the elements interact by exerting shear forces and bending moments on each other dynamically. The assumptions already made remove some freedom from the problem; this is reflected by a reduction of the number of CBCs required to be satisfied. The CBCs and corresponding quasicomparison mode families are given in Table 3.7 for elements $\mathcal{E}_1 - \mathcal{E}_2$ and $\mathcal{E}_4$. The other elements are omitted for clarity, and can be inferred by symmetry.

Substructure	Field	Admissible mode families	CBC	Quasicomparison mode families
1	u_1	CC, CF, CS, CP, PP, PC, PF, PS, FF, FP, FC, FS, SS, SP, SC, SF	$u_1\|_{\ell 1} \neq 0$	CF, CS, PF, PS, FF, FS, SS, SF
			$u_1'\|_{\ell 1} \neq 0$	CF, CP, PF, PP, FP, FF, SP, SF
			$u_1''\|_{\ell 1} \neq 0$	CS, CC, PS, PP, FS, FP, SS, SP
			$u_1'''\|_{\ell 1} \neq 0$	CC, CP, PC, PP, FC, FP, SC, SP
2	u_2	CC, CF, CS, CP, PP, PC, PF, PS, FF, FP, FC, FS, SS, SP, SC, SF	$u_2\|_0 \neq 0$	FF, FP, FC, FS, SS, SP, SC, SF
			$u_2'\|_0 \neq 0$	PP, PC, PF, PS, FF, FP, FC, FS,
			$u_2''\|_0 \neq 0$	CC, CF, CS, CP, SS, SP, SC, SF
			$u_2'''\|_0 \neq 0$	CC, CF, CS, CP, PP, PC, PF, PS,
			$u_2\|_{\ell 2} \neq 0$	CF, CS, PF, PS, FF, FS, SS, SF
			$u_2'\|_{\ell 2} \neq 0$	CF, CP, PF, PP, FF, FP, SF, SP
			$u_2''\|_{\ell 2} \neq 0$	CC, CS, PC, PP, FC, FP, SC, SP
			$u_2'''\|_{\ell 2} \neq 0$	CC, CP, PC, PP, FC, FP, SC, SP
4	u_4	CC, CF, CS, CP	$u_4\|_{\ell 4} \neq 0$	CF, CS
			$u_4'\|_{\ell 4} \neq 0$	CF, CP
			$u_4''\|_{\ell 4} \neq 0$	CC, CS
			$u_4'''\|_{\ell 4} \neq 0$	CC, CP
4	v_4	CF, CC	$v_4\|_{\ell 4} \neq 0$	CF
			$v_4'\|_{\ell 4} \neq 0$	CC

Table 3.7 Complementary boundary conditions for the L-frame structure and corresponding mode families admissible under each CBC. The letters C, F, S, and P refer to Clamped, Free, Sliding, and Pinned conditions respectively.

It remains to choose the QCF families. Table 3.8 denotes the choices employed here.

Substructure	**Field**	**R1**-QCF1	**R1**-QCF2	**R1**-QCF3
1	u_1	a_{11}FS1 +a_{21} FP0	a_{11}FS1+a_{21} FS2 +a_{31}FP0+a_{41} FP1	a_{11}FS1+a_{21} FS2 +a_{31}FS3+a_{41} FP0 +a_{51}FP1+a_{61} FP2
2	u_2	a_{12}CC1 $+a_{22}$FF0	a_{12}CC1 + a_{22}CC2 a_{32}FF0 + a_{42}FF1	a_{12}CC1+a_{22} CC2 +a_{32}CC3+a_{42} FF0 +a_{52}FF1+a_{62} FF2
4	u_4	a_{14} CF1 +a_{24} CC1	a_{14} CF1 +a_{24} CF2+a_{34} CC1 +a_{44} CC2	a_{14} CF1 +a_{24} CF2+a_{34} CF3 +a_{44} CC1+a_{54} CC2 +a_{64} CC3
4	v_4	a_{14} $\underline{\text{CF}}$1 +a_{24} $\underline{\text{CC}}$1	a_{14} $\underline{\text{CF}}$1 +a_{24} $\underline{\text{CF}}$2+a_{34} $\underline{\text{CC}}$1 +a_{44} $\underline{\text{CC}}$2	a_{14} $\underline{\text{CF}}$1 +a_{24} $\underline{\text{CF}}$2+a_{34} $\underline{\text{CF}}$3 +a_{44} $\underline{\text{CC}}$1+a_{54} $\underline{\text{CC}}$2 +a_{64} $\underline{\text{CC}}$3

Table 3.8 Explicit forms for the first, second and third order quasicomparison functions R1-QCF1, R1-QCF2 and R1-QCF3 for the L-frame.

The analysis proceeds forwards from this stage in complete analogy with Section 3.3.6. For the XBR case, the global disjoint mass and stiffness matrices have the forms

$$\mathbf{M_{GD}} = \mathrm{diag}(\mathbf{M_j}) \qquad (3.43a)$$

$$\mathbf{K_{GD}} = \mathrm{diag}(\mathbf{K_j}) \qquad (3.43b)$$

Where $\mathrm{diag}(\mathbf{A_i})$ denotes a block-diagonal matrix with blocks $\mathbf{A_i}$ where $\mathbf{i} \in \{1{:}\,\mathcal{M}\}$ and the substructure stiffness matrices and mass matrices have the forms already given.

3.4.4 Constraint and Solution

Following the template of Section 3.3.7, the constraint and solution process is now briefly outlined. The constraints not automatically satisfied by the QCFs at the nodes are described by equations $(3.42a)$-$(3.42l)$, and can be formulated as a homogeneous system $\mathbf{Ca} = 0$. In this case, the 12 constraints on the $\mathcal{NM}$ disjoint degrees of freedom that constitute the elements of $\mathbf{a}$ implies that $\mathbf{C}$ is of dimension $12 \times \mathcal{NM}$. Next, a basis for the nullspace of $\mathbf{C}$ in the disjoint trial space must be chosen. A natural choice is not immediately apparent to the author; the singular value decomposition routine *svd* from the C library LAPACK was employed by the author as a convenient means to obtain an orthonormal basis. From here, the basis vectors are readily formed into a nullspace matrix $\bar{\mathbf{C}}$ as in the preceding sections.

As before, the constrained problem is formulated by the conjugation of the disjoint global mass and stiffness matrices by $\bar{\mathbf{C}}$. the procedure can be expressed as $\mathbf{M_G} = \bar{\mathbf{C}}\mathbf{M_{GD}}\bar{\mathbf{C}}^{\mathbf{T}}$, $\mathbf{K_G} = \bar{\mathbf{C}}\mathbf{K_{GD}}\bar{\mathbf{C}}^{\mathbf{T}}$, which is the same form as (3.40).

Again, the resulting eigenvalue problem can be expressed as being of the form (3.41), namely $\mathbf{K_G a_C} = \lambda \mathbf{M_G a_C}$. Any of the standard linear algebra techniques can be employed henceforth to find the Ritz values and vectors and thus the desired approximation.

3.4.5 Evaluation of Forces

With the Ritz solutions from Section 3.4.4 it is straightforward to obtain the forces at the distal ends of the supports. Since it is well known that, for an Euler-Bernoulli beam

and an elastic rod respectively, the shear force F_{shear} and normal force F_{normal} are given by

$$F_{\text{SHEAR}} = EI \frac{\partial^3 u}{\partial x^3} \tag{3.44}$$

$$F_{\text{NORMAL}} = EA_x \frac{\partial v}{\partial x} \tag{3.45}$$

it is easy to obtain concise approximations for the forces using the Ritz solution obtained from (3.41), together with Table 3.8, by differentiating the trial functions, evaluating the derivatives at the appropriate boundary, and forming a sum weighted by the global disjoint Ritz coefficients $\mathbf{a_{GD}}$ derived previously.

3.5 Results and discussion

Results are first presented and compared for a test case with a sweep over one geometric parameter using the Rayleigh-Ritz method using admissible functions (Pinned-Pinned beam modes), the Enhanced Rayleigh-Ritz method employing the quasi-comparison functions developed above, and 3D Finite Element analysis. Subsequently, the Enhanced Rayleigh Ritz method is used to examine the dynamics of the system over a range of several parameters. Throughout this section, unless the context dictates otherwise, the parameters of the XBR are $\ell_1 = \ell_3 = 7.84 \times 10^{-3}\text{m}$, $\ell_2 = 19.32 \times 10^{-3}\text{m}$, $\ell_4 = \ell_5 = \ell_6 = \ell_7 = 15 \times 10^{-3}\text{m}$; $E = 210 \times 10^{9}\text{GPa}$, and $\rho = 7840\ \text{kg m}^{-3}$, The out of plane depth is $1 \times 10^{-2}\text{m}$ and the Poisson's Ratio is 0.28.

3.5.1 Validation and convergence

Given that the motivation underlying the investigation is to gain insight into the performance of XBMs by exploring the functional characteristics of the XBR over its parameter space, it is highly desirable to have as efficient a model as possible, in terms of degrees of freedom needed to provide a converged solution. Attention now turns to the convergence characteristics of the RRM method presented in this chapter, with comparison made to classical Rayleigh-Ritz models and to the solutions generated by COMSOL. We consider first the effect of the nodepoint ratio, $NR \equiv \frac{\ell_1}{\ell_1+\ell_2+\ell_3}$.

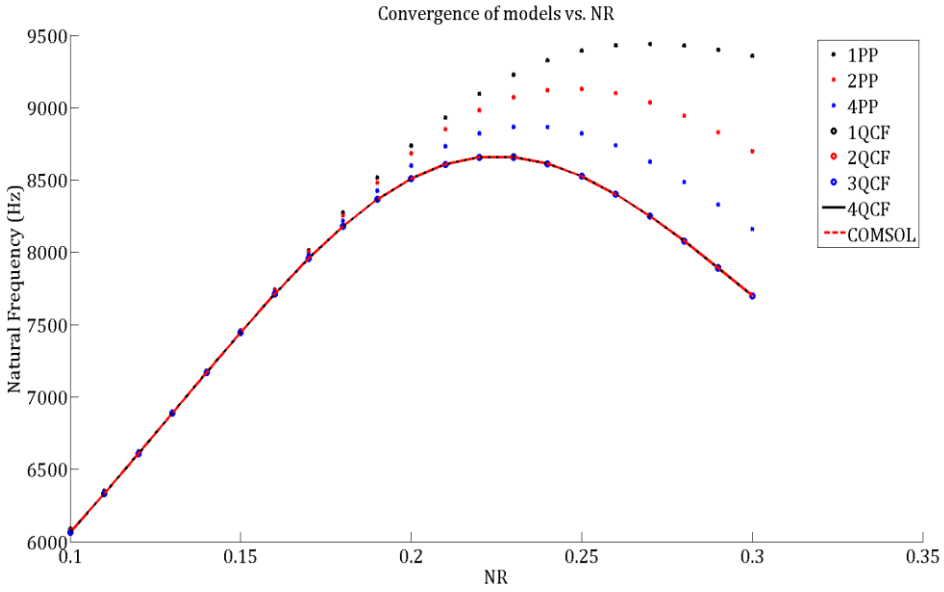

Figure 3.7 Calculated fundamental natural frequencies for the test case over a range of values of the parameter NR, calculated using the classical Rayleigh-Ritz method, the Enhanced Rayleigh-Ritz method, and a 3D FEA of the system.

Figure 3.7 shows the natural frequencies predicted by all models considered in the study. The results for the 3D FEA and the Quasi-Comparison function models agree very well indeed. Both analyses show a maximum in the natural frequency as the parameter 'NR' is varied in the vicinity of the tuned value ($NR \approx 0.224$).

On the contrary, the results for the classical Rayleigh-Ritz method using pinned-pinned flexural trial functions differ significantly from the converged results discussed. The natural frequencies agree well for smaller values of NR, for which the resonator approaches an H-shaped frame. However, pinned-pinned modes are identically zero in curvature, and hence by force balance applied bending moment at their boundaries. When the bending moment coupling becomes important to the dynamics as NR increases over about 0.2, the results diverge from the FEA /QCF results. Although convergence is seen as the DOF are increased progressively from PP1 through PP2 to PP4, it is slow and remains incomplete. Although the PP models are concordant with the predictions of the QCF and COMSOL models for lower values of NR, they diverge as NR tends to its upper limit.

This is a correlate of the inability of the classical RR method using PP trial functions to incorporate curvature at element boundaries. When NR is higher, the nodepoints

migrate towards regions of higher curvature of the sense beam, and the resulting subspace gap is larger, leading to the observed discrepancy in the results. Note that this phenomenon is not observed for the QCF models, even with the lowest DOF.

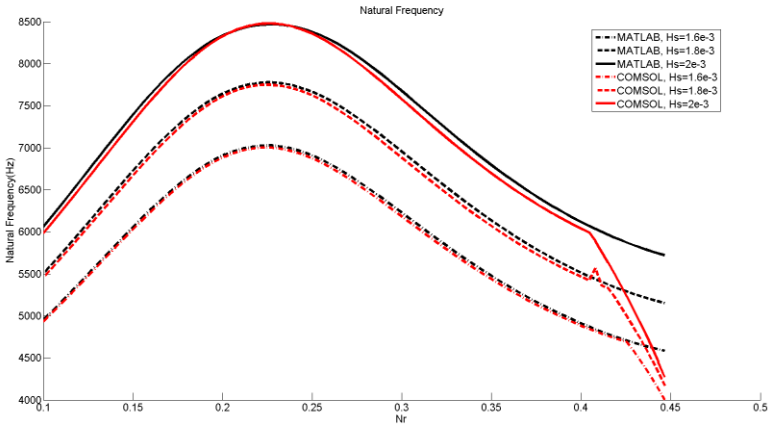

Figure 3.8. Calculated fundamental natural frequencies, over a range of values of NR for selected values of the in-plane support height Hs.

Figure 3.8 shows a good agreement between the 4QCF and COMSOL models over a wider range of the parameter NR, and for several different values of the support beam height, H_s. An abrupt change occurs in the values for the COMSOL models, but not the QCF models, for values of NR greater than about 0.4. This can be explained by realising that, if we represent the natural frequencies of the XBR and the associated parameters as dimensions in a vector space, then Figure 3.8 represents plots for the lowest natural frequency only. As NR varies, the ordering of the natural frequencies may change. The corresponding plotted curves will then intersect transversally. The analytical procedure will switch between the curves at this point, leading to a discontinuity, as observed. The transversal intersection corresponds to an *accidental degeneracy*, in which two branches of mode shapes (in parameter space) collide and exchange minimality. We will meet this phenomenon again in the sequel. The degeneracy is missed by the RRM model as the trial functions are symmetric, while the mode in question is antisymmetric and exists in the orthogonal complement of the RRM trial space in the solution space of the system.

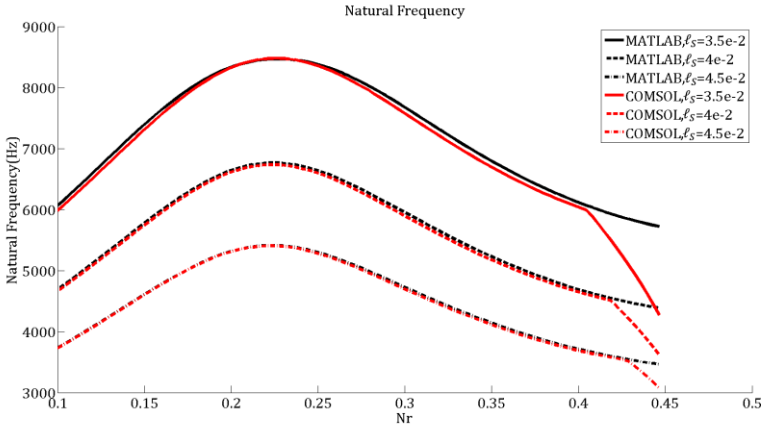

Figure 3.9 Calculated fundamental natural frequencies, over a range of values of the nodepoint ratio NR for selected values of the sense beam length ℓ_S.

Again, good agreement is seen in Figure 3.9 between the 4QCF MATLAB model and COMSOL over a wide range of NR values, for some selected values of the sense beam length. The data presented so far constitutes an independent validation of the 4QCF MATLAB model over a three-dimensional subspace of the parameter space of the model. On the basis of this robust concordance, we proceed with confidence to explore some of the features of the solutions.

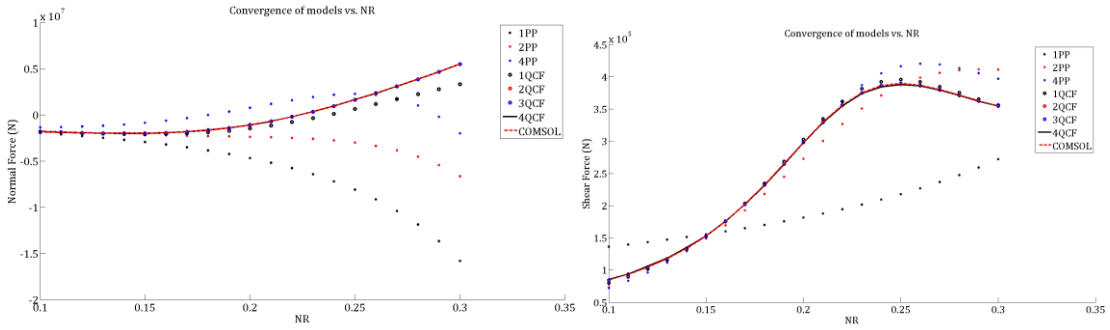

Figure 3.10 Calculated normal forces (a) and shear forces (b) for the test case, using the same analyses and parametric variation as in Figure 3.9.

Turning attention to Figure 3.10, a similar broad trend is observed. For both normal and shear force, 4QCF and 3DFEA analyses agree to within the resolution of the graphics used. Actual discrepancies were of the order of 1%. Again, 1QCF reproduced the same qualitative behaviour with slightly more numerical error. The normal force has a zero crossing at $NR \approx 0.2243$, corresponding to the zeros of the free-free fundamental mode of the sense beam with a modification at the fourth decimal place by the support-sense coupling. However, the calculated interfacial forces from the PP models are wildly in error, *even in the region where the natural frequencies have converged.* The results are unphysical, quantitatively and qualitatively, missing such essential features of the dynamics as the zero crossing of the normal force, which can be shown to be in error on the basis of simple kinematic argument. That is to say, the classical RR method appears to be adequate, both in terms of qualitative mode shapes and convergence of the calculated natural frequencies, below $NR \approx 0.2$, but gives nonsensical results for the natural boundary conditions in this case – the precise quantities of interest for support loss!

This is a striking demonstration of the power and utility of the methods of this chapter to efficiently calculate support reaction forces.

3.5.2 Parametric Study

To complete demonstration of the utility of the method, and to illustrate the impedance matching concept in a practical scenario, the 4QCF model was implemented and solved iteratively in a double nested loop configuration using

MATLAB, with a 100x100 grid of parameter values. The solve time on an Intel Xeon 2.66 GHz desktop machine with 12 GB of RAM was 6 minutes, using single-threaded, non-optimal code. In the following section, a sample of the results chosen to illustrate the interesting dynamical effects revealed by the model are presented as surface plots.

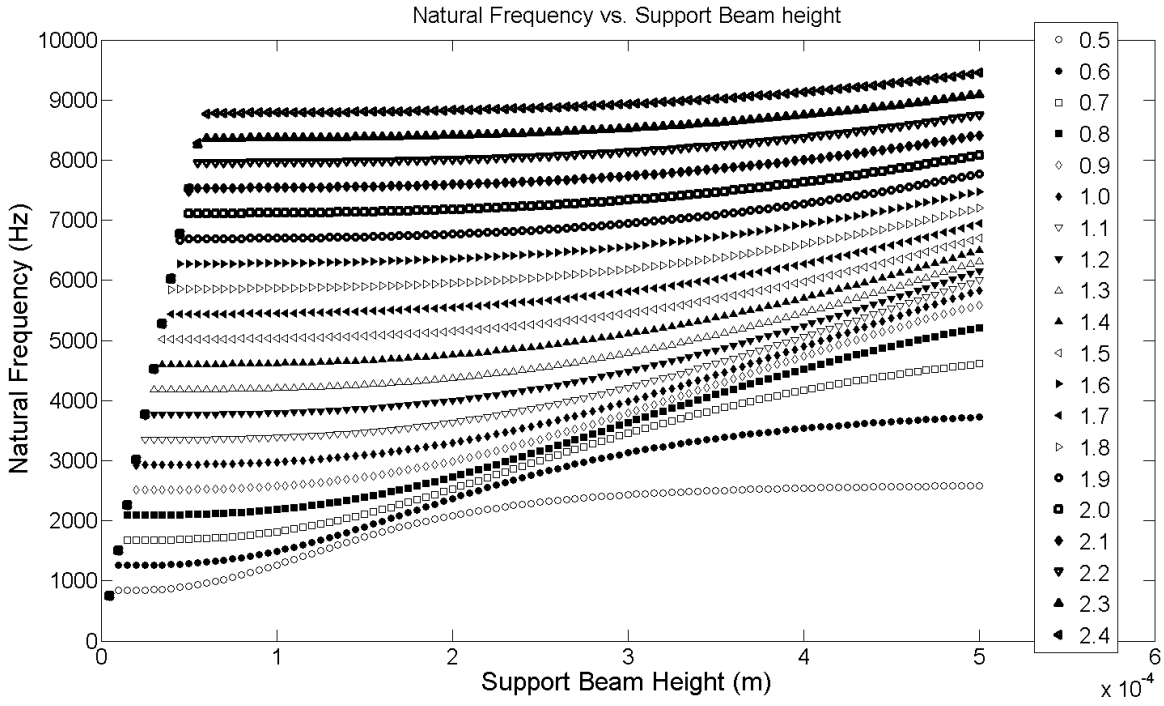

Figure 3.11 Plot of the lowest Ritz value generated for the test case using the 4QCF model. The different data series correspond to different values of the sense beam height, in mm, as indicated in the legend.

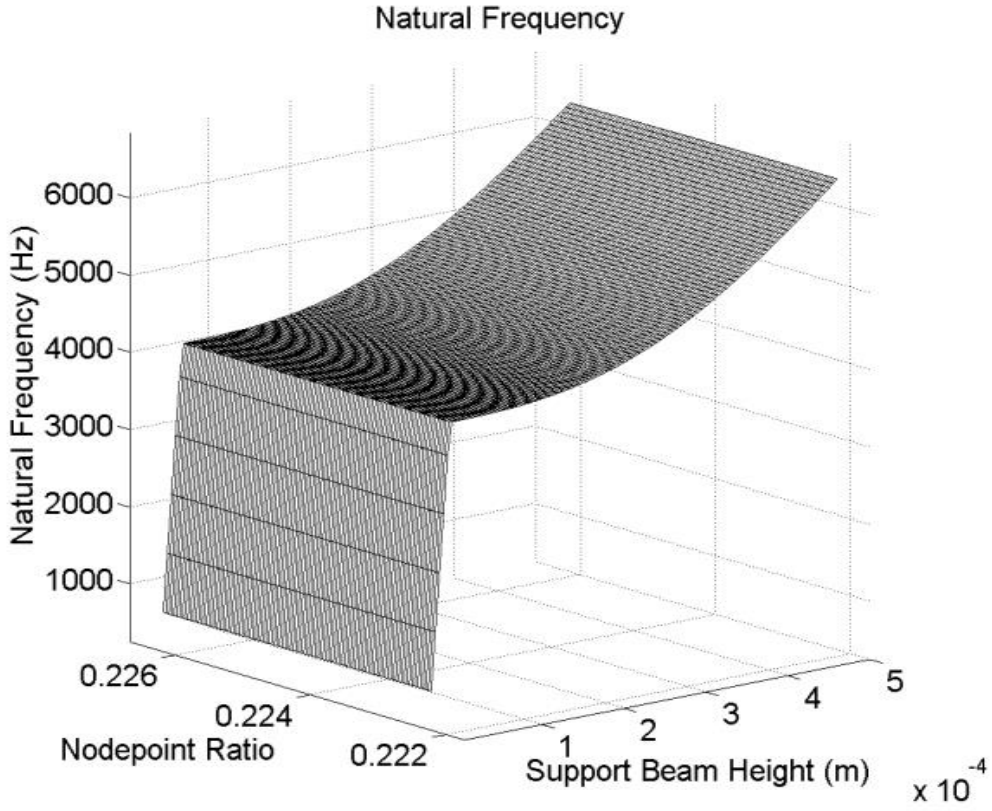

Figure 3.12 Surface Plot of the lowest Ritz value versus the parameters NR and Support Beam Height for the test case.

Figure 3.12 shows a corner point of the natural frequency with respect to the support height at around 500 microns, independent of the nodepoint ratio over the range considered. Figure 3.11 displays the same feature from a different perspective in the parameter space, and illustrates a strong linear dependence on the ratio of the sense to support beam heights. The natural frequency is relatively independent of the support beam height above a critical ratio of these two quantities, suggesting that the dynamics are dominated by the sense beam. However, below the critical ratio, the natural frequency becomes linearly dependent on the support height, with the same dependence regardless of the sense beam height. This is suggestive of the dynamics of the mode becoming dominated by the support behaviour as the sense beam height is reduced past a threshold. Indeed, an examination of the mode shapes (cf. Chapter 5) indicates that this is the case, with the majority of the displacement and energy storage taking place in the supports, with the sense beam performing a secondary role. The approximate value of the critical ratio of sense: support height is 1:30.

3.5.3 Quasi-comparison functions

The 4QCF model displays favourable convergence characteristics with respect to natural frequencies when compared to the PP model and the Finite Element Method. The advantage is significantly exaggerated in the calculation of support forces, such that the classical RR method often misses the important trends, even after eigenvalue convergence. This is a demonstration of the effectiveness of the RRM approach. One way to explain the result is with reference to the satisfaction of natural boundary conditions in a finite number of terms. This was the original justification given by Meirovitch. However, this argument is somewhat heuristic in character. More recent results on the convergence of the Rayleigh-Ritz method may offer qualitative insight into the mechanism of the improvement, and moreover, to quantitative error estimates and bounds on the magnitude of the improvement. These developments are sketched in this subsection.

For a Rayleigh-Ritz approximation in which the trial functions form a complete set (i.e. a basis for the Hilbert space of functions on the domain), convergence is guaranteed. As the Ritz values tend towards the eigenfrequencies of the problem, the Ritz vectors also tend towards the corresponding modes of vibration[28]. Note that there is no guarantee that the values for a particular point will improve as the order of approximation improves in a uniform fashion; merely that the norm of the difference between the approximate and true solutions will converge.

There are two points of interest here. Firstly, Knyazev et al.[29] derive results that imply that the subspace gap between the trial space and the invariant subspace of interest is related to the convergence of the method: specifically, that the error in the Ritz values is proportional to the sine of the gap between the trial space and the eigenvalue being approximated. If the basis of the trial space is generated as modes from a particular simple boundary condition, as in the classical Rayleigh-Ritz method, then it will inherit properties close to the boundaries from the boundary condition. For example, all clamped-clamped beam modes have zero displacement and slope in the vicinity of the boundaries; all pinned-pinned modes similarly have zero displacement and curvature and shear force. Then, the trial space spanned by a finite collection thereof must also inherit these properties. If the natural mode of interest does not

share these properties, then this introduces a mismatch between the behaviour away from the boundaries, which presumably serves well to approximate the mode if the choice of trial space is prudent, and that close to the boundaries, which differs substantially.

To apply the geometric picture of Figures 3.2 and 3.3 to the continuous case, consider a localised basis, such as the Haar basis[31] as generating a high-dimensional Euclidean Hilbert space. Some of the degrees of freedom are associated with the function in its interior; a few are associated with its value near its boundaries. Any boundary characteristics, such as nonzero displacement or slope, of the eigenvector not shared by any members of the trial space generate a corresponding mismatch in the coefficients of the boundary coordinates between the eigenvector and its projection onto the trial space. This is another way of expressing a geometric angle between the subspaces, or a subspace gap. It can be reasonably conjectured that, in the continuum limit, convergence will be harmed in a fashion quantitatively related to the induced subspace gap, as defined by the inner product on the Hilbert space. If one could obtain a quantitative estimate or analytical bound on the induced gap, a corresponding result for the convergence would follow from the referenced works. This would require assumptions or restrictions on the approximation in the bulk region, and may prove challenging.

Secondly, the convergence of the mode shapes (in the norm) and eigenvalues does not necessarily imply the convergence of the characteristics of the function, such as slope, in the vicinity of a point. For instance, the bending moment at a torsionally-sprung interface can never be expressed using pinned-pinned trial functions, even though the mode shapes and natural frequencies always are, in a mean-squared sense. For the purpose of support loss calculation, this is a profound flaw, since the values at the boundaries are precisely the quantities of interest. Gibbs- and Runge-type phenomena can result from boundary mismatches. A Sobolev norm [32] might well be more appropriate than the L^2 norm for studying convergence of the method and obtaining rigorous results justifying the use of Quasi-Comparison Functions with Rayleigh's quotient, under suitable assumptions about the solution under approximation and the trial spaces being used.

3.6 Conclusions

A new approach to modelling the modal dynamics and constraint boundary conditons in planar frame resonators, well suited to evaluating both the modal quantities of interest and boundary forces of constraint with a view to support loss calculation (cf. Chapter 4), has been developed and exposited. The method consists of an enhanced Rayleigh-Ritz-Meirovitch vibration analysis of the resonator, coupled to a substrate model based on classical 2D elastic wave theory of the type used by Jimbo and Itao et al. A set of quasi-comparison functions was proposed as part of the method, and rules for their selection in the general application of the method discussed. The use of quasi-comparison functions in the method has been compared to a more classical choice of trial function for the Rayleigh-Ritz method, and the results shown to converge far more rapidly. The approach of this paper has been shown to be numerically efficient when compared to the FEA approaches that have previously been used to attack the support loss problem, and its application to the case of a Xylophone Bar Resonator has generated original insight that is of general interest for design purposes. The root cause of this difference has been considered from the point of view of a geometric interpretation of the solutions and approximations in the Hilbert space forming the setting for the problem. Overall, the method represents significant progress over more common techniques for resonator design and optimisation. It is directly useful for examining the support loss phenomenon for in-plane vibration of planar frame resonators, and with suitable modification of the trial functions and compatibility conditions, to mechanical resonators more generally.

Further work would include extension of the model to consider nonlinearity of the resonator geometry, perhaps via a Rayleigh-Ritz-Meirovitch iterative procedure coupled to a linear analysis of the substrate, to examine the amplitude dependency of the relationship between support stiffness and damping for XBRs and more general frame resonators. Also of interest would be the development of standard QCFs for more complex resonator geometries, such as disk resonators, plates, shells, etc. Further development of the substrate model to account for the effects of torsion and three-dimensional geometry, anisotropy, finite domain sizes, and other effects

neglected in Miller and Pursey's modeling would be of value. Finally, analytical and quantitative investigation into the convergence effects of different families of trial function are ongoing in functional analysis, and results relating to the quasicomparison method would be of considerable value.

3.7 References

[1] A. W. Leissa, "The historical bases of the Rayleigh and Ritz methods," *Journal of Sound and Vibration*, vol. 287, no. 4–5, pp. 961–978, Nov. 2005.

[2] J. W. S. Rayleigh, *Theory of Sound, Volume I*. Macmillan and Co., 1877.

[3] A. Hale and L. Meirovitch, "A general substructure synthesis method for the dynamic simulation of complex structures," *Journal of Sound and Vibration*, vol. 69, no. 2, pp. 309–326, Mar. 1980.

[4] M. E. Argentati, A. V Knyazev, C. C. Paige, and I. Panayotov, "Bounds on changes in ritz values for a perturbed invariant subspace of a hermitian matrix ∗," vol. 30, no. 2, pp. 548–559, 2008.

[5] P. S. Gerard L . G . Sleijpen , Jasper van den Eshof, "Optimal a Priori Error Bounds for the Rayleigh-Ritz Method," *Mathematics of Computation*, vol. 72, no. 242, pp. 677–684, 2012.

[6] A. Knyazev, A. Jujunashvili, and M. Argentati, "Angles between infinite dimensional subspaces with applications to the Rayleigh–Ritz and alternating projectors methods," *Journal of Functional Analysis*, vol. 259, no. 6, pp. 1323–1345, Sep. 2010.

[7] D. Chang, "Freely Vibrating Beams," PhD Thesis, University of Manitoba, 1997.

[8] S. S. K. Tadikonda and H. Baruh, "Gibbs Phenomenon in Structural Mechanics," *AIAA Journal*, vol. 29, no. 9, pp. 1488–1509, 1990.

[9] A. L. Meirovitch, L., Hale, “On the substructure synthesis method,” *AIAA Journal*, vol. 19, no. 7, pp. 940–947, 1981.

[10] A. L. Meirovitch, L., Hale, “Procedure for Improving Discrete Substructure Representation in Dynamic Synthesis,” *AIAA Journal*, vol. 20, no. 8, pp. 1128–1136, 1982.

[11] L. Meirovitch and A. L. Hale, “A General Dynamic Synthesis for Structures With Discrete Substructures,” *Journal of Sound and Vibration*, vol. 85, no. 4, pp. 445–457, 1982.

[12] A. L. Hale and L. Meirovitch, “A General Procedure for Improving Substructures Representation in Dynamic Synthesis,” *Journal of Sound and Vibration*, vol. 84, no. 2, pp. 269–287, 1982.

[13] G. Sotiropoulos, “Comment on the Substructure Synthesis Methods,” *Journal of Sound and Vibration*, vol. 94, no. 1, pp. 150–153, 1984.

[14] L. Meirovitch and M. Kwak, “Inclusion principle for the Rayleigh-Ritz based substructure synthesis,” *AIAA Journal*, vol. 30, no. 5, pp. 1344–1351, 1992.

[15] L. Meirovitch and M. Kwak, “Convergence of the classical Rayleigh-Ritz method and the finite element method,” *AIAA Journal*, vol. 28, no. 8, pp. 1509–1516, 1990.

[16] L. Meirovitch and M. Kwak, “Rayleigh-Ritz based substructure synthesis for flexible multibody systems,” *AIAA Journal*, vol. 29, no. 10, pp. 1709–1719, 1991.

[17] C. W. Jen, D. A. Johnson, and F. Dubois, “Numerical Modal Analysis of Structures Based on a Revised Substructure Synthesis Approach” *Journal of Sound and Vibration*, vol. 180, no. 2, pp. 185–203, 1995.

[18] C. A. Morales, “L-shaped structure mass and stiffness matrices by substructure synthesis,” *Meccanica*, vol. 45, no. 2, pp. 279–282, Sep. 2009.

[19] C. A. Morales, “Dynamic analysis of an L-shaped structure by Rayleigh-Ritz substructure synthesis method,” *Meccanica*, vol. 44, no. 3, pp. 339–343, Mar. 2009.

[20] A. L. Meirovitch, L., Hale, “A Procedure for Improving Discrete Substructure representation in Dynamic Synthesis,” *AIAA Journal*, vol. 20, no. 8, pp. 1128–1136, 1982.

[21] C. A. Morales, “Rayleigh-Ritz Based Substructure Synthesis for Multiply Supported Structures,” *Journal of Vibration and Acoustics*, vol. 122, no. 1, p. 2, 2000.

[22] C. A. Morales, “Dynamic analysis of frames by a Rayleigh–Ritz based substructure synthesis method,” *Engineering Structures*, vol. 22, no. 12, pp. 1632–1640, Dec. 2000.

[23] C. A. Morales and R. Goncalves, “Eigenfunction convergence of the Rayleigh-Ritz-Meirocitch method and the FEM,” *Shock and Vibration*, vol. 14, no. 6, pp. 417–428, 2007.

[24] L. Meirovitch, *Fundamentals of Vibration*, International Edition,. McGraw-Hill, 2000.

[25] R. Courant, “Variational Methods for the Solution of Problems of Equilibrium and Vibration,” *Bulletin of the American Mathematical Society*, vol. 49, pp. 1–23, 1942.

[26] D. Flight, “A brief history of the beginning of the finite element method,” *International Journal for Numerical Methods in Engineering*, vol. 39, no. November 1995, pp. 3761–3774, 1996.

[27] Z. Hao, “An analytical model for support loss in micromachined beam resonators with in-plane flexural vibrations,” *Sensors and Actuators A: Physical*, vol. 109, no. 1–2, pp. 156–164, Dec. 2003.

[28] Z. Jia, “The convergence of harmonic Ritz values, harmonic Ritz vectors and refined harmonic Ritz vectors,” *Mathematics of Computation*, vol. 74, no. 251, pp. 1441–1457, Jun. 2004.

[29] A. V. Knyazev and M. E. Argentati, “On proximity of Rayleigh quotients for different vectors and Ritz values generated by different trial subspaces,” *Linear Algebra and its Applications*, vol. 415, no. 1, pp. 82–95, May 2006.

[30] H. Bang, “Analytical solution for dynamic analysis fo a flexible L-shaped structure,” *Jounral of Guidance Control and Dynamics*, vol. 19, no. 1, pp. 248–250, Jan 1996.

[31] "On the Theory of Orthogonal Function Systems,” Alfred Haar, translated from the original German by Georg Zimmermann. [Online]. Available: https://www.uni-hohenheim.de/~gzim/Publications/haar.pdf.

[32] R.A Adams, *Sobolev Spaces,* Academic Press, Boston, MA, 1975.

Chapter 4. Substrate Models

In this chapter, a set of models is developed for the XBR substrate with a view to quantifying the support loss incurred at the interface between the resonator support beams and the substrate. A brief review of the literature is proffered by way of an introduction to the topic. To begin the analysis, a model based on the work of Miller and Pursey is developed and extended to account for particular features of the XBR case. A parallel FEA of the same physics is also undertaken. A numerical study of the results and phenomena encountered therein are presented and compared between the two models. The effects of materials and geometric rescaling and tuning on the results are examined. This constitutes the first study of the radiation impedance spectrum for plane wave Kirchhoff diffraction by a free elastic double slit of finite width presented in the literature. The results are discussed in the context of XBR and double supported resonator support loss and design, and the limitations of the model considered. Finally, important further work on the subject is suggested.

4.1 Introduction

In the previous chapter, it was shown that an important determining factor in the performance of a mechanical resonator is the Q factor; it was further shown that the Support Loss phenomenon is often the dominant contribution to the resonator Q. In order to examine this effect more closely, it is necessary to examine the dynamics of elastic wave propagation in the resonator substrate in the context of the resonator geometry and configuration.

For the case of primary interest in this study –resonators fabricated using planar machining techniques – a typical substrate is a planar structure with principal dimensions many times larger than the resonator and coplanar with it. Hence, a good approximation to support loss can be obtained by treating the substrate as an elastic half-space with symmetry in the out-of-plane dimension. In this picture, the substrate dynamics reduce to two spatial dimensions, and the equations are considerably simplified.

Analysis of the whole resonator/substrate system is complicated by the disparity between the two systems. The resonator is a frame structure with physics well described by coupled beam and rod equations, as described in Chapter 3. On the other hand, the substrate is a bulk elastic field, and the full Lame-Navier equations of elasticity must be satisfied everywhere in its interior. There seems to be no straightforward way of coupling these two physical theories adequately, since the complex stress distributions and material configurations at the boundaries must in general violate the assumptions of Euler-Bernoulli theory. The problem could be formulated in terms of Helmholtz potentials, but the geometric complexity of the boundary conditions renders this approach extremely difficult to intractable.

Furthermore, deflections are expected to be many orders of magnitude larger in the resonator than in the substrate. This causes numerical difficulties for any integrated approach, since matrices containing entries of wildly differing orders of magnitude render the evaluation of determinants and other linear-algebraic computations problematic in the context of finite-precision arithmetic.

These difficulties can be reconciled by the use of an approximating assumption: that the resonator dynamics are unaffected by the small loss introduced by support loss. Given that the XBR is designed to be a high Q factor resonator, this is intuitively plausible; it will be shown to be valid in the sequel. Of course, the substrate dynamics are not independent of the resonator. This approach, then, can be briefly stated as assuming unidirectional coupling between the resonator and its support. It is equivalent to assuming Kirchhoff diffraction at the apertures representing the support-substrate interface, for incoming compressional and flexural “plane waves”. The corresponding stress sources are a uniform normal, and uniform shear and antisymmetric linear-distributed normal forces, respectively.

Computation of solutions to this approximation consists of obtaining approximations for the modal dynamics assuming a rigid substrate, such as are readily obtained from the models of Chapter 3; using these results to obtain approximate stress distributions at the interfaces; and finding the field solutions and corresponding energy radiation for the substrate with a surface stress source corresponding to these stresses.

Problems of this type have a long and rich history. After Newton's demonstration of the wave nature of light[1], Fresnel synthesized the famous Principle of Huygens[2] with his own ideas on interference to arrive at the Huygens-Fresnel Principle in 1816. A comprehensive review on wave diffraction by screens is not attempted; instead, a sketch of the current state of knowledge and a survey of related results is instead presented.

Lamb was the first to derive integral form solutions for the response of an elastic half-space to harmonic elastic loadings[3]. In his paper, the surface response of a 3-D halfspace to loading by a point or infinite line stress source was examined using contour integrals and Cauchy's theorem; for the line-source case, the problem has translational symmetry parallel to the line and the equations take on two-dimensional variation, while buried sources were considered by Lapwood in 1949[4]. The methods were adapted to find the complex radiation impedance of some finite sources, as well as the Fraunhofer diffraction fields in the asymptotic limit of large distance from the source, by Miller and Pursey in a seminal 1952 paper[5]. The authors later extended the Fraunhofer results in the far field for the three-dimensional case[6].One field in which the results were quickly adopted and used to model wave propagation phenomena of interest is geology, where an important model of stress release at a fault interface, is termed the Double Couple source, which is variously modelled as a half-plane with a uniform time-impulsive surface shear force in works such as Afandri et al.[7]. In the 1960 and 1970s, using integral methods and Laplace transforms in the time domain.

For modelling support loss in resonators, what is known from a theoretical understanding of the resonator mode structure is the approximate stress distribution arising from the (usually assumed clamped) support-substrate interface displacement gradients. What is required is an expression for the corresponding radiation loss to the bulk. The problem, formulated in this way, is identical to the Kirchhoff assumption for plane wave diffraction of incident P,S, and Rayleigh waves with intensities such that the expected spatial stress distribution is satisfied. For a singly supported resonator, this corresponds to diffraction from an aperture, which may be modelled as of finite

width or approximated as a point source, in which case the effective plane waves are averaged and applied impulsively.

Applications of the theory to support loss in mechanical resonators goes back to Jimbo and Itao's work in the Japanese language in 1968[8], who derived expressions for the radiation loss of cantilevers, but not giving explicit forms for the resulting Q factors. Their method used a halfplane (i.e. 2D plane bounded by a straight line), corresponding to in-plane vibration of a plate, or an infinite line source on a halfspace. Hao et al. gave explicit expressions for the Q of a cantilever in a 2003 paper[9], based on 1994 further investigation into fundamental mechanisms of dissipation, including support loss, in beam systems by the original Itao[10], which had yielded an expression for the damping factors. Experimental validations of the predicted Q factors from the method were given for thin monocrystalline silicon microcantilevers by Yang et al. in 2000[11], and the work extended to an analysis of dissipation in single crystal microcantilevers by Yang et al. in 2002[12]. On the other hand, Photiadis et al.[13] compared Itao's method to a similar calculation based on Bycroft's 1956 study of the radiation impedance of a halfspace loaded by a circular plate[14], finding significant discrepancy. It can be concluded that for some geometries, such as planar resonators of the same thickness as their substrate - is common among MEMS devices but not some classes of macroscopic resonator – the Miller and Pursey halfplane approach yields suitable results with one less spatial variable and resulting linear efficiency gains as the problem scales, while for resonators which are not well approximated by this assumption, the full, 3D model is required for accurate modelling. This conclusion is reinforced by further work by Photiadis[15], reviewing the Miller and Pursey and Bancroft models, before applying each to a cantilever and a clamped-clamped beam. The latter is treat as two sources attached to two halfplanes, as a bridge spans a chasm; the modal symmetry of the C-C beam leads the results to be twice that predicted for a single halfplane and does not consider interaction between the sources, beyond that expressed in the beam modal dynamics. Good experimental agreement is shown for both models in appropriate cases.

More recently, in 2009[16], Hao et al. used the results to give integral form expressions for the displacements, and hence implicitly the power spectrum, for a double buried

stress source in a halfplane, to model bulk but not surface effects arising from a double-clamped resonator, as well as a double shear and normal forces applied to the surface of a halfspace. The resulting expressions are found to depend on the distance between the sources, but are not pursued further. The model is appropriate for a planar or thin resonator on a bulk substrate, but not for the case of equal resonator and substrate thickness due to the absence of free surfaces in the plane. Additionally, it introduces another dimension of integration, making the resource cost of calculations grow by an extra linear factor in the discretisation resolution. The phenomena and energy partitioning, as well as the spectra, are not presented. Finite element modelling and validation of the support loss models has been undertaken by Ko et al[17]. Chouvion contributed related work based on his analytical wave approach to resonator modelling based on Miller and Pursey's results, and validated the predictions via numerical methods in his thesis. Previous results published by the author using Miller and Pursey's approximation to study support loss in XBRs are available[19].

Nowhere in the work presented above or elsewhere available to the author is the case of a double uniform stress source on the surface of a halfplane, corresponding to two-dimensional Kirchhoff double slit diffraction, considered. In addition, all the MEMS and support loss work makes use of a point-source approximation, so that the effects of having two or more supports on one surface of a planar substrate has not been examined in the literature. These two components are more important at higher frequencies and in larger geometries, in general, due to the wavelengths becoming commensurate with the functional dimensions in this regime. Integral form results exist for related cases, as presented above; however, no attempt has been made thus far to study the solutions or to relate the behaviour to phenomena associated with support loss. The aim of this chapter is to develop such a model, derive results, and thus to understand the phenomena of support loss in a fairly general sense, with a view to design optimisation of supported resonators and investigation of XBR performance.

What is required, then, is a general solution for the problem of Kirchhoff diffraction of elastic waves by a screen with one or more finite width slits, with the screen

presenting perfectly compliant (stress-free) boundary conditions to the continuum. The question thus posed will be answered using an analytical approach to the substrate dynamics and validated via Finite Element Analysis in this chapter.

Symbols		c_{44}	Material shear modulus
x, y, z	Spatial coordinates	$\mathbf{u}$	Displacement vector
c_{11}	Material elastic modulus	$\mathbf{A}$	Helmholtz vector potential
Φ	Helmholtz scalar potential	∇	Divergence operator
$\Psi, \widehat{\Psi}$	Equivolumial potential, Fourier transform thereof	$\varphi, \widehat{\varphi}$	Irrotational potential, Fourier transform thereof
ρ	Material density	u_i	Displacement component in the i direction
v_Ψ, v_φ	Shear, transverse bulk wave speeds	ω	Forcing frequency
ξ	Fourier variable	$\mathcal{P}$	Transverse numerator
$f(x), \hat{f}(\xi)$	Fourier transform pair	$\mathcal{Q}$	Shear numerator
A, B	Aribitrary constants	β	Ratio of shear to transverse wave speeds in bulk
$\sigma_{ij}, \sigma_{ij}^s$	Stress, surface stress	$\mathcal{R}$	Combination numerator
$\mathcal{S}, \mathcal{S}_0$	Rayleigh's equation in ξ , ζ	a	Source region width
F_N	Normal force	d	Out-of-plane depth
F_T	Transverse force	$\mathrm{u}_i^s, \overline{\mathrm{u}_i^s}$	Surface displacement in the i direction, averaged value
b	Double source separation	ζ	Scaled Fourier variable
p	Pole location on positive ξ axis	r	$\sqrt{x^2 + z^2}$
P	Power transfer	$\overline{\mathbf{u}_i^{sn}}, \overline{\mathbf{u}_i^{ss}}$	Averaged displacements

ν	Poisson's ratio	E	Young's modulus
δ	Amplitude of deformation of contour of integration	I_i	Integral contribution from i^{th} subinterval
$\Delta \mathrm{E}_{SINGLE}$	Cyclic energy transfer from a single source to the substrate	f	Excitation frequency
η	Single source similarity variable	λ_{φ}	Transverse wavelength
$\Delta \mathrm{E}_{DOUBLE}$	Cyclic energy transfer from a double source to the substrate	ς	Double source similarity variable

4.2 Analytical Halfplane Approach

The problem of elastic wave radiation in a semi-infinite half space has been studied previously. Following the approach of groundbreaking work by Lamb in 1904[3], Miller and Pursey's 1953 paper[5] arrives at closed-form expressions for the energy radiated by localised stress sources of finite extent on the surface of an infinite linear elastic half-space. The cases considered include uniform in-plane time harmonic stresses normal and parallel to the boundary. The problem is attacked using the method of Helmholtz potentials, which is effective, but restricts the analysis to the isotropic case. The development below follows the approach therein, extending it to consider more geometrically complex configurations as encountered in the XBR configuration.

4.2.1 Problem statement

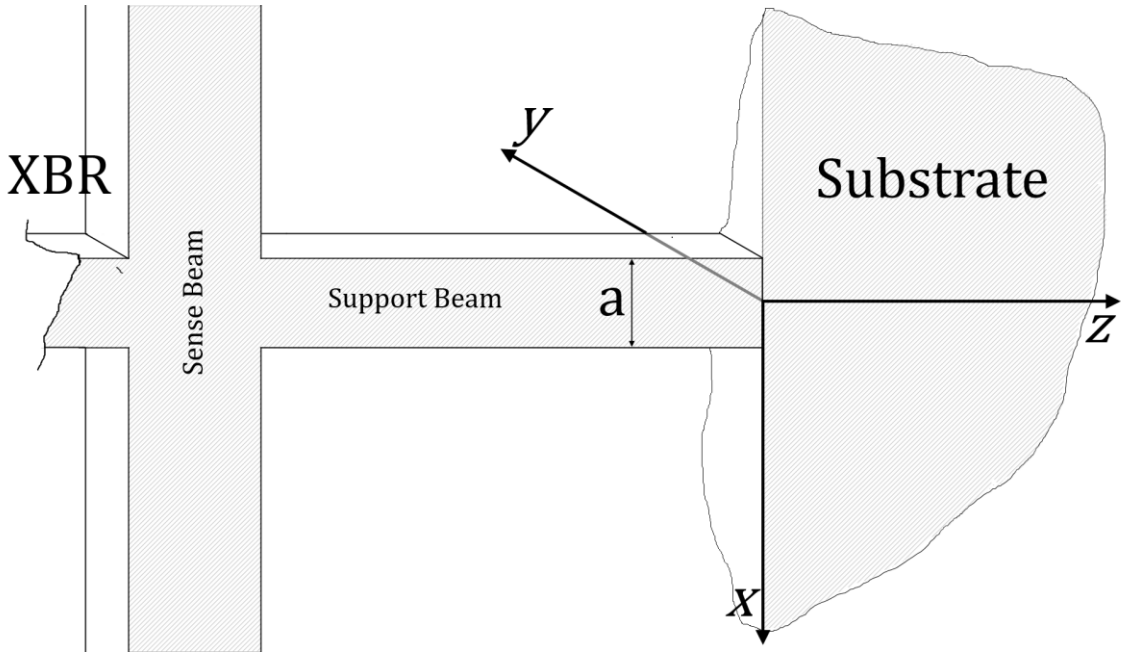

Figure 4.1 Geometric configuration and choice of coordinate for the XBR-halfplane system. The substrate is infinite in both x and y; the stress source is infinite in y and occupies $\frac{-a}{2} \leq x \leq \frac{a}{2}$.

The system under consideration is illustrated in Figure 4.1 as a view of a cross-section through $y = 0$. The domain for the substrate analysis is the region $-\infty < x < \infty, -\infty < y < \infty, \ 0 \leq z < \infty$; both the stress source and the substrate are assumed to be infinite in x and y. The cut face is indicated by diagonal hatching: stress-free interfaces are denoted in white. The support width is denoted a. Right-handed

Cartesian coordinates x, y, z, centred at the middle of the resonator-substrate interface, are introduced. Due to the translational symmetry in y, the displacement $\mathbf{u}$ at a point p with coordinates x_p, y_p, z_p can be written as $\mathbf{u}_p = \{\mathrm{u}_x, 0, \mathrm{u}_z\}$. That is to say, the system is considered as quasi-2D.

4.2.2 Equations of motion

The equations of motion for an isotropic linear elastic solid with displacement field $\mathbf{u} = \mathrm{u}_x, \mathrm{u}_y, \mathrm{u}_z$ can be written as[5]

$$c_{11}\nabla(\nabla.\mathbf{u}) + c_{44}\nabla \times (\nabla \times \mathbf{u}) = \rho \frac{\partial^2 \mathbf{u}}{\partial t^2} \tag{4.1}$$

Where c_{11} and c_{44} are the substrate material bulk and shear moduli respectively and ρ the material mass density. Under this simplifying assumption of isotropy, the structure of the Helmholtz potentials can be employed to considerably simplify the analysis. In particular, all rotation is in plane, so that the vector potential is wholly in the y direction; also, the scalar potential is only a function of x and z. That is,

$$\mathbf{A} = \nabla \times \mathbf{u} = \Psi(x, z)\mathbf{j} \tag{4.2a}$$

$$\Phi = \nabla.\mathbf{u} = \varphi(x, z) \tag{4.2b}$$

where $\mathbf{A}$ is the vector Helmholtz potential and Φ is the scalar Helmholtz potential for the displacement field $\mathbf{u}(x, y, z)$; Ψ and φ are scalar valued functions, while $\mathbf{j}$ is the unit vector in the y direction. Then, upon substitution of Equations (4.2) into (4.1), the equations of motion for the half-space can be written as

$$c_{11}\nabla(\varphi(x, z)) + c_{44}\nabla \times (\Psi(x, z)\mathbf{j}) = \rho \frac{\partial^2 \mathbf{u}}{\partial t^2} \tag{4.3}$$

The components of (4.3) can be written as

$$c_{44}\frac{\partial \Psi}{\partial x} - c_{11}\frac{\partial \varphi}{\partial z} = \rho \frac{\partial^2 \mathrm{u}_z}{\partial t^2} \tag{4.4a}$$

$$-\left(c_{44}\frac{\partial \Psi}{\partial z} + c_{11}\frac{\partial \varphi}{\partial x}\right) = \rho \frac{\partial^2 \mathrm{u}_x}{\partial t^2} \tag{4.4b}$$

Simultaneously separating variables, independent equations can be derived in the two potentials as

$$(v_{\Psi}^2 \nabla_{xz}^2 + \partial_{tt})\Psi = 0 \qquad (4.5a)$$

$$\left(v_{\varphi}^2 \nabla_{xz}^2 + \partial_{tt}\right)\varphi = 0 \qquad (4.5b)$$

where $v_{\Psi}^2 = \frac{c_{11}}{\rho}$ and $v_{\varphi}^2 = \frac{c_{44}}{\rho}$. ∇_{xz} is the divergence operator in the xz −plane, i.e. $\partial_x + \partial_z$. This formulation yields physical insight. The equations (4.5) have the form of decoupled scalar wave equations in two dimensions: one associated with the scalar potential and the other with the vector potential. That is to say, away from boundaries and inhomogeneity, disturbances propagate as two independent scalar wave fields, one associated with dilatation and the other with rotation at constant volume, with respective propagation velocities v_{φ} and v_{φ}. These are none other than the two dimensional analogues of the familiar P-and S-waves from the 3 dimensional case; in the particular geometry under consideration, they propagate in x and z independently. Assuming time harmonicity with frequency ω one can derive from (4.5) the following:

$$v_{\Psi}^2 \frac{\partial \Psi}{\partial x} - v_{\varphi}^2 \frac{\partial \varphi}{\partial z} = \omega^2 \mathrm{u}_z \qquad (4.6a)$$

$$-\left(v_{\varphi}^2 \frac{\partial \varphi}{\partial z} + v_{\Psi}^2 \frac{\partial \Psi}{\partial x}\right) = \omega^2 \mathrm{u}_x \qquad (4.6b)$$

4.2.3 Fourier transforms

First, we remove the x-dependence of (4.6) using a Fourier transform, defined here as

$$\hat{f}(\xi) = \int_{-\infty}^{\infty} f(x) e^{-i\xi x}\, dx \qquad (4.7)$$

with inverse defined as

$$f(x) = \frac{1}{2\pi} \int_{-\infty}^{\infty} \hat{f}(\xi) e^{i\xi x}\, d\xi \qquad (4.8)$$

Applying the transform (4.7) to equations (4.6) one derives

$$i\xi v_\Psi^2 \widehat{\Psi} - v_\varphi^2 \frac{\partial \widehat{\varphi}}{\partial z} = \omega^2 \widehat{u_z} \tag{4.9a}$$

$$-\left(v_\Psi^2 \frac{\partial \widehat{\Psi}}{\partial z} + i\xi v_\varphi^2 \widehat{\varphi} \right) = \omega^2 \widehat{u_x} \tag{4.9b}$$

Simultaneously separating variables, one obtains from (4.9) the following expressions:

$$\frac{\partial^2 \widehat{\Psi}}{\partial z^2} - \left(\xi^2 - \frac{\omega^2}{v_\Psi^2} \right) \widehat{\Psi} = 0 \tag{4.10a}$$

$$\frac{\partial^2 \widehat{\varphi}}{\partial z^2} - \left(\xi^2 - \frac{\omega^2}{v_\varphi^2} \right) \widehat{\varphi} = 0 \tag{4.10b}$$

Note that equations (4.10) are cast in the form of one-dimensional wave equations. The general solutions are well known. We introduce the notation

$$\mathcal{P} = \sqrt{\xi^2 - \omega^2 / v_\varphi^2} \tag{4.11a}$$

$$\mathcal{Q} = \sqrt{\xi^2 - \omega^2 / v_\Psi^2} \tag{4.11b}$$

Then the solutions to (4.11) can be written as

$$\widehat{\varphi} = A e^{-z\mathcal{P}} \tag{4.12a}$$

$$\widehat{\Psi} = B e^{-z\mathcal{Q}} \tag{4.12b}$$

For any particular case, one can determine the coefficients A and B through the application of boundary conditions; the Fourier domain representations of the stress and displacement fields everywhere in the substrate can be recovered via (4.9), and the application of the inverse transform (4.8) will yield the desired corresponding results in the real spatial domain.

4.2.4 Application of Boundary conditions

There exists only one boundary in the problem, namely $z = 0$. For a well-posed boundary value problem, boundary conditions must be specified. The simplest case is the geometry illustrated in Figure 4.1. The stresses at the free interface can be written as

$$\sigma_{zz}^{s} = (c_{11} - 2c_{44})\varphi + 2c_{44}\frac{\partial u_z}{\partial z} \tag{4.13a}$$

$$\sigma_{xz}^{s} = c_{44}\left(\frac{\partial u_z}{\partial x} + \frac{\partial u_x}{\partial z}\right) \tag{4.13b}$$

$$\sigma_{yz}^{s} = c_{44}\left(\frac{\partial u_z}{\partial y} + \frac{\partial u_y}{\partial z}\right) = 0 \tag{4.13c}$$

Or, in terms of the potentials

$$\frac{\omega^2}{\rho v_{\Psi}^4}\sigma_{zz}^{s} = 2\frac{\partial^2\Psi}{\partial x \partial z} - \left(\beta^2(\beta^2 - 2)\frac{\partial^2\varphi}{\partial x^2} + \beta^4\frac{\partial^2\varphi}{\partial z^2}\right) \tag{4.14a}$$

$$\frac{\omega^2}{\rho v_{\Psi}^4}\sigma_{zx}^{s} = \frac{\partial^2\Psi}{\partial x^2} - \frac{\partial^2\Psi}{\partial z^2} - 2\beta^2\frac{\partial^2\varphi}{\partial x \partial z} \tag{4.14b}$$

where $\beta = \frac{v_{\varphi}}{v_{\Psi}}$. The Fourier transforms of equations (4.14) are

$$\frac{\omega^2}{\rho v_{\Psi}^4}\widehat{\sigma_{zz}^{s}} = 2i\xi\frac{\partial\widehat{\Psi}}{\partial z} - \beta^4\frac{\partial^2\widehat{\varphi}}{\partial z^2} + \beta^2(\beta^2 - 2)\xi^2\widehat{\varphi} \tag{4.15a}$$

$$\frac{\omega^2}{\rho v_{\Psi}^4}\widehat{\sigma_{zx}^{s}} = -\left(\xi^2\widehat{\Psi} + \frac{\partial^2\widehat{\Psi}}{\partial z^2} + 2i\xi\beta^2\frac{\partial\widehat{\varphi}}{\partial z}\right) \tag{4.15b}$$

Expressing the potentials in the form defined by (4.12) and substituting into (4.15) gives the following relationships between the constants A and B for arbitrary applied stresses (for which a Fourier transform exists):

$$\frac{\omega^2}{\rho v_{\Psi}^4}\widehat{\sigma_{zz}} = 2i\xi\frac{\partial}{\partial z}(Be^{-zQ}) - \beta^4\frac{\partial^2}{\partial z^2}(Ae^{-z\mathcal{P}}) + \beta^2(\beta^2 - 2)\xi^2(Ae^{-z\mathcal{P}}) \tag{4.16a}$$

$$\frac{\omega^2}{\rho v_{\Psi}^4}\widehat{\sigma_{zx}} = -\left(\xi^2(Be^{-zQ}) + \frac{\partial^2}{\partial z^2}(Be^{-zQ})\right) - 2i\xi\beta^2\frac{\partial}{\partial z}(Ae^{-z\mathcal{P}}) \tag{4.16b}$$

Upon performing the differentiation and setting z=0, we obtain the equation for the stresses at the free surface in the ξ domain as

$$\frac{\omega^2}{\rho v_\Psi^4}\widehat{\sigma_{zz}^s} = -2i\xi\mathcal{Q}B - (\beta^4\mathcal{P}^2 - \beta^2(\beta^2-2)\xi^2)A$$

$$\frac{\omega^2}{\rho v_\Psi^4}\widehat{\sigma_{zx}^s} = -(\xi^2+\mathcal{Q}^2)B + 2i\xi\beta^2\mathcal{P}A$$

where the notation $\sigma_{ij}^s = \widehat{\sigma_{ij}}\big|_{z=0}$ has been employed to describe quantities evaluated at the free surface .

It remains to solve for A and B in terms of the applied stresses. (4.16b) rearranges to

$$B = \frac{(2i\xi\beta^2\mathcal{P})A - \frac{\omega^2}{\rho v_\Psi^4}\widehat{\sigma_{zx}^s}}{\mathcal{R}} \qquad (4.17a)$$

where

$$\mathcal{R} = \xi^2 + \mathcal{Q}^2 = 2\xi^2 - \omega^2/v_\Psi^2$$

On the other hand, (4.16a) can be written in the form

$$A = \frac{-\left(2i\xi\mathcal{Q}B + \frac{\omega^2}{\rho v_\Psi^4}\widehat{\sigma_{zz}^s}\right)}{\beta^2(\beta^2-2)\xi^2 - \beta^4\mathcal{P}^2} = \frac{2i\xi\mathcal{Q}B + \frac{\omega^2}{\rho v_\Psi^4}\widehat{\sigma_{zz}^s}}{-\beta^2\mathcal{R}} \qquad (4.17b)$$

Using (4.16), for a given time-harmonic distribution of stresses at the free surface, one can solve for A and B; back-substitution into (4.9) will yield $\widehat{\mathrm{u}_x}$ and $\widehat{\mathrm{u}_z}$. Taking the inverse transform (4.8) will return the desired displacements in the real domain u_x and u_z. Upon substitution of (4.17a) into (4.17b), one obtains

$$-\frac{\frac{\omega^2}{\rho v_\Psi^4}\widehat{\sigma_{zz}^s}}{\beta^2\mathcal{R}} - \frac{2i\xi\mathcal{Q}\left(\frac{\omega^2}{\rho v_\Psi^4}\widehat{\sigma_{zx}^s} - 2i\xi\beta^2\mathcal{P}A\right)}{\beta^2\mathcal{R}^2} = A \qquad (4.18)$$

After rearrangement, (4.18) can be written in the form

$$A = \frac{\omega^2\left(2i\xi\mathcal{Q}\widehat{\sigma_{zx}^s} - \mathcal{R}\widehat{\sigma_{zz}^s}\right)}{\rho v_\Psi^2 v_\varphi^2 \mathcal{S}} \qquad (4.19)$$

where

$$\mathcal{S}(\xi) = \mathcal{R}^2 - 4\xi^2\mathcal{P}\mathcal{Q}$$

Eliminating the other variable, one obtains for B the expression

$$B = \frac{\omega^2\left(2i\xi\mathcal{P}\widehat{\sigma_{zz}^{S}} + R\widehat{\sigma_{zx}^{S}}\right)}{\rho v_{\Psi}^4 \mathcal{S}} \tag{4.20}$$

The potentials can then be expressed as functions of the applied stresses as

$$\widehat{\varphi} = \frac{\omega^2\left(2i\xi\mathcal{Q}\widehat{\sigma_{zx}^{S}} - \mathcal{R}\widehat{\sigma_{zz}^{S}}\right)}{\rho v_{\Psi}^2 v_{\varphi}^2 \mathcal{S}} e^{-z\mathcal{P}} \tag{4.21a}$$

$$\widehat{\Psi} = -\frac{\omega^2\left(2i\xi\mathcal{P}\widehat{\sigma_{zz}^{S}} + R\widehat{\sigma_{zx}^{S}}\right)}{\rho v_{\Psi}^4 \mathcal{S}} e^{-z\mathcal{Q}} \tag{4.21b}$$

Upon substitution of (4.21) into (4.9), one recovers the Fourier domain displacement components as

$$\frac{1}{\rho v_{\Psi}^2}\frac{1}{\mathcal{S}}\left(\mathcal{P}(2\xi^2 e^{-z\mathcal{Q}} - \mathcal{R}e^{-z\mathcal{P}})\widehat{\sigma_{zz}^{S}} + i\xi(2\mathcal{P}\mathcal{Q}e^{-z\mathcal{P}} - \mathcal{R}e^{-z\mathcal{Q}})\widehat{\sigma_{zx}^{S}}\right) = \widehat{\mathrm{u}_z} \tag{4.22a}$$

$$\frac{1}{\rho v_{\Psi}^2}\frac{1}{\mathcal{S}}\left(i\xi(\mathcal{R}e^{-z\mathcal{P}} - 2\mathcal{P}\mathcal{Q}e^{-z\mathcal{Q}})\widehat{\sigma_{zz}^{S}} + \mathcal{Q}(2\xi^2 e^{-z\mathcal{P}} - \mathcal{R}e^{-z\mathcal{Q}})\widehat{\sigma_{zx}^{S}}\right) = \widehat{\mathrm{u}_x} \tag{4.22b}$$

At the free surface we have

$$\frac{1}{\rho v_{\Psi}^2}\frac{1}{\mathcal{S}}\left(\mathcal{P}(2\xi^2 - \mathcal{R})\widehat{\sigma_{zz}^{S}} + i\xi(2\mathcal{P}\mathcal{Q} - \mathcal{R})\widehat{\sigma_{zx}^{S}}\right) = \widehat{\mathrm{u}_z^{S}} \tag{4.23a}$$

$$\frac{1}{\rho v_{\Psi}^2}\frac{1}{\mathcal{S}}\left(i\xi(\mathcal{R} - 2\mathcal{P}\mathcal{Q})\widehat{\sigma_{zz}^{S}} + \mathcal{Q}(2\xi^2 - \mathcal{R})\widehat{\sigma_{zx}^{S}}\right) = \widehat{\mathrm{u}_x^{S}} \tag{4.23b}$$

where again the superscript notation $\widehat{\mathrm{u}_\iota^{S}} = \widehat{\mathrm{u}_\iota}|_{z=0}$ indicates evaluation at the free surface. Attention now turns to some particular cases of applied stress distributions.

4.2.4.1 Uniform normal stress

Consider the case of a uniformly distributed axial stress acting on the support-substrate interface, such as to provide a good first approximation to the stress distribution arising from axial loading of the support. Then, for the chosen geometric

configuration and coordinates, the stress σ_{zz}^{s} normal to the interface $y = 0$ can be written as

$$\sigma_{zz}^{s} = \begin{Bmatrix} 0, & x < \dfrac{-a}{2} \\ \dfrac{F_{\mathrm{N}}}{ad}, & \dfrac{-a}{2} \le x \le \dfrac{a}{2} \\ 0, & x > \dfrac{a}{2} \end{Bmatrix} \tag{4.24}$$

In this subsection, the transverse shear is assumed to be null:

$$\sigma_{zx}^{s} = 0 \; \forall x \in \mathbb{R}$$

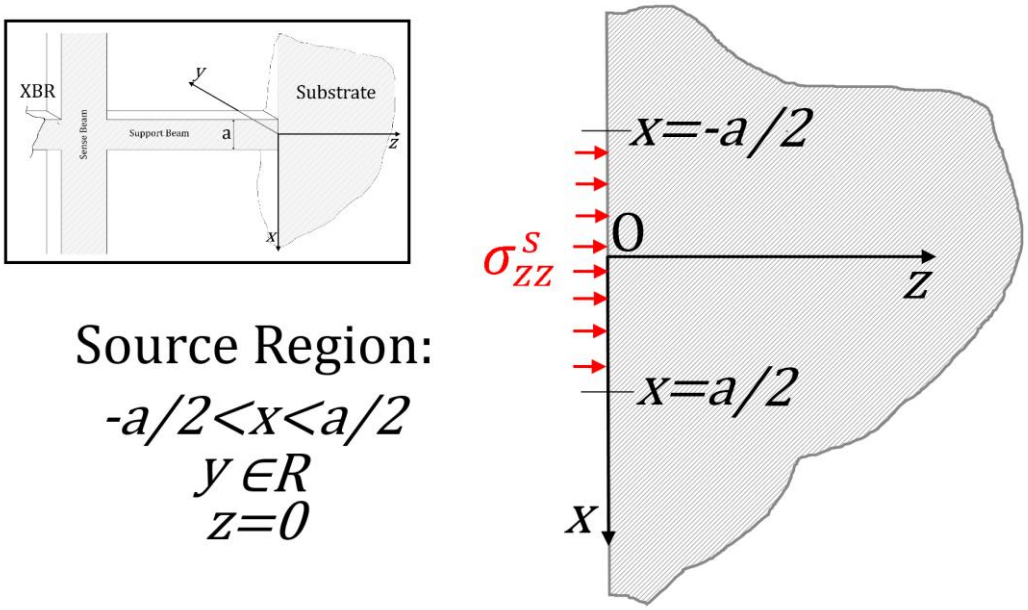

Figure 4.2 Configuration of geometry and force distribution for case of axial support loading, considered in this subsection. Shear tractions are identically zero at the free surface; normal force for $|x| > a/2$ is also identically zero.

Applying the Fourier transform (4.7)to (4.24) yields

$$\widehat{\sigma_{zz}^{s}} = \frac{F_{\mathrm{N}}}{d}\,\mathrm{sinc}\left(\frac{\xi a}{2}\right) \tag{4.25}$$

The displacement equations (4.23) take on the reduced form

$$\frac{F_{\mathrm{N}}}{\rho d v_{\Psi}^{2}}\frac{1}{\mathcal{S}}\left(\mathcal{P}(2\xi^{2} - \mathcal{R})\mathrm{sinc}\left(\frac{\xi a}{2}\right)\right) = \widehat{\mathrm{u}_{z}^{s}} \tag{4.26a}$$

$$\frac{F_{\mathrm{N}}}{\rho d v_{\Psi}^2}\frac{1}{\mathcal{S}}\left(i\xi(\mathcal{R}-2\mathcal{P}\mathcal{Q})\mathrm{sinc}\left(\frac{\xi a}{2}\right)\right)=\widehat{\mathrm{u}_x^s} \qquad (4.26b)$$

Applying the inverse transform given by (4.8) to (4.26), one has

$$\mathrm{u}_z^s=\frac{F_{\mathrm{N}}}{2\rho d\pi v_{\Psi}^2}\int_{-\infty}^{\infty}\frac{\mathcal{P}}{\mathcal{S}}(2\xi^2-\mathcal{R})\mathrm{sinc}\left(\frac{\xi a}{2}\right)e^{i\xi x}d\xi \qquad (4.27a)$$

$$\mathrm{u}_x^s=\frac{F_{\mathrm{N}}}{2\rho d\pi v_{\Psi}^2}\int_{-\infty}^{\infty}\frac{i\xi}{\mathcal{S}}(\mathcal{R}-2\mathcal{P}\mathcal{Q})\mathrm{sinc}\left(\frac{\xi a}{2}\right)e^{i\xi x}d\xi \qquad (4.27b)$$

These integrals can be further simplified if it is noticed that the quantities, $\mathcal{S}$, $\mathcal{R}$, $\mathcal{P}\mathcal{Q}$ and $\mathrm{sinc}\left(\frac{\xi a}{2}\right)$ in the integrand are all even functions of ξ, while $\sin\left(\frac{\xi a}{2}\right)$ is odd. Then, equations (4.27) reduce to

$$\mathrm{u}_z^s=\frac{F_{\mathrm{N}}}{2\rho d\pi v_{\Psi}^2}\int_{0}^{\infty}\frac{\mathcal{P}}{\mathcal{S}}(2\xi^2-\mathcal{R})\mathrm{sinc}\left(\frac{\xi a}{2}\right)\cos(\xi x)\,d\xi \qquad (4.28a)$$

$$\mathrm{u}_x^s=\frac{F_{\mathrm{N}}}{2\rho d\pi v_{\Psi}^2}\int_{0}^{\infty}\frac{i\xi}{\mathcal{S}}(\mathcal{R}-2\mathcal{P}\mathcal{Q})\,\mathrm{sinc}\left(\frac{\xi a}{2}\right)\sin(\xi x)d\xi \qquad (4.28b)$$

To obtain the average values of these displacements over the source region, we can integrate over the source region width as follows:

$$\overline{\mathrm{u}_z^s}=\frac{F_{\mathrm{N}}}{2a\rho d\pi v_{\Psi}^2}\int_{-a/2}^{a/2}\int_{0}^{\infty}\frac{\mathcal{P}}{\mathcal{S}}(2\xi^2-\mathcal{R})\mathrm{sinc}\left(\frac{\xi a}{2}\right)\cos(\xi x)\,d\xi\,dx \qquad (4.29a)$$

$$\overline{\mathrm{u}_x^s}=\frac{F_{\mathrm{N}}}{2a\rho d\pi v_{\Psi}^2}\int_{-a/2}^{a/2}\int_{0}^{\infty}\frac{i\xi}{\mathcal{S}}(\mathcal{R}-2\mathcal{P}\mathcal{Q})\,\mathrm{sinc}\left(\frac{\xi a}{2}\right)\sin(\xi x)d\xi\,dx \qquad (4.29b)$$

where we have introduced the notation $\overline{\mathrm{u}_i^s}=\frac{1}{a}\int_{-a/2}^{a/2}\mathrm{u}_i^s dx$ to denote the value of the quantity u_i^s averaged over the source region $-a/2<x<a/2$. The parity of the integrand of (4.29a) in x is even; however, the parity of the integrand of (4.29b) is odd. Hence, on changing the order of integration, Equations (4.29) simplify to

$$\overline{\mathrm{u}_z^s} = \frac{F_\mathrm{N}}{2\rho a d\pi v_\Psi^2} \int_0^\infty \frac{\mathcal{P}}{\mathcal{S}} (2\xi^2 - \mathcal{R}) \operatorname{sinc}\left(\frac{\xi a}{2}\right) \int_{-a/2}^{a/2} \cos(\xi x)\, dx d\xi \qquad (4.30a)$$

$$\overline{\mathrm{u}_x^s} = \frac{F_\mathrm{N}}{2\rho a d\pi v_\Psi^2} \int_0^\infty \frac{i\xi}{\mathcal{S}} (\mathcal{R} - 2\mathcal{P}\mathcal{Q}) \operatorname{sinc}\left(\frac{\xi a}{2}\right) \int_{-a/2}^{a/2} \sin(\xi x)\, dx d\xi = 0 \qquad (4.30b)$$

The last equation (4.30b) implies that the average transverse displacement over the source region is identically zero, because of the symmetry of the integral and the integrand. This bears an intuitive geometric interpretation: as a support member is loaded purely axially, strains in the substrate transverse to the member axis are antisymmetric with respect to the transverse coordinate. Hence, no uniform or symmetric shear stress applied over the source can do any work on these displacements. We can conclude that the nonzero but symmetric transverse strain incurred in the substrate by axial loadings does not contribute to support loss in the absence of an antisymmetric shear force distribution.

Evaluating the remaining integral (4.30a) with respect to x gives for the required average source displacement in the z coordinate as

$$\overline{\mathrm{u}_z^s} = \frac{F_\mathrm{N}}{\rho d\pi v_\Psi^2} \int_0^\infty \frac{\mathcal{P}}{\mathcal{S}} (2\xi^2 - \mathcal{R}) \operatorname{sinc}^2\left(\frac{\xi a}{2}\right) d\xi \qquad (4.31)$$

For small argument, the trigonometric term tends asymptotically to 1. This corresponds to a point source. Then, we have

$$\overline{\mathrm{u}_z^s} = \frac{F_\mathrm{N}}{\rho d\pi v_\Psi^2} \int_0^\infty \frac{\mathcal{P}}{\mathcal{S}} (2\xi^2 - \mathcal{R}) d\xi \qquad (4.32)$$

Using the definition of $\mathcal{R}$, one can write, for the point source limit,

$$\overline{\mathrm{u}_z^s} = \frac{F_\mathrm{N}\omega^2}{\rho d\pi v_\Psi^4} \int_0^\infty \frac{\mathcal{P}}{\mathcal{S}} d\xi \qquad (4.33)$$

4.2.4.2 Uniform transverse stress

Attention now turns to the case of a uniformly distributed shear load acting on the interface between the support and the substrate, which models the stress distribution arising from the constraint forces at the support-substrate interface during flexure of the support. The total force across the boundary is taken to be F_{T}. Then, for the chosen geometric configuration and coordinates, the stress σ_{zx}^{s} transverse to the interface $y = 0$ can be written as

$$\sigma_{zx}^{s} = \begin{Bmatrix} 0, & x < \dfrac{-a}{2} \\ \dfrac{F_{\mathrm{T}}}{a}, & \dfrac{-a}{2} \leq x \leq \dfrac{a}{2} \\ 0, & x > \dfrac{a}{2} \end{Bmatrix} \tag{4.34a}$$

Conversely, we now assume the normal stress is zero:

$$\sigma_{zz}^{s} = 0 \; \forall x \in \mathbb{R} \tag{4.34b}$$

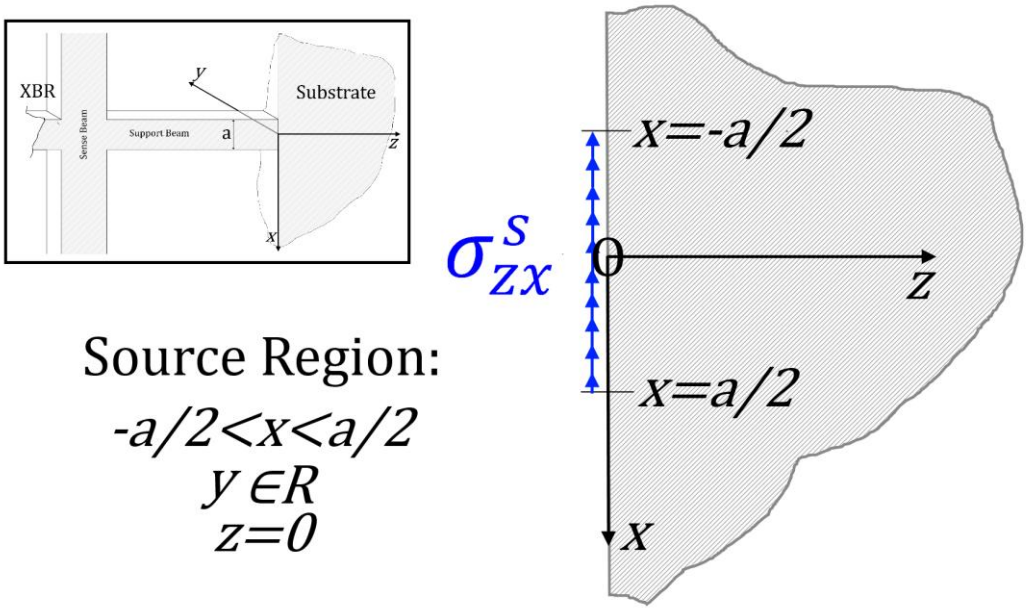

Figure 4.3 Configuration of geometry and force distribution for case of transverse support loading from flexural vibrations of the support as considered in this subsection. Normal forces are here identically zero at the free surface; shear tractions for $|x| > a/2$ are also identically zero.

As before, we apply the Fourier transform defined by (4.7) to (4.34) and obtain

$$\widehat{\sigma_{zx}^{s}} = \frac{F_{\mathrm{T}}}{d}\,\mathrm{sinc}\left(\frac{\xi a}{2}\right) \tag{4.35a}$$

$$\widehat{\sigma_{zz}^{s}} = 0 \tag{4.35b}$$

Equations (4.35) reduce to

$$\frac{F_{\mathrm{T}}}{\rho d v_{\Psi}^{2}}\frac{1}{\mathcal{S}}\left(i(2\mathcal{P}\mathcal{Q}-\mathcal{R})\mathrm{sinc}\left(\frac{\xi a}{2}\right)\right) = \widehat{\mathrm{u}_{z}^{s}} \tag{4.36a}$$

$$\frac{F_{\mathrm{T}}}{\rho d v_{\Psi}^{2}}\frac{1}{\mathcal{S}}\left(\mathcal{Q}(2\xi^{2}-\mathcal{R})\mathrm{sinc}\left(\frac{\xi a}{2}\right)\right) = \widehat{\mathrm{u}_{x}^{s}} \tag{4.36b}$$

To invert the transform and recover the spatial domain displacements, we apply (4.8):

$$\mathrm{u}_{z}^{s} = \frac{F_{\mathrm{T}}}{2\rho d\pi v_{\Psi}^{2}}\int_{-\infty}^{\infty}\frac{i\xi}{\mathcal{S}}(2\mathcal{P}\mathcal{Q}-\mathcal{R})\mathrm{sinc}\left(\frac{\xi a}{2}\right)e^{i\xi x}d\xi \tag{4.37a}$$

$$\mathrm{u}_{x}^{s} = \frac{F_{\mathrm{T}}}{2\rho d\pi v_{\Psi}^{2}}\int_{-\infty}^{\infty}\frac{\mathcal{Q}}{\mathcal{S}}(2\xi^{2}-\mathcal{R})\mathrm{sinc}\left(\frac{\xi a}{2}\right)e^{i\xi x}d\xi \tag{4.37b}$$

Again using the parity of the integrands, equations (4.37) can be put in the form

$$\mathrm{u}_{z}^{s} = \frac{F_{\mathrm{T}}}{2\rho d\pi v_{\Psi}^{2}}\int_{0}^{\infty}\frac{i\xi}{\mathcal{S}}(2\mathcal{P}\mathcal{Q}-\mathcal{R})\,\mathrm{sinc}\left(\frac{\xi a}{2}\right)\sin(\xi x)\,d\xi \tag{4.38a}$$

$$\mathrm{u}_{x}^{s} = \frac{F_{\mathrm{T}}}{2\rho d\pi v_{\Psi}^{2}}\int_{0}^{\infty}\frac{\mathcal{Q}}{\mathcal{S}}(2\xi^{2}-\mathcal{R})\mathrm{sinc}\left(\frac{\xi a}{2}\right)\cos(\xi x)\,d\xi \tag{4.38b}$$

We seek the averaged displacements over the source region by integrating again with respect to x, obtaining

$$\overline{\mathrm{u}_{z}^{s}} = \frac{F_{\mathrm{T}}}{2a\rho d\pi v_{\Psi}^{2}}\int_{0}^{\infty}\frac{i\xi}{\mathcal{S}}(2\mathcal{P}\mathcal{Q}-\mathcal{R})\mathrm{sinc}\left(\frac{\xi a}{2}\right)\int_{-a/2}^{a/2}\sin(\xi x)\,dx d\xi = 0 \tag{4.39a}$$

$$\overline{\mathrm{u}_x^s} = \frac{F_\mathrm{T}}{2a\rho d\pi v_\Psi^2} \int_0^\infty \frac{Q}{\mathcal{S}} (2\xi^2 - \mathcal{R}) \mathrm{sinc}\left(\frac{\xi a}{2}\right) \int_{-a/2}^{a/2} \cos(\xi x)\, d\xi$$

$$= \frac{F_\mathrm{T}}{\rho d\pi v_\Psi^2} \int_0^\infty \frac{Q}{\mathcal{S}} (2\xi^2 - \mathcal{R}) \mathrm{sinc}^2\left(\frac{\xi a}{2}\right) d\xi \qquad (4.39b)$$

As before, in the point source limit when the argument of the sinc term in the integrand is small, (4.39b) can be simplified to read

$$\overline{\mathrm{u}_x^s} \cong \frac{F_\mathrm{T}\omega^2}{\rho d\pi v_\Psi^4} \int_0^\infty \frac{Q}{\mathcal{S}} d\xi \qquad (4.40)$$

4.2.4.3 Symmetric distribution of two equal normal stresses

For the XBR, the supports on each side of the device can be analysed using the transverse and normal force calculations undertaken in the previous two subsections. The modal solutions for the XBR yield the required quantities F_n and F_t; evaluating the formulae (4.33) and (4.40) for each case and superposing the result will give the support loss for one support. If interactions between the displacement fields generated by each support and power transfer at the other supports are neglected, the total support loss can be calculated by multiplying the result by four.

To capture the flavour and magnitude of interaction effects, attention now turns to the symmetric configuration described in Figure 4.4.

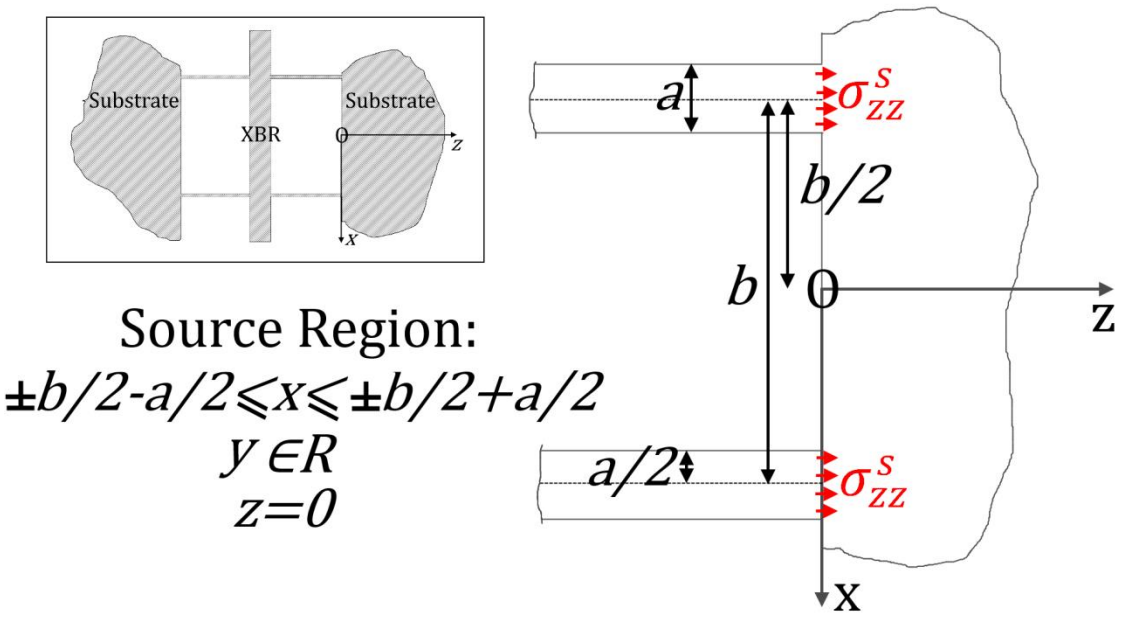

Figure 4.4 Illustration of the double normal stress source and the correspondence to an XBR in the main image and inset, respectively.

The stress at the free boundary for this case has the form

$$\sigma_{zz}^{s}=\begin{cases}0, & x<-b-\frac{a}{2}\\ \frac{F_{\mathrm{N}}}{ad}, & \frac{-b}{2}-\frac{a}{2}\le x\le\frac{-b}{2}+\frac{a}{2}\\ 0, & \frac{-b}{2}+\frac{a}{2}\le x\le\frac{b}{2}-\frac{a}{2}\\ \frac{F_{\mathrm{N}}}{ad}, & \frac{b}{2}-\frac{a}{2}\le x\le\frac{b}{2}+\frac{a}{2}\\ 0, & x>\frac{b}{2}+\frac{a}{2}\end{cases}\qquad(4.41a)$$

$$\sigma_{zx}^{s}=0\ \forall x\in\mathbb{R}\qquad(4.41b)$$

The Fourier transforms of the equations (4.41) are

$$\widehat{\sigma_{zz}^{s}}=\frac{F_{\mathrm{N}}}{d}\int_{-\infty}^{\infty}\sigma_{zz}^{s}e^{-i\xi x}dx$$

$$=\frac{-F_{\mathrm{N}}}{i\xi d}\left\{\left[e^{i\xi\frac{b}{2}}e^{-i\xi\frac{a}{2}}-e^{i\xi\frac{b}{2}}e^{i\xi\frac{a}{2}}\right]+\left[e^{-i\xi\frac{b}{2}}e^{-i\xi\frac{a}{2}}-e^{-i\xi\frac{b}{2}}e^{i\xi\frac{a}{2}}\right]\right\}$$

$$= \frac{F_{\mathrm{N}}}{d} \cos\left(\xi \frac{b}{2}\right) \operatorname{sinc}\left(\xi \frac{a}{2}\right) \tag{4.42a}$$

$$\sigma_{zx}^{S} = \widehat{\sigma_{zx}^{S}} = 0 \; \forall x \in \mathbb{R} \tag{4.42b}$$

Since the only nonzero stress present is $\widehat{\sigma_{zz}^{S}}$, the displacement equations (4.23) take on the reduced form

$$\frac{1}{\rho d v_{\Psi}^2} \frac{1}{\mathcal{S}} \left(\mathcal{P}(2\xi^2 - \mathcal{R}) \widehat{\sigma_{zz}^{S}}\right) = \widehat{\mathrm{u}_z^{S}} \tag{4.43a}$$

$$\frac{1}{\rho d v_{\Psi}^2} \frac{1}{\mathcal{S}} \left(i\xi(\mathcal{R} - 2\mathcal{P}\mathcal{Q}) \widehat{\sigma_{zz}^{S}}\right) = \widehat{\mathrm{u}_x^{S}} \tag{4.43b}$$

Combining (4.42) and (4.43) gives as a closed form representation of the Fourier transformed surface displacements:

$$\frac{F_{\mathrm{N}}}{\rho d v_{\Psi}^2} \frac{1}{\mathcal{S}} \left(\mathcal{P}(2\xi^2 - \mathcal{R}) \left(\cos\left(\xi \frac{b}{2}\right) \operatorname{sinc}\left(\xi \frac{a}{2}\right) \right) \right) = \widehat{\mathrm{u}_z^{S}} \tag{4.44a}$$

$$\frac{F_{\mathrm{N}}}{\rho d v_{\Psi}^2} \frac{1}{\mathcal{S}} \left(i\xi(\mathcal{R} - 2\mathcal{P}\mathcal{Q}) \left(\cos\left(\xi \frac{b}{2}\right) \operatorname{sinc}\left(\xi \frac{a}{2}\right) \right) \right) = \widehat{\mathrm{u}_x^{S}} \tag{4.44b}$$

We seek the inverse Fourier transform to find the surface displacements in the spatial domain, as before:

$$\frac{F_{\mathrm{N}}}{2d\rho\pi v_{\Psi}^2} \int_{-\infty}^{\infty} \frac{1}{\mathcal{S}} \left(\mathcal{P}(2\xi^2 - \mathcal{R}) \left(\cos\left(\xi \frac{b}{2}\right) \operatorname{sinc}\left(\xi \frac{a}{2}\right) \right) \right) e^{i\xi x} d\xi = \widehat{\mathrm{u}_z^{S}} \tag{4.45a}$$

$$\frac{F_{\mathrm{N}}}{2d\rho\pi v_{\Psi}^2} \int_{-\infty}^{\infty} \frac{1}{\mathcal{S}} \left(i\xi(\mathcal{R} - 2\mathcal{P}\mathcal{Q}) \left(\cos\left(\xi \frac{b}{2}\right) \operatorname{sinc}\left(\xi \frac{a}{2}\right) \right) \right) e^{i\xi x} d\xi = \widehat{\mathrm{u}_x^{S}} \tag{4.45b}$$

Since all terms in (4.45a) are symmetric in ξ about the origin, the inverse transform takes on the simpler form

$$\frac{F_{\mathrm{N}}}{2\rho d\pi v_{\Psi}^2} \int_{0}^{\infty} \frac{1}{\mathcal{S}} \left(\mathcal{P}(2\xi^2 - \mathcal{R}) \left(\cos\left(\xi \frac{b}{2}\right) \operatorname{sinc}\left(\xi \frac{a}{2}\right) \right) \right) \cos(\xi x) \, d\xi = \widehat{\mathrm{u}_z^{S}} \tag{4.46a}$$

On the other hand, all terms in (4.45b) are antisymmetric about the origin and the inversion is given by

$$\frac{F_{\mathrm{N}}}{2\rho d\pi v_{\Psi}^{2}}\int_{0}^{\infty}\frac{1}{\mathcal{S}}\left(i\xi(\mathcal{R}-2\mathcal{P}\mathcal{Q})\left(\cos\left(\xi\frac{b}{2}\right)\mathrm{sinc}\left(\xi\frac{a}{2}\right)\right)\right)\sin(\xi x)\,d\xi = \widehat{\mathrm{u}_{x}^{S}} \tag{4.46b}$$

To find the support loss contribution for this geometry, we seek the displacement averaged over both stress sources, as before. The displacements are

$$\frac{F_{\mathrm{N}}}{2\rho ad\pi v_{\Psi}^{2}}\int_{0}^{\infty}\frac{1}{\mathcal{S}}\left(\mathcal{P}(2\xi^{2}-\mathcal{R})\left(\cos\left(\xi\frac{b}{2}\right)\mathrm{sinc}\left(\xi\frac{a}{2}\right)\right)\right)\left\{\int_{\frac{-(b+a)}{2}}^{\frac{a-b}{2}}\cos(\xi x)dx + \int_{\frac{b-a}{2}}^{\frac{b+a}{2}}\cos(\xi x)dx\right\}d\xi = \overline{\mathrm{u}_{z}^{S}} \tag{4.47a}$$

and

$$\frac{F_{\mathrm{N}}}{2\rho ad\pi v_{\Psi}^{2}}\int_{-\infty}^{\infty}\frac{1}{\mathcal{S}}\left(i\xi(\mathcal{R} - 2\mathcal{P}\mathcal{Q})\left(\cos\left(\xi\frac{b}{2}\right)\mathrm{sinc}\left(\xi\frac{a}{2}\right)\right)\right)\left\{\int_{\frac{-(b+a)}{2}}^{\frac{a-b}{2}}\sin(\xi x)dx + \int_{\frac{b-a}{2}}^{\frac{b+a}{2}}\sin(\xi x)dx\right\}d\xi = \overline{\mathrm{u}_{x}^{S}} \tag{4.47b}$$

Evaluating the integrals in x yields

$$\int_{\frac{-(b+a)}{2}}^{\frac{-b}{2}+\frac{a}{2}} \cos(\xi x)dx$$

$$= \frac{\sin\left(\xi\frac{(a-b)}{2}\right)}{\xi} + \frac{\sin\left(\xi\frac{(a+b)}{2}\right)}{\xi} \qquad (4.48a)$$

$$\int_{\frac{-(b+a)}{2}}^{\frac{-b}{2}+\frac{a}{2}} \sin(\xi x)dx = -\left(\frac{\cos\left(\xi\frac{(a-b)}{2}\right)}{\xi} - \frac{\cos\left(\xi\frac{(a+b)}{2}\right)}{\xi}\right) \qquad (4.48b)$$

Using the two angle formulae to expand and simplify the trigonometric terms, one arrives at the following compact forms for (4.48a) and (4.48b) respectively:

$$\int_{\frac{-(b+a)}{2}}^{\frac{-b}{2}+\frac{a}{2}} \cos(\xi x)\,dx = \frac{2\cos\left(\xi\frac{b}{2}\right)\sin\left(\xi\frac{a}{2}\right)}{\xi} = a\cos\left(\xi\frac{b}{2}\right)\mathrm{sinc}\left(\xi\frac{a}{2}\right) \quad (4.49a)$$

$$\int_{\frac{-(b+a)}{2}}^{\frac{-b}{2}+\frac{a}{2}} \sin(\xi x)dx = -a\left(\frac{\sin\left(\xi\frac{a}{2}\right)\sin\left(\xi\frac{b}{2}\right)}{\xi\frac{a}{2}}\right)$$

$$= a\sin\left(\xi\frac{b}{2}\right)\mathrm{sinc}\left(\xi\frac{a}{2}\right) \qquad (4.49b)$$

Inserting (4.49) into (4.47), we obtain for the average displacement at the support centred at $= -b$;

$$\frac{F_{\mathrm{N}}}{\rho d\pi v_{\Psi}^2}\int_0^{\infty}\frac{\mathcal{P}}{\mathcal{S}}(2\xi^2-\mathcal{R})\cos^2\left(\xi\frac{b}{2}\right)\mathrm{sinc}^2\left(\xi\frac{a}{2}\right)d\xi = \overline{\mathrm{u}_z^s} \qquad (4.50a)$$

and

$$\frac{F_{\mathrm{N}}}{\rho d\pi v_{\Psi}^2}\int_0^{\infty}\frac{\xi}{\mathcal{S}}(\mathcal{R}-2\mathcal{P}\mathcal{Q})\cos\left(\xi\frac{b}{2}\right)\sin\left(\xi\frac{b}{2}\right)\mathrm{sinc}^2\left(\xi\frac{a}{2}\right)d\xi = \overline{\mathrm{u}_x^s} \quad (4.50b)$$

(4.50a) can be arranged into the form

$$\frac{F_{\mathrm{N}}\omega^2}{\rho d\pi v_{\Psi}^4}\int_0^{\infty}\frac{\mathcal{P}}{\mathcal{S}}\cos^2\left(\xi\frac{b}{2}\right)\mathrm{sinc}^2\left(\xi\frac{a}{2}\right)d\xi=\overline{\mathrm{u}_z^s} \tag{4.51}$$

4.2.4.4 Symmetric distribution of two opposite shear stresses

As a final particular case relating to the XBR geometry, the effects of flexure-generated shears parallel to the shear surface on a multiply – supported device are analysed hereafter. The geometric configuration is substantially similar to the previous case of the normal forces:

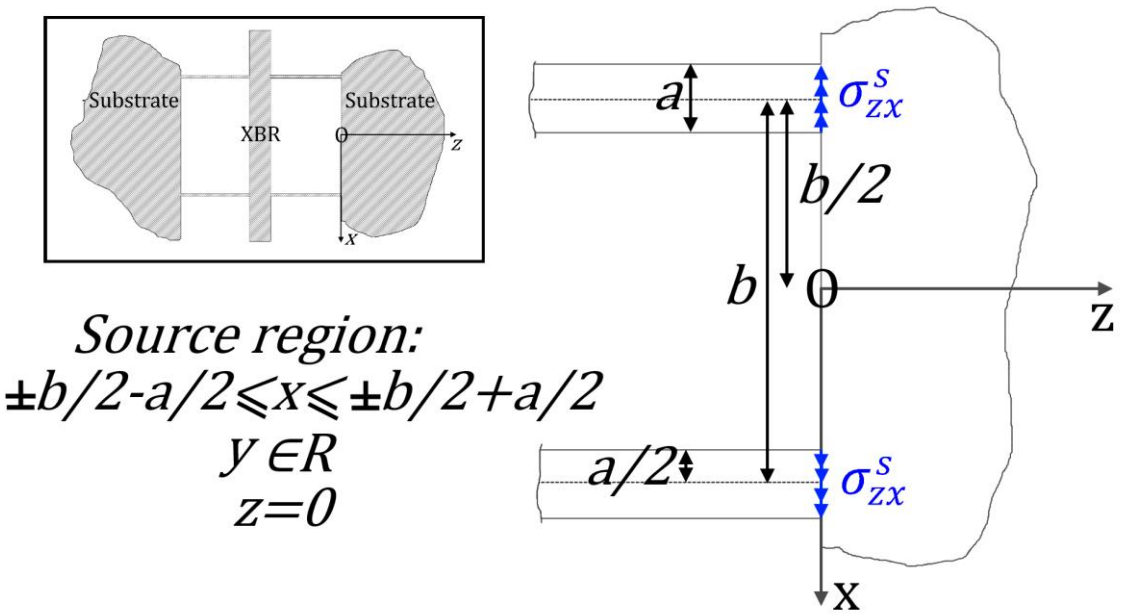

Figure 4.5 Double shear source, illustrating the correspondence to one side of an XBR attached to two planar half-substrates in the inset and the stress distribution in the main image.

The stress at the free boundary for this case has the form

$$\sigma_{zx}^s=\begin{Bmatrix}0, & x<-b-\frac{a}{2}\\ -\frac{F_{\mathrm{T}}}{ad}, & \frac{-b}{2}-\frac{a}{2}\le x\le\frac{-b}{2}+\frac{a}{2}\\ 0, & \frac{-b}{2}+\frac{a}{2}\le x\le\frac{b}{2}-\frac{a}{2}\\ \frac{F_{\mathrm{T}}}{ad}, & \frac{b}{2}-\frac{a}{2}\le x\le\frac{b}{2}+\frac{a}{2}\\ 0, & x>\frac{b}{2}+\frac{a}{2}\end{Bmatrix} \tag{4.52a}$$

$$\sigma_{zz}^{s} = 0 \; \forall x \in \mathbb{R} \tag{4.52b}$$

The Fourier transforms of 4.52 are

$$\widehat{\sigma_{zz}^{s}} = \frac{F_{\mathrm{T}}}{ad} \int_{-\infty}^{\infty} \sigma_{zz}^{s} e^{-i\xi x} dx$$

$$= \frac{-F_{\mathrm{T}}}{adi\xi} \left\{ \left[e^{i\xi\frac{b}{2}} e^{-i\xi\frac{a}{2}} - e^{i\xi\frac{b}{2}} e^{i\xi\frac{a}{2}} \right] + \left[e^{-i\xi\frac{b}{2}} e^{-i\xi\frac{a}{2}} - e^{-i\xi\frac{b}{2}} e^{i\xi\frac{a}{2}} \right] \right\}$$

$$= -\frac{2F_{\mathrm{T}}}{d} \sin\left(\xi\frac{b}{2}\right) \mathrm{sinc}\left(\xi\frac{a}{2}\right) \tag{4.53a}$$

$$\sigma_{zx}^{s} = \widehat{\sigma_{zx}^{s}} = 0 \; \forall x \in \mathbb{R} \tag{4.53b}$$

Since the only nonzero stress present is $\widehat{\sigma_{zx}^{s}}$, the displacement equations (4.23) take on the reduced form

$$\frac{1}{\rho v_{\Psi}^{2}} \frac{1}{\mathcal{S}} \left(i\xi (2\mathcal{P}\mathcal{Q} - \mathcal{R}) \widehat{\sigma_{zx}^{s}} \right) = \widehat{\mathrm{u}_{z}^{s}} \tag{4.54a}$$

$$\frac{1}{\rho v_{\Psi}^{2}} \frac{1}{\mathcal{S}} \left(\mathcal{Q} (2\xi^{2} - \mathcal{R}) \widehat{\sigma_{zx}^{s}} \right) = \widehat{\mathrm{u}_{x}^{s}} \tag{4.54b}$$

Combining (4.53) and (4.54) gives as a closed form representation of the Fourier transformed surface displacements:

$$\frac{-2aF_{\mathrm{T}}}{\rho d v_{\Psi}^{2}} \frac{1}{\mathcal{S}} \left(\xi (2\mathcal{P}\mathcal{Q} - \mathcal{R}) \sin\left(\xi\frac{b}{2}\right) \mathrm{sinc}\left(\xi\frac{a}{2}\right) \right) = \widehat{\mathrm{u}_{z}^{s}} \tag{4.55a}$$

$$\frac{-2aF_{\mathrm{T}}}{\rho d v_{\Psi}^{2}} \frac{1}{\mathcal{S}} \left(\mathcal{Q} (2\xi^{2} - \mathcal{R}) \sin\left(\xi\frac{b}{2}\right) \mathrm{sinc}\left(\xi\frac{a}{2}\right) \right) = \widehat{\mathrm{u}_{x}^{s}} \tag{4.55b}$$

We seek the inverse Fourier transform to find the surface displacements in the spatial domain, as before:

$$\frac{-aF_{\mathrm{T}}}{\rho d \pi v_{\Psi}^{2}} \int_{-\infty}^{\infty} \frac{1}{\mathcal{S}} \left(\xi (2\mathcal{P}\mathcal{Q} - \mathcal{R}) \sin\left(\xi\frac{b}{2}\right) \mathrm{sinc}\left(\xi\frac{a}{2}\right) \right) e^{i\xi x} d\xi = \widehat{\mathrm{u}_{z}^{s}} \tag{4.56a}$$

$$\frac{-aF_{\mathrm{T}}}{\rho d \pi v_{\Psi}^{2}} \int_{-\infty}^{\infty} \frac{1}{\mathcal{S}} \left(\mathcal{Q} (2\xi^{2} - \mathcal{R}) \sin\left(\xi\frac{b}{2}\right) \mathrm{sinc}\left(\xi\frac{a}{2}\right) \right) e^{i\xi x} d\xi = \widehat{\mathrm{u}_{x}^{s}} \tag{4.56b}$$

Since the integrand in (4.56a) is symmetric in ξ about the origin, the Fourier series takes on the simpler form

$$-\frac{2aF_{\mathrm{T}}}{\rho d\pi v_{\Psi}^{2}}\int_{0}^{\infty}\frac{1}{\mathcal{S}}\left(\xi(2\mathcal{P}\mathcal{Q}-\mathcal{R})\sin\left(\xi\frac{b}{2}\right)\mathrm{sinc}\left(\xi\frac{a}{2}\right)\right)\cos(\xi x)\,d\xi = \widehat{\mathrm{u}_{z}^{s}} \qquad (4.57a)$$

On the other hand, the integrand in (4.56b) is antisymmetric about the origin and the Fourier series is given by

$$-\frac{2aF_{\mathrm{T}}}{\rho d\pi v_{\Psi}^{2}}\int_{0}^{\infty}\frac{1}{\mathcal{S}}\left(\mathcal{Q}(2\xi^{2}-\mathcal{R})\sin\left(\xi\frac{b}{2}\right)\mathrm{sinc}\left(\xi\frac{a}{2}\right)\right)\sin(\xi x)\,d\xi = \widehat{\mathrm{u}_{x}^{s}} \qquad (4.57b)$$

To find the support loss contribution for this geometry, we seek the displacement at one stress source due to the effects of both sources. By symmetry, we can take twice this value to represent the overall support loss. Averaging as before over the source width – now not symmetrically positioned with respect to the origin – the displacements are

$$-\frac{2aF_{\mathrm{T}}}{\rho d\pi v_{\Psi}^{2}}\int_{0}^{\infty}\frac{1}{\mathcal{S}}\left(\mathcal{P}(2\xi^{2}-\mathcal{R})\left(\sin\left(\xi\frac{b}{2}\right)\mathrm{sinc}\left(\xi\frac{a}{2}\right)\right)\right)\int_{\frac{-(b+a)}{2}}^{\frac{-b}{2}+\frac{a}{2}}\cos(\xi x)\,dx\,d\xi = \widehat{\mathrm{u}_{z}^{s}} \qquad (4.58a)$$

and

$$-\frac{2aF_{\mathrm{T}}}{\rho d\pi v_{\Psi}^{2}}\int_{-\infty}^{\infty}\frac{1}{\mathcal{S}}\left(i\xi(\mathcal{R}-2\mathcal{P}\mathcal{Q})\left(\sin\left(\xi\frac{b}{2}\right)\mathrm{sinc}\left(\xi\frac{a}{2}\right)\right)\right)\int_{\frac{-(b+a)}{2}}^{\frac{-b}{2}+\frac{a}{2}}\sin(\xi x)\,dx\,d\xi = \widehat{\mathrm{u}_{x}^{s}} \qquad (4.58b)$$

Evaluating the integrals in x yields

$$\int_{\frac{-(b+a)}{2}}^{\frac{-b}{2}+\frac{a}{2}} \cos(\xi x)dx = \frac{\sin\left(\xi\frac{(a-b)}{2}\right)}{\xi} + \frac{\sin\left(\xi\frac{(a+b)}{2}\right)}{\xi} \qquad (4.59a)$$

$$\int_{\frac{-(b+a)}{2}}^{\frac{-b}{2}+\frac{a}{2}} \sin(\xi x)dx = -\left(\frac{\cos\left(\xi\frac{(a-b)}{2}\right)}{\xi} - \frac{\cos\left(\xi\frac{(a+b)}{2}\right)}{\xi}\right) \qquad (4.59b)$$

Using the two angle formulae to expand and simplify the trigonometric terms, one arrives at the following compact forms for (4.59):

$$\int_{\frac{-(b+a)}{2}}^{\frac{-b}{2}+\frac{a}{2}} \cos(\xi x)dx = \frac{2\cos\left(\xi\frac{b}{2}\right)\sin\left(\xi\frac{a}{2}\right)}{\xi} = a\cos\left(\xi\frac{b}{2}\right)\mathrm{sinc}\left(\xi\frac{a}{2}\right) \quad (4.60a)$$

$$\int_{\frac{-(b+a)}{2}}^{\frac{-b}{2}+\frac{a}{2}} \sin(\xi x)dx = -\left(\frac{2\sin\left(\xi\frac{a}{2}\right)\sin\left(\xi\frac{b}{2}\right)}{\xi}\right)$$

$$= -a\sin\left(\xi\frac{b}{2}\right)\mathrm{sinc}\left(\xi\frac{a}{2}\right) \qquad (4.60b)$$

Inserting these expressions into the displacement equations at the free surface, we obtain for the average displacement at the support centred at $= -b$;

$$\frac{aF_{\mathrm{N}}}{\rho d\pi v_{\Psi}^2}\int_0^{\infty} \frac{\mathcal{P}(2\xi^2-\mathcal{R})\sin^2\left(\xi\frac{b}{2}\right)\mathrm{sinc}^2\left(\xi\frac{a}{2}\right)}{\mathcal{S}}d\xi = \widehat{\mathrm{u}_z^s} \quad (4.61a)$$

and

$$\frac{aF_{\mathrm{N}}}{\rho d\pi v_{\Psi}^2}\int_0^{\infty} \frac{i\xi(\mathcal{R}-2\mathcal{P}\mathcal{Q})\sin^2\left(\xi\frac{b}{2}\right)\mathrm{sinc}^2\left(\xi\frac{a}{2}\right)}{\mathcal{S}}d\xi = \widehat{\mathrm{u}_x^s} \qquad (4.61b)$$

4.2.5 Numerical solution

The integral form representations (4.31), (4.39), (4.50), and (4.61) contain all of the information about the corresponding solutions for the halfplane, including displacements, stresses, etc. However, to perform explicit evaluation in an analytical

form is very difficult. To obtain useful information from the integrals, this subsection gives some detail about how the expressions are evaluated.

4.2.5.1 Nondimensional form of equations

The integral representations found thus far and expressed by (4.31), (4.39), (4.50), and (4.61) can be evaluated directly. However, for the purposes of numerical computation – and also to gain analytical insight - it is expedient to utilise a natural length scale to nondimensionalise the problem. An appropriate scale is provided by the transverse wavelength. We consider explicitly the simple case of the z-displacement incurred by a single normal force; the other particular cases follow a similar pattern, with the numerator being the only change.

Starting from Equation (4.31), we have

$$\mathrm{u}_z^S(x) = \frac{F_\mathrm{N}}{\rho d \pi v_\Psi^2} \int_0^\infty \frac{\mathcal{P}}{\mathcal{S}} (2\xi^2 - \mathcal{R}) \mathrm{sinc}\left(\frac{\xi a}{2}\right) \cos(\xi x)\, d\xi$$

To nondimensionalise the integral we make a change of variable according to

$$\xi = \zeta \frac{\omega}{v_\varphi} = \zeta k_\varphi \tag{4.62}$$

where k_φ is the longitudinal wave number.(4.31) is recast in nondimensional form as

$$\mathrm{u}_z^S(x) = \frac{2aF_\mathrm{N}\omega^2}{\rho d \pi v_\Psi^4} \times$$

$$\int_0^\infty \frac{\mathrm{sinc}\left(\frac{\zeta\omega}{2v_\varphi} a\right) \cos\left(\frac{\zeta\omega}{v_\varphi} x\right) \sqrt{\left(\zeta \frac{\omega}{v_\varphi}\right)^2 - \omega^2/v_\varphi^2}}{\left(2\left(\zeta \frac{\omega}{v_\varphi}\right)^2 - \omega^2/v_\Psi^2\right)^2 - 4\left(\zeta \frac{\omega}{v_\varphi}\right)^2 \sqrt{\left(\zeta \frac{\omega}{v_\varphi}\right)^2 - \omega^2/v_\varphi^2} \sqrt{\left(\zeta \frac{\omega}{v_\varphi}\right)^2 - \omega^2/v_\psi^2}} d\zeta \tag{4.63}$$

Simplifying yields

$$\overline{\mathrm{u}_z^s} = \frac{2aF_{\mathrm{N}}\beta^2}{\rho d\pi v_\Psi^2}\int_0^\infty \frac{\sqrt{\zeta^2-1}}{(2\zeta^2-\beta^2)^2 - 4\zeta^2\sqrt{\zeta^2-1}\sqrt{\zeta^2-\beta^2}}\,d\zeta$$

$$= \frac{2aF_{\mathrm{N}}\beta^2}{\rho d\pi v_\Psi^2}\int_0^\infty \frac{\mathcal{P}_1(\zeta)}{\mathcal{S}_1(\zeta)}\,d\zeta \qquad (4.64)$$

The integrand depends only on the wave speed ratio. For classical materials with a Poisson's ratio $0 < \nu < 0.5$, this takes values in the range $\sqrt{2} < \beta < 2$. This property makes numerical evaluation of the integral far more straightforward.

4.2.5.2 Evaluation

To evaluate the integral in such a manner as to correctly account for support loss, one must employ only those components of the general solution corresponding to waves propagating away from the source. The general solution contains components propagating towards and away from the source, in accord with d'Alembert's solution. Account must also be made of the Riemann surface structure of the integrand, as well as any points of discontinuity and singular points.

This can be undertaken in a fashion general to all the integrals considered in this chapter. The numerator of (4.64) is in all cases considered a smooth, bounded function of ξ. In all cases, the numerator is of order $O(\xi)$ as $\xi \to \infty$. The denominator, on the other hand, exhibits more complex behaviour. Expanding the definition, we have

$$\mathcal{S}(\xi) = (2\xi^2 - \omega^2/v_\Psi^2)^2 - 4\xi^2\sqrt{\xi^2-\omega^2/v_\varphi^2}\sqrt{\xi^2-\omega^2/v_\Psi^2} \qquad (4.65)$$

Taking the positive square root under all radicals to consider the case of waves propagating away from the source, and noting that $v_\varphi > v_\Psi$ it is seen that for $|\xi| < \frac{\omega}{v_\varphi}$ both the radicals are positive imaginary. Denote $\sqrt{\xi^2-\omega^2/v_\varphi^2} = i|\mathcal{P}|$ and $\sqrt{\xi^2-\omega^2/v_\Psi^2} = i|\mathcal{Q}|$ where it is understood that $|\mathcal{P}|$ and $|\mathcal{Q}|$ are real magnitudes. Furthermore, the first term is the square of the difference between two

real quantities, and hence it is always positive real. Denote its value by $|\mathcal{R}^2|$. Then the equation (4.65) can be written in the form

$$\mathcal{S}(\xi) = |\mathcal{R}^2| + 4\xi^2|\mathcal{P}||\mathcal{Q}| \tag{4.66}$$

It is clear that in this region, the fraction $\frac{1}{\mathcal{S}}$ is smooth, bounded and real valued. Consider next the region $\frac{\omega}{v_\varphi} < |\xi| < \frac{\omega}{v_\Psi}$. The argument proceeds as above, except for the fact that $\mathcal{P}$ is now real. Then $\sqrt{\xi^2 - \omega^2/v_\varphi^2} = |\mathcal{P}|$; (4.65) can be written

$$\mathcal{S}(\xi) = |\mathcal{R}^2| - 4i\xi^2|\mathcal{P}||\mathcal{Q}| \tag{4.67}$$

and it is shown that in this region, the denominator is complex valued. Finally, to complete the discussion, when $|\xi| > \frac{\omega}{v_\Psi}$, both the quantities $\mathcal{P}$ and $\mathcal{Q}$ are real, and $\mathcal{S}(\xi)$ has the form $|\mathcal{R}^2| - 4\xi^2|\mathcal{P}||\mathcal{Q}|$ and is again real. In this region, there exists a point where the terms cancel, since

$$|\mathcal{R}^2| = 4i\xi^2|\mathcal{P}||\mathcal{Q}| \tag{4.68}$$

At this (real) value, denoted p, $\mathcal{S}$ is zero and all the displacement integrals have a pole. To see the behaviour of the function in detail, consider the analytical continuation to the whole complex plane (punctured twice by the aforementioned poles).

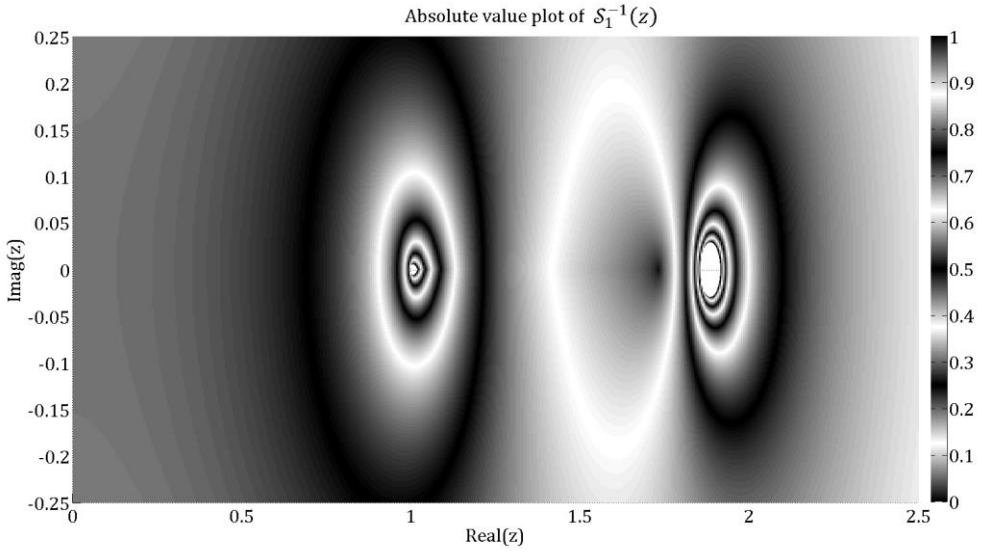

Figure 4.6 Absolute value of $\mathcal{S}_1^{-1}(z)$ for $0 < \text{Real}(z) < 2.5, -0.25 < \text{imag}(z) < 0.25$.

The three singular points of the function are clearly visible on the real axis at $\text{Real}(z) = \{1, r, p\}$. The white region around the pole corresponds to $|\mathcal{S}_1^{-1}(z)| > 1$.

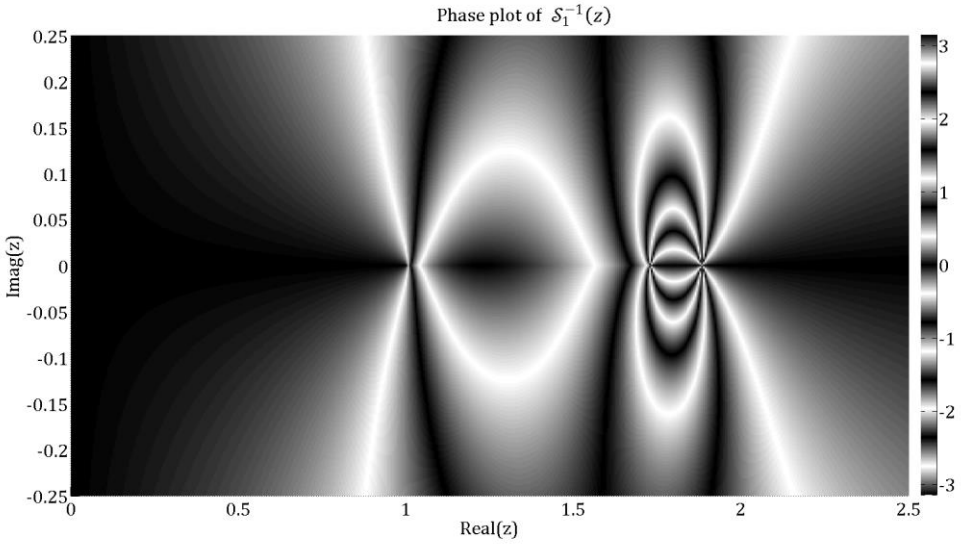

Figure 4.7 Phase of $\mathcal{S}_1^{-1}(z)$ for $0 < \text{Real}(z) < 2.5, -0.25 < \text{imag}(z) < 0.25$. The phase is 0 for $0 < \text{Real}(z) < 1$ and π for $\text{Real}(z) > p$ on the real axis ($\text{imag}(z) = 0$); between r1 $< \text{Real}(z) < r$ on the real axis, the phase can be seen to vary continuously.

The complex plots in Figures 4.6 and 4.7 illustrate the qualities of $\mathcal{S}$ as ζ varies in the region of interest. For the purposes of this work, the interest lies in integrals of the form

$$\int_0^\infty \frac{F_i(\zeta)}{\mathcal{S}_1(\zeta)} d\zeta \tag{4.69}$$

where F_i is a piecewise smooth bounded function on $0 < \zeta < \infty$ of $O(\mathcal{S}_1)$ as $\zeta \to \infty$ depending on the boundary conditions, and the points of discontinuity correspond to $\text{Real}(\zeta) = \{1, r, p\}; \text{imag}(\zeta) = 0$. The integral is to be taken along the real axis. However, the presence of singular points at the aforementioned discontinuities must be accounted for. To achieve the desired modification, the contour can be deformed in a clockwise sense around the singularity, so that (4.69) becomes

$$\mathrm{u}_i^S = I_1 + I_2 + I_3 + I_4 + I_5 + I_6 + I_7$$
$$= \int_0^{1-\delta} \frac{F_i(\xi)}{\mathcal{S}(\xi)} d\xi + \int_{C1} \frac{F_i(\xi)}{\mathcal{S}(\xi)} + \int_{1+\delta}^{r-\delta} \frac{F_i(\xi)}{\mathcal{S}(\xi)} + \int_{C2} \frac{F_i(\xi)}{\mathcal{S}(\xi)} d\xi$$
$$+ \int_{r+\delta}^{p-\delta} \frac{F_i(\xi)}{\mathcal{S}(\xi)} + \int_{C3} \frac{F_i(\xi)}{\mathcal{S}(\xi)} + \int_{p+\delta}^{\infty} \frac{F_i(\xi)}{\mathcal{S}(\xi)} \qquad (4.70)$$

Where δ is a small quantity and the contours $C1, C2, C3$ are taken to be a piecewise continuous curve such as to pass around the corresponding singular point in a clockwise sense with a winding number of zero. Without any important loss of generality, the form $C = \mathrm{tri}\left(\frac{\xi - p}{\delta}\right)$ is convenient and will be employed for the computational purposes of the following sections.

Since the singular points at $\mathrm{Real}(\zeta) = \{1, r\}; \mathrm{imag}(\zeta) = 0$ are branch points, the contributions of the corresponding contours tend to zero as $\delta \to 0$; therefore (4.70) can be simplified to

$$\mathrm{u}_i^S = I_1 + I_3 + I_5 + I_6 + I_7 \qquad (4.71)$$

I_6 in (4.71) has a limit as $\delta \to 0$. By Cauchy's Principal Value Theorem, it makes a contribution of the form $i\pi \times \mathrm{Res}(p)$, where $\mathrm{Res}(p)$ signifies the residue at p. The procedure is illustrated graphically in Figure 4.8.

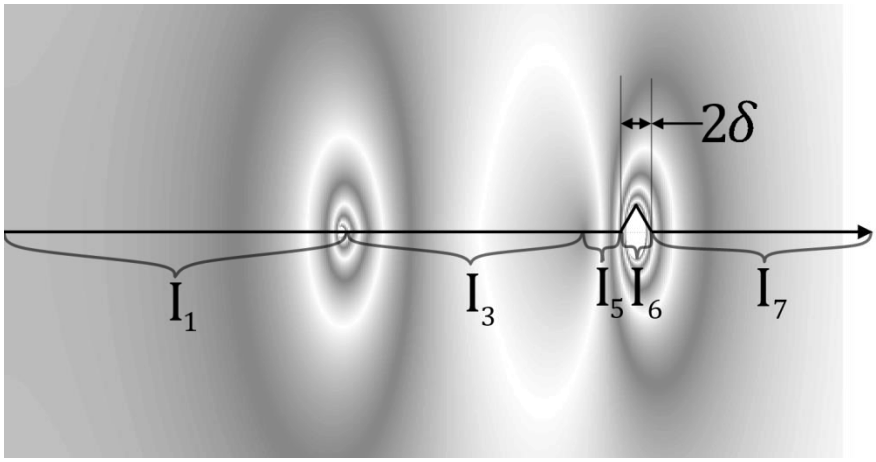

Figure 4.8 Contour of integration and five integral components superposed on magnitude plot of $\mathcal{S}_1^{-1}(z)$. The fifth integral I_7 extends to infinity.

4.2.5.3 Energy Transfer

The models and solutions expressed thus far provide predictions for the complex valued surface displacements incurred; however, the quantity of interest is in fact the energy transferred from the idealised source to the substrate, and these quantities must be related. From fundamental physical principles of classical mechanics, the rate of energy transfer P can be expressed as

$$\mathrm{P} = \int_{\mathrm{SRC}} \mathbf{F}.\mathbf{v}\,\mathrm{dx} = \mathrm{i}\omega|\mathbf{F}|\bar{\boldsymbol{u}} \tag{4.72}$$

Where the quantities $|\mathbf{F}|$ and $\bar{\boldsymbol{u}}$ are matrices indexed by the stress contributions and the integral is taken over the source region. For a source composed of a superposed uniform normal and transverse force, the explicit form of (4.72) is

$$\mathrm{P} = \mathrm{i}\omega \begin{bmatrix} \overline{\mathbf{u}_z^{sn}} & \mathbf{u}_x^{sn} \\ \mathbf{u}_z^{ss} & \overline{\mathbf{u}_x^{ss}} \end{bmatrix} \begin{bmatrix} |\mathrm{F}_N| \\ |\mathrm{F}_T| \end{bmatrix} \tag{4.73}$$

The quantity P thus defined is complex valued. Taking the total energy transfer to be equal to the time integral of P, it can be concluded that an oscillatory contribution arising from the imaginary part of P and a time-linear contribution arising from the real part of P are generated. These correspond to the conservative energy exchange between the resonator and the substrate generated by modal behaviour in the substrate and energy flux generated by the excitation of propagating waves respectively. It is the latter that is of interest. If the behaviour of the substrate were to be lumped as a port receptance boundary condition on the resonator supports then the oscillatory contribution would appear as a large, finite, real stiffness, while the linear contribution would be an imaginary part of the stiffness, leading to a loss angle and energetic decay of the resonator motion. The imaginary and real components of $\bar{\boldsymbol{u}}$ contribute to the real and imaginary component of P respectively, regardless of the relative phase of the forces.

By this argument, we can separate the elastic and “dissipative” effects of the substrate on the resonator by considering the real and imaginary components of the surface displacements, averaged over the source region.

4.3 Finite Element Approach

4.3.1 Problem formulation

To provide an independent validation of the analytical work from Section 4.2, the Finite Element code COMSOL Multiphysics was employed to model the system. The general thrust of this computational approach is to treat the substrate as a finite elastic body, with the boundaries distal to the free surface terminated with a Perfectly Matched Layer (PML). This approach numerically closes the problem without introducing spurious reflection. This is an aspect of the assumption that all energy leaving the source propagates without reflection.

4.3.2 Physical constitutive relationships

The bulk domain is modelled as a linear elastic isotropic 2 dimensional half space, in concordance with the assumptions of the analytical model. The constitutive relationship solved for can be written as

$$\rho\omega^2\mathbf{u} - \nabla.\sigma = Fe^{i\varphi} \tag{4.74}$$

$$\sigma - \sigma_0 = \mathbf{C}\colon(\varepsilon - \varepsilon_0 - \varepsilon_i) \tag{4.75}$$

$$\varepsilon = \frac{1}{2}(\nabla\mathbf{u} + (\nabla\mathbf{u})^{\mathrm{T}}) \tag{4.76}$$

Where ρ is the material density, ω is the excitation frequency, $\mathbf{u}$ is the displacement vector, ∇ is the divergence operator in two dimensions, σ is the stress tensor, F is the applied harmonic body force with phase φ, σ_0 is the initial stress, $\mathbf{C}$ the elastic compliance tensor, ε the deviatoric strain, ε_0 the initial strain, and ε_i the inelastic strain. That is to say, a harmonic analysis at frequency ω was undertaken; all boundary loads are harmonic at this frequency, and phases can freely vary throughout the domain.

To model the physical problem exactly is impossible given finite computational resources, since the domain must be unbounded to allow waves to propagate without

reflection. To surmount this difficulty, the approach suggested by Berenger [20]and termed Perfectly Matched Layers (PML) is adopted, wherein the material properties are made complex-valued in the PML region. The dissipative contribution is introduced adiabatically, minimising reflection.

This approach allows for the simulation of wave propagation in unbounded media, such as is required for the present study. The PML was constructed under the assumption of radial propagation away from the origin, with the matching wavelength tuned to the bulk transverse wavelength. Since an important contribution to the energy loss will be shown to be Rayleigh surface waves, which are known to propagate at wavelengths close to but slightly greater than the bulk shear wavelength, and given that the method is robust to moderate mistuning, this choice is apposite.

4.3.3 Geometry

The geometric configuration employed for comparison is outlined in Figure 4.9.

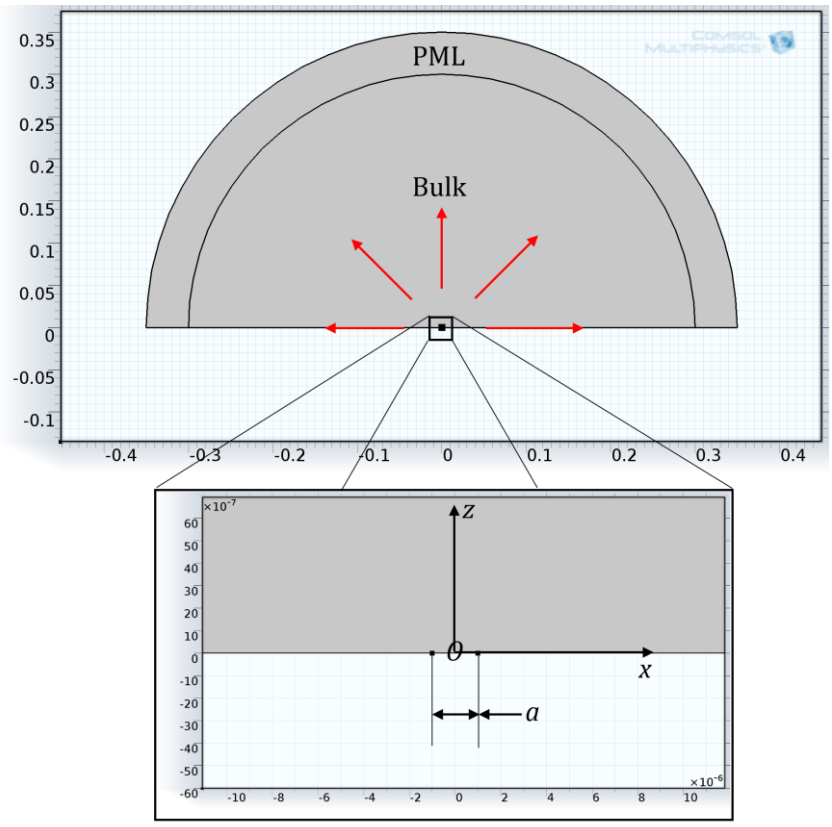

Figure 4.9 Geometry used in COMSOL FE simulation of the substrate. The elastic constitutive relations and material properties from Equations (4.74)-(4.76) and Table 4.1 respectively are applied in the domain labelled Bulk; the domain labelled PML is a perfectly matched layer to close the problem numerically [20].

4.4 Results and discussion

In this section, some results of the COMSOL and MATLAB models developed above are examined. The simplest case of a uniform normal stress is examined in detail, and close agreement is found between the two independent modeling routes. Next, a few select solutions for the more complex cases are presented to demonstrate the validity of the model extension. Finally, the validated models are amalgamated into a series of general formulations appropriate to the analysis of support loss in XBRs under various different scenarios. The solutions obtained in Chapter 3 for the forces of constraint under different parameter choices for the XBR are used as inputs to the general model; the results are presented and discussed from the perspective of XBR function and Q optimization.

4.4.1 Single stress source

The case of a single stress source as modelled herein can be viewed as the Kirchhoff diffraction assumption applied to single-slit, finite width elastic wave diffraction. The source is correspondingly composed of a superposition of contributions from uniform normal and uniform shear sources, and is perhaps the simplest case of practical interest for fairly general supported resonator geometries. Modelling a multiply-supported resonator using this approximation is equivalent to assuming independence of energy loss contributions from the supports. It constitutes an apposite test bed for the modelling, capable of demonstrating the analytical approach without introducing unnecessary complexity. It also allows the reader to develop some intuition and feel for the behaviour of the substrate in response to changes in the model parameters. Intuitively, the halfspace response to a harmonic stress distributed over a finite width a would be expected to constitute, in general, two bulk waves and one surface wave carrying energy away from the source. These phenomena will be explored and quantified in this subsection.

The analytical model is solved for constant material and geometric parameters, given in Table 4.1, for various frequencies, and the results compared to the COMSOL Finite Element simulation. The displacements at the free interface in the x and z direcetions are respectively given by Equations (4.28) and (4.38). Numerical evaluation of the

integrals by the techniques discussed in Section 4.2.5 for differing values of x allows one to map out the free surface displacement predictions for this case. Similarly, evaluating the nodal surface displacements arising from the COMSOL model allows a corresponding prediction to be drawn from the FE model. The displacements are complex-valued functions of x; the absolute values, as well as the real and imaginary components, are employed for the comparison and validation of the models. Subsequently, the validated analytical model is used to explore the relationships between the model parameters and the predicted response, and the results are interpreted in the context of support loss and resonator design.

As an introductory case, the models are compared at a fixed frequency $f = 10^4\ Hz$. This frequency is of the order of magnitude of the natural frequency of the macroscopic XBR prototypes presented in Chapter 6, and hence is of direct interest. First, real and imaginary displacement vector fields obtained by Finite Element analysis are displayed as a concrete visual representation of the solutions, followed by comparison of the free surface displacements predicted by the models.

Model Parameters

Parameter	Models	Value	Symbol
Poisson's Ratio		0.3	ν
Young's Modulus		200×10^9 Pa	E
Mass Density		7.85×10^3 kg m^{-3}	ρ
Transverse Force		1 N	F_{T}
Normal Force		1 N	F_{N}
Source Width		1×10^{-4} m	a
Source Separation		2×10^{-3} m	b

Table 4.1 Parameters used in evaluating the numerical models, except where explicitly stated otherwise.

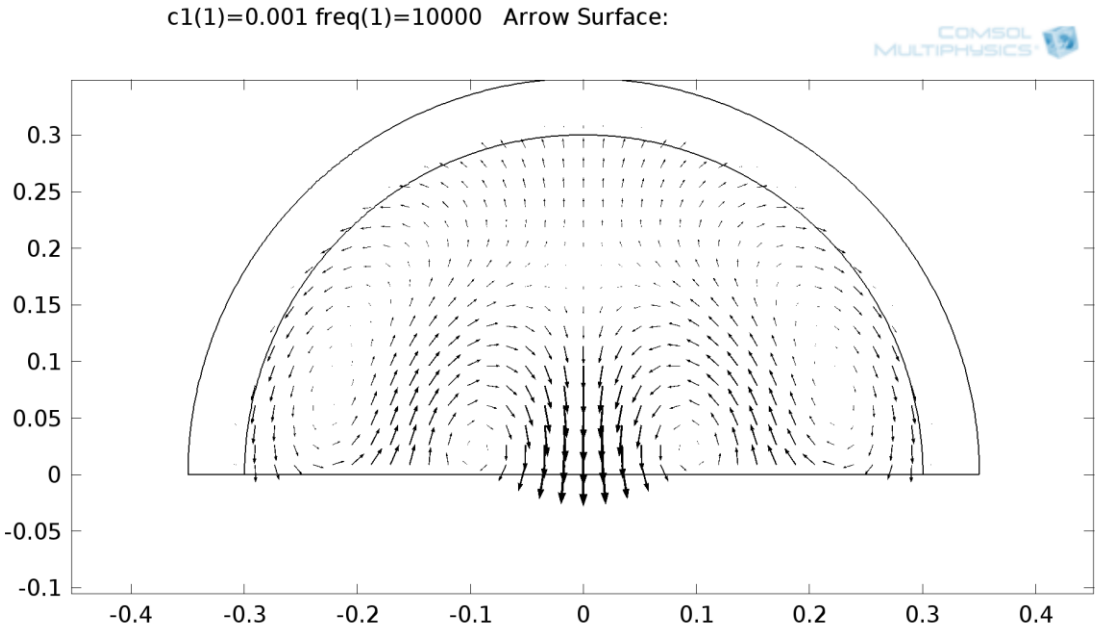

Figure 4.10 Real component of displacement vector field, from COMSOL simulation.

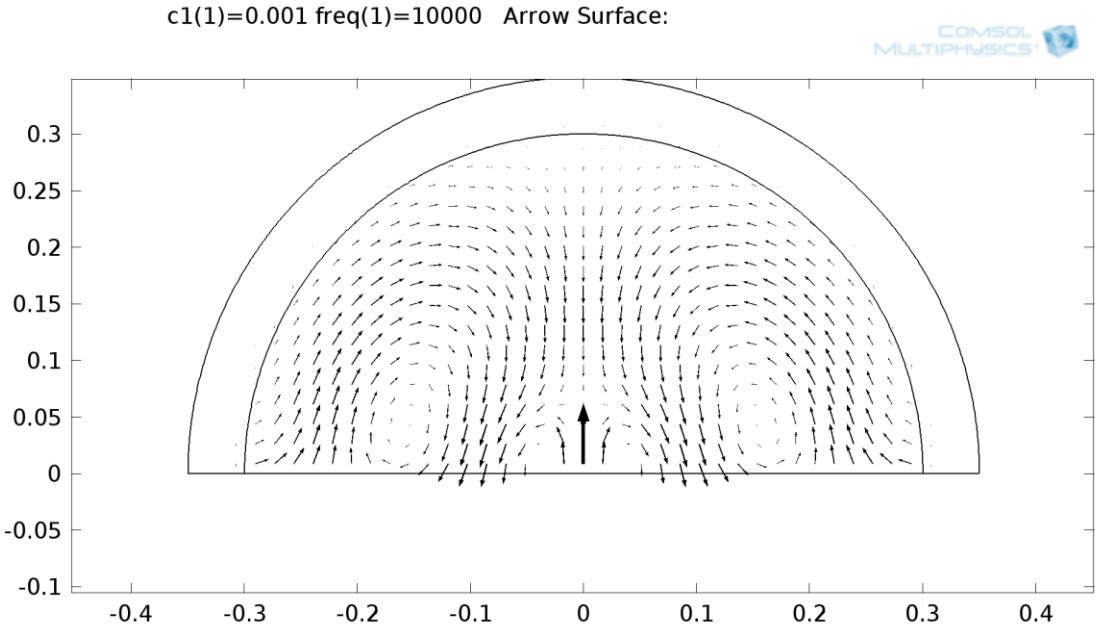

Figure 4.11 Imaginary component of displacement vector field, from COMSOL simulation.

It can be observed in Figures 4.10 and 4.11 that, for both the real and imaginary fields, the z components are symmetric and the x components antisymmetric about the z axis. At the origin, both real and imaginary displacements are zero in x and nonzero in z. Comparing the vector displacement fields generated by the analytical and COMSOL models over the computational domain as exhibited above would be one possible

means of cross-validating the models. However, visual analysis of results presented in this form contains more information than is necessary for validation. Furthermore, the potentials generated in the bulk material are expressed by (4.12) as simple exponents of the surface potentials; validation of the surface potentials thus provides validation of the bulk solutions.

On this basis attention is henceforth restricted to the evaluation and comparison of displacements at the free surface of the domain.

4.4.2 Free surface displacements

The models are evaluated for the corresponding surface displacements in a region of the origin $-0.3 < x < 0.3$ for $f = 10^4$ Hz. The absolute values predicted by the COMSOL and MATLAB models are examined first, followed by a comparison of the real and imaginary components thereof.

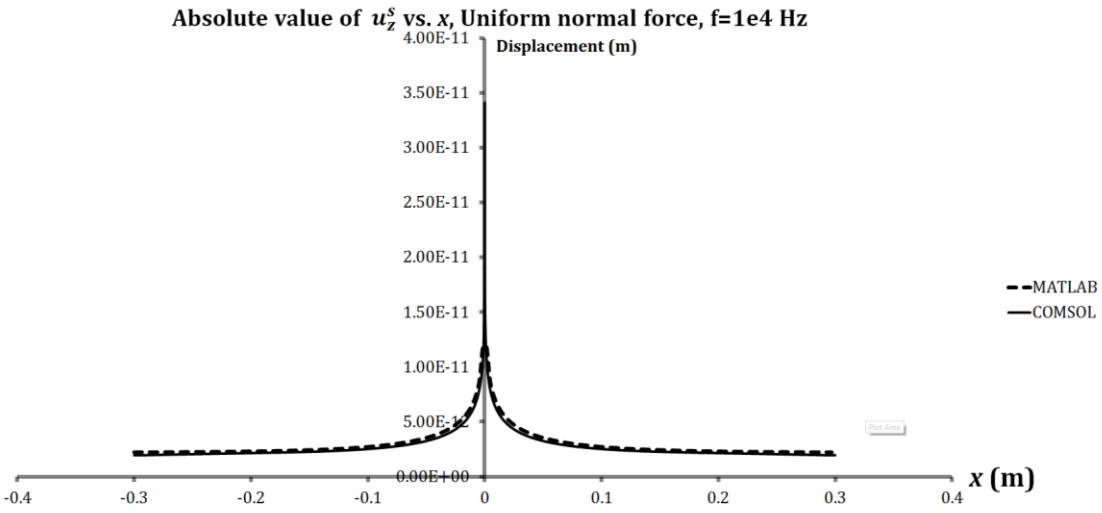

Figure 4.12 Absolute magnitude of the transverse displacement u_z^s at the free interface incurred by an applied normal force.

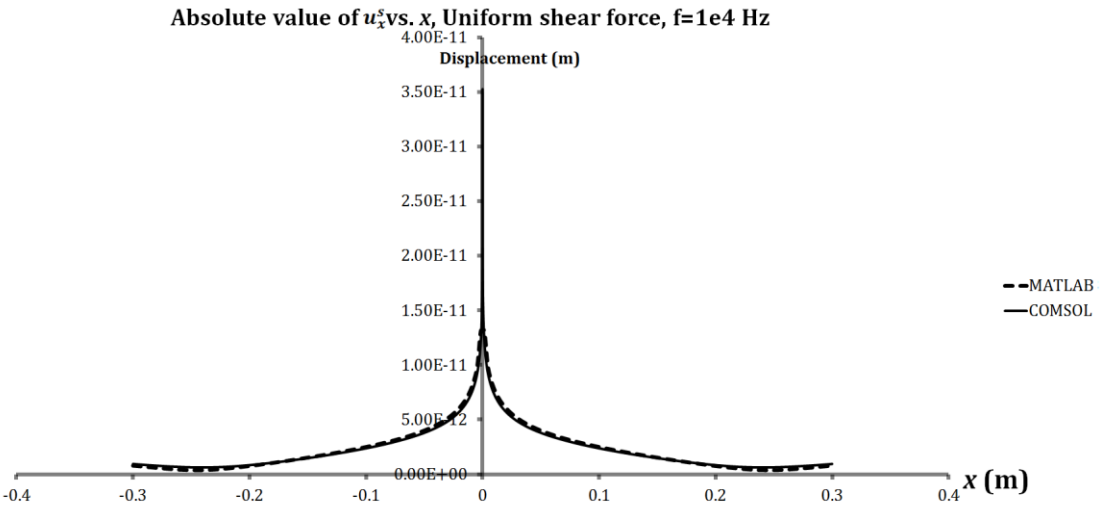

Figure 4.13 Absolute value of $\boldsymbol{u_x^s}$ plotted against x, as predicted by the COMSOL and MATLAB models.

Figures 4.12 and 4.13 show superb agreement at this frequency between the MATLAB model and the COMSOL model, for the corresponding displacements incurred by a normal force and a shear force respectively. Discrepancies are less than 5 per cent everywhere, except in a small vicinity of the origin, where the MATLAB model predicts a lower peak value. To obtain more information about the structure of the solutions, we consider the real and imaginary components of displacement independently for the same parameters.

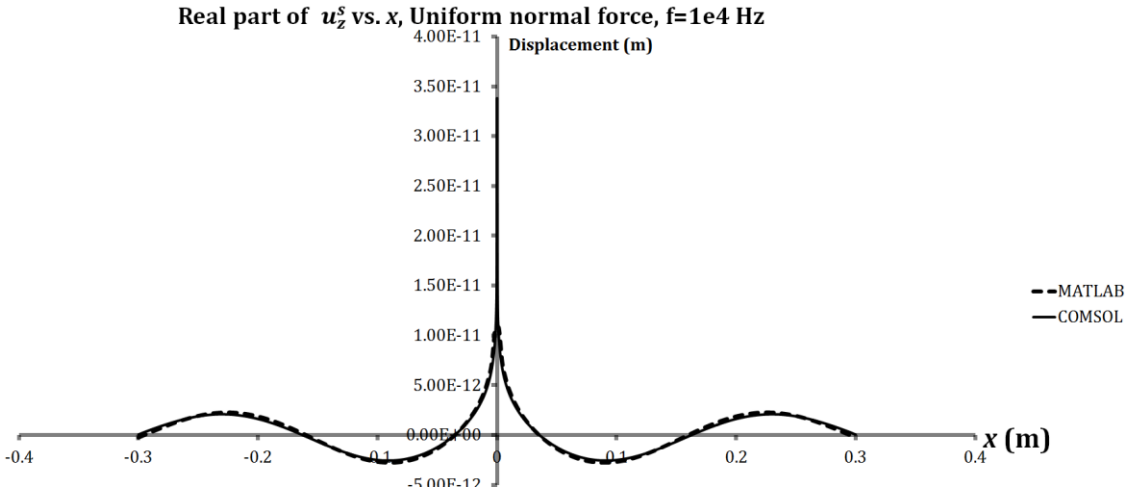

Figure 4.14 Real component of $\boldsymbol{u_z^s}$ incurred by a symmetric single normal force.

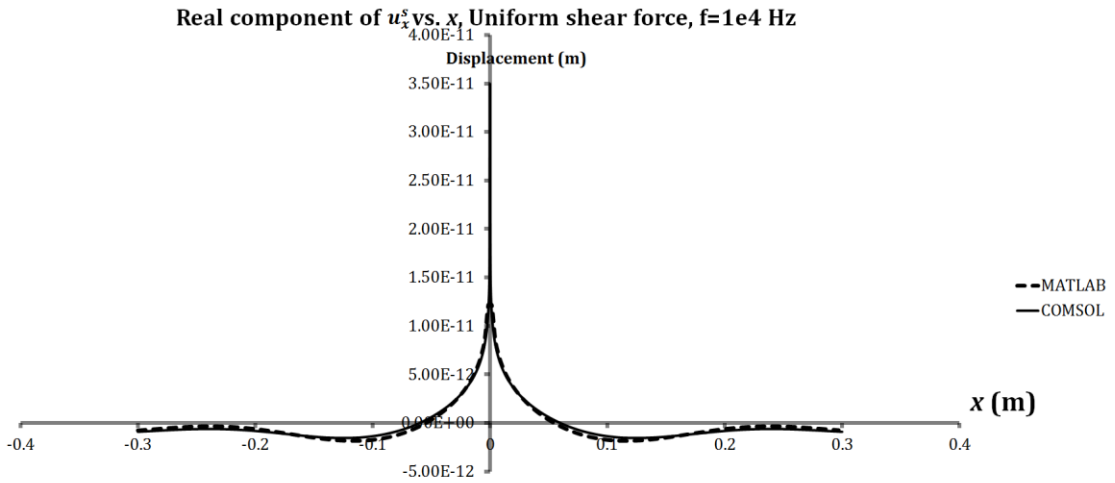

Figure 4.15 Real component of $\boldsymbol{u_x^s}$ incurred by a symmetric single shear force.

The real components of the corresponding surface displacements are displayed in Figures 4.14 and 4.15 for the cases of a normal and transverse uniform force respectively. The close agreement seen in the absolute magnitude plots is replicated. Both cases also have the form of a localised peak around the stress source and a sinusoid away from it.

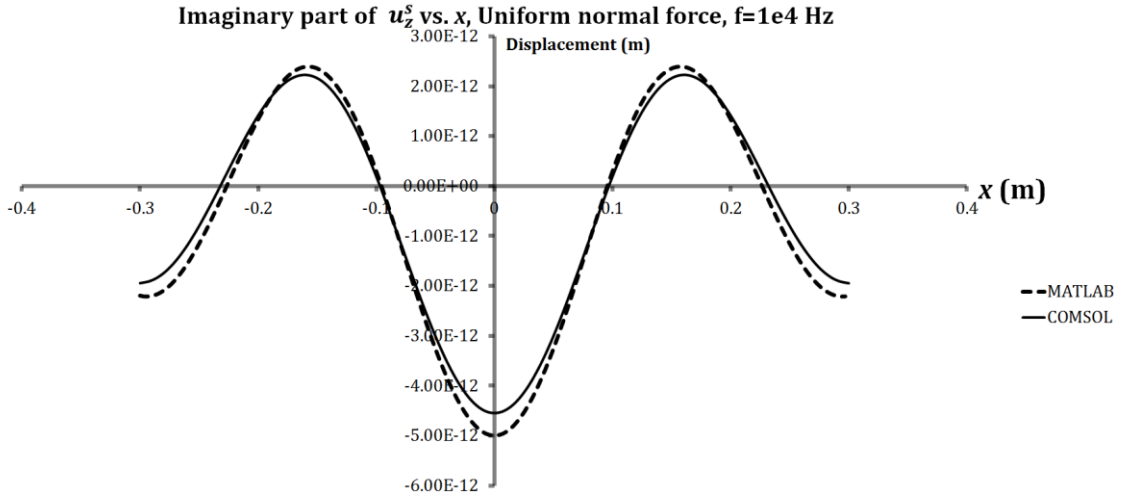

Figure 4.16 Imaginary component of $\boldsymbol{u_z^s}$incurred by a symmetric single normal force.

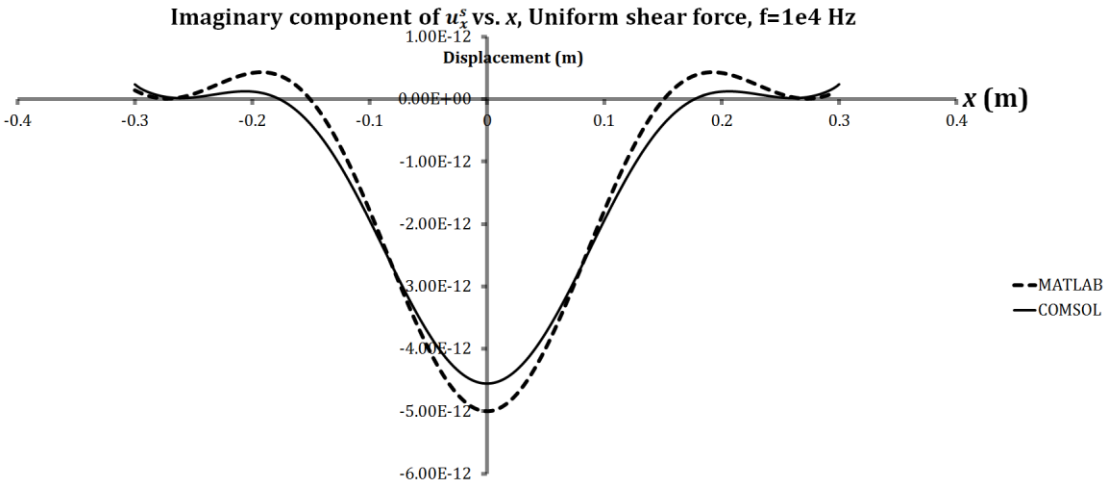

Figure 4.17 Imaginary component of $\boldsymbol{u_x^s}$ incurred by a symmetric single normal force.

Again, good agreement is seen between the models in Figures 4.16 and 4.17, with complete concordance in the qualitative trends and close quantitative agreement. Given the mathematical independence of the approaches and the agreement in the magnitude and phase behaviour exhibited, it can be concluded that at the frequency considered, both models are valid predictors of the complex displacement behaviour of the substrate for the corresponding displacements.

Since the Fourier transform of the stress distribution is identical for the cases of transverse and normal force, and given the similar forms of the equations for the vector and scalar potentials relating to shear and transverse bulk waves respectively, a degree of similitude may be expected between the forms of the solutions, and is observed in comparing (4.14)-(4.15) to (4.16)-(4.17). The most visually striking feature of both solutions is a sharp localised peak in the real (but not imaginary) components of the corresponding displacements in the vicinity of the origin, i.e. at the source region where nonzero stress is applied. The pure real nature of this feature implies its association with elastic, conservative energy storage, and not with propagating waves and net energy transfer over a harmonic cycle, by the implications of Section 4.2.5.

The absolute displacement in both models appears to trend towards an asymptotic, constant value outside of a neighbourhood of the origin. Examining the real and imaginary components, the constant amplitude appears to be constituted as a sinusoidal real part superposed on a cosinusoidal imaginary part. Including the harmonic time factor, the v displacement appears to have the form

$$\begin{Bmatrix} e^{i(\omega t-\frac{x}{2\pi\lambda})}, x>0 \\ e^{i(\omega t+\frac{x}{2\pi\lambda})}, x<0 \end{Bmatrix} \tag{4.77}$$

That is to say, it consists of constant amplitude sinusoidal waves propagating away from the source region. Energy considerations suggest that this must be a surface wave, since in two dimensions a free surface wave propagates without attenuation while bulk waves attenuate as $1/r$, where $r=\sqrt{x^2+z^2}$, due to partitioning of the constant energy flux over a wavefront length increasing linearly with distance from the source.

Closer to the source, the solution has the form of a sharp peak superposed on the surface wave. The peak is pure real; the imaginary component can be seen in Figure 4.16 to be smooth near the origin; in particular its gradient is 0 at the origin, whereas the first derivative of the real component is discontinuous there.

It was shown in Section 4.2.5 that the real component of the surface displacement at the source is associated with conservative elastic energy exchange between the resonator and the substrate, while the imaginary component is associated with excitation of propagating waves and resultant energy transfer. In light of these facts, the localised real peak can be associated with the small but nonzero compliance of the physical boundary conditions for the XBR resonator problem; it is not associated with energy transfer and wave propagation, and is therefore of secondary interest, from a support loss perspective. On the other hand, the presumed surface wave makes a substantial contribution to the imaginary component of displacement, corresponding to the viscous component of the same boundary conditions. To clarify these phenomena, we attempt to identify the origins of the localised peaks and the travelling wave in terms of the integral decomposition.

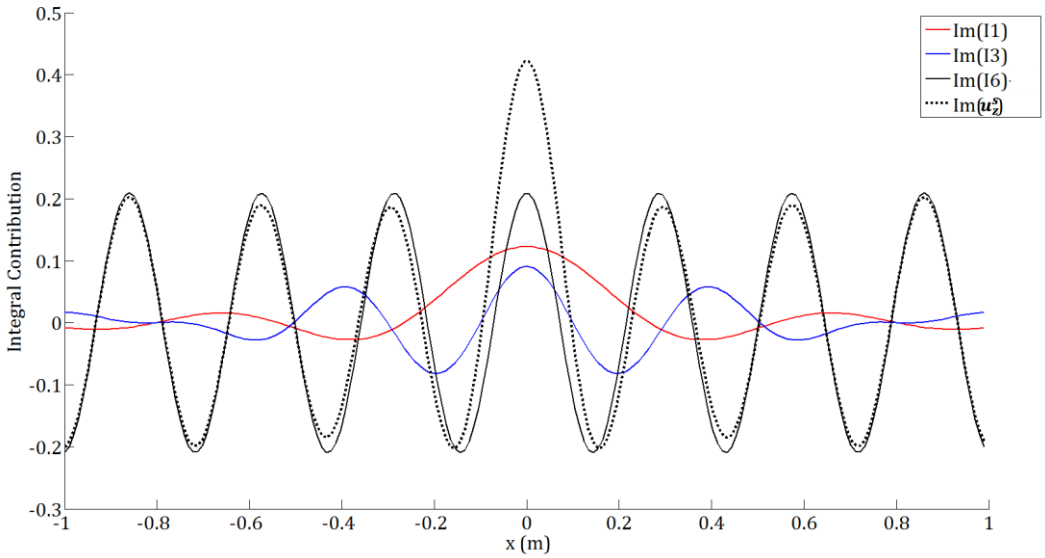

Figure 4.18 Imaginary contributions to displacement $\boldsymbol{u}_z^s$ arising from the integral components as defined in Section 4.2.5. All other integral components are negligible.

Three of the integrals contribute to the imaginary part of the displacement, as can be seen in while only two contribute to the real part of the displacement, as illustrated in Figures 4.18 and 4.19. The components corresponding to I_1 and I_3 decay rapidly with increasing x, while the contribution from I_6 is a sinusoid of constant amplitude in x. The contributions represent propagating bulk transverse waves, bulk shear waves, and Rayleigh waves, respectively. At the source, the total contribution from bulk and shear waves is very close to being equal to the Rayleigh component. This implies that energy is partitioned roughly equally between bulk and Rayleigh surface waves, with transverse waves being slightly the larger of the bulk wave components for the case considered.

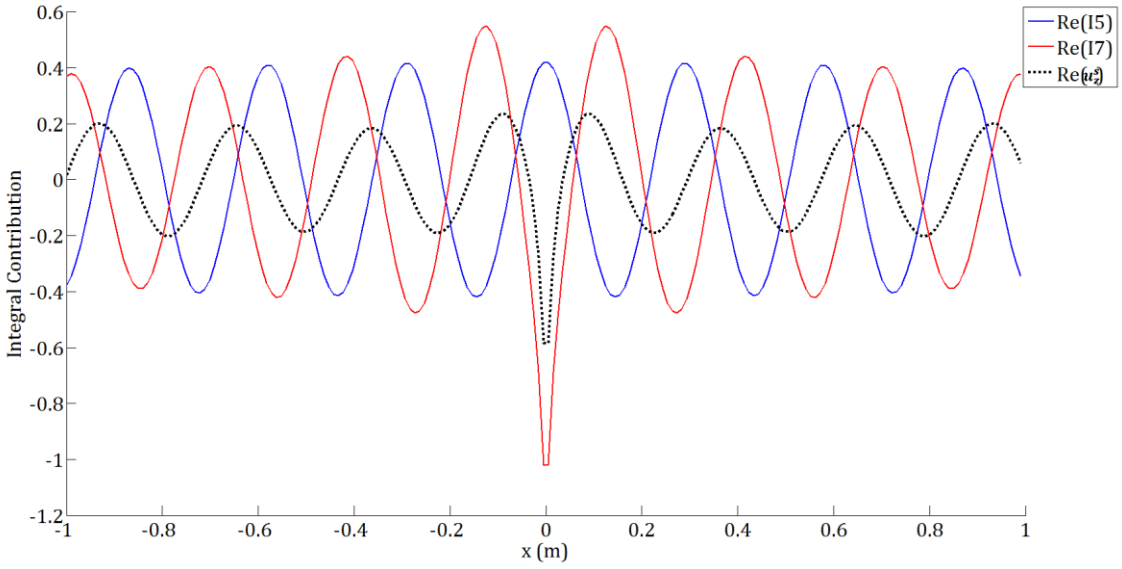

Figure 4.19 Real contributions to displacement $\boldsymbol{u}_z^s$ arising from the integral components as defined in Section4.2.5. All other integral components are negligible.

The situation is rather different for the real displacement contribution. Only two components contribute, namely I_5 and I_7. The localised peak is seen to be entirely due to the latter, corresponding to the integral $\int_{p+\delta}^{\infty} \frac{\mathcal{P}_1}{\mathcal{S}_1}$. This term accounts for the Fourier components of the rectangle function boundary stress imposed earlier in this chapter. The fast variation associated with the local stress source thus is comprised entirely of high order Fourier components.

We now briefly consider the case of the complementary displacements, that is to say, the transverse displacements incurred by a normal force and the normal displacements incurred by a transverse force. The absolute values are plotted for the same parameters as in the above in Figures 4.20 and 4.21:

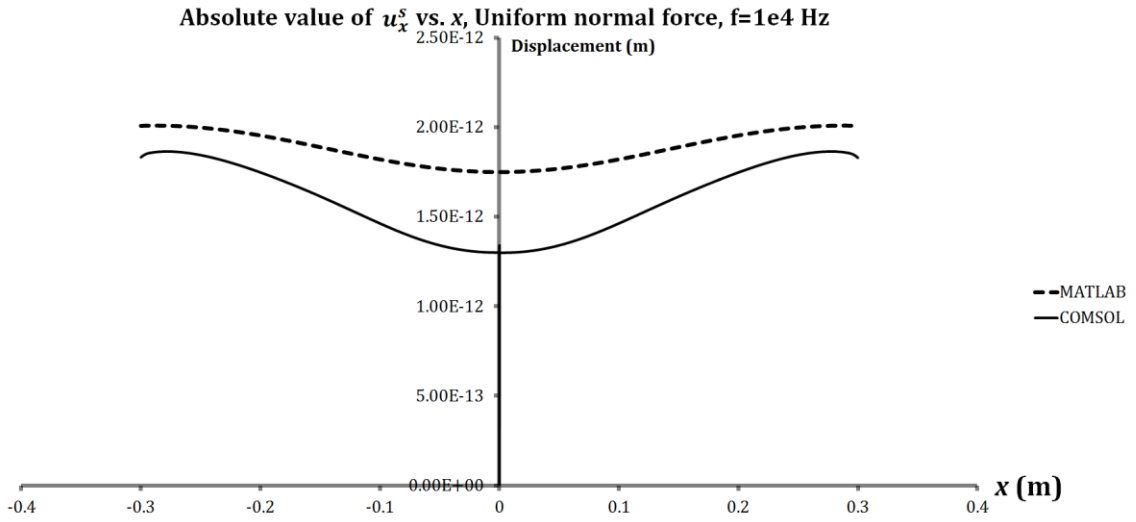

Figure 4.20 Absolute value of the complementary surface displacements incurred by a normal force, as predicted by the COMSOL and MATLAB models.

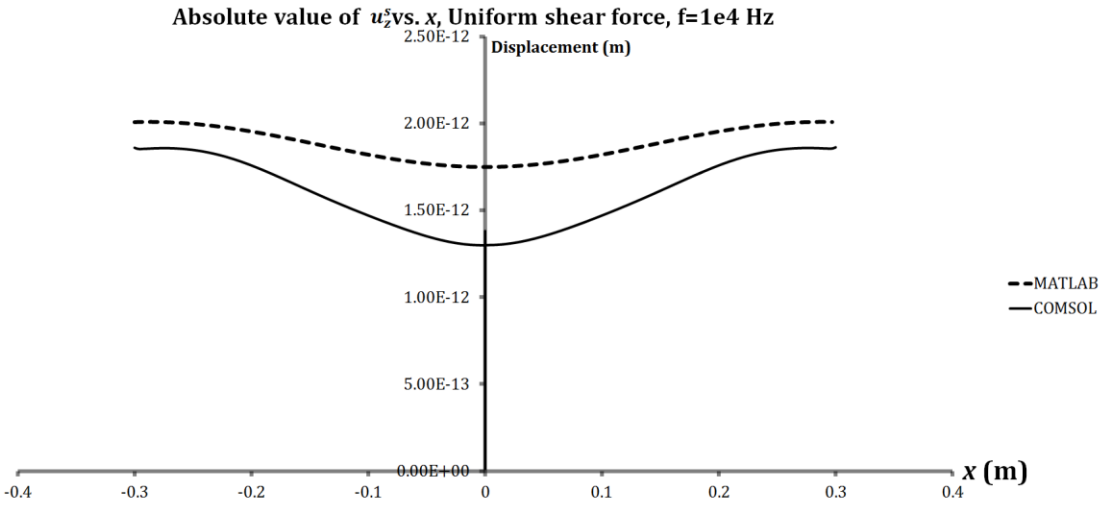

Figure 4.21 Plot of the absolute value of the complementary surface displacements incurred by a transverse force, according to the MATLAB and COMSOL models.

Again, good agreement is seen between the forms predicted by the models. The sharp peaks observed for the corresponding displacements are absent here, indicating that the observed phenomenon of a large localised elastic contribution is absent for the corresponding displacement case. The imaginary component of the complementary displacements are expected to be 0 at the origin, and antisymmetric about it, as can be deduced from the corresponding integral equations. Since the source region is symmetric, the inner products $\int_{-a/2}^{a/2} \boldsymbol{\sigma}_{xz}^{s} \boldsymbol{u}_{z}^{s}$ and $\int_{-a/2}^{a/2} \boldsymbol{\sigma}_{zz}^{s} \boldsymbol{u}_{x}^{s}$ should be identically zero, demonstrating that for the case of a single source, no work can be done by the normal

force on the (complementary) normal displacements incurred by a transverse force, and vice versa. To check this prediction, it serves to examine the complementary imaginary displacements.:

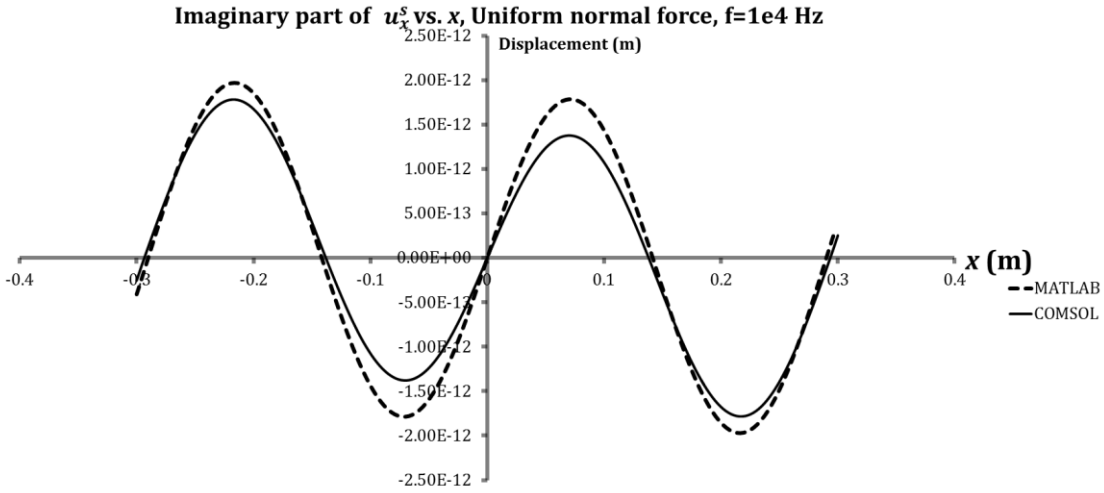

Figure 4.22 Imaginary component of the complementary displacement $\boldsymbol{u_x^s}$ incurred by normal force.

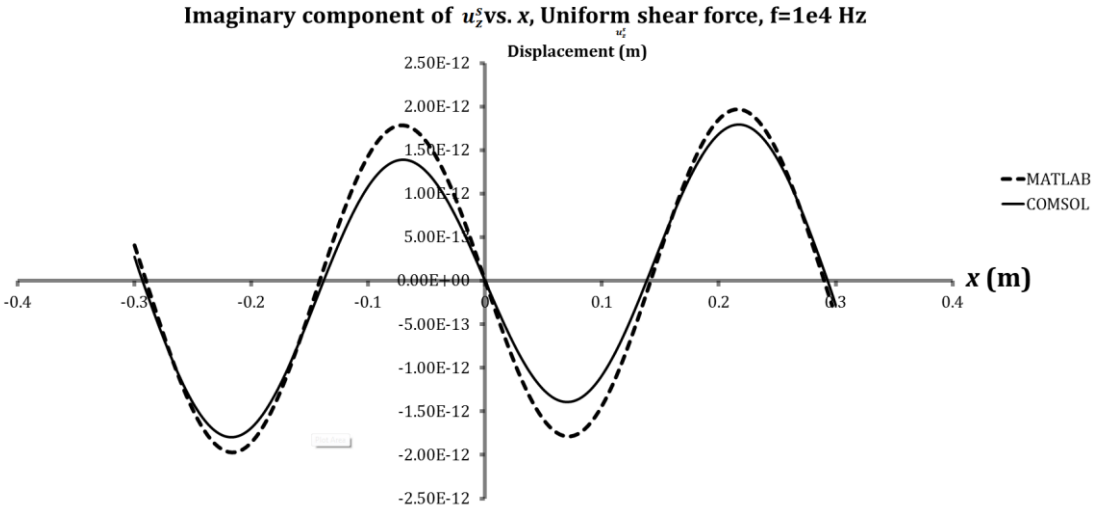

Figure 4.23 Imaginary component of the complementary displacement $\boldsymbol{u_z^s}$ incurred by normal force.

The predicted behaviour about the origin is observed, validating the model and the paradigm. Given the demonstrated behaviour of the corresponding and complementary surface displacements, the averaged displacement matrix is diagonalised and the energy loss for the case of a general single stress source (4.73) reduces to

$$\mathrm{P} = \mathrm{i}\omega \begin{bmatrix} \overline{\mathbf{u}_z^{sn}} & 0 \\ 0 & \overline{\mathbf{u}_x^{ss}} \end{bmatrix} \begin{bmatrix} |\mathrm{F}_N| \\ |\mathrm{F}_T| \end{bmatrix} \tag{4.78}$$

The work done over a harmonic cycle for the case of a single uniform stress source $\Delta \mathrm{E}_{SINGLE}$ can thus be written as

$$\Delta \mathrm{E}_{SINGLE} = \frac{|F_{\mathrm{N}}|^2}{\rho d v_{\Psi}^2} \mathrm{Im}\left(\int_0^{\infty} \frac{\mathcal{P}_1}{\mathcal{S}_1} \mathrm{sinc}^2\left(\frac{\zeta \omega a}{2 v_{\varphi}}\right) d\zeta \right) + \frac{|F_{\mathrm{T}}|^2}{\rho d v_{\Psi}^2} \mathrm{Im}\left(\int_0^{\infty} \frac{\mathcal{Q}_1}{\mathcal{S}_1} \mathrm{sinc}^2\left(\frac{\zeta \omega a}{2 v_{\varphi}}\right) d\zeta \right) \tag{4.79}$$

In the next subsection, we consider the phenomenology associated with these quantities for a range of parameters.

4.4.3 Source averaged surface displacements

In the previous subsection, the displacements at the free surface predicted by the analytical model was compared to a FE model of the same problem. Superb, pleasing concordance between the two approaches was evident. On this basis, we can confidently proceed to use the analytical model to examine the response of the substrate and the corresponding energy loss as the parameters of the model are varied. Since the energy loss is shown by (4.79) to be a simple quadratic with constant coefficients in the applied forces, the displacements are considered. The form of the resulting displacements mirrors that of the energy loss for unit forcing, up to a multiplicative constant.

First, the effect of varying the width of the source over a range of excitation frequencies is studied:

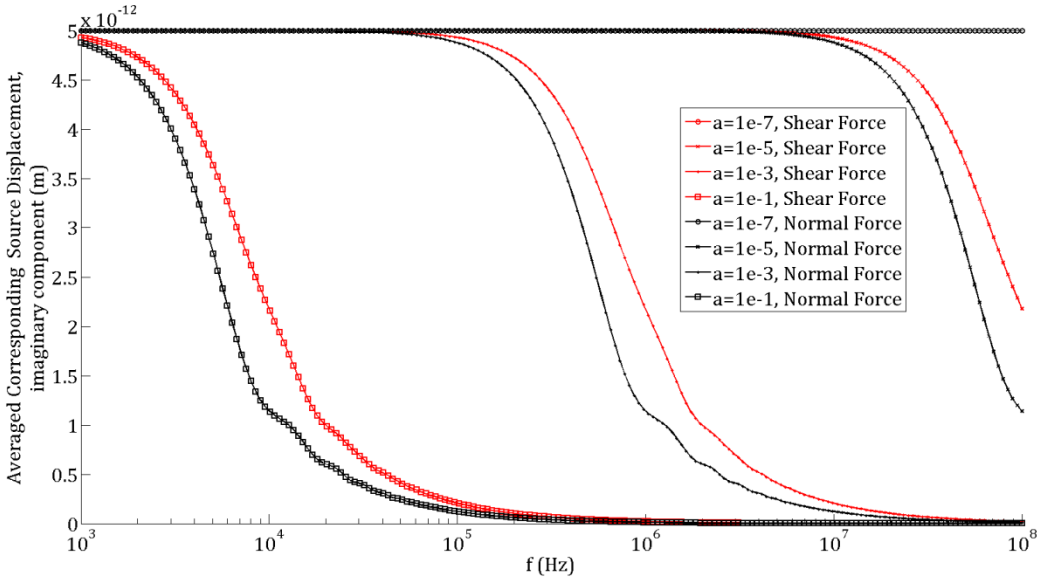

Figure 4.24 Plot of imaginary component of source-averaged corresponding surface displacement $\overline{\boldsymbol{u}_z^S}$ and $\overline{\boldsymbol{u}_x^S}$ incurred by applied normal and shear forces respectively, vs. frequency f, for a range of source widths a. The abscissa is logarithmic.

Figure 4.24 reveals several rather general features of the structure of the problem. Firstly, in the low frequency limit, it can be seen that all the curves tend asymptotically to a constant value. On the other hand, in the high frequency limit, all the curves tend asymptotically to zero. Furthermore, in the transition region between the limits, there is a scale independence of the behaviour, in that the curves for different source widths all have an identical form save for a frequency shift. In fact, the relationship can be shown to be linear; multiplying the source width by a factor of 100 shifts the curve downwards in frequency by the same factor. This is a consequence of the fact that in the integrand of (4.79), the only term depending on a or ω is of the form

$$\operatorname{sinc}^2\left(\frac{\zeta\omega a}{2v_\varphi}\right)$$

Thus, there exists a similarity variable $\eta = \frac{\omega a}{2v_\varphi}$ such that the above can be written as $\operatorname{sinc}^2(\zeta\eta)$. If one scales a according to $\tilde{a} = ka$ and ω according to $\tilde{\omega} = \frac{\omega}{k}$, then η and hence the integral and its consequent displacements are unchanged. Note that the similarity variable can be viewed as $\eta = \frac{a}{2\lambda_\varphi}$, where λ_φ is the bulk transverse wavelength.

To see the cause of the low-frequency limiting behaviour, recall that the limit of the sinc function as its argument tends towards zero is unity. Since it was shown in the previous subsection that the only integrals to contribute to the imaginary displacement are I_1, I_3 and I_6 we need only examine the case where $0 < \zeta < p \approx 2$. Then, to a close approximation, the imaginary displacement can be expressed as a fixed quantity arising as the imaginary part of $\int_0^p \frac{\mathcal{P}_1}{\mathcal{S}_1} \mathrm{sinc}^2(\zeta\eta) d\zeta$. This frequency-domain product can be viewed as the convolution in the time domain of the boundary conditions with the Green's function $\frac{\mathcal{P}_1}{\mathcal{S}_1}$ between the same limits.

The situation is made clear by graphical representation of the trigonometric term in the integrand:

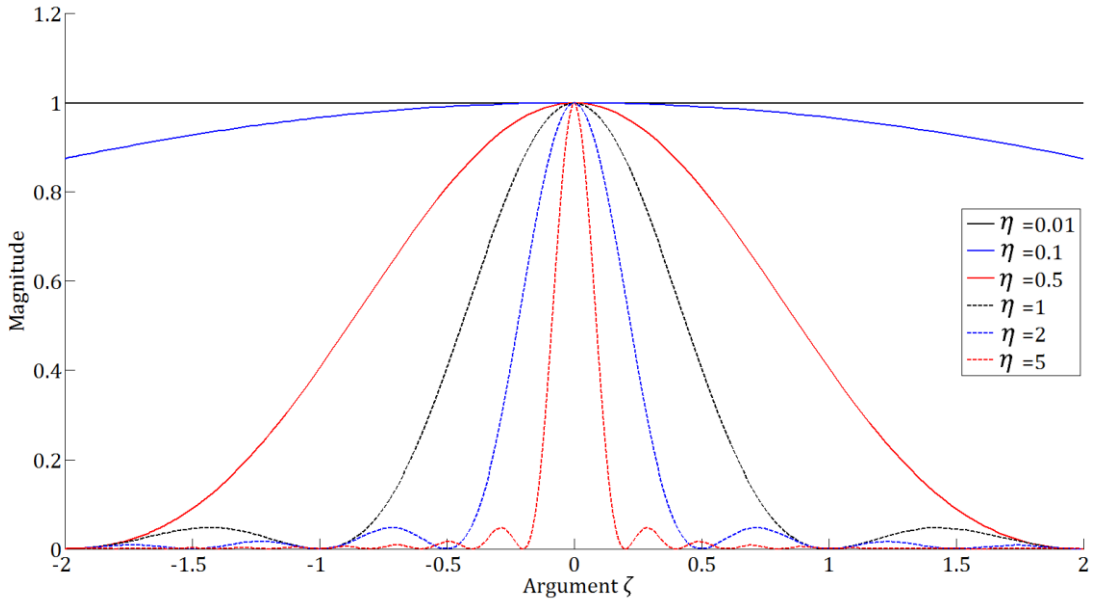

Figure 4.25 Plots of $\mathrm{sinc}^2(\zeta\eta)$ for several values of the similarity variable η.

The mechanism of the transition and scale invariance is now plain. When the similarity variable $\eta \ll 1$, as for the solid black line in Figure 4.25, the area under the curve (AOC) tends asymptotically to a rectangle with area 2; any change in a will be inconsequential so long as this condition is met. As η is increased – for example, moving along one curve in Figure 4.24 by increasing the excitation frequency at constant a, the area begins to decrease as the curvature of the corresponding integrand $\mathrm{sinc}^2(\zeta\eta)$ gradually becomes nonnegligible, corresponding to the smooth transition observed. The area under the curve reaches a value of 1, which is to say half

the peak, for $\eta \approx 0.454$. The small ripples observed for $\eta > 0.5$ incur an oscillatory contribution to the curves, as seen in Figure 4.24; however, they remain monotone throughout. In the limit $\eta \to \infty$, the AOC tends to zero. Physically, this corresponds to a uniform oscillating normal force where the source width is substantially larger than the bulk transverse wavelength at the corresponding excitation frequency.

The practical consequences of the preceding discussion are manifest. If for a particular resonator geometry $\eta \ll 1$ then the support loss per cycle is independent of frequency and leg width. This case is henceforth referred to as the *small η limit*; the criterion $\eta \ll 1$ can be expressed as $\frac{a}{\lambda_\varphi} \ll 2$. The functional independence of the surface displacements and hence the incident power from the system parameters breaks down at higher frequencies as $\eta \to 0.5$ from below.

For beam resonators, since the flexural wave speed is lower than the bulk transverse wave speed, the flexural wavelength of the support would need to be short compared to its width, violating the assumption that the resonator is composed of beams, in that transverse resonance would occur and the resulting strains would invalidate the assumption that plane cross-sections remain planar. In particular, the stresses at the source region would be expected to switch sign one or more times under these conditions, coupling in to substrate waves with corresponding short wavelengths relative to a and preventing the suppression of support loss observed in the numerical results. The form of the variation would need to be accounted for in the integral equation formulation. However, consider the case in which a different resonator geometry is tethered via slender members to its substrate. Bulk acoustic wave resonators are of this type, and have resonant frequencies frequently in the MHz and sometimes GHz regions, with principal dimensions of the order of millimetres to centimetres. Slender tethers would be forced into compressive vibration by any component of displacement normal to the resonator surface at the points of attachment. The theory and results developed herein can be applied directly to such devices.

The decomposition (4.71) can be used to separate the bulk and Rayleigh wave contributions to the surface displacements. These contributions vary in absolute magnitude and relative proportion as the similarity variable is changed. The form of this variation is shown in Figure 4.26:

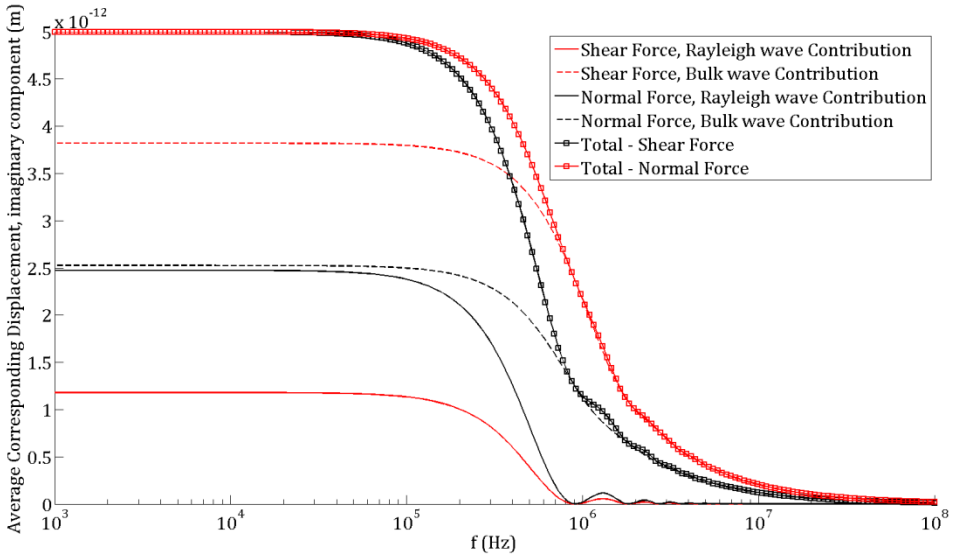

Figure 4.26 Rayleigh wave and bulk wave contributions to the source-averaged corresponding surface displacement $\overline{\boldsymbol{u}_z^s}$ and $\overline{\boldsymbol{u}_x^s}$.

Since any arbitrary change in material stiffness or density, excitation frequencies and/or source geometry which does not change the modelling assumptions can be accounted for using the similarity approach developed above, the only remaining model parameter whose effect has not been evaluated is the Poisson's ratio, which is evaluated next.

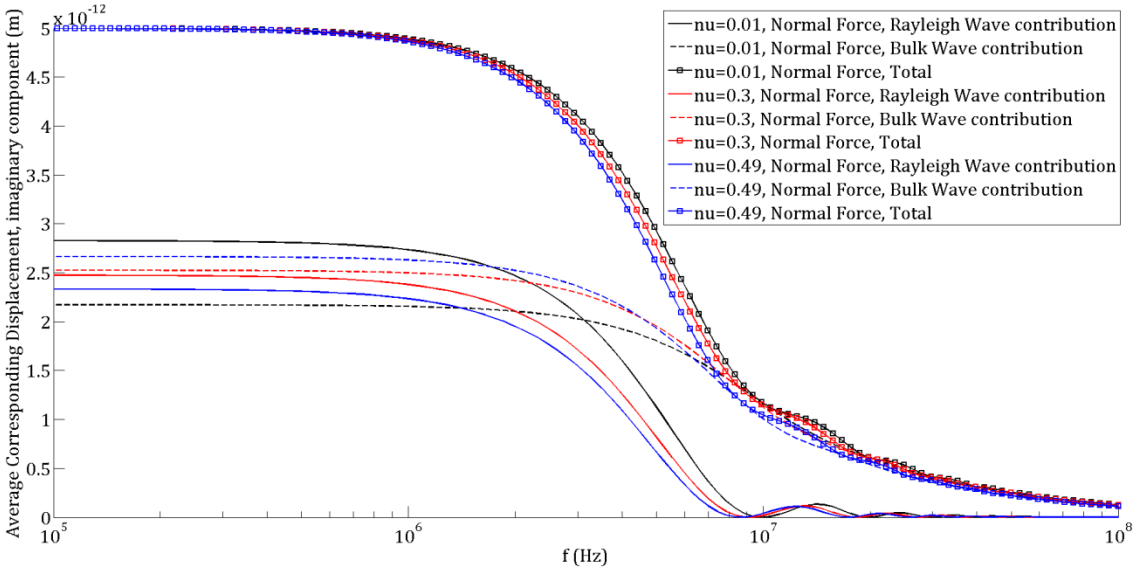

Figure 4.27 Frequency domain plot of imaginary displacement contributions from Rayleigh and bulk waves, as well as the total imaginary displacements, for two extremal and one medial value of the Poisson's ratio nu.

The values of the turning points for the Rayleigh contribution can be seen to vary slightly with the Poisson's ratio, as does the total imaginary displacement in the transition region. However, the same low-frequency and high-frequency limits are approached for any of the Poisson's ratios investigated, at least for the normal force case. It can be concluded that the Poisson's ratio has a moderately small effect on the power spectrum of a single source.

4.4.4 General double source

The case of a double source under the modelling assumptions of this work can be viewed as Kirchhoff double-slit diffraction of elastic waves in the limit of a compliant screen, such that interactions between the source can arise from surface and bulk waves. As a consequence, as well as the expected bulk and surface wave generation phenomena explored in Section 4.4.1, interaction phenomena can be anticipated to emerge from the modelling, corresponding to constructive and destructive interference of elastic surface and bulk waves emanating from each finite-width slit having an effect on the averaged displacements over the source regions. We begin, as in the case of a single source, by considering the free surface displacements.

4.4.5 Free surface displacements

Following the established pattern, we first examine the absolute values of the corresponding displacements for the cases of normal and shear forces. We consider here a higher frequency, so as to emphasise interesting interaction behaviour, which occurs over several wavelengths.

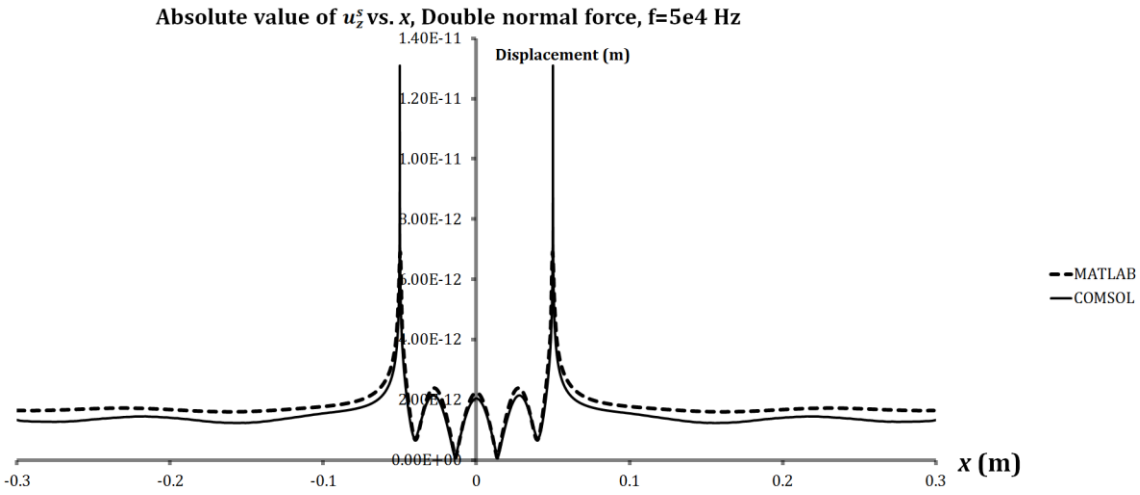

Figure 4.28 Plot comparing the predicted absolute value of the corresponding surface displacement $\overline{\boldsymbol{u}_z^s}$ incurred by an applied double normal force as x varies, from the MATLAB and COMSOL models.

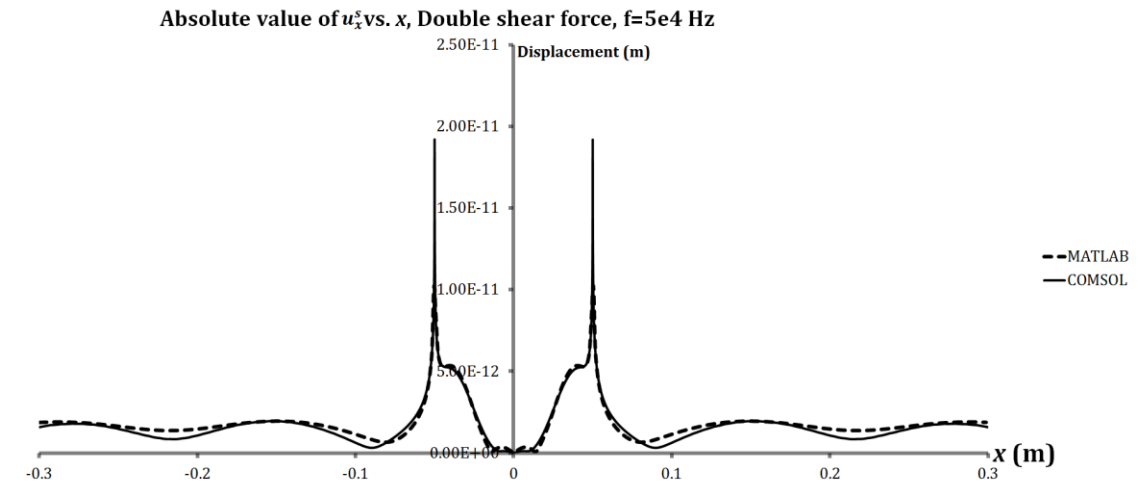

Figure 4.29. Plot comparing the predicted absolute value of the corresponding surface displacement $\overline{\boldsymbol{u}_x^s}$ incurred by an applied shear force as x varies, from the MATLAB and COMSOL models.

As for the case of a single source, agreement between the models in Figure 4.29 is excellent, validating the analytical modelling well. The forms of the displacements have some similarities to the former case, with localised peaks at the source regions at

$|x| \approx 0.05\,m$ and roughly constant behaviour in the region outside them, with some periodic beating in the region $|x| > 0.05\,m$, outside the sources. New behaviour can be expected in the region $|x| < 0.05\,m$, that is to say between the sources, since outgoing waves from each source will interact. Indeed, the waves can be expected to be symmetrically counterpropagating in the case of double normal forcing, leading to standing waves with absolute nodes, as observed in Figure 4.28; whereas antisymmetrically counterpropagating waves between the sources in the case of the double shear force are expected and observed in Figure 4.29. These phenomena will be shown to have consequences for the energy losses associated with the sources and hence the multiply-supported resonator design, in the sequel.

To untangle the behaviour, as well as for completeness, we now turn attention to the real and imaginary components of the corresponding displacements.

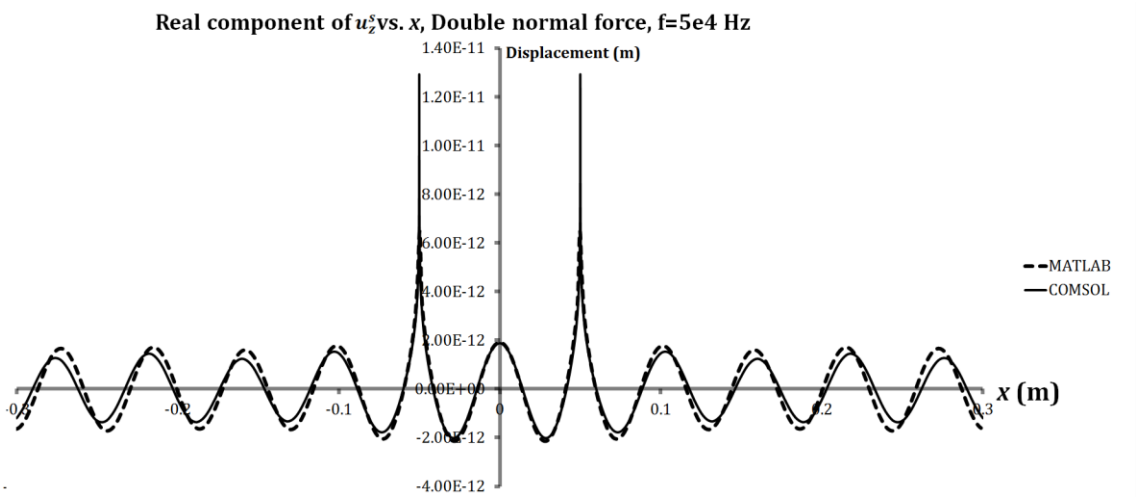

Figure 4.30 Plot comparing the predicted real component of the corresponding surface displacement $\overline{\boldsymbol{u}_z^s}$ incurred by an applied double normal force.

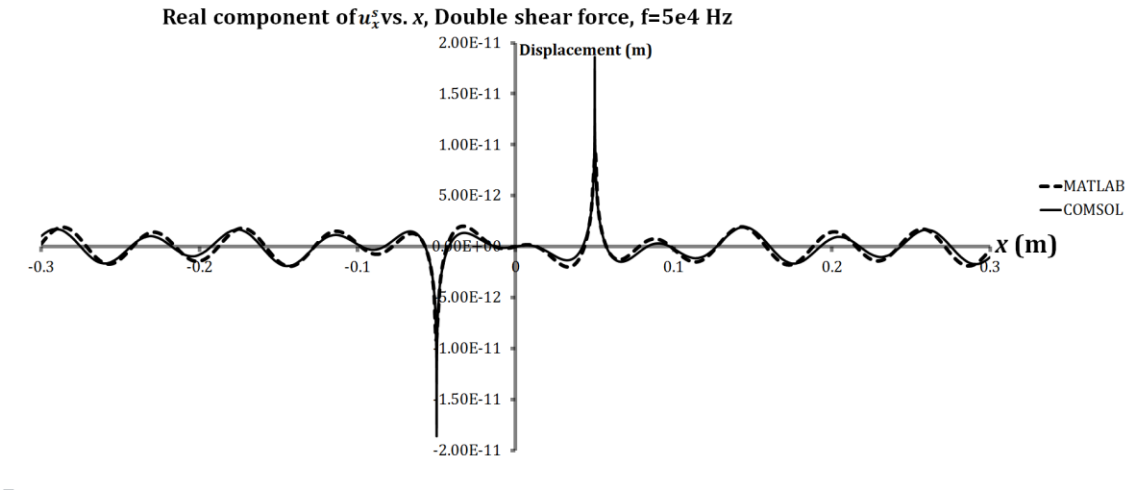

Figure 4.31 Plot comparing the predicted real component of the corresponding surface displacement $\overline{\boldsymbol{u}_x^s}$ incurred by an applied double shear force.

Looking past the superb concordance between the two modelling approaches, phenomenological parallels can be drawn again between the single source model and the double source model presented here. As expected, the symmetry of the solutions follows that of the applied stresses – symmetric for the double normal force and antisymmetric for the double shear. Again, the real components contain the localised peaking behaviour observed in the absolute value plots, suggesting its association with the conservative part of the energy dynamics between the resonator and the substrate and plays no role in determining the resonator Q.

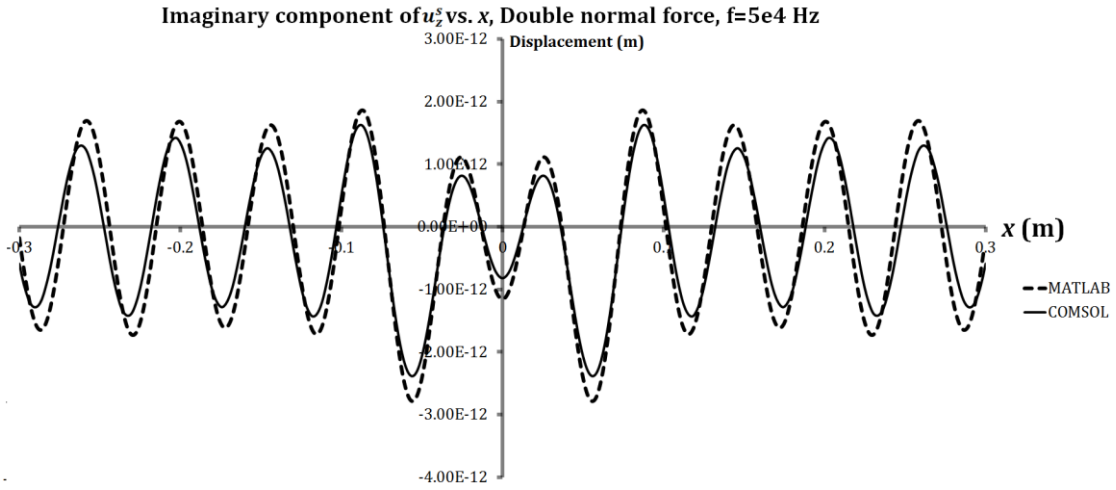

Figure 4.32 Plot comparing the predicted imaginary component of the corresponding surface displacement $\overline{\boldsymbol{u}_z^s}$ incurred by an applied double normal force.

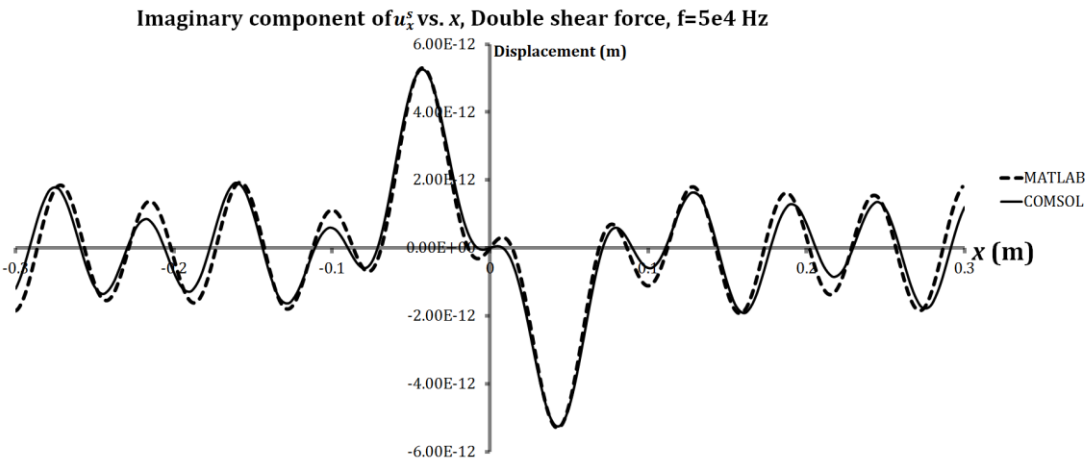

Figure 4.33 Plot comparing the predicted imaginary component of the corresponding surface displacement $\overline{\boldsymbol{u}_x^s}$ incurred by an applied double shear force.

Lastly, consider the form of the surface-averaged displacements, described in the general case by (4.71). In contradistinction to the case of a single force source, there is a nonzero imaginary contribution to the complementary displacement at a source (labelled the first source for convenience of argument), arising from the surface components of the Rayleigh and bulk waves generated by the second source. Then, the averaged displacement matrix is not diagonal. The general form of the source displacements can be written as

$$\mathrm{P} = \mathrm{i}\omega \begin{bmatrix} \overline{\mathbf{u}_z^{sn}} & \overline{\mathbf{u}_x^{sn}} \\ \overline{\mathbf{u}_z^{ss}} & \overline{\mathbf{u}_x^{ss}} \end{bmatrix} \begin{bmatrix} |\mathrm{F}_N| \\ |\mathrm{F}_T| \end{bmatrix} \tag{4.80}$$

The work done over a harmonic cycle for the case of a single uniform stress source can thus be written as

$$\Delta \mathrm{E}_{DOUBLE}$$
$$= \frac{|F_{\mathrm{N}}|^2}{\rho d v_{\Psi}^2} \mathrm{Im}\left(\int_0^{\infty} \frac{\mathcal{P}_1}{\mathcal{S}_1} \mathrm{sinc}^2\left(\frac{\zeta \omega a}{2v_{\varphi}}\right) \cos^2\left(\frac{\zeta \omega b}{2v_{\varphi}}\right) d\zeta \right.$$
$$\left. + \int_0^{\infty} \frac{\zeta(2\mathcal{P}_1\mathcal{Q}_1 - \mathcal{R}_1)}{\mathcal{S}_1} \mathrm{sinc}^2\left(\frac{\zeta \omega a}{2v_{\varphi}}\right) \cos\left(\frac{\zeta \omega b}{2v_{\varphi}}\right) \sin\left(\frac{\zeta \omega a}{2v_{\varphi}}\right) d\zeta \right)$$
$$+ \frac{|F_{\mathrm{T}}|^2}{\rho d v_{\Psi}^2} \mathrm{Im}\left(\int_0^{\infty} \frac{\mathcal{Q}_1}{\mathcal{S}_1} \mathrm{sinc}^2\left(\frac{\zeta \omega a}{2v_{\varphi}}\right) \sin^2\left(\frac{\zeta \omega b}{2v_{\varphi}}\right) d\zeta \right.$$
$$\left. + \int_0^{\infty} \frac{\zeta(\mathcal{R}_1 - 2\mathcal{P}_1\mathcal{Q}_1)}{\mathcal{S}_1} \mathrm{sinc}^2\left(\frac{\zeta \omega a}{2v_{\varphi}}\right) \cos\left(\frac{\zeta \omega b}{2v_{\varphi}}\right) \sin\left(\frac{\zeta \omega a}{2v_{\varphi}}\right) d\zeta \right) \quad (4.81)$$

In the next subsection, we consider the phenomena arising from these quantities for a range of parameters and limiting cases.

4.4.6 Source averaged surface displacements

The spatial plots of the displacement given in the preceding section demonstrate the ability of the analytical modelling to accurately predict the phase and magnitude behaviour of an elastic half-plane in response to a general superposition of double transverse and shear forcing, at least in the vicinity of the parameters plotted for. Interaction between the two sources can be seen in that the behaviour between the sources differs from that beyond either source, in terms of x.

However, the most important results from the point of view of resonator design and support loss are the power fluxes predicted by the modelling. The general behaviour in this region is complicated. One source of complexity is due to interactions between two scales – the width of each source and the separation between them. It was shown in Section 4.4.1 that, for sufficiently low frequencies or sufficiently small source widths, the behaviour became independent of frequency, corresponding in the limit to the behaviour of a point excitation source, while more complex behaviour was exhibited when the wavelength became commensurate to the source width a. To examine two-source interaction effects, we consider first the case of vanishingly small source width, so that we effectively study a system of two point sources. Only

subsequently is the domain of consideration extended to account for the effects of finite source width.

To gain some introductory insight and make some deductions about the expected behaviour, we consider next the *corresponding* displacements for the double normal and double shear force cases. The source-averaged displacements given by (4.50) and (4.61), after employing the simplifying change of variable (4.62), have the form

$$\frac{4F_{\mathrm{N}}}{\rho d v_{\Psi}^{2}} \int_{0}^{\infty} \frac{\mathcal{P}_1}{\mathcal{S}_1} \cos^2\left(\frac{\zeta \omega b}{2v_{\varphi}}\right) \mathrm{sinc}^2\left(\frac{\zeta \omega a}{2v_{\varphi}}\right) d\zeta = \overline{\mathrm{u}_z^{sn}} \qquad (4.82a)$$

$$\frac{4F_{\mathrm{N}}}{\rho d v_{\Psi}^{2}} \int_{0}^{\infty} \frac{\mathcal{Q}_1}{\mathcal{S}_1} \cos^2\left(\frac{\zeta \omega b}{2v_{\varphi}}\right) \mathrm{sinc}^2\left(\frac{\zeta \omega a}{2v_{\varphi}}\right) d\zeta = \overline{\mathrm{u}_x^{ss}} \qquad (4.82b)$$

Where it is understood that the subscripts denote the sense of force application, i.e. that $\overline{\mathrm{u}_z^{sn}}$ represents the source-averaged surface displacement incurred by a double normal force in the direction of the force, and conversely for $\overline{\mathrm{u}_x^{ss}}$.

As in the case of a single source, since cos is real for all real arguments, we need only consider the range $0 < \zeta < p$, where p is close to 2. In the point-source (low-frequency) limit, we have

$$\frac{4F_{\mathrm{N}}}{\rho d v_{\Psi}^{2}} \mathrm{Im}\left(\int_{0}^{p} \frac{\mathcal{P}_1}{\mathcal{S}_1} \cos^2\left(\frac{\zeta \omega b}{2v_{\varphi}}\right) d\zeta \right) = \mathrm{Im}(\overline{\mathrm{u}_z^{sn}}) \qquad (4.83a)$$

$$\frac{4F_{\mathrm{N}}}{\rho d v_{\Psi}^{2}} \mathrm{Im}\left(\int_{0}^{p} \frac{\mathcal{Q}_{1_1}}{\mathcal{S}_1} \sin^2\left(\frac{\zeta \omega b}{2v_{\varphi}}\right) d\zeta \right) = \mathrm{Im}\left(\overline{\mathrm{u}_x^{ss}}\right) \qquad (4.83b)$$

This immediately suggests a second similarity variable of the form

$$\varsigma = \frac{\omega b}{2v_{\varphi}} \qquad (4.84)$$

reducing (4.83) to

$$\frac{4F_{\mathrm{N}}}{\rho d v_{\Psi}^{2}} \int_{0}^{p} \frac{\mathcal{P}_1}{\mathcal{S}_1} \cos^2(\zeta\varsigma)\, d\zeta = \overline{\mathrm{u}_z^{sn}} \qquad (4.85a)$$

$$\frac{4F_{\mathrm{N}}}{\rho d v_{\Psi}^{2}} \int_{0}^{p} \frac{\mathcal{P}_1}{\mathcal{S}_1} \sin^2(\zeta \varsigma)\, d\zeta = \overline{\mathrm{u}_x^{SS}} \qquad (4.85b)$$

Thus, the windowing or convolution effect already observed for the case of a single source of finite width is repeated, but with an oscillatory, non-decaying kernel. Instead of the oscillatory decay associated with the kernel $\mathrm{sinc}^2(\zeta\eta)$, constant amplitude oscillation is anticipated once the similarity variable ς is large enough such that the trigonometric term oscillates sufficiently quickly with respect to the variation in the windowing function $\frac{\mathcal{P}_1}{\mathcal{S}_1}$. In the other limit of vanishing ς, the trigonometric term tends to unity for the double normal force and zero for the double shear force, and the integral has the identical form to that for a single normal force in the former case and tends to zero in the latter. Since this limit corresponds to the two stress sources approaching each other and eventually superposing to form a single stress source, which will reinforce in the double normal case and cancel in the double shear case due to the opposing direction of the shears, this is intuitively consistent. Between the limits, interactions between the form of the windowing functions and the kernels are expected to produce a transition region. We turn now to numerical results to support these hypotheses.

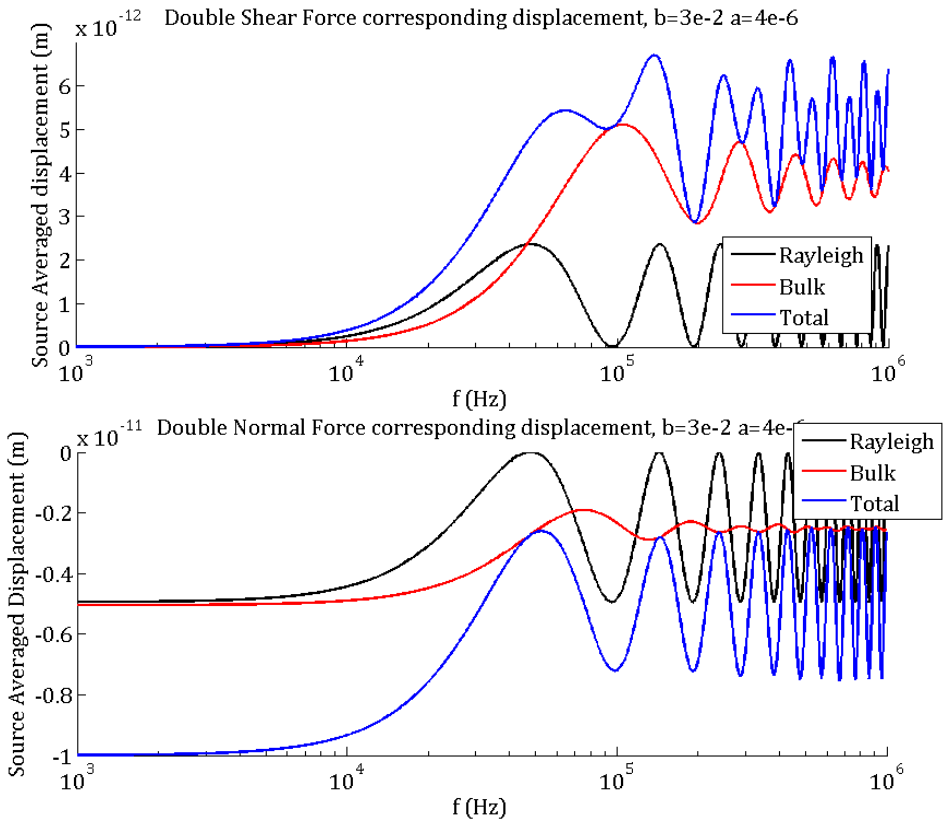

Figure 4.34 Plot of contributions to and total value of the source-averaged corresponding imaginary surface displacement $\overline{\boldsymbol{u}_z^{sn}}$ and $\overline{\boldsymbol{u}_x^{ss}}$ incurred by applied normal and shear forces (top and bottom respectively), vs. frequency f. The abscissa is logarithmic.

The plots in Figure 4.34 are revealing. We need only consider the effect of frequency; the equations (4.85) are symmetric in b and ω in this point-source limit. In the low-frequency case (which, through the similarity variable representation (4.84), can be seen to be equivalent to $b \to 0$) the total imaginary corresponding displacement and consequent power transfer tends asymptotically to zero, whilst the corresponding quantity tends to twice the single-source value for the normal force case. Since the normal forces are assumed to have the same sense, their effects in the low-frequency limit convolve with the Green's function in a constructive interference; conversely, the shear forces are assumed to be of opposite sense and interfere destructively, nulling the power transfer in the low frequency limit.

These results are in complete concordance with the physical considerations previously discussed. In the high frequency limit, corresponding to large b relative to the wavelengths involved, the behaviour is more complicated.

In the case of a double normal force, the Rayleigh contribution is seen to be of constant amplitude and period in both cases (when one accounts for the logarithmic abscissa), with its value alternating between a maximum when the Rayleigh components from each source are in phase and zero when they are in antiphase and cancel.

The bulk contribution consists of a decaying oscillatory component, representing interaction between the bulk waves generated at the second source with the first and having the form of the order zero order Bessel function, superposed on a smooth S-shaped curve representing energy loss to the bulk material. The overall form is given by

$$J_0(k_b x) + \tanh(x - k_b) \tag{4.86}$$

Thus, the total imaginary displacement component coincides with the bulk contribution at the zeroes of the cosinusoidal Rayleigh component; that is to say, when the tuning condition

$$b = n\lambda_R \tag{4.87}$$

is met, where λ_R is the Rayleigh wavelength and n is a natural number. Beating between the sinusoid and the Bessel function is observed in the irregular character of the total imaginary displacement in the transition region, i.e. for frequencies in the vicinity $10^5 < f < 10^6$ in Figure 4.34.

Most of the above discussion applies directly to the case of a double shear case, with a phase shift in the Rayleigh component and a change in the Bessel function from order 0 to order 1, such that the values decay exponentially as f (or b) tends to zero.

A major difference between the power transfers incurred by single and double stress sources is exposed in (4.50) and (4.61). The complementary source-averaged displacements incurred by a double normal source are nonzero, and thus the presence of an in-phase double shear source will lead to work being done and a non-vanishing energy transfer contribution. This is a consequence of displacements engendered by the second source at the first source, and conversely; furthermore, a similar argument applies in the opposite case, to wit, an in-phase double normal source will do work on

the displacements generated by a double shear source. These energy transfers correspond to the off-diagonal entries in the matrix in (4.73).

The form of the relationships is expected to depend on the bulk and Rayleigh couplings between the two sources, as in the above. However, the tanh component corresponding to direct bulk losses cannot be present. Physically, one might expect a sinusoidal contribution from Rayleigh waves, vanishing as the sources are identified, to be superposed on a decaying oscillatory contribution of Bessel form from the bulk waves.

Additionally, by the reciprocal principle, work done by one source on the displacements generated by another should be unchanged if the corresponding and complementary source are exchanged; this would correspond to symmetry of the matrix in (4.73). On this basis, we expect the complementary displacements to be equal for double and normal sources of equal magnitude.

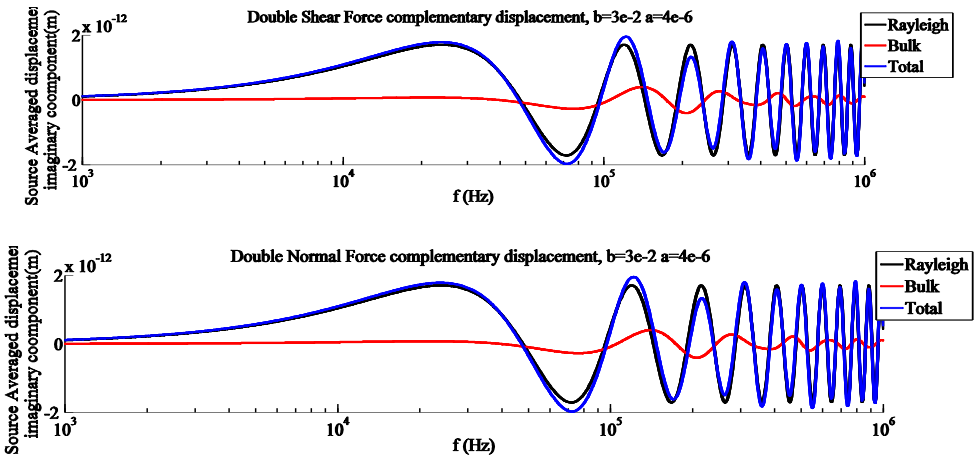

Figure 4.35 Plot of contributions to and total value of the source-averaged *complementary* imaginary surface displacement $\overline{\boldsymbol{u}_x^{sn}}$ and $\overline{\boldsymbol{u}_z^{ss}}$ incurred by applied normal and shear forces (top and bottom respectively), vs. frequency f. The abscissa is logarithmic.

Again, the predicted effects are observed, and the modelling paradigm is further validated. The complementary displacements are symmetric, and consist of zero mean oscillatory contributions: a Bessel function representing the bulk contribution, decaying as the source separation measured in wavenumbers falls, and a sinusoid representing the Rayleigh contribution.

Attention now turns to interaction effects between the source width a and the source separation b. We consider the case of the corresponding displacements first.

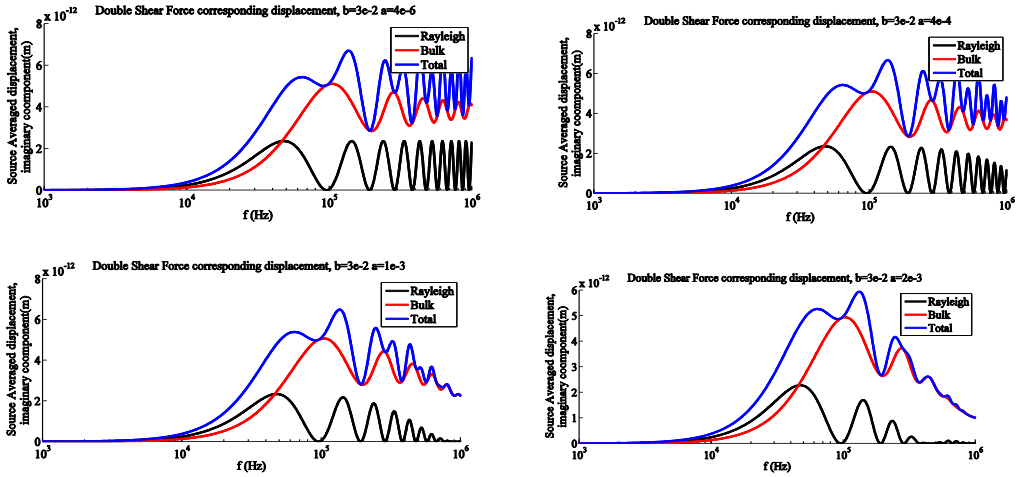

Figure 4.36 From top right to bottom left, plots of corresponding displacement contributions for the case of an applied double shear force as the source width a takes the values $4 \times 10^{-6}, 4 \times 10^{-4}, 1 \times 10^{-3}, 2 \times 10^{-3}$ respectively.

The first plot in Figure 4.36 represents the point source limit over this frequency range. In the second, third, and fourth plots, the source width is increased into the transition region. In all cases, the low frequency behaviour is unaffected, while as the frequency becomes commensurate to the wavelengths involved, attenuation is observed. The attenuation is stronger for larger values of the source width. The overall effect can be seen as a product in the frequency domain of the point-source limit interaction of the two sources with the self-interaction of the single source of finite width, as plotted in Figure 4.23.

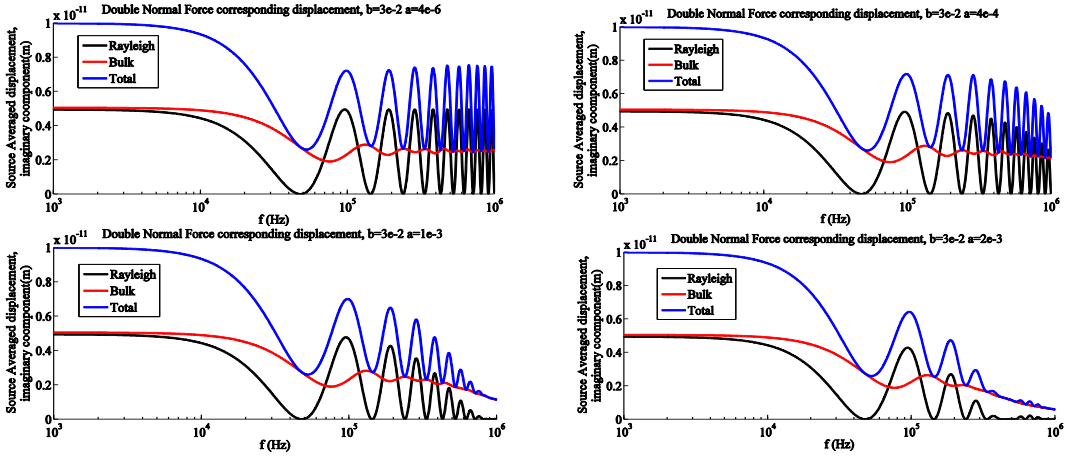

Figure 4.37 From top right to bottom left, plots of corresponding displacement contributions for the case of an applied double normal force as the source width a takes the values $4 \times 10^{-6}, 4 \times 10^{-4}, 1 \times 10^{-3}, 2 \times 10^{-3}$ respectively.

Figure 4.37 shows the same data as Figure 4.36 for the case of a double normal force. The broad trends of low-pass filtering of the double-source response by the effect of

finite source width are replicated. The low-frequency limit remains nonzero, while the relative magnitudes of the excited bulk waves is different and generally smaller than for the double shear case. The effect of finite source width on the response of a double source can be summarised as a low-pass filtering; this effect is made explicit in the response curves plotted in 4.38.

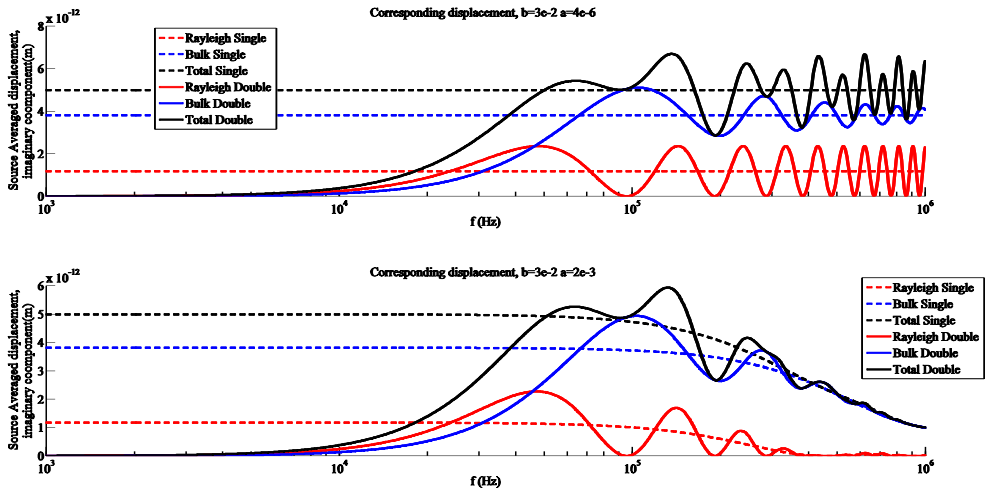

Figure 4.38 Comparison of the source-averaged imaginary displacement components for a point and finite source. The upper plot shows the point-source limit; the lower shows the transition region. The low-pass filtering effect of the finite source width on the double source behaviour is evident.

4.4.7 Input power spectrum and cyclic energy loss

The imaginary component of source-averaged displacement for the cases of a general uniform single and double stress source, corresponding to a single-supported and double-supported resonator respectively, have been examined at some length in Sections 4.4.1 and 4.4.2. For the singly-supported cases, the energy transfer behaviour was shown to be decoupled in the contributions from shear and normal force; therefore, the relationship between applied force and resulting substrate displacement is a sum of contributions consisting of a simple multiplication by a scalar factor depending only on the material properties and the *corresponding* applied forces, in which the sum is biquadratic, and expressed by (4.79).

On the contrary, it has been shown that in the doubly-supported case, nonzero source-averaged complementary imaginary displacements are incurred, in general. The energy transfer generated by a superposition of normal and shear stress is coupled, and is not a linear sum of the double shear and double normal force

contributions. In this subsection, the power transfer is evaluated as a function of the applied force components. Thereby, the input power spectrum for a general uniform double source is obtained. As a first step to illustrate the approach, we take the case of a single source.

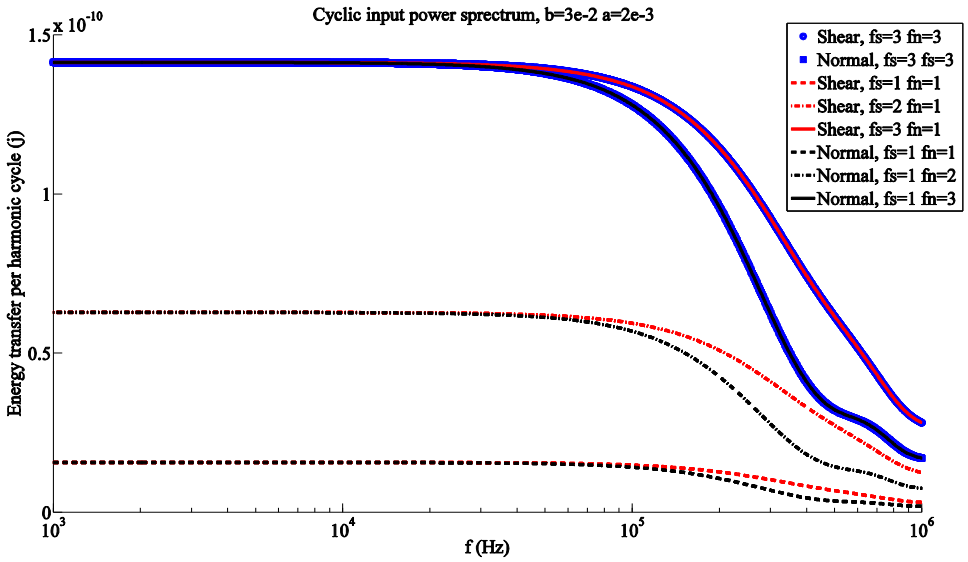

Figure 4.39 Cyclic input power spectrum, for the case of a general uniform single forcing, as the force components are varied.

The cyclic input power spectrum for an applied shear or normal force is seen to tend towards the same limit for an applied normal or shear force of equal magnitude. The value of this limit is quadratic in the applied force, as can be straightforwardly deduced from the expression (4.73):

$$P = F.\dot{u} \propto |F| \times u;\ u \propto F, \therefore P \propto |F|^2$$

where the second assertion follows by linearity of the equations of motion. The individual energy transfer curves are identical in form (up to a multiplicative constant) to the corresponding imaginary displacement curves. Furthermore, it is clear that no interaction is observed between the complementary force and the cyclic input power spectrum, in that a tripling of the complementary force leaves the spectrum unchanged, which is reflected in the superposition of the first and fifth, and second and eighth series in the plot, respectively for shear and normal uniform single sources.

We now examine the corresponding quantities for the case of a double source.

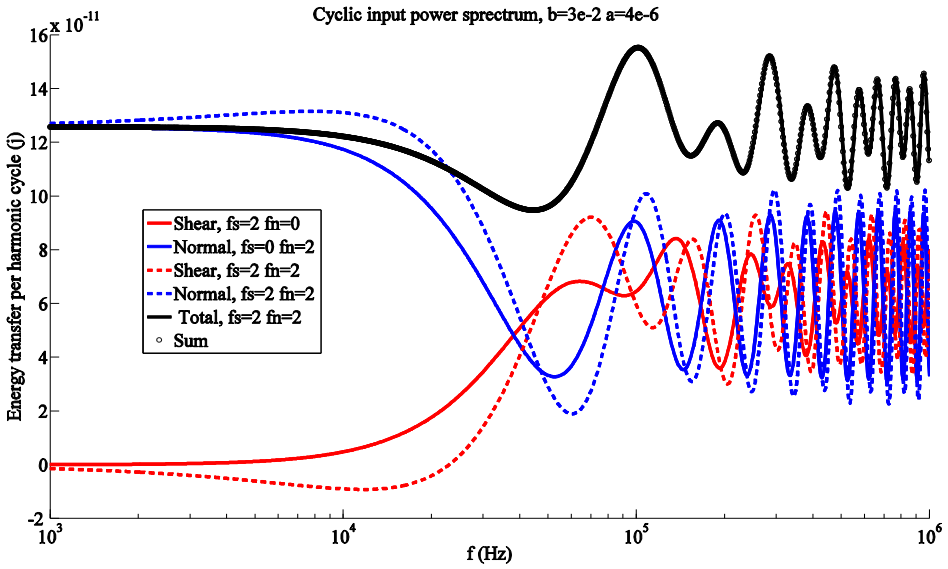

Figure 4.40 Input cyclic power spectrum for a general double source with different load superpositions. The blue plots correspond to double normal forces; the red, to double shear forces. The black line corresponds to the total cyclic energy transfer for simultaneous double normal and shear loading; the black circles to the sum of the contributions from the individual loadings.

Figure 4.40 shows the variation in input power with respect to frequency for three different loading scenarios: a double shear force with null normal force; a double normal force with null shear; and the simultaneous application of both double forces. From the previous discussion, it would be expected that the complementary energy transfers are affected by the presence of a corresponding force, and this is seen to be the case; the dotted lines, corresponding to a superposed force situation, differ substantially from the solid lines, corresponding to separate application of double normal and shear forces.

However, a result that is very important and yet not immediately obvious is shown by the plots in black. The total energy transfer for the superposed loading is plotted as a solid black line; the sum of the individual energy transfers for the separate loadings is plotted as a series of circular markers. The two plots coincide, implying that the total energy transferred in the superposition is equal to the sum of the energies transferred by the individual loads in the superposition, despite the coupling between them. This is a direct consequence of the symmetry of the matrix in (4.73), which implies that it can be rotated with constant trace into a diagonal matrix; the coordinates would then correspond to a linear combination of the shear and normal loadings. This is in turn a

ramification of the *principle of reciprocality* for elastic waves, and ultimately of the self-adjoint nature of the governing operator.

Thus, the difference in cyclic energy transfer seen in Figure 4.40 between the solid and dashed blue plots, corresponding to the normal force with and without a simultaneously applied shear, is balanced exactly by an equal and opposite decrease in the cyclic energy transfer for the shear force. Indeed, since the shear force cyclic input power tends to zero in the low-frequency limit, the graph dips below zero, and for low frequencies the shear source becomes an energy sink. The surface displacements from Rayleigh and bulk waves excited by one normal source does positive work on the complementary displacement incurred at the other shear source, and the total energy transfer is unchanged.

It can be concluded that the total cyclic energy transfer incurred by a superposition of double normal and double shear forces is equal to the sum of the energy transfers from the sources considered separately. Although interaction effects will change the distribution of the power transfer between the sources, the total magnitude will be conserved.

4.4.8 Summary

To summarise, in this section, the expressions developed for the displacements incurred by single and double stress sources of finite width have been investigated and the behaviour characterised over all scales of validity. The modelling has been validated by comparison to Finite Element simulation. Surface and bulk wave contributions for general single and double sources, as well as the effect of the Poisson's ratio on the results, has been investigated. This work constitutes the first evaluation of the power transfer spectrum of elastic wave diffraction from a single or double uniform stress source of finite width extant in the literature.

4.5 Conclusions, limitations, and further work

The work undertaken in this chapter was begun with the intention of characterizing support loss in resonators supported by slender beams, with direct application to the XBR case. In the course of the investigation, it has been necessary to evaluate the power transfer from a general single source and a general double source, respectively

composed of a superposition of uniform normal and shear stresses. Thus, the input power spectrum for finite width single and double stress sources for an elastic isotropic medium has been evaluated. These problems can be viewed mathematically as finite single- and double-slit diffraction of elastic waves by a stress-free screen, respectively, and to the best knowledge of the author constitute the first treatment of this problem in the literature. As by-products, integral form expressions, along with a corresponding method for the systematic numerical evaluation thereof, have been derived in the form of the equations derived in Section 4.2 and evaluated in Section 4.4. As well as a quantification of the input power impedance, insight into the application of the reciprocality principle to symmetric double stress sources has been gained: to wit, it has been shown that the power spectrum of superposed shear and normal stress sources has a different distribution from that of the sources applied separately, but that the incurred total power transfer is conserved. It has also been shown in general that interaction phenomena of the order of the value of the measurement are incurred for a double source, which are not at all addressed by the Miller and Pursey approximation.

The author contends that this work is the first application of the elastic wave double-slit problem (finite or otherwise) to support loss models for MEMS devices, and additionally the first paper to address support loss from a double supported resonator on a bounded substrate, or to examine the interaction phenomena in detail. Aside from the theoretical interest, direct application may be found to modeling and mitigating support loss in supported mechanical resonators, and in particular XBRs. This is explored further in the sequel.

Some important observations from the support loss perspective are that for some choices of geometry and frequency of the resonator – in particular high-Q reservoirs attached by thin nodal ligaments, such as XBRs and certain suspended bulk resonator geometries – if the supports attach to a common substrate, then the radiation impedance can be more or less than twice the Miller and Pursey approximation (as has previously been modeled), with nontrivial consequences for support Q. In particular, constructive or destructive interference of Rayleigh waves, which do not diminish with distance for the present geometry, will respectively generate substrate resonances or

antiresonances, enhancing or diminishing energy transfer. By choosing the design support separation to be close to a half-integer multiple of the Rayleigh wavelength (with a small correction from bulk effects) at the operating frequency, support Q can be doubled and energy transfer halved from the Miller and Pursey approximation.

For MEMS devices with large planar substrates, the support Q model is expected to be accurate. However, macroscopic resonators will require large substrates to achieve limiting behavior appropriate to the models presented here. A valuable further contribution, then, would account for scattering and diffraction effects in a finite substrate where dissipation was localized in a smaller vicinity of the source, as for the prototypes presented in Chapter 6. The author suggests three possible approaches as viable here: modeling lossy inclusions in the half-plane, which has been described in the literature, to approximate bolted connections and fittings; using a Voight fractional-order elasticity model to simulate dry friction between substrate layers, again problematic in experiment; and numerical simulation using COMSOL or similar commercial code to model dissipative effects.

Another valuable extension would be to consider the effects of anisotropy, since many of the materials used in MEMS processes are anisotropic. However, this material assumption renders the analytical calculations far more difficult, as the Helmholtz scalar potentials must be replaced with a four dimensional vector potential analogous to the electromagnetic vector potential even in the two dimensional case, due to so-called beam steering. Numerical modeling would be suitable for a study of this type.

Finally, from a theoretical perspective, the resulting field at infinity as a function of polar coordinates would complete the characterization of the elastic-wave double slit problem. In the point-source approximation, the resulting displacement field in the bulk is expected to be a superposition of shear and bulk waves, beating spatially due to the difference in propagation velocities and decaying as 1/r, whilst at the free surface a Rayleigh wave will propagate without attenuation. The Fraunhofer diffraction pattern will be more complicated than for either the two-slit electromagnetic or acoustic problems, due to this complication. Treating the bulk and shear waves separately and superposing the result, one expects a pattern resembling the acoustic case for each wave type; their superposition will generally have modulated periodicity in the radial

coordinate and periodicity or quasiperiodicity in the radial coordinate, each having two Fourier components corresponding to the wave types. However, a complete derivation of this type is not needed for support loss applications, and remains an open problem.

4.6 References

[1] I. Newton, *Opticks: Or, a Treatise of the Reflections, Refractions, Inflections and Colours of Light*. Google Books, 1730.

[2] C. Huygens, *Traitė de la Lumiere*. Leyden / Gutenburg, 1690.

[3] H. Lamb, “On the Propagation of Tremors over the Surface of an Elastic Solid,” *Philosophical Transactions of the Royal Society A: Mathematical, Physical and Engineering Sciences*, vol. 203, no. 359–371, pp. 1–42, Jan. 1904.

[4] E. R. Lapwood, “The Disturbance Due to a Line Source in a Semi-Infinite Elastic Medium,” *Philosophical Transactions of the Royal Society A: Mathematical, Physical and Engineering Sciences*, vol. 242, no. 841, pp. 63–100, Jul. 1949.

[5] G. F. Miller and H. Pursey, “The Field and Radiation Impedance of Mechanical Radiators on the Free Surface of a Semi-Infinite Isotropic Solid,” *Proceedings of the Royal Society A: Mathematical, Physical and Engineering Sciences*, vol. 223, no. 1155, pp. 521–541, May 1954.

[6] G. F. Miller and H. Pursey, “On the Partition of Energy between Elastic Waves in a Semi-Infinite Solid,” *Proceedings of the Royal Society A: Mathematical, Physical and Engineering Sciences*, vol. 233, no. 1192, pp. 55–69, Dec. 1955.

[7] O.F. Afandi and R.A. Scott, “Excitation of an Elastic Half-Space by a Time-Dependent Dipole-I. The Surface Displacements due to a Surface Dipole,” I*nternational Journal of Solids and Structures*, vol. 8, pp. 1145–1161, 1972.

[8] Y. Jimbo and K. Itao, “Energy Loss of a Cantilever Vibrator,” *Journal of the Horological Institute of Japan(In Japanese)*, vol. 47, pp. 1–15, 1968.

[9] Z. Hao, “An analytical model for support loss in micromachined beam resonators with in-plane flexural vibrations,” *Sensors and Actuators A: Physical*, vol. 109, no. 1–2, pp. 156–164, Dec. 2003.

[10] H. Hosaka, K. Itao, and S. Kuroda, “Damping characteristics of beam-shaped micro-oscillators,” *Sensors and Actuators A: Physical*, vol. 49, no. 1–2. pp. 87–95, Jun-1995.

[11] J. Yang, T. Ono, and M. Esashi, “Mechanical behavior of ultrathin microcantilever,” *Sensors and Actuators A: Physical*, vol. 82, no. 1–3, pp. 102–107, May 2000.

[12] J. Yang, T. Ono, and M. Esashi, “Energy Dissipation in Submicrometer Thick Single-Crystal Silicon Cantilevers,” vol. 11, no. 6, pp. 775–783, 2002.

[13] D. M. Photiadis and J. A. Judge, “Attachment losses of high Q oscillators,” *Applied Physics Letters*, vol. 85, no. 3, p. 482, 2004.

[14] G. N. Bycroft, “Forced Vibrations of a Rigid Circular Plate on a Semi-Infinite Elastic Space and on an Elastic Stratum,” *Philosophical Transactions of the Royal Society A: Mathematical, Physical and Engineering Sciences*, vol. 248, no. 948, pp. 327–368, Jan. 1956.

[15] J. A. Judge, D. M. Photiadis, J. F. Vignola, B. H. Houston, and J. Jarzynski, “Attachment loss of micromechanical and nanomechanical resonators in the limits of thick and thin support structures,” *Journal of Applied Physics*, vol. 101, no. 1, p. 013521, 2007.

[16] Z. Hao and Y. Xu, “Vibration displacement on substrate due to time-harmonic stress sources from a micromechanical resonator,” *Journal of Sound and Vibration*, vol. 322, no. 1–2, pp. 196–215, Apr. 2009.

[17] J. H. Ko, J. Jeong, J. Choi, and M. Cho, “Quality factor in clamping loss of nanocantilever resonators,” *Applied Physics Letters*, vol. 98, no. 17, p. 171909, 2011.

[18] H. Grigg and B. J. Gallacher, “Efficient Parametric Optimisation of Support Loss in MEMS beam resonators via an enhanced Rayleigh-Ritz method,” *Journal of Physics: Conference Series*, vol. 382, no. 1, 2012.

[19] J.-P. Berenger, “A perfectly matched layer for the absorption of electromagnetic waves,” *Journal of Computational Physics*, vol. 114, no. 2, pp. 185–200, Oct. 1994.

Chapter 5. Optimisation

In this chapter, a synthesis of existing results on losses in mechanical resonators with the modelling work of previous chapters is formulated, giving a fairly complete quantitative characterisation of dissipative processes in XBR resonators. Next, noise analysis on XBM systems is performed. Previous modelling is extended to create a numerical tool capable of analysing XBR performance quickly, efficiently, and across a wide range of scales.

It is shown that parametric drive would be useful in developing a high-precision macroscopic XBR, which might find gainful use in terrestrial navigation applications. Additionally, theoretical limits on device performance at the microscale are discussed and potential applications are considered. Thus, a theoretical framework for discussing and predicting the force and field sensitivities of flexural XBRs of arbitrary geometry and isotropic material properties is proposed. Principles of XBR design are enunciated.

5.1 Introduction

The analysis presented in Chapter 2 provides a useful model of the XBM system from a control perspective, given the XBR's electromechanical characteristics and the choice of applied controls. On the other hand, the work in Chapters 3 and 4 provides a model capable of efficient evaluation of the mechanical performance and support dissipation respectively of the XBR system respectively as functions of the chosen geometry.

This chapter combines these approaches with approximations for other dissipative sources and noise to yield an integrated optimization tool for the XBR. The output consists of a prediction for the intrinsic limits on the sensitivity of the resulting sensor in terms of generalized force. The effect of noise is considered explicitly, and found to partition the performance behavior of an XBM into two regimes, corresponding to resonator or electronic noise dominance respectively. A model for the performance of the resonator in the presence of noise is developed, combining the approaches of the previous chapters with new modeling and extensions of techniques already in the

literature to constitute a system-level performance metric for an XBM. The model is implemented in MATLAB; the code is available online (Cf. Chapter 1).

Fundamental principles that will be frequently employed in this chapter include the Fluctuation-Dissipation Theorem (FDT) and the Equipartition Theorem (ET). The essence of the content of these classical theorems of equilibrium thermodynamics can be summarised as follows. Each degree of freedom of an equilibrium system possesses the same energy, related to the average energy of the system by Boltzmann's constant and the temperature. Dissipation consists of energy loss from the system to heat in its environment. However, the coupling is of course symmetric. This fact implies that thermal fluctuation in the environment is associated with a fluctuating force acting on the system, introducing noise. This thermal noise is shown in what follows to constitute a fundamental limit on the sensitivity of a mechanical resonant sensor.

There follows a numerical study of the performance of a Fused Silica high-Q XBR and a copper XBM, particular cases chosen for their theoretical and practical interest. The results highlight for the first time the existence of optimality conditions, dependent on all the geometric and material parameters, as well as the desired modality of operation. The overarching goal here is to develop a set of general guiding principles for the particular cases, and more widely to highlight the existence and importance of changes in the sensitivity of resonant sensors based on an XBR over the geometric and material parameter space.

Symbols		τ_{RELAX}	General relaxation time
ω, ω_n	Period of oscillation, natural frequency	η	Loss factor
S	General relaxation strength	$E, E_i, \bar{E}$	Youngs modulus, of i^{th} element, complex form
R	Ratio of sense to support energy storage	I, I_i	Second moment of area, of i^{th} element
A_x	Cross-sectional area	ρ	Material density
$\mathrm{R_E}$	Relaxation strength of Young's modulus	Q	Quality factor
T	Temperature	α	Linear coefficient of thermal expansion
η, η_B		b	
		ΔE	Cyclic energy loss
R_V	Sense to support potential energy ratio	V	Potential energy
X, X_i	Mode shape, i^{th} mode shape	x, x_i	Coordinate, of i^{th} beam
δ	Surface layer thickness	b	Out-of-plane width
h	In-plane height	D_S	Surface damping factor
P	Pressure	ℓ	Length
w	Out-of-plane width	ρ	Material density
h_0	Capacitive gap in reference configuration	M_{mol}	Molar mass
R	Ideal gas constant	$\hat{T}$	Slow time envelope of response amplitude
F	Forcing strength	$\mathrm{K_0}$	Generalised stiffness

Q_P	Parametric Q factor	ω_n	Natural Frequency
Φ_P	Parametric Phase	F_{NT}	Thermal-mechanical noise force
k_B	Boltzmann's constant	M_0	Generalised mass
$F_{LORENTZ}$	Lorentz force	$\Delta\omega$	Bandwidth
F_0^2	Generalised Lorentz force	$\mathrm{B}, \mathrm{B}_{\mathrm{MIN}}$	Magnetic field, minimum detectable
G_P	Parametric gain	X	Mode shape
ω_{CF1}	Clamped-Free fundamental natural frequency of an Euler-Bernoulli beam	K_{CF1_0}	Generalised stiffness of fundamental Euler-Bernoulli clamped-free mode
Q_{CF1}	Quality factor of clamped-free fundamental mode of an Euler-Bernoulli beam	V_{bias}	Electrode bias voltage
$\beta_n\ell$	Mode length factor	χ	Mode shape factor
		I_0	Sense current material density
I_{NP}, F_{NP}	Preamplifier noise current, equivalent noise force	I_{NT}, F_{NT}	Thermal-mechanical equivalent noise current, noise force
s		η_T	Thermal relaxation time
C_V	Heat capacity at constant volume	p	
NR	Nodepoint Ratio	Ri	Sense beam aspect ratio
Rs	Support beam in-plane height to sense beam length ratio	RL	Support beam length to sense beam length ratio
F_{EQ}	Equivalent force	$\ell_{SUPPORT}$	Support beam length
h_{SENSE}	Support beam in-plane height	ℓ_{SENSE}	Sense beam length
$h_{SUPPORT}$	Support beam in-plane height		

5.2 Q contributions in XBRs

Dissipation is a thermodynamic concept relating to the transfer of energy from ordered to disordered states. In particular, it has meaning only in a closed system with environment. In this context, any process that turns work or internal energy into heat, or does work on the environment, is considered to be dissipative. For instance, dry or viscous friction converts macroscopically ordered kinetic energy into macroscopically disordered heat, constituting a source of dissipation. To make analysis of the resultant effects tractable, it is necessary to identify and model the sources of dissipation explicitly.

In Chapter 2, an analytical model was presented for the XBR dynamics. Damping was assumed using a Rayleigh dissipation function; this is equivalent mathematically to assuming velocity-proportional damping for the harmonic case. However, no attempt is made there to examine the fundamental cause of the dissipation; the functional relationship is assumed to be of the viscous form, with the corresponding damping factor to be determined. Parametric pumping is shown therein to be capable of mitigating the amplitude effects of damping. However, in what follows it will be shown that in-phase components of thermal noise are amplified along with the desired signal. However, downstream noise arising from sense electronics is not affected; in the regime where downstream noise dominates, parametric amplification is expected to be beneficial.

To obtain a full understanding of dissipation in XBRs, consideration is now given to several sources of dissipation that are of relevance here. A brief review of the literature on each is given during the discussion, and the necessary modifications for application to the XBR case are made and discussed. The most applicable results are exhibited in Table 5.2 in the summary.

5.2.1 Bulk loss

Bulk Loss, also known variously as intrinsic loss, material damping, etc., refers to sources of dissipation arising from the composition of the resonator bulk material and ensuing irreversible processes during mechanical vibration. The physics is strongly

dependent on the material type, with metallic materials exhibiting quite different phenomena to semiconductors and other crystals, and is also predicated on the frequency and amplitude of excitation, as well as the temperature. In all cases, ordered elastic strain energy stored in deformed chemical bond configurations is converted to disordered heat in the bulk material. Dislocations, crystal imperfections, grain boundaries, microvoids and cracks, and other sources of disorder contribute to these effects in a fashion dependent on the form of the geometry and the vibrational displacements, as well as the frequency of excitation or resonance.

Very often, the process takes the form of an anelastic relaxation with a characteristic time scale τ_{RELAX}. When $\omega\tau_{RELAX} \approx 1$ then the period of oscillation is comparable to the relaxation period and significant loss occurs. When $\omega\tau_{RELAX} \gg 1$ then the period of oscillation is short compared to that of relaxation, and an adiabatic condition exists in which little relaxation and concurrent loss occurs. Conversely, when $\omega\tau_{RELAX} \ll 1$, then the oscillation is slow compared to the relaxation, and an isothermal, or fully relaxed, condition exists. In either of these limits, dissipation becomes very small. The comparison of timescales is described by a Lorentzian or Debye peak of the form $\eta = S\frac{\omega\tau_{RELAX}}{1+(\omega\tau_{RELAX})^2}$, where S is the "relaxation strength", or energy loss corresponding to a complete relaxation from the adiabatic to the isothermal state.

To make a connection to the system dynamics, it is necessary to introduce a term describing the dissipative action of the relaxation. One possible line of thought relates bulk losses to strains via the introduction of a complex Young's modulus $\bar{E}$ and a loss factor η , so that

$$\bar{E} = E(1 + i\eta) \tag{5.1}$$

Consider the effect of 5.1 on Rayleigh's method applied to a system of beams. The associated Rayleigh's quotient can be used to derive the dependence of the resulting natural frequency estimate as

$$\omega_n \leq \sqrt{R} = \sqrt{\frac{\bar{E}I\sum_{i=1}^{n}\int_0^{\ell_i}(u'')^2}{\rho A_x\sum_{i=1}^{n}\int_0^{\ell_i}u^2}} = \sqrt{E(1+i\eta)}\sqrt{\frac{I}{\rho A_x}}\sqrt{\frac{\sum_{i=1}^{n}\int_0^{\ell_i}(u'')^2}{\sum_{i=1}^{n}\int_0^{\ell_i}u^2}}$$

(5.2)

The inequality is exact when the trial function corresponds to a mode shape and has square-root dependence on the error in the trial function in the vicinity of the true mode shape. Taking the binomial expansion of the first radical and discarding higher order terms yields

$$\sqrt{\bar{E}} = \sqrt{E}\left(1 + \frac{i\eta}{2} - O(\eta^2)\right) \tag{5.3}$$

Factoring the Young's modulus and taking the case where the trial function is a true mode, we have

$$\overline{\omega_n} \approx \omega_n\left(1 + \frac{i\eta}{2}\right) \tag{5.4}$$

The Q factor contribution can be written as simply

$$Q^{-1} = \frac{2Im(\omega_n)}{Re(\omega_n)} = \eta \tag{5.5}$$

The phenomenon of intrinsic bulk loss is well studied. In Fused Silica, recent experiments[1–6] have yielded experimental values for high-purity annealed Fused Silica at standard temperature and frequencies of interest in this study. In copper, bulk loss mechanisms are also well characterised[7–9]. A detailed review and model for these loss mechanisms and in particular their frequency dependence is beyond the scope of this work: instead, the most suitable values will be adopted as a fixed parameter of the model. The values used are given in Table 5.2.

5.2.2 Thermoelastic Damping

Thermoelastic damping (TED) refers to a bulk relaxation effect caused by irreversible heat transfer that occurs due to dilatational strain and the antecedent oscillating thermal gradients induced in the bulk material of a resonator undergoing oscillatory motion. It was initially studied by Zener[10] in his seminal paper of 1930; the theory was extended and made slightly more precise, at the expense of increased algebraic complexity, by Lifshitz and Roukes (L&R hereafter) in 2000[11]. Zener's approach usually agrees with L&R's to within 1 per cent, and always to within 15 per cent;

furthermore, it is more intuitively transparent, fitting as it does within the framework described for bulk loss above. It is adopted herein.

In TED, the relaxation time is dependent on the applied strain field and hence on the geometry and modal characteristics, as opposed to an intrinsic mechanism. This feature distinguishes TED from intrinsic bulk loss. Figure 5.1 illustrates the mechanism.

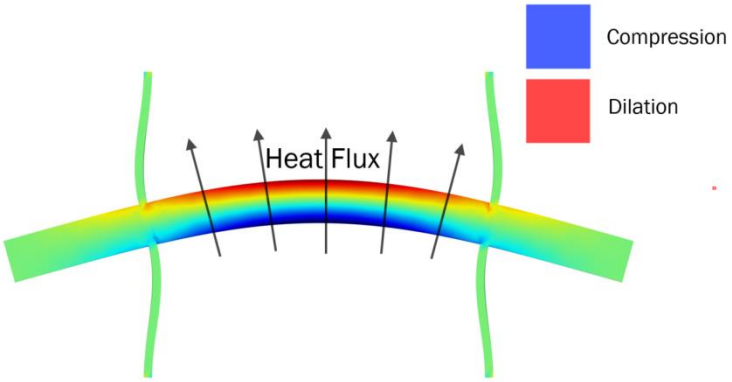

Figure 5.1 Illustration of the mechanism of TED, using a COMSOL FE analysis of an XBR. The heat map represents local volume change.

For an ideal resonator without loss, energy is exchanged between potential and kinetic energy over the harmonic cycle in a conservative fashion. The resulting strain fields cause localised variation in temperature, as shown in Figure 5.1. No dissipation has occurred at this stage; the temperature is behaving as an energy storage reservoir, and would contribute to the energy gradient for the generalised coordinate, modifying the generalised stiffness. The energy remains ordered.

The dissipative contribution arises due to irreversible heat transfer down thermal gradients in the material. This constitutes conversion of the ordered elastic strain energy into macroscopically disordered heat. It reduces the amplitude of the vibration, and appears in the equations of motion as a damping source and corresponding fluctuating noise force. Closed form analytical expressions are available from the above references for simple geometries. The assumptions used to derive the expressions are generally quite mild. They include:

- Linear isotropic elasticity and thermal diffusivity
- Elastic wavelength >> mean free path
- Elastic wavelength >> beam thickness

Under these conditions, TED in a thin beam can be quantified by the approximate expression of Zener[12]:

$$Q_{\mathrm{TED}}^{-1} = \mathrm{R_E}\left(\frac{\omega_0\tau}{1+\omega_0^2\tau^2}\right);\ \tau = \frac{b^2}{\pi^2\eta}\ ;\ \mathrm{R_E} = \frac{E\alpha^2 T}{C_v} \qquad (5.6)$$

Where $\mathrm{R_E}$ is the relaxation strength of the Young's modulus, E is the Young's modulus itself, C_v is the heat capacity at constant volume, α is the coefficient of thermal expansion, T is the ambient temperature, b is the beam out-of-plane depth, and η is the thermal diffusivity. This formulation is insightful; it expresses the TED contribution as a Debye peak, relating the timescale for thermal effects, τ, to the natural frequency of vibration. (5.6) is maximal with value $\frac{\mathrm{R_E}}{2}$ when $\omega_0\tau = 1$, and tends asymptotically to zero in the limits $\tau \to 0$ and $\tau \to 0$ for constant ω_0.

In L&R, this expression is shown to incur errors of order 1-2% for the cases of practical interest, tending asymptotically towards about 10% in the high-frequency limit.

In this picture, the mode shapes are not considered, since the third assumption renders their influence negligible (since the dominant heat transfer is transverse to the beam axis). Thus, the heat conduction equation can be reduced under these conditions to a one-dimensional form across the beam height, neglecting axial heat transfer as the corresponding gradients are vanishingly small. The error pointed out by L&R comes from the truncation of the series solution used to solve the thermal part of the coupled thermomechanical equations of motion.

From (5.6), what is necessary to minimise TED is thus to mistune the natural frequency of the resonator from the thermal scale of the diffusion. In the limit $\omega_0\tau \gg 1$, the system is asymptotically adiabatic; the time available for irreversible heat flow is vanishingly small. In the other limit $\omega_0\tau \ll 1$, the system is asymptotically isothermal; strain changes are so slow that the temperature gradients and the resulting dissipation is vanishingly small.

Equation (5.6) pertains to single beam resonators, and not frames such as the XBR. It is necessary to make some modifications before applying the theory to the case of

frame resonators. Let the frame be substructured into i elements, as described in Chapter 3. For each element, the assumptions of the L&R theory are satisfied; each is a thin beam structure undergoing primarily flexural vibrations with wavelengths long compared to the beam thickness. Adding the assumption heat flow "around the corners" - that is, between the sense beam and the support beam – is negligible is consistent with the assumptions already made neglecting axial heat transfer. The resulting insight is that, under vibration at a global natural frequency ω_n, the dissipation in each beam element is well approximated by the L&R theory, but the energy storage is not. The Zener Q contribution can be written as

$$Q_{ZENER}^{-1} = 2\pi \frac{\Delta E}{V} \tag{5.7}$$

Hence, the corresponding approximation for the cyclic dissipation is given by

$$\Delta E_{ZENER} = \frac{Q_{ZENER}^{-1} V}{2\pi} \tag{5.8}$$

By the preceding argument, for a substructured frame resonator, the total cyclic dissipation ΔE_{TOTAL} is given in terms of the element L&R contributions, evaluated at the global natural frequency:

$$\Delta E_{TOTAL} = \sum_{i=1}^{n} \Delta E_i = \frac{1}{2\pi} \sum_{i=1}^{n} (Q_{ZENER}^{-1} V)_i \tag{5.9}$$

The corresponding stored total energy can also be represented as a sum over the element energy losses in terms of the total mode shapes as:

$$V_{TOTAL} = \sum_{i=1}^{n} V_i = \sum_{i=1}^{n} \int_0^{\ell_i} E_i I_i \ddot{X}_i^{\,2} \, dx_i \tag{5.10}$$

Combining the results yields an approximation for the global Q of a substructured frame in terms of the known global natural frequency and element mode shapes as

$$Q_{FRAME}^{-1} = 2\pi \frac{\Delta E_{TOTAL}}{V_{TOTAL}} = 2\pi \frac{\sum_{i=1}^{n} (Q_{L\&R}^{-1} V)_i}{\sum_{i=1}^{n} V_i} \tag{5.11}$$

As an elementary fact worthy of note, this can be viewed as a special case of the Rayleigh's quotient, of finite dimension n. Q_{XBR}^{-1} is equal to the sum of the individual contibutions *if and only if* the V_i are an eigenvector of the linear dilatation operator defined by the Q_i. This circumstance corresponds to several trivial cases, such as V_i having a single nonzero component (only one element participates in the mode), or the elements being identical, in terms of both the Q and the stored energy in the global solution (cf. Section 3.2).

For the XBR case, the decomposition need not be along the lines of the seven elements described in Chapter 3. For symmetric modes, all the supports participate symmetrically in the resonance and can be considered as a single substructure. Similarly, the three sense beam elements can be regarded here as a single element. The expression (5.11) now reads

$$Q_{XBR}^{-1} = \frac{Q_{SENSE}^{-1} V_{SENSE} + Q_{SUPPORT}^{-1} V_{SUPPORT}}{V_{SENSE} + V_{SUPPORT}} = \frac{Q_{SENSE}^{-1} + Q_{SUPPORT}^{-1} R_V}{1 + R_V} \tag{5.12}$$

Where the ratio of the stored energy in the support to the sense beam is denoted by R. This form is particularly easy to implement during post-processing of the RRM solutions obtained in Chapter 3. The results are presented and discussed in the sequel. This approach is extended to use existing forms given in the literature for the other loss mechanisms considered below to the XBR case.

5.2.3 Surface Loss

Surface loss is a damping source that is particularly significant on the microscale. It arises from surface effects – adsorbents, surface energy, defects, etc., as the name suggests. It becomes increasingly dominant with increasing miniaturisation, as the surface area to volume ratio increases linearly with downscaling. It is rather difficult to find quantitative analytical approaches to modelling of the phenomenon in the literature, as opposed to experimental results pertaining to particular cases[13][14]. In the 2002 paper by Yang et al.[15], an expression for surface loss, based on assumptions of a linear elastic-Newtonian viscous layer of thickness $\delta \ll \min(b, h)$ overlying a linear elastic isotropic beam, is given as

$$Q_{SURFACE} = \frac{bh}{2\delta(3b+h)}\frac{E}{E_{DISS}} \tag{5.13}$$

Where E_{DISS} is the imaginary component of the surface layer Young's modulus and the other quantities are as previously defined. This provides a useful theoretical framework for the analysis of surface loss and its parametric dependence, but the parameter E_{ds} is typically inferred by experiment, as it is expected to depend on the detail of adsorbates, oxides, residual stresses and defects that constitute the surface layer.

For the purpose of extrapolating to the present case, it was not practical within the scope of the project to begin experimental characterisation of surface properties under experimental conditions. Instead, inference is made from existing results. Taking the limiting case of high out-of-plane aspect ratio for the sense and support beams, i.e. $\frac{b}{h} \gg 1$, in the surface loss dominant regime one has directly from (5.13)

$$Q^{-1} \approx \frac{6\delta}{h}\frac{E_{DISS}}{E} = \left(\frac{V}{S}\right)^{-1}\frac{3\delta E_{DISS}}{E} = D_S\left(\frac{V}{S}\right)^{-1} \tag{5.14}$$

Where the surface dissipation factor D_S is defined by the expression $\frac{3\delta E_{DISS}}{E}$. Data is available from Advanced LIGO from which is possible to infer this parameter, and is summarised below.

Study	Material	D_s
[3]	Suprasil 2	$1.21 \times 10^{-11}\ m$
	Suprasil 312	$6.5 \times 10^{-12}\ m$

Table 5.1 A summary of surface loss-limited Q factors in beam microresonators and the corresponding inferred surface dissipation factors, as defined by (5.14).

The values above are not applicable to the analysis of metallic resonators in the present study. Studies on surface losses in metal resonators are not available to the

author; in any case, the relatively large bulk and thermoelastic effects in metals are likely to render surface effects negligible for all but the smallest length scales.

Under the aforementioned assumptions, for a beam resonator, surface loss is approximated by

$$Q_{SURFACE} = \frac{h}{2D_s} \tag{5.15}$$

Since surface effects constitute perturbative local dissipation contributions, no interaction between the surface dissipative processes in the sense and support beams is anticipated. We adopt the approach of the previous subsection to substructure the XBR into the sense beam and the lumped support beams. The parallel argument again yields (5.12). As in the TED case, this constitutes a new approximate expression for surface losses in an XBR, and again this will generalise directly to other substructured systems, such as frame resonators, for which the assumptions of the theory are valid.

5.2.4 Gas Damping

Gas Damping refers to any dissipative effects having their origin in the gaseous environment of a resonator. For instance, a cantilever in a free gaseous half-space undergoing small-amplitude deflection may incur several conceptually separate sources of damping. Laminar oscillatory flow of the gas environment will be produced by harmonic displacements of the beam, dissipating the kinetic energy of the vibration to heat in the gas. Acoustic waves will also be produced, propagating energy away from the resonance and constituting a source of dissipation in the system. These effects are grouped under the term free space gas damping.

More complicated (and generally much more dissipative) forms of gas damping arise when the resonant body is in close proximity to other bodies. The capacitive gaps that exist in any electrostatic transducer are primary examples. A thin, almost planar film of gas can be trapped between the electrode and the resonator. If the primary direction of displacement coincides with the normal to the plane of the film, the motion of the resonator acts to harmonically pump gas into and out of the gap at the boundaries. Several conceptually and mathematically separate sources of dissipation can arise

directly from this interaction, depending on the operating conditions and geometry. This mode of gas damping is termed squeeze-film damping.

In a similar vein, a thin gas layer may be trapped between the resonator and its substrate with the film oriented such that the displacement vector of the resonator is parallel to the plane. In this configuration, the gas film is sheared, rather than squeezed. This leads to a quite different functional expression for the damping, with respect to the squeeze-film case. The term *slide-film damping* is used widely in the literature to refer to this phenomenon. The two different configurations are illustrated in Figure 5.2.

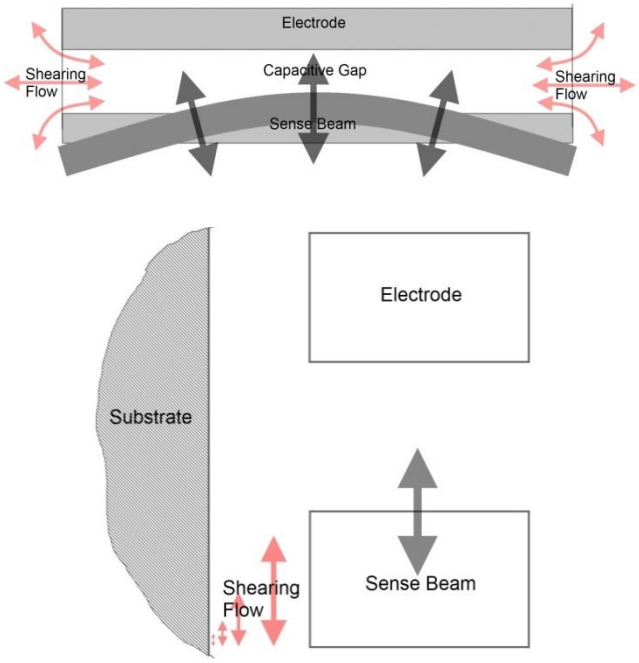

Figure 5.2 Top to bottom, Illustration of the mechanisms of squeeze-film and slide-film damping.

Squeeze-film and slide-film damping, where present, generally dominate any free space damping component. An excellent review of gas damping effects is given in the 2007 paper[16] by Bao et al. Therein can be found an in-depth examination of the mechanisms and physics of the dissipative effects of thin gas films in mechanical resonators.

In the present work, the prototype designs presented in Chapter 6 are designed such as to eliminate any slide films, by ensuring adequate out-of-plane clearance between the resonator and its substrate. However, squeeze-film losses cannot be so easily

mitigated. Thus, squeeze-film losses during operation of an XBR under medium vacuum are considered in the evaluation. Bao et al. give as an experimentally-validated expression in this pressure regime the following:

$$Q_{\mathrm{GAS}}^{-1} = (2\pi)^{\frac{2}{3}} \frac{2(\ell + w)P}{h\omega_1 \rho h_0} \sqrt{\frac{M_{\mathrm{mol}}}{RT}} \tag{5.16}$$

Equation (5.16) is applicable for a thin cuboidal film undergoing squeezing normal to its largest areas in the molecular regime, which is to say at pressures such that the continuum approximation is inapplicable and the gas molecules can be treat as kinetic particles neglecting interaction. This requires that the mean free path of the molecules is much larger than the capacitive gap, so that plate-molecule collisions are predominant and molecule-molecule collisions are negligible. For air, the mean free path can be approximated as

$$MFP = 10^{-2}P \tag{5.17}$$

Where MFP is the mean free path length in metres and P is the gas pressure in Pa. Since the principal dimension of the capacitive gaps considered in this study and more generally in typical capacitive actuators are on the order of $100\mu m$, it can be safely concluded that at pressures of 1 Pa or less, the conditions are met and the equation is applicable. Since no electrodes are in close proximity to the sense beams, no account needs be made of the loss therein; however, to consider the breakdown of the dominance of the modal participation by the sense beam it is necessary to account for energy storage in the sense beam. The corresponding modification to (5.12) is

$$Q_{\substack{XBR \\ GAS}}^{-1} = \frac{Q_{SENSE}^{-1}}{1 + R} \tag{5.18}$$

5.2.5 Support Loss

A model for support loss in the XBR case was developed in detail in Chapter 4. The literature on support loss in other beam resonators is also discussed therein, and does not bear recapitulation here. The models presented there are appropriate to XBRs with large substrates with good separation between the left- and right- hand sides of the resonator, which is well met for micromachined devices. Finite-substrate effects in

macroscopic resonators are likely to reduce the support Q further with a similar parametric variation (i.e. quadratic dependence on the support forces), but are beyond the scope of this project.

5.2.6 Summary

Expressions have been derived or obtained for XBRs for dissipative contributions in XBRs that are valid for a wide range of length scales. The important results are presented in summary form in Table 5.2.

Source	Analytical expression (cantilever)	Reference	XBR modification
Squeeze-film damping	$Q_{\mathrm{GAS}}^{-1} = (2\pi)^{\frac{2}{3}} \frac{2(\ell + b)P}{h\omega_1 \rho h_0} \sqrt{\frac{M_{\mathrm{mol}}}{RT}}$	[16], Equation 5.19	$\frac{Q_{SENSE}^{-1}}{1 + R_V}$
Thermoelastic damping	$Q_{\mathrm{TED}}^{-1} = \left(\frac{6}{\xi^2} - \frac{6(\sin(\xi) + \sinh(\xi)}{\xi^3 \cos(\xi) + \cosh(\xi)}\right)$	[12], Equation (19)	$\frac{Q_{SENSE}^{-1} + Q_{SUPPORT}^{-1} R_V}{1 + R_V}$
Support loss	$Q_{\mathrm{SUPPORT}} = \left[\frac{0.24(1-\nu)}{(1+\nu)\Psi}\right] \frac{1}{(\beta_N \chi_N)^2} \left[\frac{\ell}{b}\right]^3$	[17], Equation (39)	See Chapter 4
Surface loss	$\frac{2Q(3b + h)}{Ebh}$	[15]	$\frac{Q_{SENSE}^{-1} + Q_{SUPPORT}^{-1} R_V}{1 + R_V}$
Intrinsic loss	$Q_{INTRINSIC}^{-1} = \frac{\mathrm{Re}(\omega_n)}{\mathrm{Im}(\omega_n)}$	-	$\frac{Q_{SENSE}^{-1} + Q_{SUPPORT}^{-1} R_V}{1 + R_V}$

Table 5.2 Dissipation contributions as characterised in the literature for a cantilever, under appropriate assumptions.

5.3 Magnetometer analysis

In Chapter 2, it was shown that, if parametric drive is assumed but nonlinear effects are neglected (or mitigated by the techniques of that chapter), the response is approximated by Equation (2.69). For a general forcing of strength $|\mathrm{F}|$ (in newtons), the response can be written in the modal generalized coordinate $\hat{T}$ as

$$\hat{T} = \frac{|\mathrm{F}|}{4\mathrm{K}_0} \mathrm{Q}_P \cos(\omega_n \hat{t} + \Phi_P) \tag{5.19}$$

It is clear from this formulation that the response under the assumed controls that the steady-state response is proportional to the forcing strength and Q_{P}, and inversely proportional to the classical generalised stiffness. Q_{P} reduces to the classical Q factor when electrostatic stiffness modulation effects are neglected, but can be made arbitrarily large by an appropriate choice of the phases and magnitudes of the frequency components of the electrostatic voltage. The quantity can be regarded as an effective Q factor for the system under the action of time-dependent electrostatics. In principle, then, the maximum parametric gain G_P, definied by $G_P = \frac{\mathrm{Q}_P}{Q}$, is infinite. However, in practice, nonlinear effects preclude the unbounded amplification of a desired signal in this fashion by the onset of chaotic instability[18]. Some values of G_P reported in the literature are summarised below.

Title and lead author	Best stable parametric gain achieved	Reference
Thompson, M.J. et al., "*Parametrically Amplified X-Axis Lorenz Force Magnetometer*"	82.5	[19]
	51	[20]
Hu, Z. et al., "*An Experimental Study of High Gain Parametric Amplification in MEMS*"	100	[18]
Sharma, M. et al., " *Parametric Amplification / Damping in MEMS Gyroscopes*"	25	[21]

Table 5.3 A selection of representative values for achieved stable parametric gain from the MEMS literature

The author of the present work is not aware of any modelling work in the literature capable of capturing the onset of parametric instability in a relevant fashion. The approach adopted in the design analysis that follows will be to assume a representative value for the achievable parametric gain, and to neglect the influence of design on the onset of parametric instability.

5.3.1 Response of a resonant sensor in the presence of noise

According to the model presented by Equation (5.19), the response exhibits infinitely fine resolution of the input signal $B(t)$. This ideal performance is of course not realised in practice. Often, the most important limiting factor in sensor performance is the presence of noise. For the following noise analysis, it is convenient to employ the language of signal processing to express the system response in terms of block diagrams and transfer functions in the frequency domain.

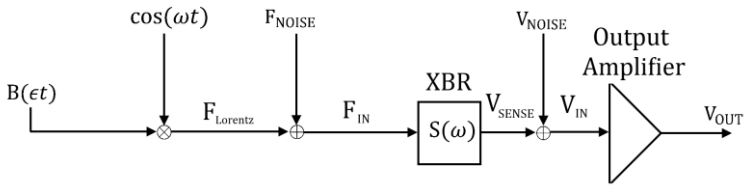

Figure 5.3. Noise model of XBR sensor system (After [19]).]

From the perspective of design and optimisation, it is necessary to quantify the performance of such a system in the presence of noise. Attention now turns to answering this question. The methodology is developed in a general fashion applicable to all resonant Lorentz magnetometers; the simple model of a cantilever resonator is first considered to illustrate the principles, before examining the particular case of the XBM.

The most fundamental noise source present in any resonant magnetometer system is Brownian noise associated with thermodynamic heat in the system. Brownian noise has been well characterised in the literature[22], [23]. Using the Fluctuation-Dissipation theorem and the Equipartition Theorem, the spectral power density of the generalised noise force F_{NT} arising from Brownian thermal motion in a particular mode of a mechanical resonator, assumed to be in thermodynamic equilibrium, can be shown to be [24]

$$F_{\mathrm{NT}}^2 = 4k_B TC = 4k_B T \frac{M_0 \omega_n}{Q} \tag{5.20}$$

where k_B is Boltzmann's constant, T is the ambient temperature, C is the motional resistance, and the quantities ω, M_0 and Q are respectively the generalised stiffness, natural frequency, generalised mass, and corresponding classical Q factor. Application

of parametric amplification will amplify the in-phase, but not the out-of-phase, component of this noise[25]. Assuming the noise is not phase correlated with the response leads to the expression for the total thermal noise power density in the measurement bandwidth F_{NT} as

$$F_{NT}^2 = (2 + 2G_P^{-1})k_B TM\frac{\omega_n}{Q} \tag{5.21}$$

where F_{NT} is the time-averaged RMS noise force component at resonance under high-gain parametric amplification. On the other hand, the power density of the signal of interest is the generalised Lorentz force $F_{LORENTZ}$ acting on the resonator divided by the bandwidth $\Delta\omega$, yielding:

$$\frac{F_{LORENTZ}^2}{\Delta\omega} = \frac{B^2 F_0^2}{\omega/Q} \tag{5.22}$$

Where the term F_0 represents the generalised Lorentz force acting on the resonator per unit applied field. Assume that the field strength corresponding to the minimum detectable signal B_{MIN} occurs at a signal-to-noise ratio of unity. It follows from (5.21) and (5.22) that at the detection limit,

$$\frac{B_{\mathrm{MIN}}^2 F_0^2}{\left(\frac{\omega_n}{Q}\right)^2 (2 + 2G_P^{-1})k_B TM} = 1 \tag{5.23}$$

And hence

$$B_{MIN} = \frac{\sqrt{(2 + 2G_P^{-1})k_B TK_0}}{QF_0} \tag{5.24}$$

B_{MIN} is seen to depend on the modal factors χ and $\beta_n\ell$; the environmental and material properties T, E and k_B; resonator geometric parameters ℓ, b and h; and the resonator classical Q.

As a simple illustrative example, the method is applied explicitly to calculate the noise-limited sensitivity of a cantilever-based Lorentz magnetometer, before proceeding to numerical evaluation for the XBR case.

5.3.2 Sensitivity of a Cantilever Lorentz magnetometer

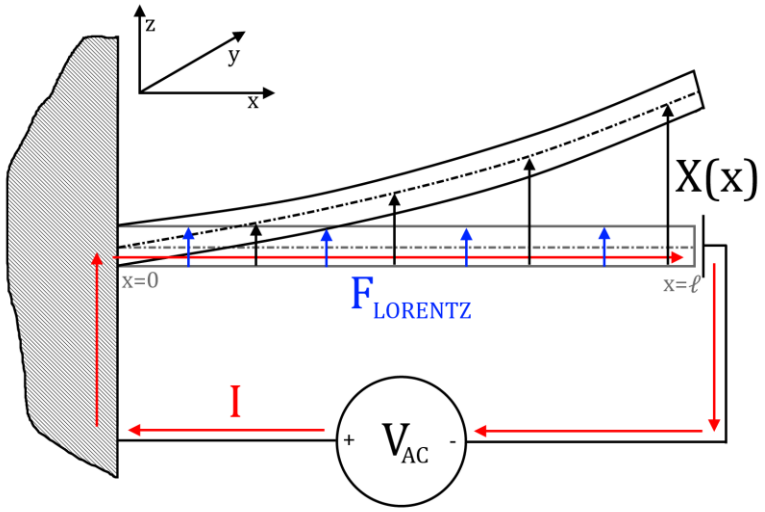

Figure 5.3 Clamped-Free Lorentz magnetometer. In the illustrated coordinate system, the applied magnetic field B is assumed constant and parallel to the y direction. The current I is assumed spatially uniform. Since I is time-harmonic, the Lorentz force and resulting deflection are also time-harmonic.

The fundamental mode shape and corresponding natural frequency for a cantilever can be given explicitly in terms of the beam geometry and material parameters in the following forms[26]

$$X(x) = \sin\left(\frac{1.875}{\ell}x\right) - \sinh\left(\frac{1.875}{\ell}x\right) + 1.3622\left(\cos\left(\frac{1.875}{\ell}x\right) - \cosh\left(\frac{1.875}{\ell}x\right)\right) \tag{5.25}$$

$$\omega_{CF1} = 3.516\sqrt{\frac{Ebh^3}{12\rho A_x \ell^4}} \tag{5.26}$$

The corresponding generalised stiffness is then given by

$$K_{CF1} = EI\int_0^{\ell}(XX'''')^2 dx \tag{5.27}$$

The support losses in a clamped-free beam resonator undergoing vibration in its fundamental mode are known to be of the form[17]

$$Q_{CF1} = 2.081\left(\frac{\ell}{h}\right)^3 \tag{5.28}$$

where the numerical constant depends only on the Poisson's ratio of the material and well-known modal factors; its form is related to the integrals dealt with in Chapter 4, and is given explicitly in the reference. In the case of a constant amplitude time-harmonic uniform current and constant transverse magnetic field, the generalised Lorentz force power $F^2_{LORENTZ}$ can be expressed in terms of the resonator mode shape $X(x)$ as

$$F^2_{LORENTZ} = (BF_0)^2$$
$$= B^2 I^2 \left(\int_0^{\ell} X^2 dx \right)^2 \qquad (5.29)$$

Assuming the current is set by choosing a thermally limited current density I_0, and by combining (5.25)-(5.29), (5.24) can be explicitly cast as

$$B_{MIN} = \frac{\sqrt{Ebh^3(2 + 2G_P^{-1})k_B T \int_0^{\ell} (XX'''')^2 dx}}{2.081 \left(\frac{\ell}{h}\right)^3 I_0 bh \int_0^{\ell} X^2 dx} \qquad (5.30)$$

For the case of a practical system with capacitive readout and active preamplification of the output signal as described in Figure 5.4, account needs to be made of two further mechanisms: the capacitive transduction and the input-referred electronic noise of the preamplifier.

The capacitive transduction translates the dependence of the resonator displacement amplitude into an output current displacement amplitude. The relation is expressed by (2.40) Assuming a constant bias voltage, one can describe the signal output current I_{out} as

$$I_{out} = V_{bias} \frac{dC}{dt} = V_{bias} \frac{i\omega_n \varepsilon_0 A_x}{h_0^2} \frac{|F|Q}{K_0} G_P \qquad (5.31)$$

Solving for the equivalent force corresponding to a current at the preamplifier input F_{EQ}, one has

$$\frac{K_0 h_0^2 I_{out}}{Q V_{bias} G_P \omega_n \varepsilon_0 A_x} = F_{EQ} \qquad (5.32)$$

Introducing an input-referred current noise density for the preamplifier circuit I_{NP} and the equivalent force density F_{NP} the output signal to noise ratio (SNR) is given by combining (5.32) with (5.21) and (5.22) as

$$SNR = \frac{F_B^2}{\Delta\omega(F_{NT}^2 + F_{NP}^2)}$$

$$= \frac{B^2 F_0^2}{\frac{\omega_n}{Q}\left((2 + 2G_P^{-1})k_B T M \frac{\omega_n}{Q} + \left[\frac{K_0 h_0^2 I_{PN}}{Q V_{bias} G_P \omega_n \varepsilon_0 A_x}\right]^2\right)} \tag{5.33}$$

And the field sensitivity is

$$\frac{\sqrt{(2 + 2G_P^{-1})k_B K_0 T + \frac{1}{Q}\left[\frac{K_0 h_0^2 I_{PN}}{V_{bias} G_P \omega_n \varepsilon_0 A_x}\right]^2}}{Q F_0} = B_{MIN} \tag{5.34}$$

By using parametric amplification, it is possible to force the electrical noise floor below the thermal noise floor, such that the thermal limit is achieved, if

$$\frac{Q V_{bias} G_P \omega_n \varepsilon_0 A_x (2 + 2G_P^{-1}) k_B T}{h_0^2} \gg I_{NP}^2 \tag{5.35}$$

for the maximal attainable stable parametric gain.

Some calculated numerical values for a cantilever with the properties given in Table 5.4 under a uniform scaling are plotted in Figure 5.4.

Parameter	Description	Value	Unit	Comment
$Material$	–	–	–	Steel
T	Ambient temperature	300	K	Lab temperature
I_0	Sense current density	5×10^6	$A\,m^{-2}$	Thermal limit for steel wire in vacuum
I_{NP}	Input-referred current noise	1×10^{-8}	A	Typical for low-cost electronics
ℓ	Length (axial)	$1 \times 10^{-S}, S \in \{2:4\}$	m	Swept parameter
b	Depth (out of plane)	$\ell \times r$	m	Fixed aspect ratio
h	Height (in plane)	$\ell \times r$	m	Fixed aspect ratio
r	Aspect ratio	$r \in \{5,10,15\} \times 10^{-2}$	–	Stepped parameter

Table 5.4 Cantilever properties and parameters. Coordinate references are with respect to Figure 5.4.

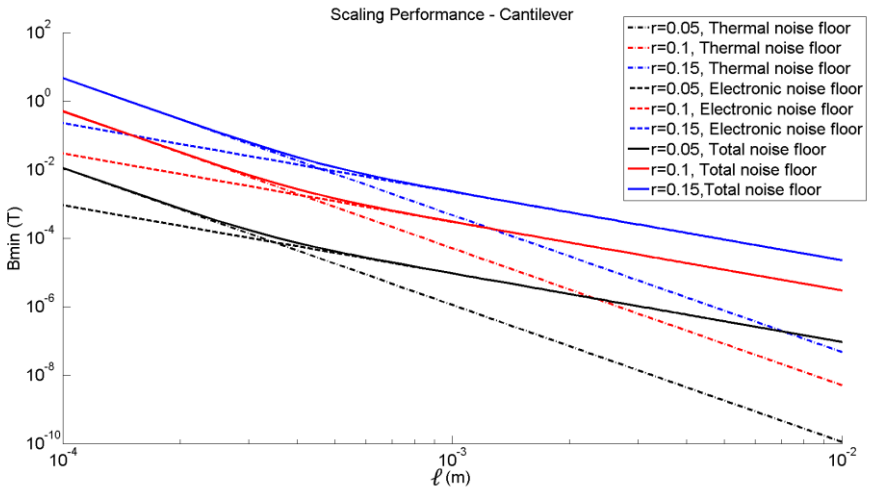

Figure 5.4 Plots of thermal, electrical, and total noise limits detectable field B_{MIN} as the cantilever length ℓ is changed, for several fixed values of the aspect ratio. For each plot, the in-plane aspect ratio and the absolute out-of-plane depth are held constant.

In Figure 5.4, the Brownian limits on a macroscopic cantilever Lorentz magnetometer are illustrated. The range of field sensitivities for the chosen parameter values is from the order of single $T/\sqrt{Hz}$ for a $100\mu m$ cantilever of $15\mu m$ thickness to a value on the order of 10 $\mu T/\sqrt{Hz}$ for a $1cm$ cantilever of $500\mu m$ thickness. The trend for more slender structures yielding higher sensitivity is made plain.

The information presented in this subsection would allow a designer to optimise a *support-loss dominant* resonant cantilever for use as a Cantilever Lorenz Magnetometer (CLM) by minimising the noise floor. The forms of (5.34) suggests some simple design rules for some assorted scenarios:

- If no geometric constraint is reached, then maximise out-of plane depth b and length ℓ, while minimising the in-plane height h. A cost function for maximisation is then given by $P = h^{\frac{7}{2}}\ell^{-\frac{11}{2}}b^{-\frac{1}{2}}$.
- If b is constrained (for example by a maximum available substrate thickness or etch depth in micromachined cantilevers), then the length should again be maximised while the aspect ratio is minimised. The corresponding cost function is $P = r^{\frac{7}{2}}\ell^{-2}$.
- If the aspect ratios are held fixed, the profit function is of the form $B_{MIN} \propto s^{-5/2}$, where s is a scaling parameter; hence make the cantilever as large as possible.

In summary, the analysis of noise-floor performance for the CLM has been constituted by the following steps:

- Derive the dependence of the minimum detectable signal on the environment and resonant properties of the device
- Examine the relations between the resonator geometry and the quantities of interest
    - The formulations presented here are specific to the cantilever, and do not generalise directly to more complex geometries.
    - For the XBR case, numerical formulations have already been presented in the preceding chapters for obtaining these quantities

- Derive design optimisation criteria for noise floor performance.

An important goal of the current work is to develop tools to allow the development of expressions of this form for the XBR case, considering *all* relevant sources of dissipation and general enough to deal with a wide range of length scales and materials. However, the derivation is less straightforward. In particular, closed-form analytical expressions for the support Q factor are not available and have proven difficult to obtain for the XBR, owing to the wave dynamical interactions in the substrate.

5.3.3 Sensitivity of an XBR

The condition (5.34) assumes the resonant frequency, mode shapes and support loss behaviour of a cantilever beam. It provides the designer with a closed-form characterisation of the limiting performance of such a device under parametric control, provided that the terms are well characterised and no unanticipated noise sources are present.

The thermal noise floor model was developed for the cantilever as

$$B_{MIN}^{THERMAL} = \frac{\sqrt{(2 + 2/G_p)K_0 k_B T}}{F_0 Q} \tag{5.36}$$

To account for the effects of noise in the detection electronics, we introduce a representative current noise PSD for a low-noise current preamplifier as given for a typical modern instrument by [27] as

$$I_{NP}^2 \approx (5 \times 10^{-14})^2 \tag{5.37}$$

Referring this current to the resonator as an equivalent force, we obtain

$$F_{NP} = \frac{I_{PN}\sqrt{M_0 K_0} h_0^2}{V_{BIAS}\varepsilon_0 A_x Q G_P} \tag{5.38}$$

The SNR is again given by

$$SNR = \frac{F_B^2}{\Delta\omega(F_{NT}^2 + F_{PN}^2)} \tag{5.39}$$

This is the formulation that was used to evaluate the noise-limited spectral resolution of the XBRs. When the thermal noise dominates, parametric gain yields a factor asymptotically approaching $\sqrt{2}$. However, when the electrical noise dominates, parametric gain can be used to push down the noise floor and increase the sensitivity in a linear fashion until the thermal limit is hit or parametric instability sets in.

To evaluate the expression, numerical values for the following quantities are required

- Mode shapes and natural frequencies
    - Achieved via the RRM model presented in Chapter 4
- Q factor
    - Support loss studied in Chapter 4
    - Other sources considered in Section 5.2
- Generalised Lorentz force, generalised stiffness
    - Can be easily evaluated by employing the RRM solutions

It should be noted that the generalised stiffness and generalised force have different dependencies on the mode shape, and thus their modal dependence does not cancel for an XBR.

5.4 Q factors and resonant sensing performance

The major contributions to dissipation for monolithic planar beam resonators over the range of scales relevant to the problem are discussed in Section 5.2. From this position, it is possible to evaluate the terms in the performance metric developed in Section 5.3.2 to examine the expected performance of an XBM as a function of the geometry, the noise characteristics of the ancillary electronics, and the material and environmental parameters. An exhaustive characterisation of XBR properties across all materials and scales is of course not possible. With a view to the potential applications, two materials – Fused Silica and Copper - corresponding to suitable choices for an XBM fabricated via Wire EDM and for a standalone high-Q resonator in an insulating material not suitable for an XBM.

In the numerical study that follows, the performance model is evaluated over a number of different governing length scales, set by fixing the length of the sense beam

ℓ_{SENSE} to one of four values, such that $\ell_{SENSE} \in \{3 \times 10^{-1}, 3 \times 10^{-2}, 3 \times 10^{-3}, 3 \times 10^{-4}\}$. A common out-of-plane thickness d_{COMMON} is assumed for each length scale, defined by $d_{COMMON} = \frac{\ell_{SENSE}}{3}$. The other parameters required to completely define the XBR geometry are the sense beam in-plane height h_{SENSE} and the support beam length and in-plane height, $\ell_{SUPPORT}$ and $h_{SUPPORT}$ respectively. It is more convenient to define these quantities by their corresponding ratios to the governing length scale, termed Ri, RL, and Rs respectively. Thus, the relationships $h_{SENSE} = \frac{\ell_{SENSE}}{R_L}$, $\ell_{SUPPORT} = \frac{\ell_{SENSE}}{R_L}$, and $h_{SUPPORT} = \frac{\ell_{SUPPORT}}{R_S}$ hold. Before proceeding to the analysis, a brief review and summary of the XBR parameters utilised in the modelling and the values they assume for the particular material cases is given here.

Parameter	Cases examined	Symbol/ abbreviation	Comment
Material	Copper, Fused Silica	-	Wire EDM / Semiconductor processes
Sense Beam Length	3×10^{-1} – $3 \times 10^{-4}\ m$	ℓ_{SENSE}	Macroscale - Microscale
In-plane aspect ratio of sense beam	11-25	RI	P3A=15 P3B=45
Ratio of lengths of sense and support beams	3-8	RL	P3A=P3B=6
In-plane aspect ratio of support beam	5-25	RS	P3A=P3B=25
Node point ratio	0.2-0.25	NR	As defined in Chapter 4

Table 5.5 Description and range of parameters evaluated in the subsequent analysis. Cf. Chapter 6.

We proceed to the analysis, organising by material. The first to be considered is Fused Silica.

5.4.1 Fused Silica: Losses

Fused silica is an amorphous glass consisting of the compound silicon dioxide formed by high-temperature melting and thermal fusion of silica crystals. The resulting highly pure material has unusual thermal and mechanical properties that permit fabrication of low loss, high Q mechanical resonators. It is typically produced as sheet of varying thickness and dimensions. Water jet cutting can be used to fabricate precision planar

structures in fused silica. The surface finish can then be flame polished just below the melting point, followed by a slow anneal, to relax residual stresses and surface roughness, thus avoiding performance degradation via surface and bulk losses. It has been shown experimentally that beam resonators are capable of realising extremely high Q factors in fused silica, due to the low bulk, surface and TED losses encountered. Support loss is often a limiting factor on fused silica resonator Q factors. The XBR geometry is well suited to these properties, in that the extremely high support Q factors achievable will allow the low intrinsic loss properties to be reflected in the total Q. Its potential as a high-Q XBR will be assessed in this context. Note that it is not a suitable material for an XBM, since it is nonconductive and the introduction of a conductive skin or tracks would both severely degrade the surface Q, whilst imposing a relatively low limit on the maximum applicable sense current before thermal effects intervene compared to a solid-conductor XBR.

In order to utilise the performance model, input material parameters are required and provided as summarised in Table 5.6.

Parameter	Description	Value	Reference	Comment
η_B	Bulk loss factor	2.32×10^{-8}	[2]	Annealed Suprasil 312
D_S	Surface loss factor	0.05	[14]	Annealed Suprasil 312
η_T	Thermal diffusivity	8.14×10^{-7}	[1]	Generic
α	Linear coefficient of thermal expansion	3.9×10^{-7}	[1]	Generic
C_V	Volumetric heat capacity	1.694×10^{6}	[1]	Generic
p	Environmental Pressure	$1 \times 10^{-4}\ Pa$	-	Cf. Chapter 6
$T_{AMBIENT}$	Ambient temperature	2.93×10^{3}	-	Controlled lab environment

Table 5.6 Model input parameters considered for Fused Silica

At each scale, dissipation contributions and their parametric dependence are examined. The first case to be considered is that of a macroscopic planar XBR with a large planar substrate, fabricated from sheet, operated in vacuum at room temperature. The model predictions for the total Q factor under these conditions, as the support location parameter NR is varied against the in-plane aspect ratio Ri, are given below:

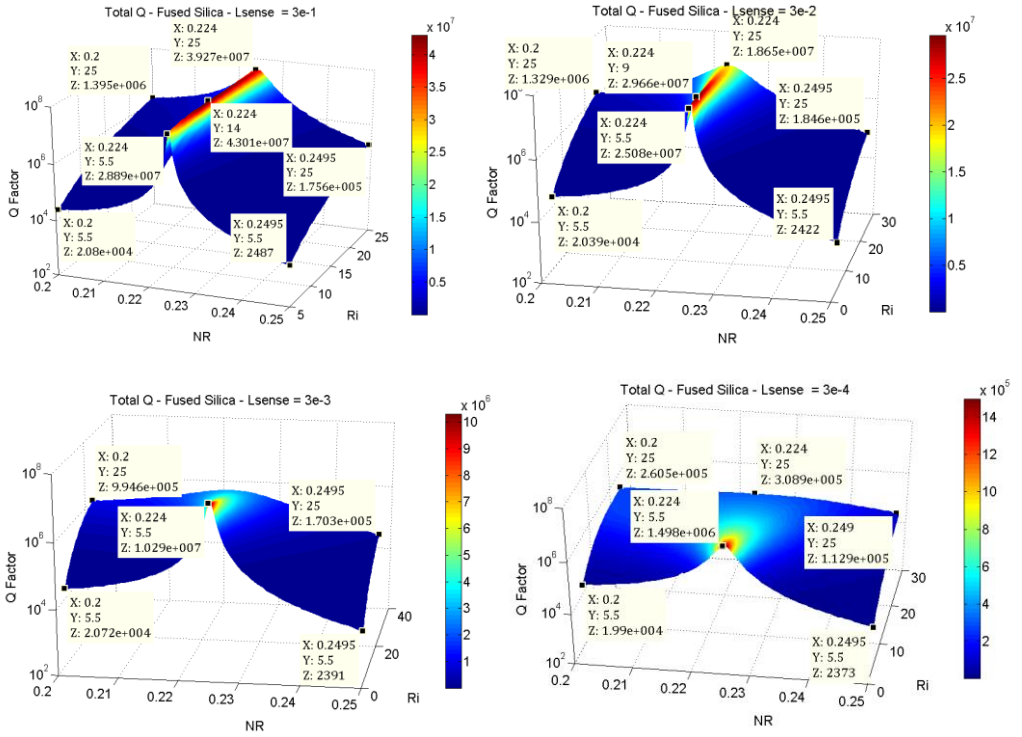

Figure 5.5 Total Q factor of a Fused Silica XBR under the specified conditions, as the parameters Ri and NR are varied over a 100x100 equidistant grid, for selected values of the sense beam length scale.

Several trends are interesting to observe in the data presented in Figure 5.5. Firstly, the quality factors show a peak around the expected optimal NR value for all scales, implying that the XBR design is yielding significant improvement in the quality factor. For the larger length scales, there is an optimum RI value. However, for the smaller length scales, the Q factor is higher for smaller RI values (thicker sense beam) over the range considered. Secondly, the predicted Q factors are high, with peak values in the range $Q = 1.5 \times 10^6 - 4.5 \times 10^7$ from the shortest to the longest length scales. These high theoretical values, which are in line with the best results presented in the literature[3], are close to the bulk loss limits on the larger length scales; another mechanism must limit Q factors on smaller scales.

The very high support Q generated by the XBR geometry, as well as the assumptions of a well-prepared sample with very good bulk and surface loss properties and the excellent thermoelastic dissipation of the material, demonstrate the potential of the XBR geometry to produce superb high Q resonators at all the scales considered.

The effect of the nodal impedance tuning is shown by the reversal in the Q factor trend for tuned NR values. When the NR value is close to the optimum, a thicker sense beam can be used to store more energy and hence improve the Q; conversely, for the mistuned cases the Q factors decrease monotonically with a thicker sense beam, implying that the increased dissipation more than offsets the greater energy reservoir provided by increasing the sense beam thickness under this condition.

The dissipative behaviour clearly varies with scale. The overall Q factors are progressively lowered as the length scale is decreased, while the Q peak around the tuned NR value becomes less pronounced. The dominant sources of dissipation that limit Q and explain the forms shown in Figure 5.5 are studied next.

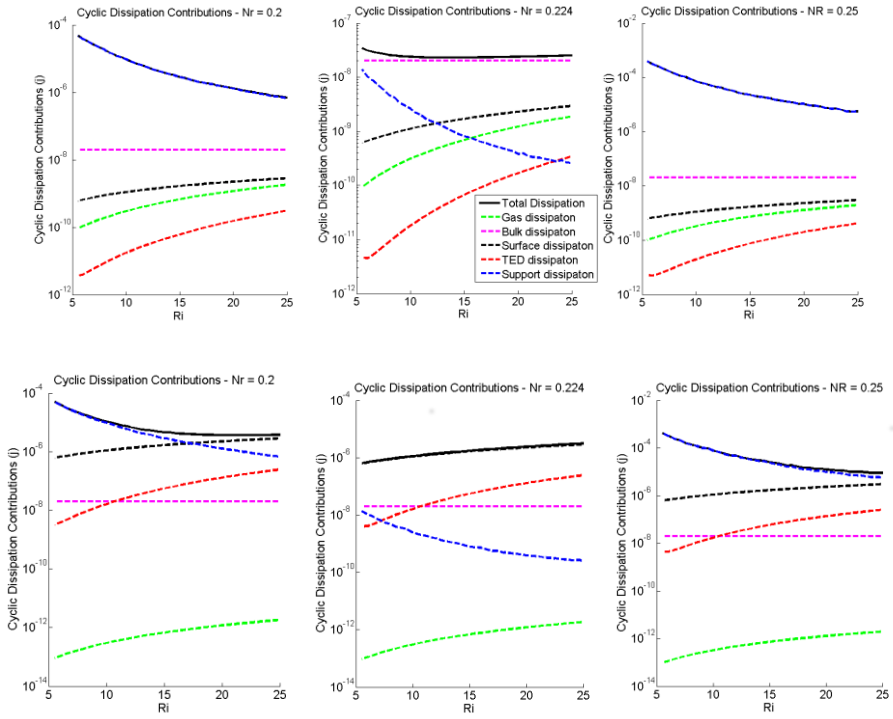

Figure 5.6 Top to bottom, Comparison of cyclic dissipation contributions from all considered sources for fused silica XBR for the largest and smallest length scales considered, respectively. The values are plotted for the tuned nodepoint ratio and also for two mistuned values, as indicated in the individual plots. Comparison is made at room temperature under medium vacuum conditions.

For all the plots in Figure 5.6, the contribution from support loss decreases as Ri increases; the reason will be examined subsequently. The contribution is mitigated by fully four orders of magnitude for the tuned value, compared to the mistuned values, for both length scales. Bulk loss remains constant, as expected, while TED, gas

damping, and surface losses increase with increasing Ri. On the largest scale, bulk loss is dominant when NR is tuned; on the smallest, surface effects dominate. The support loss contribution does not change with scaling. This is concordant with the previously reviewed analytical results for cantilevers.

The mechanism by which the support-tuning peak is progressively masked as the length scale is decreased is seen to be the scale-related increase of surface and TED effects. Considering the top row of plots, which pertain to the largest length scale, dissipation is dominated by support loss at all mistuned nodepoint ratios, while at the tuned nodepoint ratio support loss is strongly attenuated and a combination of bulk and gas effects dominate. Notably, for a tuned XBR, low values of the in-plane aspect ratio Ri are favourable, while for a mistuned design (such as a Clamped-Clamped or H-frame resonator), it is favourable to have a smaller Ri in order to mitigate support loss. TED effects are the smallest effect for nearly all parameter choices on this length scale and for this material choice.

On the other hand, looking at the bottom row of plots corresponding to the smallest length scale considered, the situation is different. The relative contribution of surface effects is greater at this scale, commensurate to the linear increase in surface area: volume as the scale is linearly decreased over four orders of magnitude. The TED contribution is also significantly increased relative to the other effects at this length scale. Surface effects dominate over most parameter choices considered, with the exception of some competition from support loss at the mistuned NR =0.25 at the lower Ri values. It should be noted that even this mistuned case is superior to a clamped-clamped or cantilever in terms of minimal support loss by at least an order of magnitude; the relative insignificance of support loss at these aspect ratios is a manifestation of how effective the operating principle is at mitigating support loss.

Another salient observation from the dissipation contribution components presented is the striking difference in support Q between the optimal case, and the mistuned cases, where respectively the support beams are attached to close to the distal ends and the centre of the sense beam. It should be noted that this change corresponds to a total geometric mistuning of the order of $\pm 2.5\%$ over the range considered. The corresponding support Q contributions differ by a factor that is close to $10^{3.5}$. This is a

striking demonstration of the power of the geometric impedance tuning corresponding to the notion of an XBR to reduce the support loss by a linear factor exceeding ten thousand; and of the need to consider fine tolerances and mistuning effects in designing a supported resonator for high Q.

In contradistinction to the larger length scales, it is seen in Figure 5.6 that higher Q factors are obtained at smaller Ri values at the microscale, due to mitigation of the dominant surface effects in this limit. Competition from support loss for the mistuned case generates another turning point and corresponding parametric optimum for NR =0.25, Ri=13.

To examine the operating principle in more detail, attention is directed to the relative contribution from the shear and normal forces at the support-substrate interface, corresponding to flexural and axial loading of the support element:

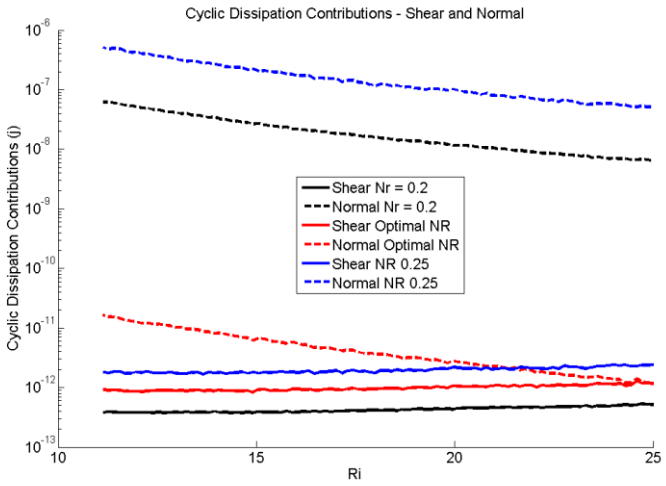

Figure 5.7 Dissipation contributions to support loss from shear and normal forces at the support-substrate interface, for the tuned NR value and two others as indicated, for a fused silica macroscopic XBR with sense beam length $3x10^{-1}m$ at room temperature under medium vacuum conditions.

One particular case is considered in Figure 5.7, but the patterns are similar, with a little quantitative variation, across all models considered here. The dotted lines refer to losses due to axial loading, while the solid lines refer to losses due to flexure in the support. It is striking that for the mistuned NR values, corresponding to the black and blue plots, the normal loss is strongly dominant, approaching five orders of magnitude greater at low Ri values; whereas, for the optimal NR, the normal losses are

attenuated strongly while the flexural losses remain of the same order. Indeed, for Ri values greater than about 21, flexural loss is dominant. This effect corresponds to nulling of axial support loss by placing the supports at the node points of the vibration, and constitutes the first theoretical or quantitative justification of the geometric impedance tuning design principle of the Xylophone Bar Resonator

The transmission of waves from the sense beam to the substrate can be regarded as a port impedance, due to the existence of the Green's function. The dominant part of the reciprocal impedance, for NR values away from tuning, is shown here for the first time to be very strongly attenuated, because the fundamental mode of the sense beam is orthogonal to travelling axial waves in the support, at and only at the tuned value.

Returning to Figure 5.6, the Q peaks around the optimal NR value, but the peak is only around a linear factor of three or four greater than the mistuned values. This effect is due to the way in which Q contributions sum in a parallel fashion to produce the overall Q, combined with the effect of the exchange of dominance between support loss and the aggregated effects of gas, bulk, and TED dissipation that occurs at tuned NR values.

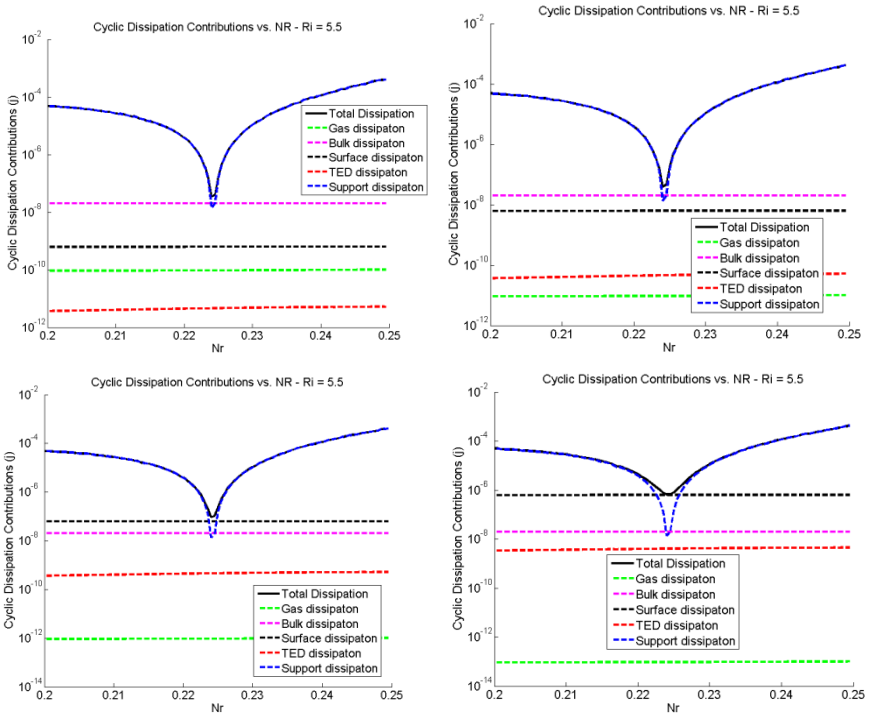

Figure 5.8 Top left to bottom right, contributions from different mechanisms of dissipation in a fused silica XBR with fixed beam lengths and aspect ratios as NR is varied in an interval of the optimal value, for a length scale of 3×10^{-1}, 3×10^{-2}, 3×10^{-3}, and 3×10^{-4} metres respectively.

In Figure 5.8, it can be seen that for the largest length scales, support loss varies over five orders of magnitude for the given modulation of NR. This is the direct effect of the geometric impedance tuning in an XBR. The blunting of the total Q by surface effects as the scale is decreased is also evident again here. The width of the dissipation antipeak at the point where it is crossed by the bulk dissipation curve represents the interval over which the largest single dissipative contribution is support loss; that is to say, the support loss-dominant regime. Its value is around $NR = NR_{OPTIMAL} \pm 0.025\%$, indicating that for the dimensions considered, the manufacturing process tolerance needs to be much smaller than $75\mu m$ in order not to significantly attenuate the resulting device Q, on a part with largest functional dimension $\ell = 300mm$. The corresponding sensitivity on the smallest scale is relatively lower, but demands the absolute tolerance be much smaller than $750nm$ in order to maintain Q, highlighting the need for high precision manufacturing in order to fully exploit the potential available.

Some results on the predicted flexural mode shapes are presented next, and their variation is interpreted in the context of the preceding results.

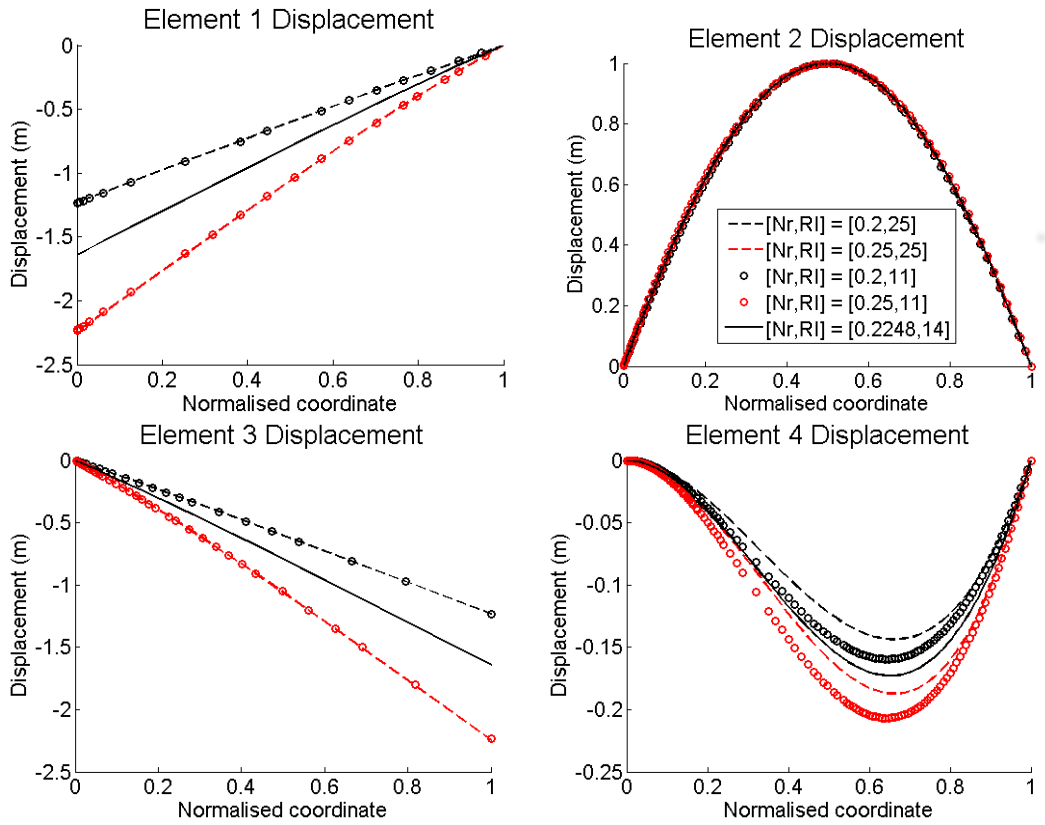

Figure 5.9 Top left to bottom right, Transverse deflection in the fundamental mode for a fused silica XBR: left, central, and right elements of the sense beam, and one of the four support beams, plotted for $Lsense = 3 \times 10^{-1}$ and some selected pairs of values for NR, Ri.

The forms of the mode shapes presented in Figure 5.9 reveal some interesting features. The deflection in the sense beam, but not the support beams, depends on the in plane sense aspect ratio Ri. This can be interpreted as a manifestation of dominance of the sense beam over the modal dynamics: the system is well approximated by taking the sense beam's mode shape to be fixed (and close to that of a free-free beam when NR is tuned), driving the sense beam whilst itself only being infinitesimally perturbed by the interaction. Mathematically, the modal mass participation factor of the sense beam is dominant. The response of the whole dynamical system, including the substrate, can be approximated as a one-way chain of couplings: the sense beam dominates the support beam, which in turn dominates the substrate, as per Chapter 3. In this picture, as the sense beam in plane aspect ratio is varied, the support beam is forced at a different frequency but in the same modality,

and responds with a different modal superposition to satisfy the dynamic boundary conditions (neglecting the perturbative contribution from support loss, which leads to a small travelling wave in the sense beam and support beam motions being superposed on the modal solution corresponding to energy efflux). This picture is in concordance with the results of numerical computation.

Attention turns next to consideration of the effects of tuning the other parameters defining the XBR geometry, Rs and Rl.

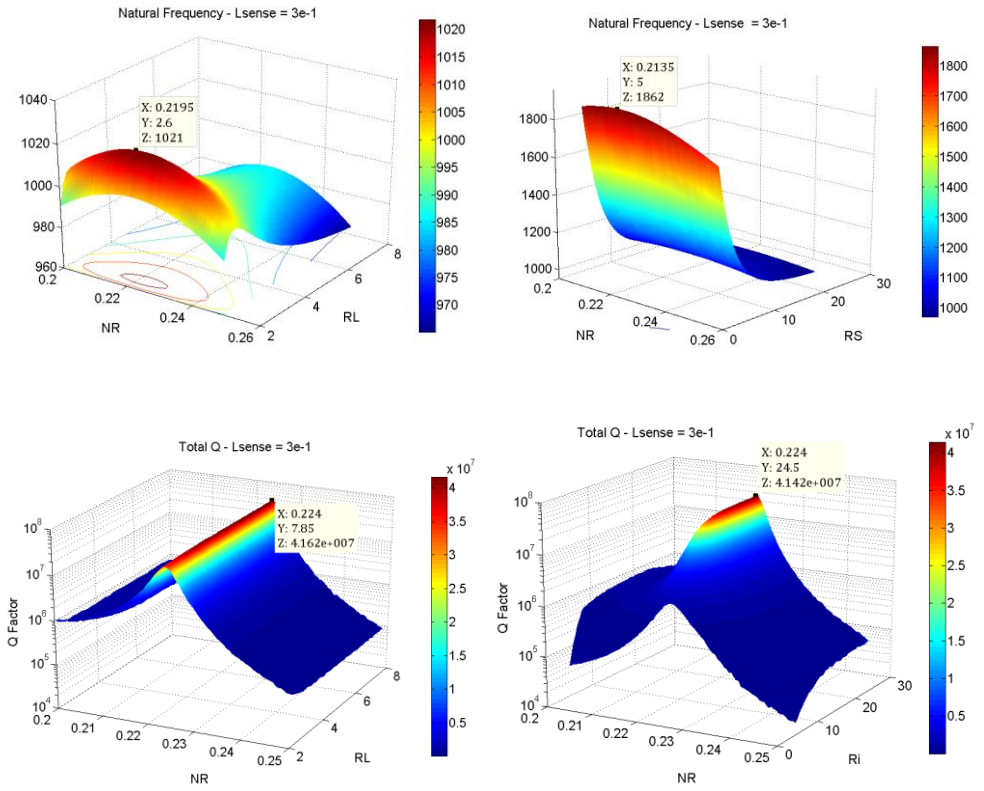

Figure 5.10 Variation of natural frequencies and total Q factor of a Fused Silica XBR at the largest length scale considered, as the parameters RS and RL are varied.

It is clear from Figure 5.10 that the natural frequencies and Q factors do not depend strongly on the length of the support beam for the range of parameters considered, as would be expected for a dominant sense beam. The natural frequency exhibits a marked peak at RL=2.6, corresponding to equal natural frequencies of the support and sense beams, considered independently. Above this value, in the sense-dominant picture, the support beam is being driven above its natural frequency: below, it is being driven below its natural frequency, in the fundamental pinned-pinned mode.

On the other hand, both quantities vary in a more pronounced fashion with the sense beam aspect ratio Rs, particularly at the smaller values considered, corresponding to a thick support beam. As the modal participation of the support becomes more significant at small RS values, where the support beam is being driven well below its natural frequency while its flexural stiffness rises cubically, it pushes the system natural frequency up. Correspondingly, the flexural component of support loss begins to dominate, pulling the total Q down. For the parameters considered, the transition

region above which the Q factor and natural frequency is roughly independent of the support thickness is between 10 and 15.

5.4.2 Copper: Losses

Copper is in many ways an ideally suited material for fabrication of a macroscopic XBR by planar manufacturing techniques. It is readily available in sheet or plate in a range of thicknesses in highly pure grades, since mass produced electrical goods utilise the low resistivity of high purity, oxygen-free copper in commercial volumes. A suitable choice here is ASTM Grade 1 (C10100). It is specified as at least 99.99% pure, with less than 0.0001% oxide content. Its thermal conductivity is the highest of any metal, while its electrical resistivity is amongst the lowest. These attributes are ideal for high electrical performance, in that the sense current is limited by both quantities in a linear fashion so that the aggregate effect of a uniform scaling of both values is quadratic. However, the gains in sensitivity yielded by the excellent thermal properties of copper must be evaluated against the potentially adverse TED tuning, with respect to the beam natural frequencies and thermal relaxation times. Its relatively high bulk loss effectively masks surface and gas effects, which are therefore excluded from the analysis.

Parameter	Description	Value	Reference	Comment
η_B	Bulk loss factor	5×10^{-4}	[8]	Annealed C10100, STP
η_T	Thermal diffusivity	1.11×10^{-4}	[8]	C10100
C_V	Volumetric heat capacity	3.45×10^{6}	[8]	C10100

Table 5.7 Model input parameters considered for Fused Silica.

The total Q factors at all length scales, are presented below.

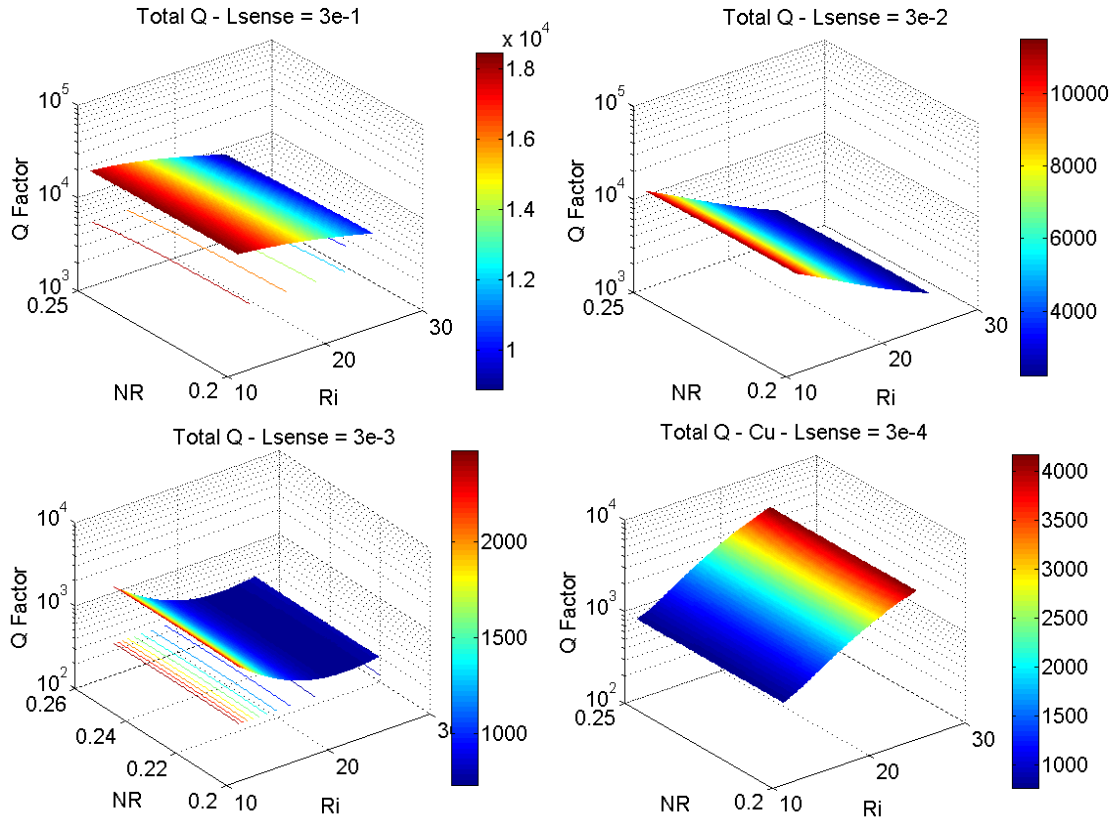

Figure 5.11 Plots of total Q against Ri and NR for a copper XBR over the 4 length scales considered.

The most dramatic difference evident in Figure 5.11 from the fused silica case is in the form of the variation in the total Q. with NR. It is almost independent of NR for the considered parameters, implying that support loss is not a significant contribution to total dissipation for this particular case. On the other hand, it shows quite pronounced dependence on Ri, which changes sense as the length scale varies. The peak Q factors are four orders of magnitude lower than the equivalents in Fused Silica. To ascertain the limiting factors on the Q factor, it serves to examine the dissipation contributions. Only the extremal length scales need be considered to illustrate the trend.

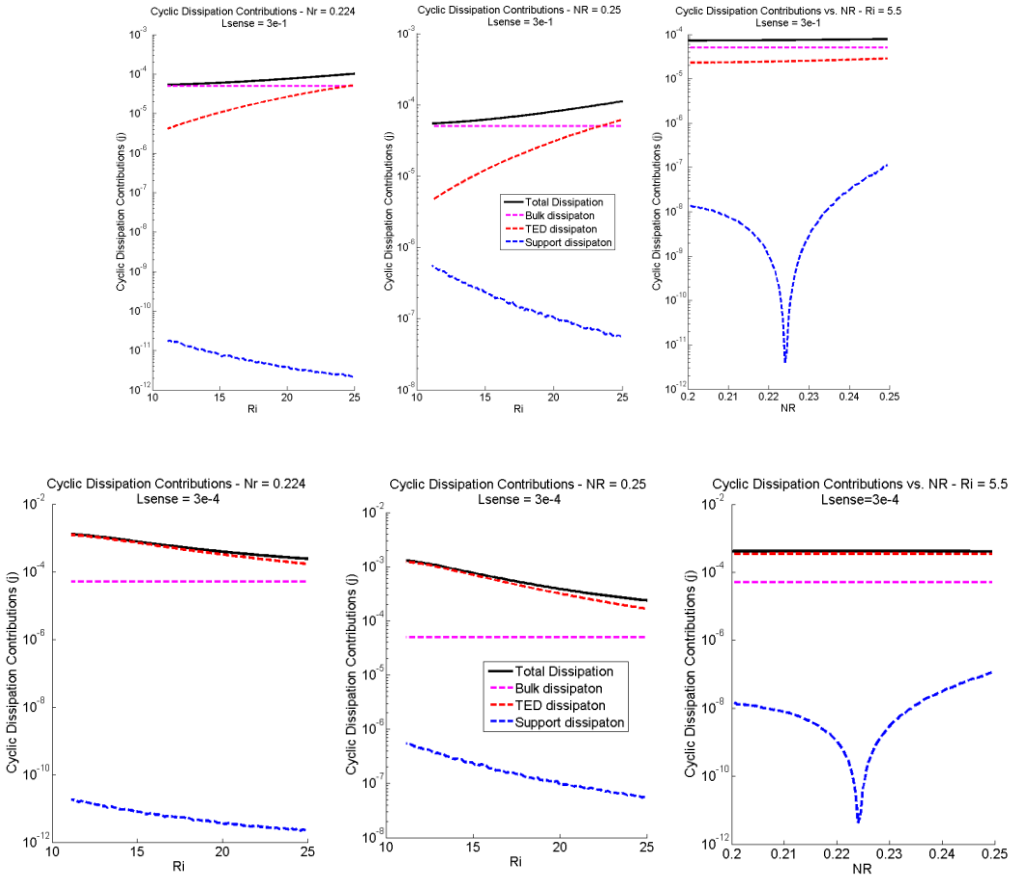

Figure 5.12 Dissipation contributions against NR and RI for the largest and smallest length scales considered, as calculated for copper XBRs.

The dominant effects on all scales and for all considered parameter permutations in Figure 5.12 are bulk loss and TED. On the smaller length scale, TED dominates, showing a trend towards lower loss and higher Q as Ri is increased. On the other hand, for the largest length scale bulk loss predominates, with TED losses increasing at higher Ri values. Support loss is around two orders of magnitude lower than these effects at 2.5% mistuned NR, falling to over six orders of magnitude at the tuned NR over both length scales considered. The change in the sense of the dependence of total Q on Ri observed in Figure 5.11 is shown to be on account of TED losses exhibiting the same behaviour. On application of Zener's formula 5.6 to the sense beam, it can be seen that the relaxation peak is encountered for Ri around 20 on the length scale $Lsense = 3e - 3$. For the larger length scales, the relaxation time is longer than the natural frequency: for smaller scales it is shorter, for the range of Ri values and hence sense beam thicknesses considered. From a design perspective, then, the optimal

choice of sense beam height depends on understanding where on the Zener anelastic relaxation curve the design lies, and choosing the thickness to mistune the relaxation time accordingly.

5.4.3 Force and Field Sensitivities

The foundational interest in the resonant properties of XBRs lies in exploiting high-Q behaviour as components in a larger system. Although the high predicted Q factors certainly would allow the XBRs to be gainfully employed in timing circuits and signal processing applications, attention is concentrated here on the particular case of the copper XBM. Two aspects are considered: the thermal noise-limited force resolution, and the field sensitivity as an XBR. Additionally, force resolution is considered for the silicon XBR.

The field sensitivity is presented as a series of surface plots. In each plot, a geometric parameter is varied against a uniform scaling factor. All quantities are scaled in a consistent fashion, including the resonator geometry, the capacitive gap, and its biasing voltage. Electrical current noise is held fixed, corresponding to an external current-to-voltage converter.

The sensitivity is determined by a complicated interaction between thermal and electrical noise, dissipation, and mode related characteristics such as generalised mass, stiffness, and Lorentz force. In each case, an attempt is made to understand the underlying mechanism accounting for the observed patterns.

5.4.4 Fused Silica: Sensitivity

Firstly, we consider the limits on generalised force sensing using a Fused Silica XBR. It is not appropriate to consider the field sensitivity or the electrical noise floor in the XBR context here, since the resistive nature of the material precludes the application of a sense current or capacitive actuation. Instead, the generalised force detection limits imposed by the assumed thermal noise floor is presented. The form of (5.39) indicates that this limit depends only on the generalised mass and stiffness of the resonator, and the dissipation. The XBM case is more complex; this quantity interacts with electrical noise and the generalised Lorentz force; it is considered subsequently.

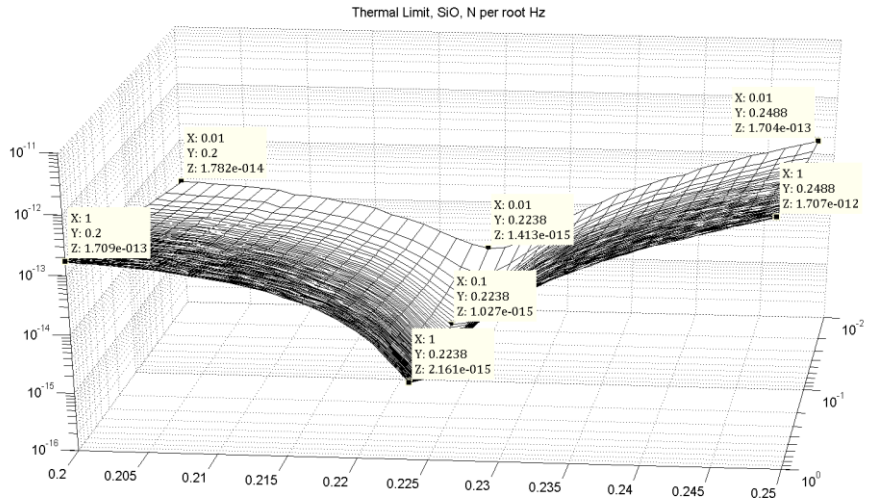

Figure 5.13 Thermal limits on force sensing for a Fused Silica XBR, as the parameter NR is varied against uniform scaling over two orders of magnitude. The length scale zero is $Lsense = 3 \times 10^{-1}\ m$.

The form the thermal limit plotted in Figure 5.13 exhibits a deep valley around NR =0.2242. The z axis is logarithmic, and yet the valley is pronounced nevertheless, illustrating clearly the advantage of using an XBR geometry to mitigate support loss. The penalty for mistuning of the order of 5 per cent varies between one and three orders of magnitude, decreasing with length scale by around one order of magnitude over the two orders of length scale presented. There is a locally optimal scale between the extrema considered, close to $Lsense = 3 \times 10^{-2}\ m$; the minimum detectable force is on the order of $1 \times 10^{-15}\ N$; the thermal limit is less than 50% larger than this value at the shortest length scale.

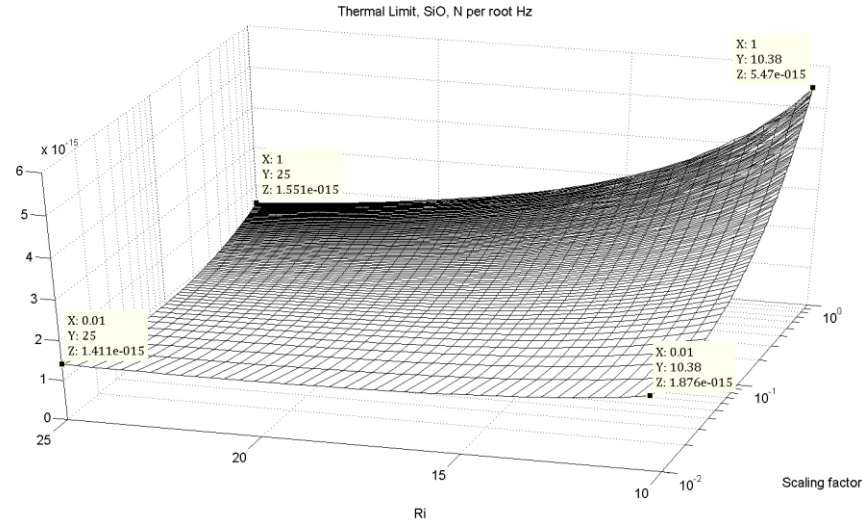

Figure 5.14 Surface plot of thermal limits on force sensing for a Fused Silica XBR, as the parameter Ri is varied against uniform scaling over two orders of magnitude.

The variation of the force sensitivity as the in-plane aspect ratio Ri is changed is plotted in Figure 5.14, for the optimal node point ratio. This can be seen as the product space of the valley floor in Figure 5.13 and another dimension of the parameter space, namely the scaling parameter. There is little attenuation in the force sensitivity with scale for the larger Ri values (thinner sense beams), while there is a somewhat pronounced decrease at the lower Ri values. In the other direction, Ri seems to have little effect at the smaller length scales, but a moderate increase at lower Ri (thicker sense beam) is seen at larger scales. Locally optimal scales can be seen to exist as Ri is varied, and are examined in Figure 5.15.

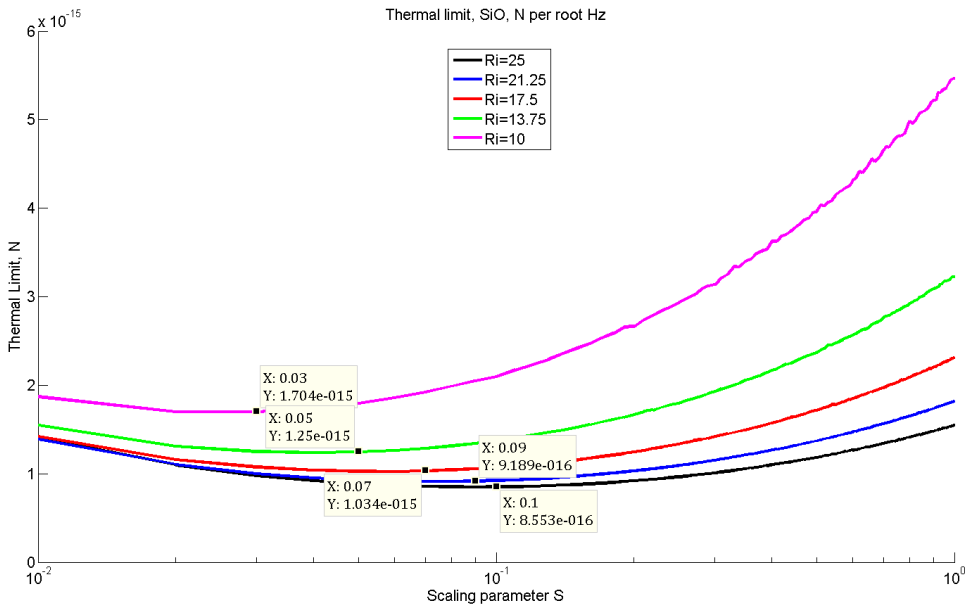

Figure 5.15 Thermally limited force sensitivity for a Fused Silica XBR against scale for several values of the in-plane aspect ratio Ri.

It is clear that to each Ri value corresponds a unique sensitivity-maximising length scale. Correspondingly, by plotting the locus of the minimal limit as Ri varies, it is possible to obtain a plot of the optimal Ri value for an arbitrary scale. It is interesting that the sensitivity is larger for a thinner sense beam over the range of parameters considered. To try to draw out the underlying cause of the trends in the data, we return to dissipative contributions as the parameters are varied.

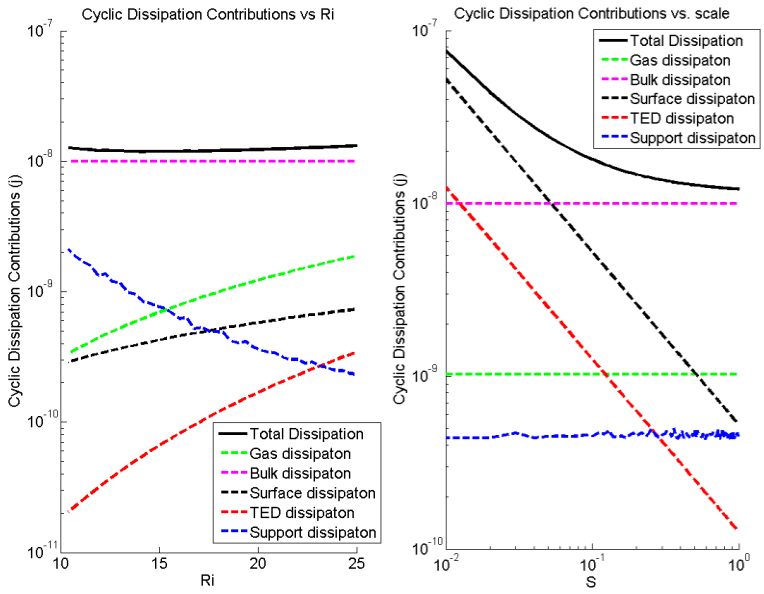

Figure 5.16 Right to left variation of the dissipation contributions for a Fused Silica XBR with Ri and scaling respectively, for a Silica XBR. The length scale datum is $L_{SENSE} = 3 \times 10^{-1}\ m$.

In Figure 5.16, the left hand plot shows a minimum in total dissipation. The dominant component is bulk dissipation, unsurprisingly, since support loss has already been shown to have been attenuated by the geometric impedance tuning, the assumed pressure is very low, and the scale is large, mitigating the effects of TED and surface loss. An examination of the form of the thermal limit given by (5.36) shows that the limit also depends on the product of the generalised force and generalised mass, which also influences the minimum location as the parameters are varied. However, it is monotone increasing in Ri and monotone decreasing in S; it does not generate the minima but shifts them.

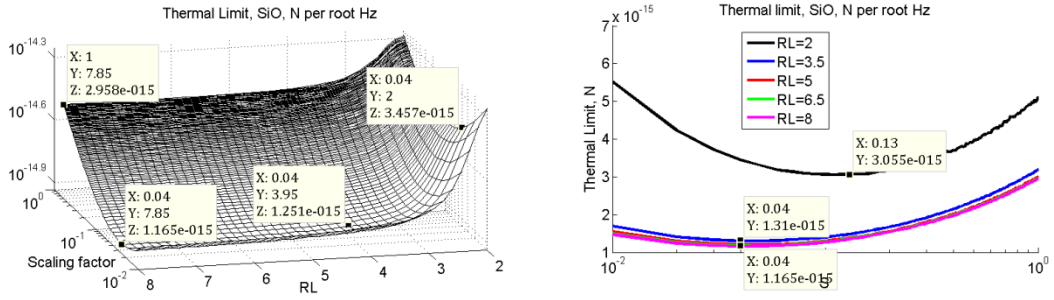

Figure 5.17 Left to right, surface plot and slices of the thermal force limit for a Fused Silica XBR as a function of the parameters RL and S.

For most of the range of parameters considered in Figure 5.17, the thermal limit does not vary as RL is varied. This is a corollary of the sense-dominant regime for these parameter choices. The dissipation and modal qualities are dominated by the sense beam; extending the support has little influence. This is significantly violated only for the longest support beams considered, which have a half-length of one half of the total sense beam length, making the total in-plane aspect ratio of the device square. From the right hand plot in Figure 5.17, in this region, a locally optimal scale exists and does not depend on RL; but that, in a vicinity of the extremal value, the sensitivity is significantly reduced and the optimal scale is shifted towards the larger end of the range considered. The modal dynamics explain this phenomenon.

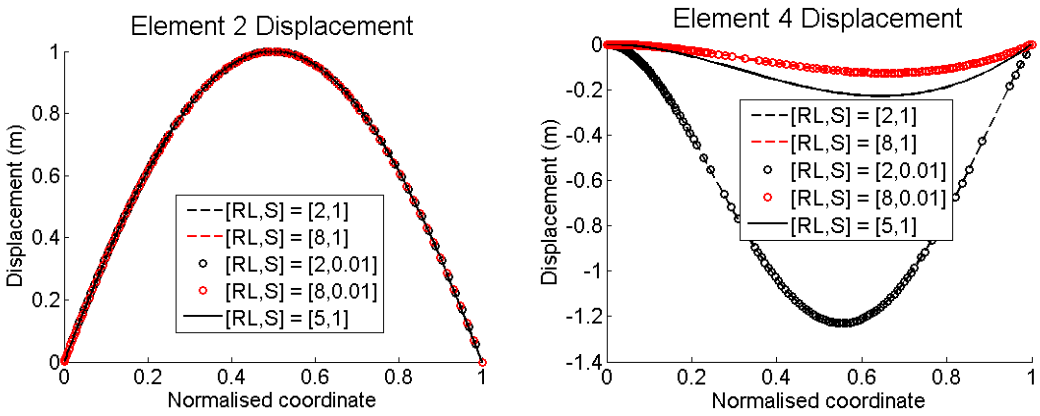

Figure 5.18 Left to right, global XBR fundamental mode shape plotted for Elements 2 and 4, the sense and support beams respectively, as the parameters S and RL are varied.

The support mode shape hardly changes over most of the range considered. For the extremal value of RL, however, the deflection in the support is exaggerated significantly. This corresponds to the domination of the modal dynamics by the sense beam being violated. The increased modal participation of the support beams, with the attendant dissipation, explains the observed forms.

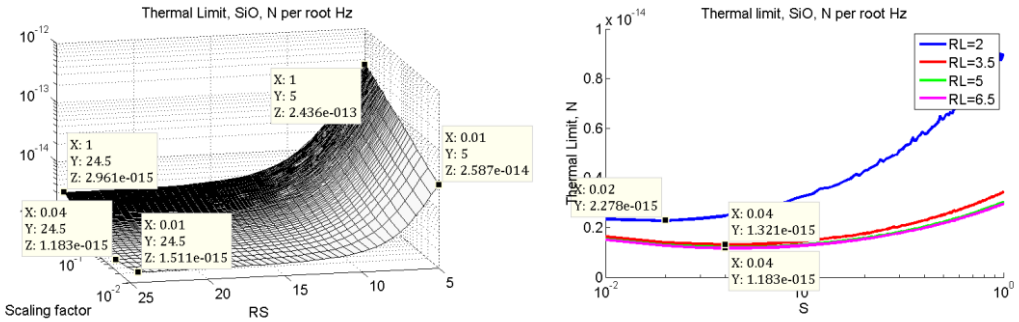

Figure 5.19 Left to right, surface plot and slices of the thermal limits on force sensing for a Fused Silica XBR as the parameters RS and S are varied.

The form of the variation in Figure 5.19 is very similar to that for RL. However, an examination of the mode shapes shows no exaggeration of the displacements to increase modal participation. Instead, the modal displacements remain roughly constant, while the strain energy stored in the supports increases with the third power of the support beam height in the resonator plane. Again, scale optima are demonstrated to depend on the chosen value of RS. The thermal limits on sensitivity and their relationships to the geometric parameters and modal qualities have been thoroughly explored for the case of a fused silica XBR as a force sensor.

5.4.5 Copper: Sensitivity

We turn now to the case of the copper XBM. The geometric-modal interaction and scaling is expected to follow the same pattern as for silica. However, it has been previously shown that levels and dominant mechanisms of dissipation vary substantially between the two materials. In addition, two further complications are encountered: the variation of the generalised force with the geometry; and electrical noise.

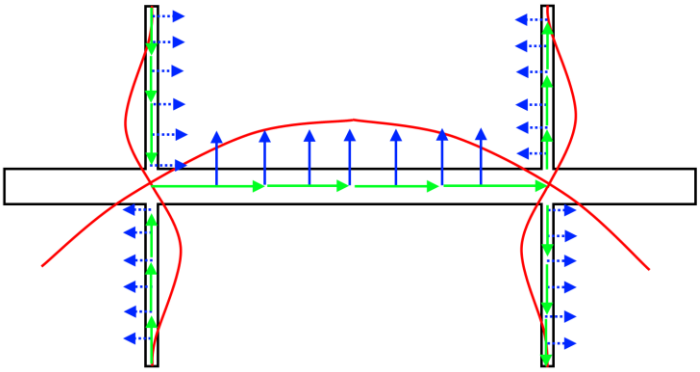

Figure 5.20 Illustration of the Lorentz force and mode shape of an XBR that give rise to the generalised Lorentz force. The mode shape is indicated in red, the current flow in green, and the Lorentz force density in blue. Solid arrows are shown where the sense of the mode and the Lorentz force agree: dotted arrows denote opposing senses.

The generalised force is defined in Chapter 2 as the integral over the XBR of the product of the mode shape with the force density. It can be readily seen that the contribution from the support beams *opposes* that of the sense beam, so that if the area under the local mode shape in the central portion of the sense beam is exactly half that for the sense beam, then when the current splitting is accounted for, then the contributions will exactly balance and the generalised Lorentz force will be zero. Longer supports will lead to a negative coupling with respect to the central displacement of the sense beam. Since the contribution from the support beams opposes that from the sense beam, the largest positive coupling (in this coordinate convention) can be realised by letting the support length tend to zero while maintaining its aspect ratio. In this limit, the integrals over the support beams vanish. Additionally, the sense current density is limited by the cross sectional area of the supports available to conduct current into and heat out of the device. Electrically, then, a short, wide sense beam is optimal. However, the effect on the dissipation of

these parametric changes has been shown to be detrimental. The opposition between these two countervailing costs from an optimisation perspective might be reasonably expected to lead to local optima, with a sense beam shorter than the crossover length but not so short as to effect the modal dynamics and wide enough to carry a reasonable sense current without again causing increased dissipation by violating the modal dominance of the sense beam.

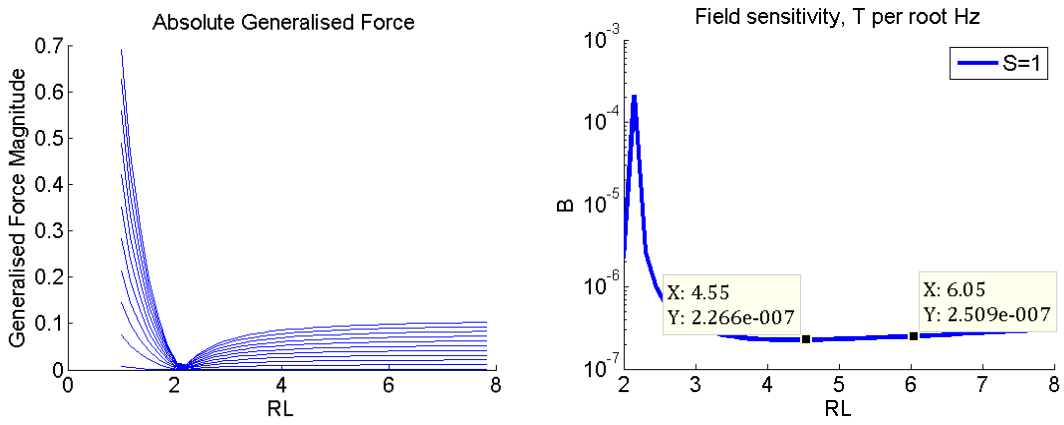

Figure 5.21 Right to left, generalised force curves for several different length scales, and the resulting field sensitivity, plotted as functions of RL. For this analysis, the parameters were chosen such that $RI = RS = 25$.

The zeroing of the generalised force is predicted to occur when $\ell_{SUPPORT} \approx \frac{1}{2 \times NR}$ if the in-plane aspect ratios are similar, implying $RL \approx 2.23$, which agrees well with the data presented in Figure 5.21. The resultant sharp spike in the minimum detectable field is only limited by the resolution of the numerical grid. As expected, a minimum occurs due to the trade-off between dissipation and generalised force. Upon further examination, the location of the minimum does not appear to change with scale.

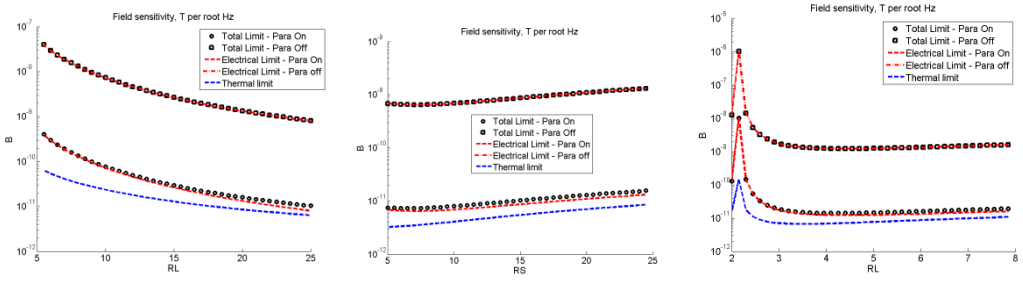

Figure 5.22 Left to right, variation in predicted field sensitivity for a copper XBR with tuned NR as the parameters Ri, RS, RL, and S are varied. The length scale datum is $\ell_{SENSE} = 3 \times 10^{-2}$.

In Figure 5.22, it can be seen that the field sensitivities predicted by the model for a copper XBR without parametric effects are limited by electrical noise, even with the

very low level of input noise associated with the HF2 current amplifier chosen. The electronic noise floor is linear in this parameter, according to the model. The broad trends in the behaviour can be described as favouring a larger Ri value, a smaller RL value, and an optimal RS value. The action of parametric drive is to amplify both thermal noise and signal power by the parametric gain, G_P. Assuming a value of $G_P = 100$, consistent with the literature, pushes the electronic noise floor close to the thermal limit for this geometry, improving sensitivity by a factor close to 100.

5.4.6 Discussion of design

In this subsection, the lengthy results and discussion presented above are summarised from the perspective of resonator/sensor design.

5.4.7 Fused Silica

It has been shown that an XBR in fused silica at the larger length scales is capable of achieving the very high bulk loss limits of the material at room temperature. The extremely low intrinsic, TED and surface losses associated with this material make support loss a dominant factor if the geometric design is not carefully chosen. The corresponding high sensitivity to mistuning of NR is reflected in the sharply peaked forms displayed in Figure 5.10, demanding a precise accounting for the sense-support coupling in the design process in order to achieve maximal Q factors. The other geometric parameters also have a tuning influence, albeit a far less pronounced one.

The highest Q factors predicted in the present study were achieved at the parameter values:

- $L_{SENSE} = 300 \times 10^{-3}\ m$
- Minimise RI $(RI = 10)$
- $RS \geq 15$
- Little dependence on RL in the range $2 \leq RL \leq 8$ considered.

The resulting Q factors are predicted to be on the order of 4×10^7, which is in line with the bulk Q of the material and the highest recorded values in the literature. The most sensitive XBR to applied forces for Fused Silica over the evaluated parameter ranges is achieved at:

- $L_{SENSE} = 27 \times 10^{-3}\ m$
- Maximise RI $(RI = 25)$
- Maximise RS $(RS = 25)$
- Maximise RL $(RL = 8)$

This can be interpreted as simultaneously minimising the support thickness and length, while making the sense beam as thick as possible.

Although this configuration does not produce the highest Q resonator, it achieves the best balance between stiffness and Q factor. The predicted force sensitivity is on the order of $5 \times 10^{-16}\ N$, which is at the higher end of the published values around this length scale.

5.4.8 Copper

The preceding analysis shows the dominant loss mechanism to be thermoelastic in this material and geometry. For a length scale around 3mm, the natural frequencies are tuned to the Zener thermal relaxation time, leading to maximal dissipation. The ratio of thermal relaxation time to natural period scales as ℓ^1, so that at larger length scales $\omega\tau > 1$; to increase the mistuning, the results show that sensitivity is maximised by having a low Ri value and a thick sense beam. On the other hand, at the microscale $\omega\tau < 1$ and a thinner sense beam is more favourable. For this geometry, since support loss is not an important mechanism for the XBR, precise NR tuning is not critical to performance.

In terms of design for maximum field sensitivity as an XBR, the model indicates the following parameter choices as optimal:

- NR – insensitive for $0.2 \leq NR \leq 0.25$ for a large planar substrate – may be higher for more dissipative real substrates - choose optimised value $NR = 0.2242$ to maximise support loss suppression
- Maximise RI $(RI = 25)$
- Minimise RS $(RS = 25)$
- Optimum at $(RL = 3.7)$

Further work is needed to establish the behaviour outside of the considered parameter range, although manufacturing difficulties may present realisation of the predicted structures outside of these ranges due to the high aspect ratios implied. The model predicts electronic noise-limited performance with these parameter choices and a length scale of $3 \times 10^{-2}\ m$ on the order of 1 $nT/\sqrt{Hz}$, which is sufficient to be useful in precision inertial navigation applications. By applying parametric amplification with a gain of 100, it is predicted to be possible to push this figure close to the thermal noise floor, achieving sensitivity on the order of $10pT/\sqrt{Hz}$, which makes high-precision inertial measurement of quickly varying applied rates possible, as required for aerospace and military applications.

5.5 Conclusions

In this chapter, dissipation processes in XBRs have been studied. Extant work in the literature on TED, bulk loss, and surface loss have been combined with the original modeling already undertaken to formulate a general model for the performance of an XBR. The influence of environmental white noise on the signal, of both thermomechanical and electronic origins, has been included. Finally, a detailed numerical study has been undertaken for the particular cases of an XBR in copper, intended as an XBM prototype, and also in Fused Silica as a standalone high-Q resonator.

The modeling approach adopted is efficient enough to allow for a reasonably thorough examination of the quantities of interest on the parameter space of the device. Each of the surface plots shown corresponds to solution for $10^4 - 10^6$ parameter combinations, and the computational runs were undertaken on a workstation with 12GB of ram. Conversely, an adequate solution of a FE model to account for the equivalent phenomena with a minimal mesh density using COMSOL took a few seconds, making iteration on the scale displayed here prohibitively expensive in terms of computational cost. Several of the parameters were shown for the first time to possess local optimal parameter values with regard to sensitivity; that is, turning points in the sensitivity function, defined on a linear submanifold of the parameter space, in contrast to intuitive expectation that a particular limit (e.g. maximal sense

beam thickness, minimal support thickness) would be optimal. It has thus been shown that detailed consideration of the modal dynamics is necessary in order to obtain an optimal force or magnetic field sensor; and that the approach adopted herein is suitable and efficient.

The results demonstrate the potential for developing a sensitive XBM in copper; such a device is presented in the following chapter. Since TED is shown to be so dominant in this case, the thermal noise floor is relatively high and thermally-limited performance is achievable in a practical implementation with noisy electronics. The corresponding thermal limits to sensitivity and predicted Q factors have been presented, and correspond to a magnetometer of medium sensitivity.

The results show that an XBR in Fused Silica does not suffer from this limitation, potentially allowing extremely high Q factors to be realized. If such a device can be fabricated without undue material damage remaining after flame polishing, extremely high Q factors are predicted.

5.5.1 Further Work

The model presented provides a quantitative metric for the predicted sensitivity of a resonant XBR/XBM for a given choice of defining parameters. While numerical precision is not expected due to the nature of measurements of very high Q devices, the trends observed equip the designer with information not available to intuition or descriptions of the XBR as a free-free beam about the likely effect of changing the resonator geometry, as well as providing conceptual insight.

However, one of the limitations in the way in which the results are presented is that only one parameter is varied at a time, over a range considered reasonable in light of existing designs and the geometric tolerances of the chosen manufacturing route. In undertaking to develop such a model, it was the author's intention to use the performance metric along with a global constrained optimisation procedure to arrive at a truly optimal XBR design; this work is ongoing. A constrained optimisation program, for which a technique like simulated annealing would be appropriate in this case, would save significant time and effort on the part of the designer in performing

manual exploration of the parameter space, and would ultimately result in an equally-well or better tuned resonator geometry.

Further work is needed to develop and characterize the concept of an XBR in Fused Silica, which have never been reported on either theoretically or experimentally. Since capacitive actuation is not possible in insulating materials, this would entail development of another transduction scheme. PZT transduction would be difficult to implement without spoiling the superb surface loss properties of the silica, and the nature of the fundamental mode of the XBR precludes substrate excitation. These considerations make optical forcing and transduction an interesting prospect for realizing the intrinsic potential of this type of resonator.

Another difficulty in applying the modeling to the case of micromachined devices is the assumption of isotropy. Many materials utilized in micromachining high-Q resonators, including Si, SiGe, and LiNbO3, are crystalline. It would be of great value to extend the numerical formulation to handle anisotropic materials. Advances in all aspects would be of interest, including resonator modal analysis and substrate propagation analysis in anisoelastic materials.

For materials and geometric configurations for which TED is dominant, the restriction to beam geometry for the sense element is nontrivial. In particular, from a design perspective, it would be of great value to make the thickness much larger relative to the wavelength, so that the relaxation time could be tuned away from the natural frequency. However, the underlying Euler-Bernoulli beam theory is limited as regards how far the model can be relied on in this limit. Developing a more general model – perhaps based on a Timoshenko beam formulation of the RRM model – would allow the study of quasi-bulk or plate resonators using the techniques of this thesis.

5.5.2 Summary

The work in this chapter demonstrates the power and flexibility of the modelling approach developed. The results show the feasibility of producing a sensitive XBM from copper, particularly on larger length scales, owing to the high sense currents that can be supported by this material. In addition, it is shown that the Q factors in such a device are limited by TED, such that the very high support Q factors generated by the

XBR geometry cannot be fully exploited in this material. Fused Silica is considered as an alternative XBR material. Although it is not suitable for XBM fabrication since it is an electrical insulator, the prospect of readily manufacturing extremely high-Q resonators remains tantalising.

5.6 References

[1] A. Heptonstall, G. Cagnoli, J. Hough, and S. Rowan, "Characterisation of mechanical loss in synthetic fused silica ribbons," *Physics Letters A*, vol. 354, no. 5–6, pp. 353–359, Jun. 2006.

[2] K. Numata, K. Yamamoto, H. Ishimoto, S. Otsuka, K. Kawabe, M. Ando, and K. Tsubono, "Systematic measurement of the intrinsic losses in various kinds of bulk fused silica," *Physics Letters A*, vol. 327, no. 4, pp. 263–271, Jul. 2004.

[3] S. D. Penn, A. Ageev, D. Busby, G. M. Harry, A. M. Gretarsson, K. Numata, and P. Willems, "Frequency and surface dependence of the mechanical loss in fused silica," *Physics Letters A*, vol. 352, no. 1–2, pp. 3–6, Mar. 2006.

[4] W. J. Startin, M. A. Beilby, and P. R. Saulson, "Mechanical quality factors of fused silica resonators," *Review of Scientific Instruments*, vol. 69, no. 10, p. 3681, 1998.

[5] A. V. Cumming, A S. Bell, L. Barsotti, M. A. Barton, G. Cagnoli, D. Cook, L. Cunningham, M. Evans, G. D. Hammond, G. M. Harry, A Heptonstall, J. Hough, R. Jones, R. Kumar, R. Mittleman, N. a Robertson, S. Rowan, B. Shapiro, K. A Strain, K. Tokmakov, C. Torrie, and A A van Veggel, "Design and development of the advanced LIGO monolithic fused silica suspension," *Classical and Quantum Gravity*, vol. 29, no. 3, p. 035003, Feb. 2012.

[6] I. A. Bilenko and K. S. Lourie, "Measurements of effective noise temperature in fused silica fiber violin modes," *Physics Letters A*, vol. 305, no. 1–2, pp. 31–36, Nov. 2002.

[7] M. S. Blanter, I. S. Golovin, H. Neuhauser, and H.-R. Sinning, *Internal Friction in Metallic Materials*. Springer, 2007, pp. 372–374.

[8] D. H. Niblett, “Low-Frequency Measurements on the Bordoni Internal Friction Peak in Copper,” *Journal of Applied Physics*, vol. 32, no. 5, p. 895, 1961.

[9] V. K. Paré, “Study of the Bordoni Internal Friction Peaks in Copper,” *Journal of Applied Physics*, vol. 32, no. 3, p. 332, 1961.

[10] C. Zener, “Internal Friction in Solids. I. Theory of Internal Friction in Reeds,” *Physical Review*, vol. 52, no. 3. pp. 230–235, Aug-1937.

[11] R. Lifshitz and M. Roukes, “Thermoelastic damping in micro- and nanomechanical systems,” *Physical Review B*, vol. 61, no. 8, pp. 5600–5609, Feb. 2000.

[12] S. J. Wong, C. H. J. Fox, and S. McWilliam, “Thermoelastic damping of the in-plane vibration of thin silicon rings,” *Journal of Sound and Vibration*, vol. 293, no. 1–2, pp. 266–285, May 2006.

[13] Z. Shi-gong, “Laser Generation of Surface Waves on Cylinder with a Slow Coating Laser Generation of Surface Waves on Cylinder with a Slow Coating,” vol. 4314, 2008.

[14] J. Yang, T. Ono, and M. Esashi, “Investigating surface stress: Surface loss in ultrathin single-crystal silicon cantilevers,” *Journal of Vacuum Science & Technology B: Microelectronics and Nanometer Structures*, vol. 19, no. 2, p. 551, 2001.

[15] J. Yang, T. Ono, and M. Esashi, “Energy Dissipation in Submicrometer Thick Single-Crystal Silicon Cantilevers,” vol. 11, no. 6, pp. 775–783, 2002.

[16] M. Bao and H. Yang, “Squeeze film air damping in MEMS,” *Sensors and Actuators A: Physical*, vol. 136, no. 1, pp. 3–27, May 2007.

[17] Z. Hao, “An analytical model for support loss in micromachined beam resonators with in-plane flexural vibrations,” *Sensors and Actuators A: Physical*, vol. 109, no. 1–2, pp. 156–164, Dec. 2003.

[18] Z. Hu, B. J. Gallacher, K. M. Harish, and J. S. Burdess, “An experimental study of high gain parametric amplification in MEMS,” *Sensors and Actuators A: Physical*, vol. 162, no. 2, pp. 145–154, Aug. 2010.

[19] M. J. Thompson and D. A. Horsley, “Parametrically Amplified Z -Axis,” vol. 20, no. 3, pp. 702–710, 2011.

[20] M. J. Thompson and D. A. Horsley, “Parametrically amplified MEMS magnetometer,” *TRANSDUCERS 2009 - 2009 International Solid-State Sensors, Actuators and Microsystems Conference*, pp. 1194–1197, Jun. 2009.

[21] M. Sharma, E. H. Sarraf, and E. Cretu, “Parametric Amplification / Damping in MEMS Gyroscopes,” *Quadrature*, pp. 617–620, 2011.

[22] T. H. Lee and A. Hajimiri, “Oscillator Phase Noise : A Tutorial,” *IEEE Journal of Solid-State Circuits*, vol. 35, no. 3, pp. 326–336, 2000.

[23] T. B. Gabrielson, “Mechanical-thermal noise in micromachined acoustic and vibration sensors,” *IEEE Transactions on Electron Devices*, vol. 40, no. 5, pp. 903–909, May 1993.

[24] C. T.-C. Nguyen, “Micromechanical Resonators for Oscillators and Filters,” in *IEEE Ultrasonics Symposium*, 1995, pp. 489–499.

[25] D. Rugar and P. Grütter, “Mechanical parametric amplification and thermomechanical noise squeezing.,” *Physical review letters*, vol. 67, no. 6. pp. 699–702, 05-Aug-1991.

[26] S. S. Rao, *Mechanical Vibration*. Pearson, 2004.

[27] “HF2TA Current Amplifier Datasheet” Zurich Instruments, 2013.

Chapter 6. Design, fabrication, and testing of an XBM

In this chapter, the concept of a macroscopic copper XBM is proven by experiment. A novel mechanical design for an XBR is presented. Specialised electronics to drive the XBM and to detect its response are also presented.

In order to characterise the device performance, a specialised test rig is required. To this end, designs for a vacuum chamber and Maxwell Coil are presented, and the performance of the rig is characterised in terms of vacuum, field strength, and field uniformity.

A fabrication route for the optimised XBM design is presented, and the resulting device characterised. The results are compared to the modelling chapters in terms of Q factors, natural frequencies, and field sensitivity.

6.1 Introduction

The objective of the work in this chapter is to provide proof-of-concept for a metallic XBM under capacitive transduction, incorporating resonator geometry choices informed by the results of Chapter 5, along with the necessary sense and drive electronics to operate the device under open loop conditions; and to provide a two-point validation of the performance modeling.

This chapter is organized into two main sections. In the first, the experimental setup is presented, including design and fabrication of the necessary ancillary electronics for operation as an XBM. In the second, XBR designs are presented and discussed, followed by an exposition of the results obtained. Finally, the chapter is reviewed and conclusions are drawn.

Symbols		V_{HOM}	Homodyne output voltage
V_{IN}	Input voltage	V_{OUT}	Output voltage
ω_{out}	HF2LI output frequency	ϕ	Phase shift of input relative to output
P1, P2, P3A, P3B	Prototype designations	ℓ_{SENSE}	Sense beam length
$\ell_{SUPPORT}$	Support beam length	h_{SENSE}	Sense beam height
$h_{SUPPORT}$	Support beam height	NR	Nodepoint Ratio
$\mu^1, \mu^2, \overline{\mu}$	First, second, average alignment values	ℓ_e	Electrode length
θ	Alignment angle	X	Mode shape
G_{PREAMP}	Preamplifier gain	$\bar{X}$	Average displacement over plated electrode region
$V_{OUTPUT\ PREAMP}^{P3A}$	Predicted output voltage from P3A	$V_{OUTPUT\ PREAMP}^{P3B}$	Predicted output voltage from P3B

6.2 Overview of testing configuration

The general configuration illustrated in Figure 6.1 was employed throughout the testing. The XBR assembly, including the MACOR substrate and electrodes, was mounted directly on a corresponding fitting incorporated as part of the Maxwell Coil formers. The coil itself was housed in a bell jar and baseplate vacuum chamber, and driven from an external current source.

The primary instrument used for signal generation and readout was a Zurich HF2LI high-frequency lock-in amplifier[1], employed in an open-loop configuration to provide input drive and forcing signals to the XBR and to capture the readout signal from the output preamplifier. The salient performance characteristics of the device are listed in Table 6.1 for reference.

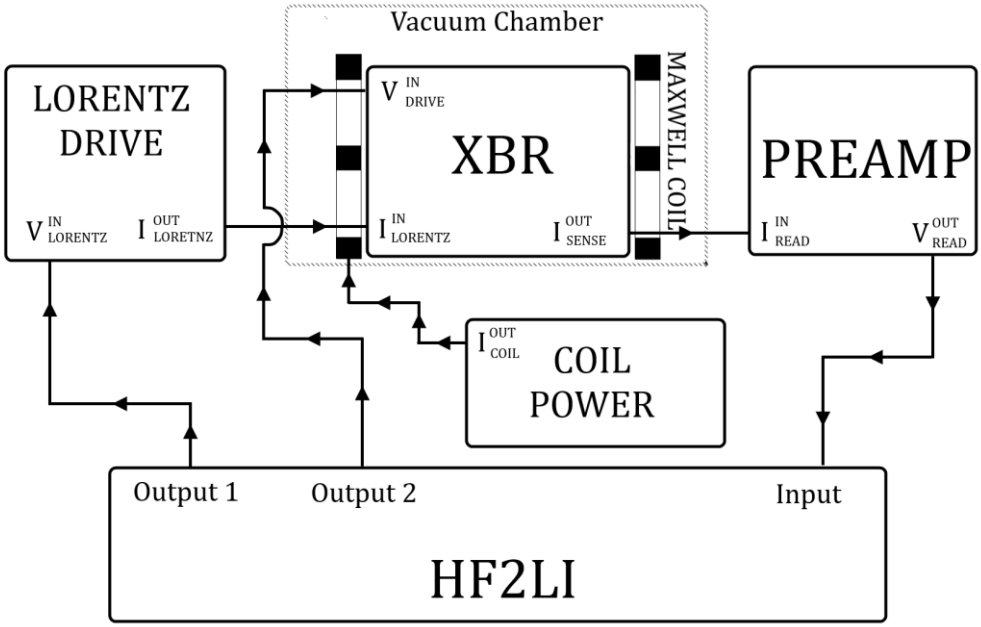

Figure 6.1 Signal level schematic of the measurement and testing setup employed. Current return and ground paths, as well as ancillary power units, are omitted for clarity.

The process of measurement can be summarised as:

- Mount and orient the fabricated XBR prototype in the Maxwell Coil assembly, energise the drive and sense electrodes, and apply medium vacuum
- Apply a known field by exciting the Maxwell Coil

- Use the HF2LI to excite the Lorentz Drive current source amplifier, which in turn drives the large AC sense current through the XBR, in a frequency sweep across the range of interest
- Excite the drive electrodes with control signals as necessary; e.g. parametric pumping, forcing.
- Measure the output current generated by the sense electrodes, after current-to-voltage conversion and preamplification, using the HF2LI

In the next subsections, the lab instruments used in assembly and characterisation are discussed.

6.2.1 Zurich HF2LI Lock-In Amplifier

Figure 6.2 Zurich HF2LI Lock-in Amplifier

The Zurich HF2LI is a modern and versatile lock-in amplifier. The design purpose is to perform synchronous measurement in order to extract a signal with a known carrier frequency from a noisy background. The mode of operation relies on internal generation of an arbitrary frequency signal (up to 6 independent frequencies, in the case of the HF2LI) with high stability and low noise. The signal is output to and interacts with the test specimen. The return signal is read in via an ADC, and digitally multiplied by the original. The result is digitally integrated over one sample time.

$$V_{HOM} = \int_0^{\frac{1}{S}} V_{IN} V_{OUT}\, dt = \int_0^{\frac{1}{S}} |V_{IN}| \sin(\omega_{out} t + \phi)\, |V_{OUT}| \sin(\omega_{out} t)\; dt$$

$$= |V_{IN}||V_{OUT}| \int_0^{1/S} \sin(2\omega_{out}t + \phi) + \sin(\phi)\ dt \qquad (6.1)$$

The ideal mixer properties generate a term at twice the input frequency and a DC term. The resulting mixed signal is then aggressively low-pass filtered, such that the resulting signal is of the form

$$|V_{IN}||V_{OUT}| \int_0^{1/S} \sin(\phi)\ dt + O(Att) \qquad (6.2)$$

where Att is the stopband attenuation. This configuration provides amplitude- and phase-sensitive information for the modulation of a signal at the carrier frequency, while very strongly rejecting off-resonance noise, allowing for the extraction of the carrier modulation at very adverse signal-to-noise ratios. Given that the performance for the macroscopic XBR is expected to be limited by electronic noise by the considerations of Chapter 6, this unit provides an ideal signal input/output and data capture tool for use in sensor prototyping.

Parameter	Value	Unit	Comment
S	4.6×10^5	Hz	Sampling rate
Ω_{in}^{h}	1×10^6	ohm	Input impedance (high level setting)
f_{MIN}	7×10^{-7}	Hz	Minimum input frequency
f_M	5×10^7	Hz	Maximum input frequency
f_{OSC}	1×10^7	Hz	Reference oscillator frequency
V_{NOISE}	5×10^{-9}	$V/\sqrt{Hz}$	Input white noise floor
N	2 input, 2 output	-	Number of channels

Table 6.1 Relevant performance parameters for the Zurich HF2LI, as given by the datasheet.

6.2.2 Mitutoyo QuickScope QS-LZB Optical Measuring Microscope

It was shown in the preceding chapter that the electronic noise limit is inversely proportional to the square of the capacitive gap. One of the biggest challenges in fabricating capacitively actuated devices arises in attempting to produce thin, high aspect-ratio capacitive gaps. In order to quantitatively assess alignment for the prototypes, a Mitutoyo QS-LZB vision measuring microscope was employed throughout[2].

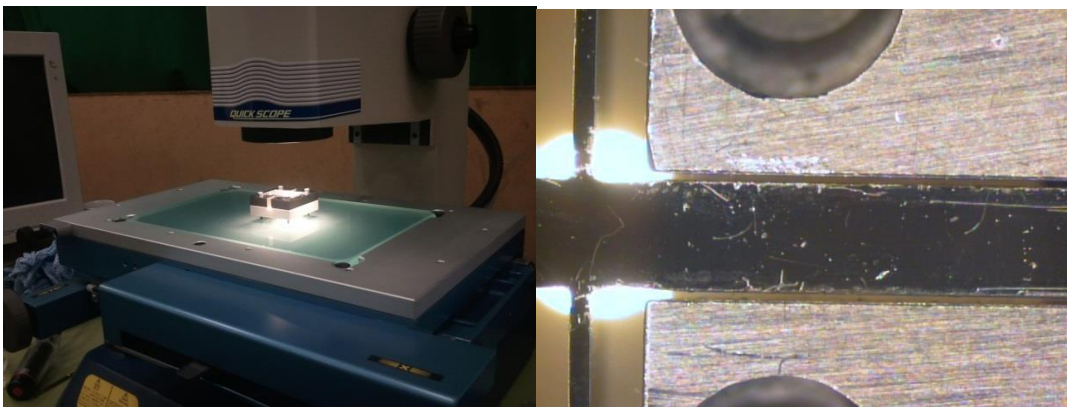

Figure 6.3 Left to right, overview P1 during alignment confirmation using the QS-LZB measuring microscope and output detail showing the capacitive gap between the central electrodes and the sense beam.

The device uses image processing algorithms to obtain quantitative measurement of component geometry and positioning. Typically, the user specifies a feature type, such as a straight line or a circle, and uses a software tool to select the region of interest; the processing algorithms then uses the contrast change at feature edges to resolve the geometry. For the electrode alignment, the parallelism tool was used, which takes two points from each of the edges to be aligned and constructs a corresponding set of straight lines, returning a midpoint separation and out-of-parallel angle. For each measurement, ten such points were taken, and the mean and standard deviation computed.

To undertake this process using lens ring-lighting is problematic. In particular, rounding or burrs on component edges introduce uncertainty into the resolution of sharp edges. To facilitate the alignment, stage lighting was employed to shine through the substrate and the capacitive gaps (but not the components), leaving the components silhouetted and the gaps illuminated, as can be observed in the right hand photo in Figure 6.3.

6.3 Fabrication route

Given that one of the objectives is to provide proof-of-concept for a planar device to be miniaturised using surface micromachining techniques and to validate modelling based on 2D assumptions, a planar manufacturing route was required. It is not possible to use true micromachining on this scale, due primarily to the large feature sizes and etch depths called for. Possibilities for cutting complex shapes from thin

planes include laser, water jet, and plasma cutting, as well as Wire EDM. The properties of these processes are summarised below.

Process	Draft angle	Maximum depth of cut	Heat affected zone size	Kerf width	Accuracy
Water Jet	$0.5^{\circ} - 2^{\circ}$	$> 500\ mm$	None	$0.1\ mm$	$0.025\ mm$
Plasma Jet[3]	$0.5^{\circ} - 5^{\circ}$	$> 150\ mm$	$1\ mm$	$0.05\ mm$	$0.2\ mm$
Laser[4]	$1^{\circ} - 3^{\circ}$	$> 6.35\ mm$	$1\ mm$	$0.1\ mm$	$0.2\ mm$
Wire EDM[5]	None	$> 300\ mm$	$0.1\ mm$	$0.1\ mm$	$0.0025\ mm$

Table 6.2 Comparison of manufacturing processes considered for the XBR prototypes.

All of the profiling methods considered are capable of cutting the required geometries. No difficulty with depth of cut or kerf width would be anticipated, given the order of the principal dimensions already mentioned.

The electrode transduction surfaces were expected to be formed by out-of-plane cuts. Additionally, thin supporting structures of high in-plane and out-of-plane aspect ratio are required, for which even a moderate absolute error could constitute significant relative error and create nontrivial disruption of the geometric impedance tuning.

Another important consideration is heat diffusion in high aspect ratio structures. The geometric restriction of heat diffusion to one or two dimensions for such a feature increases the localised heating and hence HAZ size, compared to the nominal values in Table 6.2. This renders the primarily thermal methods unsuitable for the work in this project.

Summing up, the lack of any draft angle associated with Wire EDM, and none of the other profiling techniques considered here, combined with its superior accuracy and repeatability, gives it a pronounced advantage. On the other hand, a small HAZ still

exists for EDM, which is completely eliminated in water jet cutting. On balance, it was decided to employ Wire EDM for the fabrication of the XBRs by profiling of an initial plate blank. Further work to explore XBRs with low out-of-plane aspect ratios fabricated using high-precision CNC water jet cutting would be of value, but was not explored further within the time and cost constraints of the project.

6.4 Ancillary Instrumentation design

In order to move from an XBR with magnetic-field dependent response to an XBM, it is necessary to amplify the tiny capacitive output currents at high gain using a preamplifier. As discussed in Chapter 5, the sensitivity of the resulting device is often determined by the noise floor on the output preamplifier. Additionally, the large AC currents required for Lorentz Drive mandate the inclusion of a voltage driven current source in the test rig, capable of delivering multiple amps into low impedance variable loads. Suitable electronic devices were developed during the project and are presented here.

An environmental factor of paramount importance is ambient electromagnetic noise (Cf. Chapter 5). In particular, the high-gain sense electronics amplify any input noise signal component at the measurement frequency by the same factor as the signal, with the detrimental effects on sensitivity explored in the preceding chapter. The sensitivity of the integrated device is determined to a large extent by the intensity of ambient EM noise in the measurement bandwidth. Therefore, the signal path must be shielded. The output signal path from the sense electrode to the input of the preamplifier is particularly vulnerable, as any noise introduced at this stage is seen at the HF2LI input amplified by the gain of the preamplifier, which is of the order of 10^7.

6.4.1 Output Preamplifier

The output preamplifier is designed to take a signal from each of the two sense electrodes, located symmetrically about the sense beam. The resulting differential signal input to the preamplifier can be decomposed into common-mode and differential-mode signals. Deflection of the sense beam increases the capacitance of one transducer whilst synchronously decreasing that of its partner, generating a differential mode signal.

Electromagnetic interference in the measurement bandwidth have wavelengths on the orders of kilometres to metres. If the signal paths are kept close to one another, then any induced noise in the inputs will be predominately of the common-mode type. An additional spurious common-mode source is presented by any fluctuating voltage induced in the sense beam by parasitic resistance in the current return path. Therefore, for an ideal capacitive XBR, a differential instrumentation amplifier configuration would reject the majority of the spurious signals, reducing the electronic noise floor, which is expected to limit device sensitivity.

An additional complication is introduced by real imperfection in the electrical circuit elements constituting the feedback circuit employed for gain amplification and in asymmetry in the capacitive gaps related to the electrode location tolerances. The effect of these asymmetries is to introduce a spurious differential-mode signal from the sources already mentioned. In order to mitigate this effect and maximise operational performance, it is desirable to have adjustable gain for each of the differential mode inputs to allow fine-tuning.

The final design employed two gain stages per input, followed by analogue summing of the outputs and a further gain stage before signal output to the HF2LI. The circuit is described below.

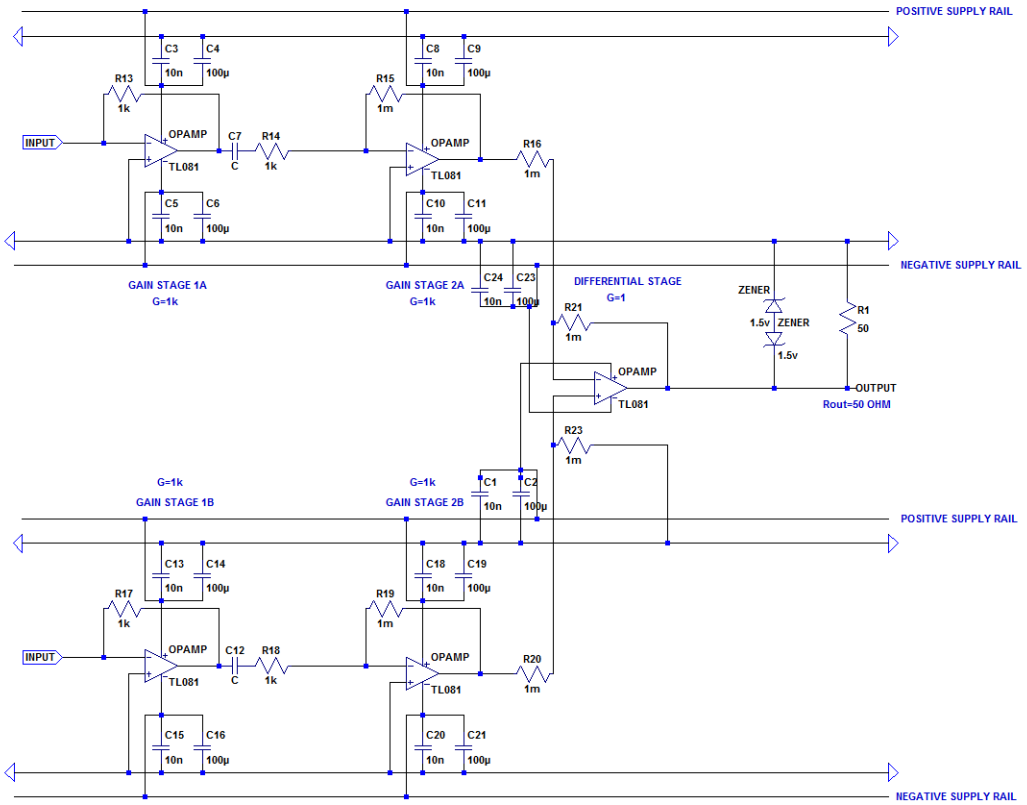

Figure 6.4 Circuit schematic for Output Preamplifier. Each input passes through one transimpedance gain stage, which is AC coupled to a second voltage gain stage. The difference in the resulting signals is then extracted by a unity gain differential stage. Output impedance is matched to 50 ohm.

The circuit is designed to obtain a high stable gain from a capacitive load with flat frequency and phase response in the audio bandwidth, and to match the input impedance of the Zurich for optimal sensitivity. G=1000 for each gain stage for a total gain of 10^6 V/A. For the safety of the HF2LI, the output is equipped with a 1.5V Zener clamp, limiting the working dynamic range to <1V at the output.

The circuit was hand-soldered on Veroboard and mounted in a grounded metal case to act as a second Faraday cage. Signal and power inputs and outputs are provided via BNC connector and shielded cable, minimising the effects of noise bypassing the electrical shielding via the power and signal conductors. In this configuration, no components on the signal path are exposed to noise; indeed, two concurrent Faraday cages are provided for all elements except for the leads from the sense electrodes, which enjoys the protection of the outer Faraday cage (Cf. Section 6.4.3) and were made as short as possible to minimise leakage noise effects.

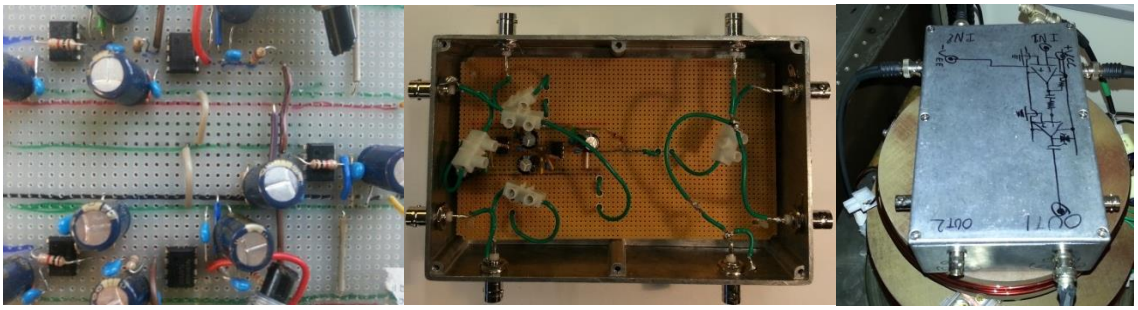

Figure 6.5 From left to right, detail of Veroboard configuration; overview of circuit board mounted in shielded housing; and the completed preamplifier mounted on the Maxwell coil.

6.4.2 Lorentz Drive Amplifier

It was shown in Chapter 5 that in order to maximise sensitivity in a macroscopic device, the highest sense current sustainable under thermal constraint should be used. To obtain a variable-amplitude, frequency swept response in order to characterise resonator Q and XBM sensitivity for several different resonators and applied fields, it is necessary to have available constant current in the audio frequency range with arbitrary amplitude up to the maximum required. Conversely, the HF2LI output stages are designed to deliver voltage to high-impedance resistive loads drawing small currents; this is generally true of the signal generation sources that would be used for a widely manufactured device. In order to manufacture a functioning macroscopic XBM, it is therefore necessary to include a voltage-to-current amplifier design. Such a design as to be appropriate for the P3 series prototypes is presented here. Adapting the implementation to a design for mass manufacture would pose technical challenges that are beyond the scope of the present work.

Two LM675 power op-amps[6] were employed in a self-balancing dual-channel output stage configuration. Each was ballasted by a 4 ohm, 30 watt thin-film power resistor. Heat dissipation for each ballast and op-amp was provided by natural convection via an extruded aluminium heat sink. In this configuration, variations in load resistance are balanced out by the second feedback loop so that the desired approximation to an ideal current source can be maintained.

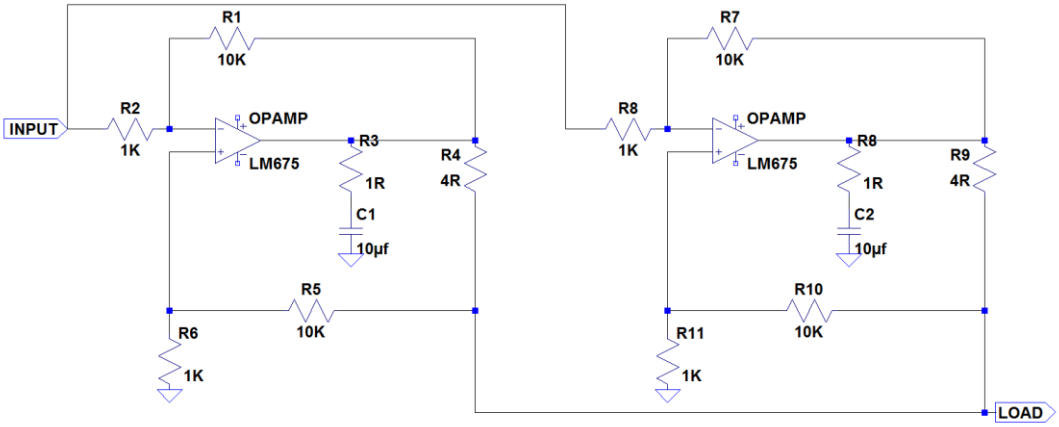

Figure 6.6 Circuit diagram for the Lorentz drive amplifier.

The power supply was buffered using an electrolytic capacitor and a Mylar film capacitor in parallel. The circuits were assembled on Veroboard and mounted on a fire-treated MDF backing board.

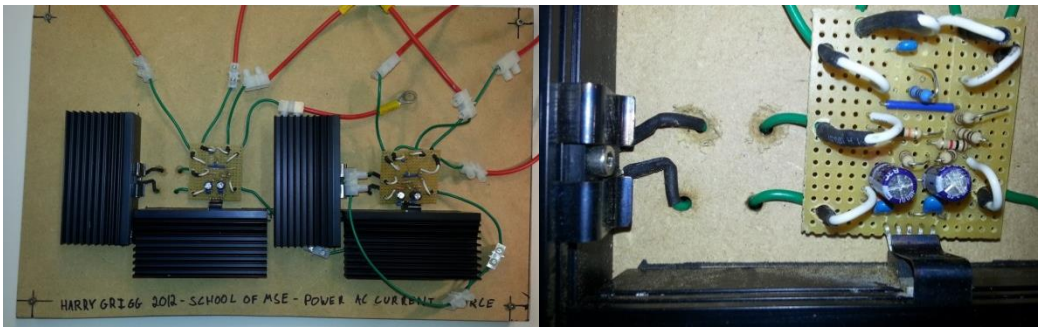

Figure 6.7 Left to right, overview and detail of implemented Lorentz drive amplifier. The large black extrusions are the heat sinks, against which the op amps and ballasts are retained via spring steel clips.

The power delivery was stress tested using a low-impedance wire load and a 4 ohm power resistor for 24 hours each, without problem. The frequency response was characterised; the device was able to deliver 8 amps AC at frequencies between 1 and 10 kHz at $\pm 2\ dB$ in both amplitude and phase into both loads, setting the limit for the applicable sense current for the experiments.

6.4.3 Test chamber

To test the function of the fabricated prototypes as an XBM, the primary independent variable is the local magnetic field in the vicinity of the XBR. Ideally, the field should be uniform, time-independent, transverse to the plane of the XBR, and controllable to arbitrary field strength. Atmospheric pressure is another environmental variable that

was shown in Chapter 6 to have an important bearing on the performance of the device. An ideal experiment would allow arbitrary control of the atmospheric pressure in the vicinity of the XBR. In the next subsections, an environmental and noise control apparatus is presented and discussed.

6.4.4 Vacuum Chamber

No extant vacuum chamber to which the research group has access could accommodate the necessary geometric and feedthrough requirements to test the prototype XBRs. Therefore it was necessary to design and fabricate such a chamber. Given the circular profile and rectangular axial section of a field coil, the most efficient use of space can be achieved using a cylindrical vacuum chamber. On this basis, it was decided to employ a bell-jar to form the top part of the vacuum manifold. A requirement base plate with the required number and type of feedthroughs was thus established.

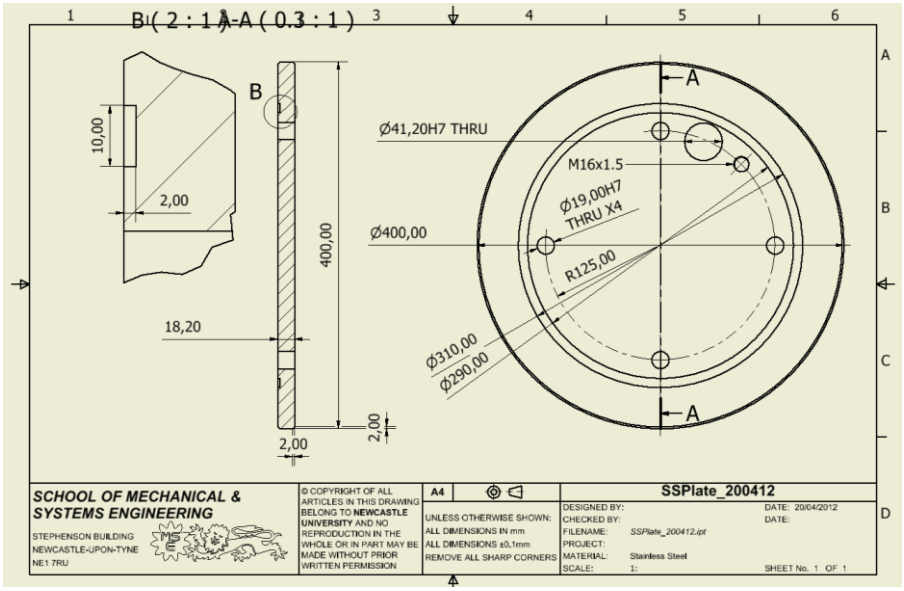

Figure 6.8 Engineering drawing for vacuum chamber base plate, as fabricated. Grounding connections are not shown for clarity.

The baseplate was turned from nonmagnetic 316L stainless steel blank to match the ancillaries and prevent corrosion, then bored to take the feedthroughs. The capacitive drive and sense signals along with the electrode energising voltages were routed via three VG Scienta EFT920 tubulated flange components with external BNC connectors, welded into the baseplate in-house via TIG. The larger ZEFT34A was employed for the

Lorentz drive current, with 4x5mm stainless steel bus bars each capable of handling 40A steady-state. From an electrical perspective, the baseplate was grounded and connected to the implosion shield surrounding the bell-jar to form a Faraday cage, providing the first line of defence for the sensitive electronics inside from ambient EM noise.

Figure 6.9 Left to right, bottom and top of the baseplate undergoing final assembly, after welding. The ZEFT34A appears toward the left of both photos as the larger feedthrough with 4 current elements.

Grounding was provided by means of $2.25mm^2$ copper multicore cable insulated by PTFE, bolted to the baseplate via crimped eyelet.

6.4.5 Maxwell Coil

In order to impose the desired uniform, controlled field, a field coil is employed. A simple solenoid could have been used, but the resulting field is nonuniform spatially, leading to spurious out-of-plane couplings and resultant error. A pair of solenoids arranged as a Helmholtz coil is often employed for the purpose of generating a region of uniform magnetic field, and performs adequately in this role.

However, James Clark Maxwell designed an arrangement of three solenoids, such that each lies on the surface of a sphere in three dimensions, with their planes parallel and their axes collinear[7], which offers superior performance, all other factors being equal. Maxwell showed that, for a particular choice of the latitude coordinates of the coils, the derivatives of the magnetic field vanish at the centre up to sixth order. The volume of uniform field is approximately three times greater than in the Helmholtz case. The beautiful field pattern that results is ideal for the purpose at hand.

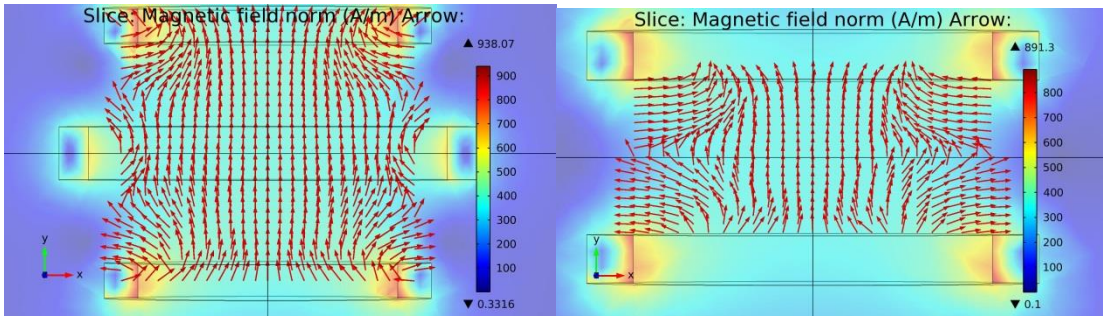

Figure 6.10 From left to right, simulated magnetic field distribution in the interior of a Maxwell and Helmholtz coil. The heat map indicates the magnetic field strength norm; the arrows indicate the local field direction, and are length normalised. The X component of the field is exaggerated by a factor of 10 in both cases.

Figure 6.10 is a comparison of COMSOL simulations of the Maxwell and Helmholtz coils considered. Both have equal outer diameters. The region of uniform field encompasses more of the interior of the coil for the Maxwell design than that of Helmholtz. An additional advantage from an experimental perspective is that the middle coil provides a convenient point of attachment and support for the XBR assembly.

To fabricate the coil, double-insulated Magnetemp CA200 copper transformer wire of 1mm diameter was wound on to custom made Tuffnall formers by hand. The formers were spatially separated and maintained in their proper orientation by the use of aluminium spacers. The former for the middle coil also contains an extended shelf and the appropriate fittings to support the XBR prototype assemblies. The coil assembly drawing is presented in Figure 6.11.

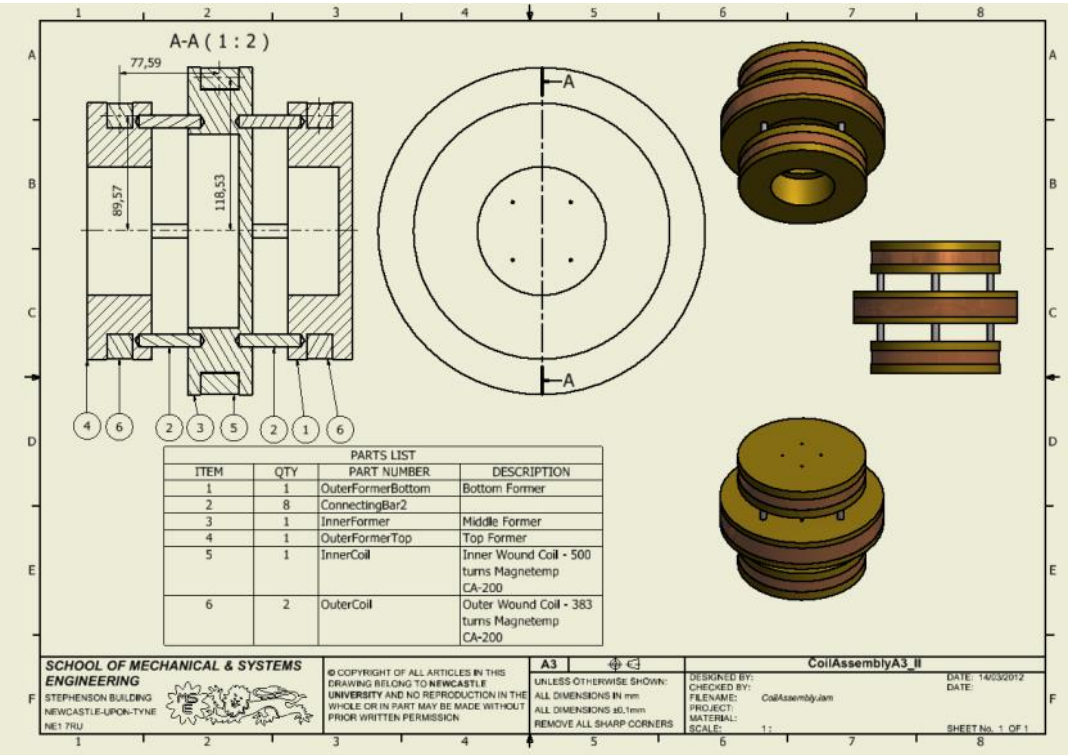

Figure 6.11 Engineering assembly drawing for the Maxwell Coil, as fabricated. The coil centre coordinates are illustrated.

The coil formers were turned from Tuffnall cylindrical blanks at low speed in the MSE Workshop at Newcastle university. Each coil was then manually wound while still attached to the lathe chuck, allowing the wire spool to rotate on a frictional bearing to generate and regulate the tension.

Figure 6.12 Turning of the formers and winding of the coils.

The winding pattern employed a regular hexagonal close-packed structure through manual regulation of the winding process and appropriate choice of the slot width to be a half-integer multiple of the wire diameter. Each coil was wound separately, with the trailing wires subsequently joined by means of standard 15A connector block.

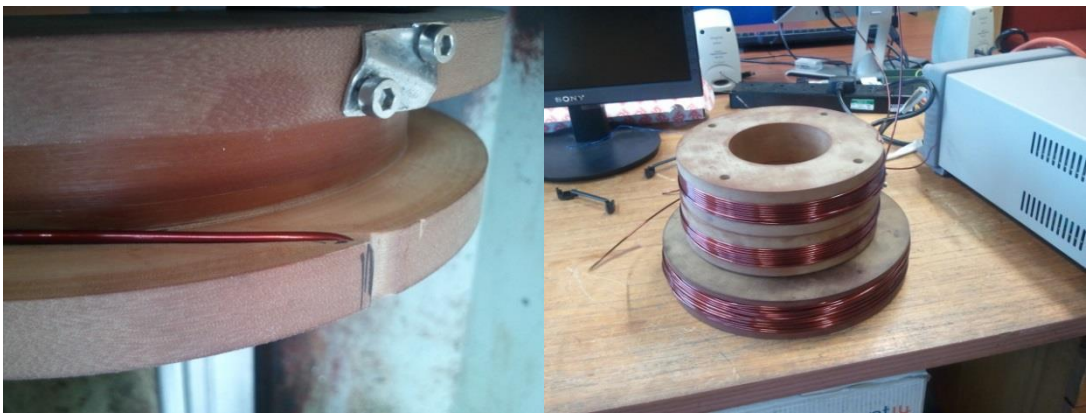

Figure 6.13 Detail of trailing wire connection and overview of fabricated coils before location and interconnection.

The assembled coil was tested for field strength and uniformity using the handheld magnetoresistive DC Milligauss Meter MGM from Trifield, Inc[8]. The results are displayed and compared to simulation in Figure 6.14.

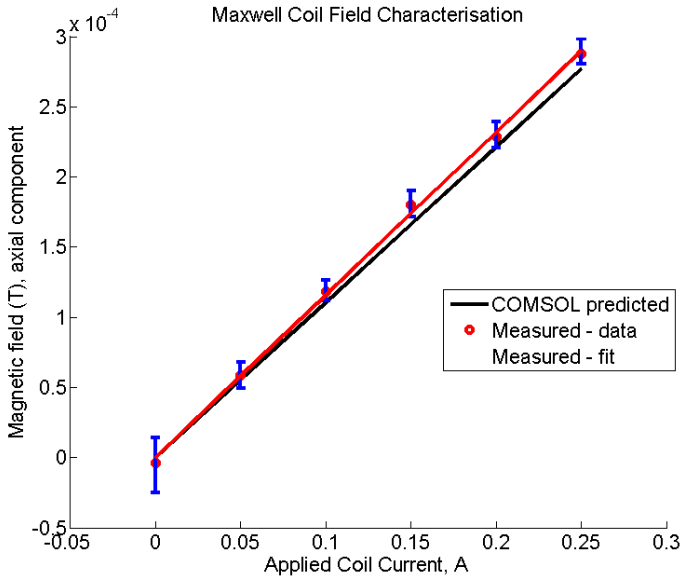

Figure 6.14 Simulated vs. measured magnetic field strength in the axial direction in the coil centre, as the applied field current is varied. The black line is the prediction. The red circles are the mean measured values, and the red line is the least-squares best fit. Error bars represent the range of observed measurements over ten iterations.

The coil performs as expected, with a slightly larger field measured than the COMSOL prediction. The gradient of the best-fit curve gives the field response of the coil as $1.159\ mT/A$.

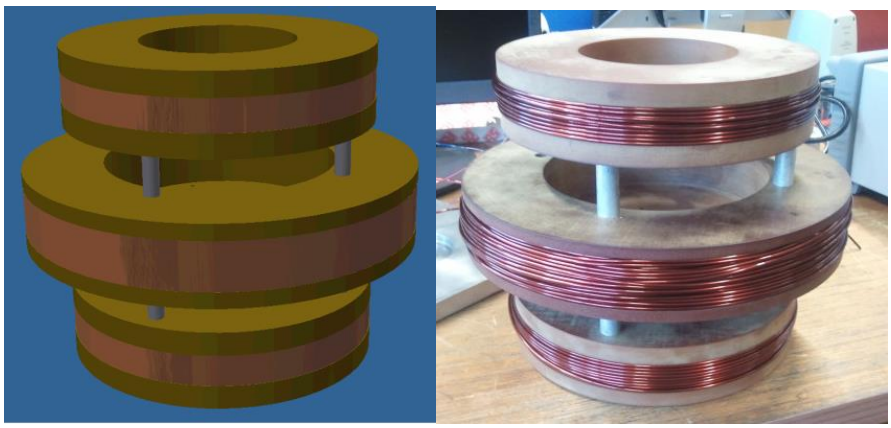

Figure 6.15 From left to right, CAD 3D representation of coil design and finished Maxwell coil.

6.4.6 Assembled test rig

The assembled test rig, consisting of the XBR assembly and preamplifier mounted in the Maxwell coil, in turn secured to the baseplate and encased in the bell jar and Faraday cage, was mounted on an optical table in an atmospherically-controlled lab.

Figure 6.16 The assembled test rig configuration. The upper part of the Faraday cage/implosion shield has been removed for clarity.

In this arrangement, the first line of defence separating the sensitive electronics from EM interference is the Faraday cage comprised by the base plate and implosion shield, with secondary shielding of the amplifier afforded by its housing. All inputs were further insulated from high-frequency EM interference using ferrite beads and suitable capacitive connections to the base plate. This configuration was employed for all the experiments reported on in the results section of this chapter.

6.5 Prototypes

In this section, the important XBR prototype assemblies fabricated during the project, comprising the XBR, its substrate and fittings, and the electrode assemblies, are presented and discussed.

6.5.1 Prototypes 1 and 2

The first prototyping work on the first prototype XBR, termed Prototype 1 or P1, was intended to establish a workable fabrication route to be employed in subsequent prototyping; in particular, to develop a technique for aligning the electrodes to the resonator such that the capacitive gaps could be controlled to the design specifications. This issue poses some nontrivial technical issues. Since the field sensitivity in the electronic-noise dominated regime was shown in Section 5.3 to depend on the reciprocal of the capacitive gap, minimising this quantity effectively mitigates electronic noise and is integral to obtaining a high performance device.

6.5.2 Materials selection

The first design choice to be made was material selection. Important requirements include:

- High electrical and thermal conductivities, to facilitate a large sense current
- High thermal conductivity, again to increase the sense current that can be applied

For this initial prototype, it was decided to use mild steel for the resonator, with aluminium electrodes and MACOR machineable ceramic substrate. These materials have the requisite electrical and mechanical properties to function as a capacitively sensed XBM, although the nonlinear magnetic behaviour of the resonator makes analysis of the field sensitivity and corresponding angular measurement very difficult. Stainless steel was employed for P2, to minimise the magnetic nonlinearity and hysteresis, at the expected cost of reduced field sensitivity.

6.5.3 Resonator geometry

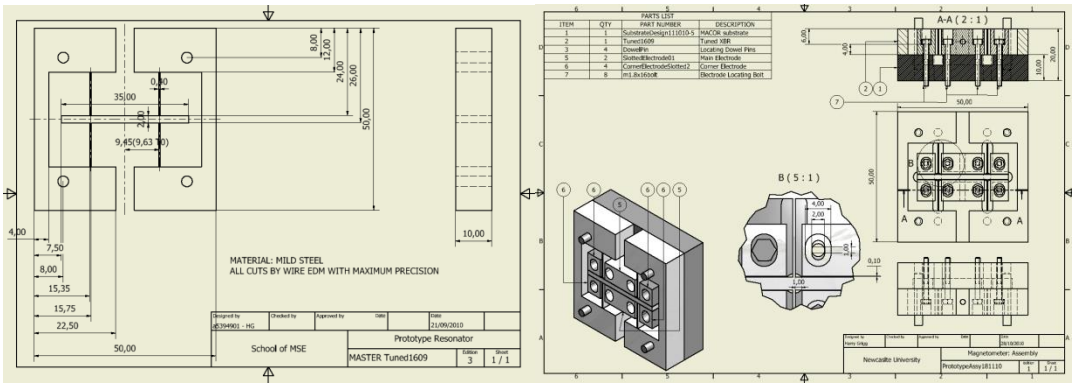

Figure 6.17 Left to right, engineering design for P1 resonator and assembly including substrate, as fabricated. Capacitive gaps are shown as 100μm.The dimensions are summarised in Table 6.3.

At this stage, the analytical modelling was ongoing; without such guidance, the geometry was chosen to test the limits of the manufacturing process, in terms of high in- and out-of-plane aspect ratio supports. The chosen overall dimensions are $50\,mm \times 50\,mm \times 20\,mm$, for P1 and $30\,mm \times 30\,mm \times 20\,mm$ for P2, with the resonator and its substrate each being of thickness $10\,mm$.

Parameter	P1	P2
ℓ_{SENSE}	$3.5 \times 10^{-2}\,m$	$2 \times 10^{-2}\,m$
$\ell_{SUPPORT}$	$15 \times 10^{-3}\,m$	$7.42 \times 10^{-3}\,m$
h_{SENSE}	$2 \times 10^{-3}\,m$	$1 \times 10^{-3}\,m$
$h_{SUPPORT}$	$4 \times 10^{-4}\,m$	$2 \times 10^{-4}\,m$
NR	0.2242	0.2242
b	$1 \times 10^{-2}\,m$	$1 \times 10^{-2}\,m$
Material	Steel AISI 4030	Stainless Steel AISI 316L

Table 6.3 Summary of the geometric and material parameters used for P1 and P2.

6.5.4 Electrodes

The most technically challenging aspect in realising P1 was the location of the electrodes, such that the designed capacitive gaps of $100\mu m$ could be achieved. The approach adopted used slotted electrodes to provide the necessary freedom for alignment, with shims to set the spacing correctly and elastomeric components providing pretension.

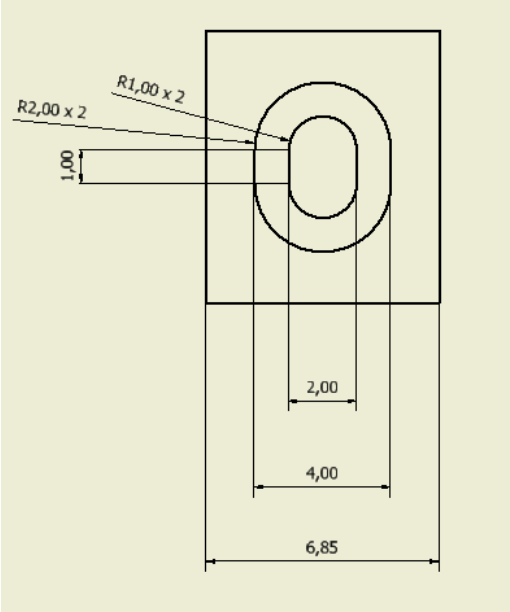

Figure 6.18 Detail from engineering drawing for slotted corner electrode, as fabricated.

After alignment, the QuickScope was employed to check the separation and parallelism of the electrode and the sense beam. To ascertain alignment, a measurement of separation was performed at each end of the electrode to be aligned using the point-and-line perpendicular distance tool. The left-hand measurement in the machine coordinate system is termed μ^1; the corresponding right-hand measurement is termed μ^2. Each measurement was undertaken in three stages:

- Acquire 2 CNC coordinates of points on the proximal edge of the electrode to establish a baseline:

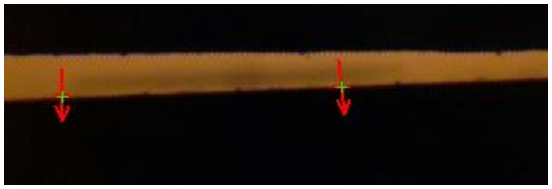

Figure 6.19 . Acquiring baseline coordinates on the electrode via the QS-LZB.

- Acquire one CNC coordinate of a point on the corresponding edge of the sense beam:

Figure 6.20 Acquiring corresponding measurement point coordinates on the sense beam.

- Evaluate the perpendicular distance between the point and the baseline to give a measurement μ_i^j of the local separation between the edges:

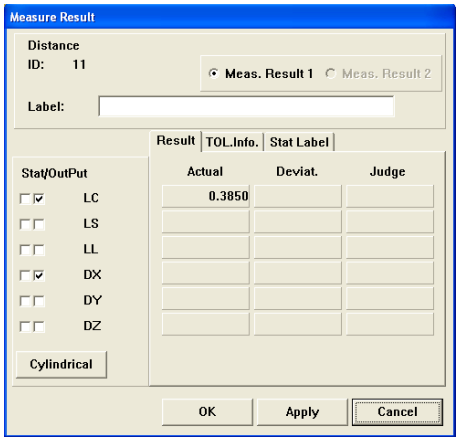

Figure 6.21 Measurement result, showing here the value $\mu_i^j = 385 \times 10^{-6}\, m$.

Each measurement was performed over ten iterations and then averaged according to

$$\mu^j \equiv \frac{1}{10}\sum_{i=1}^{10} \mu_i^j \tag{6.3}$$

The mean of each pair of iterated measurements gives an estimate of the mean capacitive gap according to

$$\bar{\mu} = \frac{1}{2}\sum_{j=1}^{2} \mu^j \tag{6.4}$$

The spread of the measurement pair divided by the resonator length gives a measure of the out-of-parallel angle according to

$$\tan\theta = \left(\frac{\mu^1 - \mu^2}{\ell_e}\right) \approx \theta \tag{6.5}$$

The final alignment results are summarised in Table 6.4.

Statistic	Design value	Measured value	Relative error
μ^1	$100 \times 10^{-6}\ m$	$103 \times 10^{-6}\ m$	0.03
μ^2	$100 \times 10^{-6}\ m$	$114 \times 10^{-6}\ m$	0.14
$\bar{\mu}$	$100 \times 10^{-6}\ m$	$108.5 \times 10^{-6}\ m$	0.085
θ	0°	0.03°	-

Table 6.4 Results of alignment procedure applied to P1.

These results were achieved using 100 micron spring steel shim sheet manually cut to size. The angular alignment is good, and the absolute spacing is satisfactory. Attempts were made to further reduce the gap using thinner shim; however, it was not found to be possible to remove thinner shim without tearing while using a sufficiently strong elastomer to overcome friction between the electrode, the substrate and the retaining bolts.

6.5.5 Substrate

The substrate serves two functions within the XBR assembly: to locate the XBR and its electrodes relatively in space; and to provide electrical isolation of the electrodes and the resonator from one another. Moreover, the substrate must fulfil these roles in such a manner as to allow the resonator to move freely, with minimal friction.

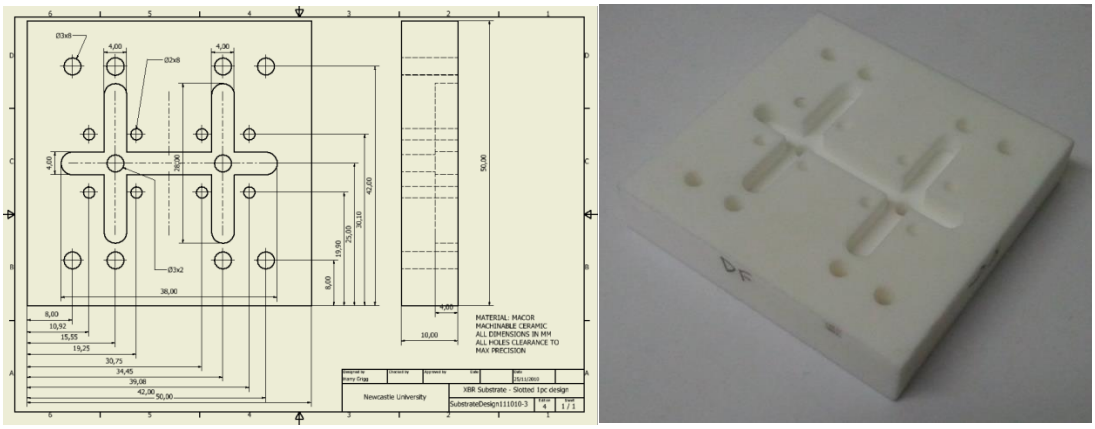

Figure 6.22 Left to right, engineering drawing of the substrate for P1, and the finished substrate after fabrication.

For the first prototypes, the contact area between the resonator and the substrate was maximised. It was conjectured that this might best replicate the analytical "clamped" condition imposed by the methods of analysis. However, the need to allow the free motion of the XBR structure itself without introducing slide-film damping necessitated the machining of shallow trenches beneath its extent, as shown in Figure 6.22.

6.5.6 Fabricated prototypes

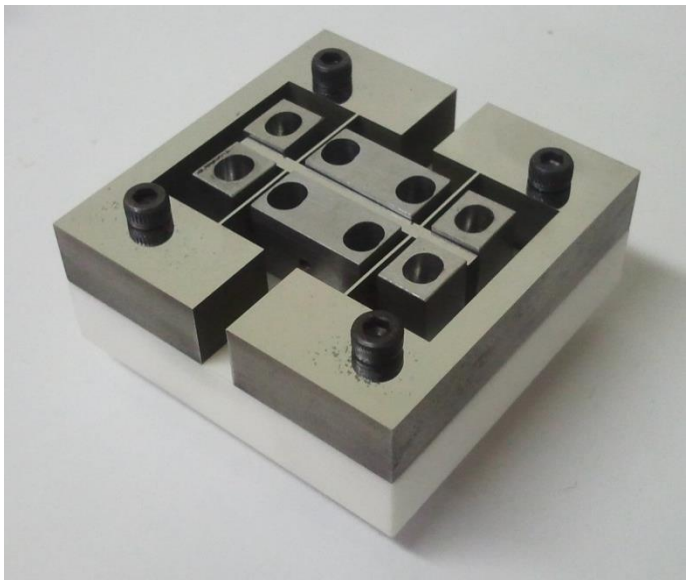

Figure 6.23 The assembled P1 device, prior to electrode alignment.

The primary interest in P1 and P2 was the development of a feasible route to manufacturing a functional macroscopic XBM prototype. Component fabrication was successful for P1, while P2 sustained heat damage to the support beams, leading to a non-functional device.

Initially, after assembly neither device produced an audible tone when struck with a short aluminium bar. After separating the resonator and its substrate, however, the P1 XBR could be heard to ring.

It was conjectured that dry friction between the resonator and the substrate might be leading to the heavily damped response observed, despite the substrate trenches designed to mitigate this problem. The results were later viewed in light of the knowledge gained through the work presented in Chapter 5, which explain mechanical losses of an XBR to its supports in terms of exciting elastic waves in an infinite *conservative* substrate. The complications for the XBR are twofold: the substrate is small relative to the elastic wavelength; and it is dissipative, in that contacts between the XBR and the substrate at points of asperity would lead to dry friction and a corresponding modification of the energy flux with distance from the support attachment. The reflections created by this interaction would affect the impedance of the support-substrate interface, potentially increasing damping substantially. The form of the dependence is likely to resemble that for the case of an infinite substrate, since displacements will remain proportional to the corresponding applied forces as long as the adjusted model remains linear.

To establish the hypothesised loss mechanism, the XBR and electrodes were elevated above the substrate using rubber washers. The ring down behaviour of the resulting device was captured using a condenser microphone as a crude first characterisation of the P1 XBR. The electrodes were removed for this test to minimise the effects of gas film damping, since no vacuum chamber was available at this stage of the project.

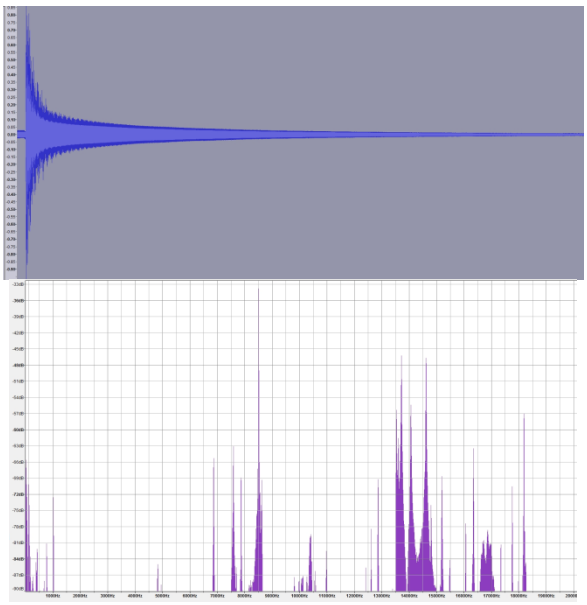

Figure 6.24 Top to bottom, time-domain and frequency-domain spectrum for P1 under manual excitation. The large peak in the bottom plot corresponds to the XBR mode.

The recorded natural frequency matches closely the RRM model prediction in Figure 6.24. Additionally, the Q factor in air was very high. Let $\tau = \frac{Q}{2\pi\omega_n}$ be the time taken for decay by a factor of $1/e$, which can be measured from the data to be 0.36 seconds. Then, the Q factor is given by $0.36 \times 2\pi\omega_n = 3.08 \times 10^3$, which is close to the thermal limit predicted for this material and geometry in Chapter 5.

It was decided to assess the feasibility of device characterisation under intrinsic capacitive actuation and sensing of the response using Laser Doppler Vibrometry, at atmospheric pressure. A Polytec OFV 512 unit was employed, with signal generation and detection via a HP 3562A Dynamic Signal Analyser.

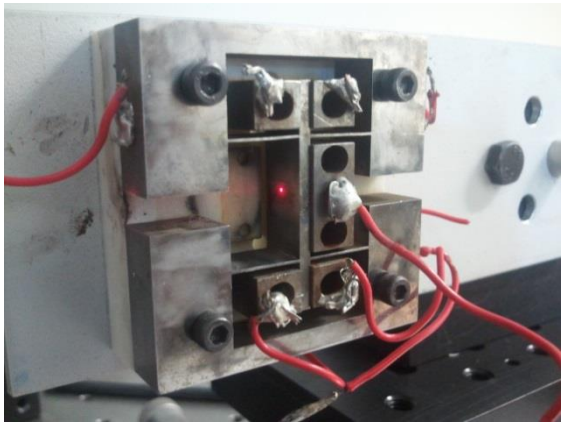

Figure 6.25 An attempt to characterise P1 via Laser Doppler Vibrometry.

No consistent results could be obtained via this technique, likely due to oxidation and roughness of the surface of the device degrading specular reflection to the point where a signal was very hard to achieve, although transient spiking could be observed in the frequency spectrum in the vicinity of the measured natural frequency with vigorous manual excitation. This negative result ruled out the use of laser Doppler vibrometry for device characterisation, at least without further surface treatment of the sense beam, which would be extremely difficult to execute given the geometric constraints and the support compliance inherent in the device geometry.

An additional complicating factor was the introduction of squeeze-film damping when the electrodes were reattached and aligned. Under this assembly condition little or no ringing was audible on manual excitation, implying the introduction of a new dominant dissipation contribution from squeeze-film damping under the ambient test conditions and in particular at atmospheric pressure.

A comparison is made between the predicted and experimental results in Table 6.5.

Result	**P1 – Predicted**	**P1 - Measured**
Natural Frequency	8.510×10^4	8.550×10^4
Q factor in free air	-	3.06×10^3
Capacitive gap	$100\mu m$	$108.5\mu m$

Table 6.5 Comparison between observed quantities and values predicted via the Chapter 5 model for the prototype P1.

6.5.7 Prototypes 3A and 3B

The second round of prototyping was undertaken in the summer of 2012, after the modelling work was mainly completed. Under the constraint of the chosen fabrication and testing route, it was decided to produce two resonators, with identical geometry and materials save for the sense beam thickness, with a view to providing a two-point validation of the modelling approaches.

The lessons learned from P1 and P2 were accounted for in updating the designs. Specifically, the observed HAZ damage in P2 with $200\mu m$ supports led to the selection of copper, to allow the design to exploit the benefits of thin supports expressed in Chapter 4, and the multiple-electrode configuration, which proved very difficult from the point of view of instrumentation and signal conditioning and seemed to offer little from an analytical one, was dropped in favour of using two electrodes only, positioned symmetrically about the sense beam. In order to precisely locate smaller capacitive gaps and hence to obtain cubic improvement in the electronic noise sensitivity limit, the location mechanism was redesigned for the P3 prototypes.

6.5.8 Materials selection

The modelling work predicts higher Q factors are often obtained when one uses thinner support beam geometry. However, this implies the creation of higher aspect ratio support structures, capable of dissipating less heat before thermal runaway and melting. This message was reinforced experimentally by the HAZ damage evident in the supports of P2.

Additionally, the maximum allowable sense current was shown in Chapter 6 to be linearly related to the sensitivity of the device, under common operating conditions. This is also limited by thermal considerations. Since the heat generated by a resistor for a given current is proportional to the resistance value, minimising electrical resistivity is also pertinent.

To mitigate these problems, it was decided to make high thermal and electrical conductivity a priority in material selection for this round of prototyping.

6.5.9 Resonator geometry

The P3 series resonators were machined by Wire EDM from a $100 \times 100 \times 10mm$ blank of C10100 copper plate. A $200 \times 200 \times 10mm$ aluminium jig was cut from plate to provide location during the machining, and the blank was bolted to the jig via 4 M6 corner holes. The engineering drawings from which the devices were fabricated are exhibited below.

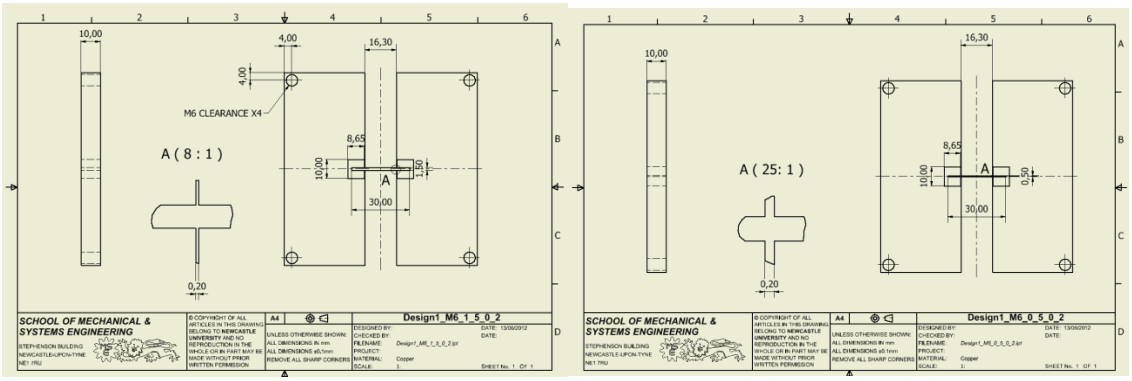

Figure 6.26 Left to right, engineering designs for P3A and P3B XBRs, as fabricated.

The geometric parameters defining the devices are exhibited in Table 6.6.

Parameter	P3A	P3B
L1	$3 \times 10^{-2}\ m$	$3 \times 10^{-2}\ m$
L2	$5 \times 10^{-4}\ m$	$5 \times 10^{-4}\ m$
H1	$1.5 \times 10^{-3}\ m$	$0.5 \times 10^{-3}\ m$
H2	$2 \times 10^{-4}\ m$	$2 \times 10^{-4}\ m$
NR	0.2242	0.2243
b	$1 \times 10^{-2}\ m$	$1 \times 10^{-2}\ m$
Material	Copper, C10100	Copper, C10100

Table 6.6 Parameters defining the P3 series of prototypes.

6.5.10 Electrodes

In Chapter 5, it was shown that, in the electronic noise limited regime, it is necessary to make the capacitance of the transduction electrodes as high as possible. Assuming fixed geometry, the most straightforward way to achieve this end is via minimising the capacitive gap.

The work undertaken on P1 established that it is very difficult to use the shim location method to accurately align a capacitive gap below 100 microns. It was therefore decided to design a new mechanism for precision electrode location for use with the P3 series. The selected final design is based on screw actuation with force multiplication and distance division provided via an inclined plane. The fabricated location mechanism is illustrated in Figure 6.27:

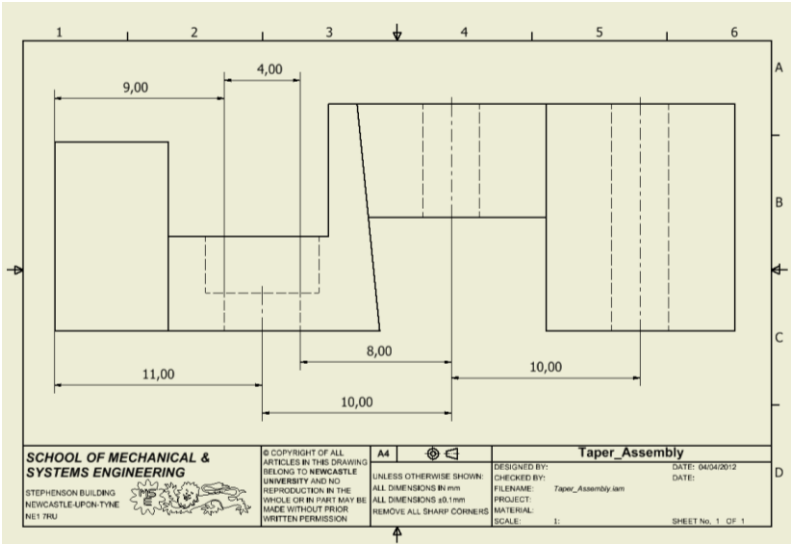

Figure 6.27 Engineering assembly drawing of electrode location mechanism, as fabricated.

With reference to Figure 6.27, three components are shown. The rightmost component, having a rectangular profile with a central hole pair for M3 bolted affixation to the substrate, is a stator, which braces the central component. This is the inclined-plane actuator, which is located by two through M3 bolts. As the bolts are tightened against captive nuts, the actuator is drawn downards. This drives the left-hand component – the electrode – towards the sense beam. The electrode is constrained in two degrees of freedom by two M2 bolts in slotted holes, as for the electrodes in P1, with the applied torque set empirically so as to prevent unwanted play but to allow the desired driven motion.

The clearance of the bolt holes in the actuator was chosen so as to allow for a few degrees of asymmetric tightening, which has the effect of rotating the sense electrode about an axis perpendicular to the plane of the resonator. This allowed fabrication misalignment within the tolerance of the adjustment to be dialed out, minimising the

necessary trimming of the sense preamplifier and hence improving common-mode noise rejection.

The adjustment sensitivity for the mean displacement can be rougly approximated as follows. Let the mean displacement of the beam relative to an arbitrary reference configuration be denoted $\bar{d}$; the mean displacement of the upper surface of the actuator relative to the same reference configuration be $\bar{a}$; and the mean angle through which the drive bolts have been turned be $\bar{\theta}$. The geometric parameters are the angle made by the actuator/electrode interface with the vertical in the plane of Figure 6.27, denoted φ, and the pitch of the bolt, denoted p. We then have

$$\bar{d} = \bar{\theta} p \tan\varphi \tag{6.6}$$

In the implementation, M3 ISO metric bolts with coarse thread were used, $p = 500$ microns/turn, or $P = 73.5$ microns/radian, and $\tan\varphi$=0.1. Then,

$$\bar{d} = 7.35\bar{\theta}\ \mu m \tag{6.7}$$

For a ballpark estimate, it is reasonable to assume control of the angular coordinate of the bolts, using manual tightening via hexagon key, to within 10°. The corresponding uncertainty in $\bar{d}$ is then $\pm 1.3\mu m$, enough to achieve a relative error below 0.1 on a $15\mu m$ capacitive gap.

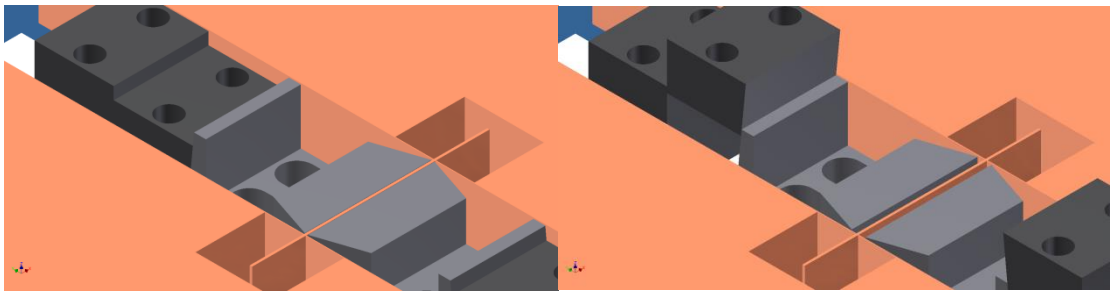

Figure 6.28 Left to right, engineering CAD representations of electrode location mechanism in the open and closed positions, omitting fasteners for clarity but showing the P3B XBR.

Alignment was characterised as for P1 using the QS-LZB and the same prodecure as described in Section 6.2.2. The results for the final devices are presented in Table 6.7.

Statistic	Design value		Measured value		Relative error	
	P3A	P3B	P3A	P3B	P3A	P3B
μ^1	10	10	9.4	8.8	0.06	0.12
μ^2	10	10	10.4	9.5	0.04	0.05
$\bar{\mu}$	10	10	9.9	9.15	0.01	0.085
θ	0°	0°	0.0030°	0.0024°	-	-

Table 6.7 Characterisation of capacitive gaps according to mean gap and out-of-parallel angle achieved for P3A and P3B prototypes.

In the author's judgment, these numbers represent the best repeatable performance achievable via the present location methodology and metrology. In particular, it was difficult to acquire reliable data points using the available tools and algorithms at the achieved alignment precision, and impossible beyond, due to the low amount of light able to penetrate such a small aperture. The relative error in P1 of 1% implies that differential-mode trimming of the preamplifier would be of the same order, since the electrical component tolerances are substantially better, so that common-mode EM noise leakage bypassing the Faraday cages would be expected to be attenuated by around two orders of magnitude by the differential configuration.

The method could be extended to encompass alignment on the scale of single microns and beyond by using a transparent substrate, more powerful illumination, and/or a more sensitive CCD in the measurement instrumentation. Given the Ra on the machined faces achievable using Wire EDM without post processing is of the order of $0.1\mu m$ (and hence the larger asperities are 3-5 times greater), such changes would be expected to approach the machining limit on the capacitive gap with the chosen fabrication route; application of the methods of Chapter 5 shows that achieving the thermal noise floor would then be possible without parametric amplification.

6.5.11 Current path

It has already been mentioned that an important source of spurious common-mode signals in the measurement bandwidth was the harmonic voltage applied to the sense beam due to resistance in the return path for the large applied sense current. Of course, since the current is AC, both arms of the circuit are subject to this requirement. Minimising the resistance of this path was therefore of considerable importance to device performance.

To this end, contact was made to each side of the XBR via four eyelets crimped to insulated cable and fitted over the bolts retaining the XBR to the MACOR substrate. Each of the four leads was terminated within 100mm in a gold connector block. The current was guided to the power feedthrough via 4AWG audio-quality wire inside the vacuum chamber, and the external connections to the Lorentz drive amplifier were made using the same medium.

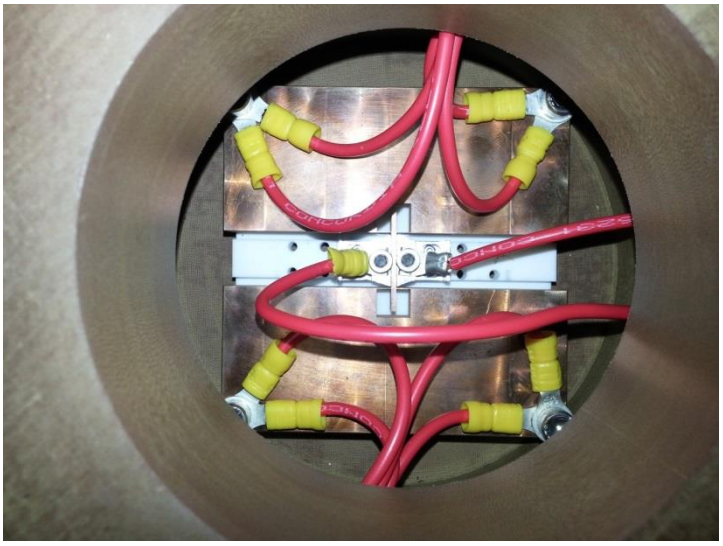

Figure 6.29 Detail of sense current path through the XBR. The direction of flow is from top to bottom. The left-to-right connections are the sense electrodes.

6.5.12 Substrate

Based on the experience gained in developing P1 and P2 – in particular, the stark contrast in the observed Q factors due to structural damping associated with the mechanical fastening between the resonator and its substrate; and also to accommodate the redesigned electrode location mechanism, the substrate was completely redesigned for the P3 devices.

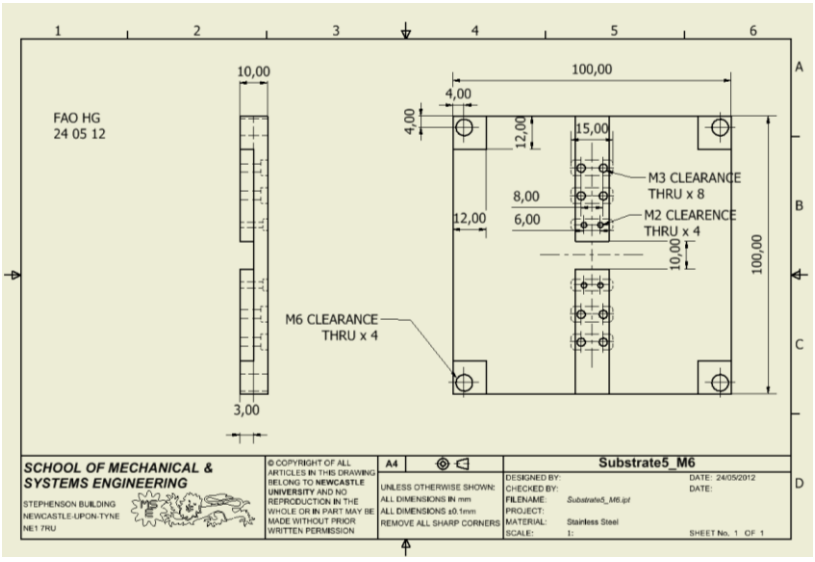

Figure 6.30 Engineering drawing of the substrate for P3 devices, as fabricated.

The anchoring of the resonator to the substrate, in opposition to that of P1, is as small as possible within the limitations of the materials and fastening mechanisms used, while the fastenings are made larger to accommodate more forceful clamping.

6.5.13 Complete P3 assembly

The fabricated components were assembled by hand in the Newcastle University MSE workshop. In each case, the resonator was first unbolted from the jig. In order to affix the resonator to the substrate without damaging the fragile support beams, the broken edges of the component were forcibly clamped between two plywood supports. The sense current connections described in Section 5.2.4 were aligned with the corner holes in the resonator, which in turn was located relative to the MACOR substrate, before the bolted connections made fast. At this stage, the resonator was suspended clear of the MACOR in its operational configuration. Next, the electrode assembly was affixed in the open position and lightly fastened. After the QuickScope was used to align the capacitive gaps, the electrodes were permanently located by the through screws; the electrode location mechanism was subsequently removed to allow electrical contact to be made.

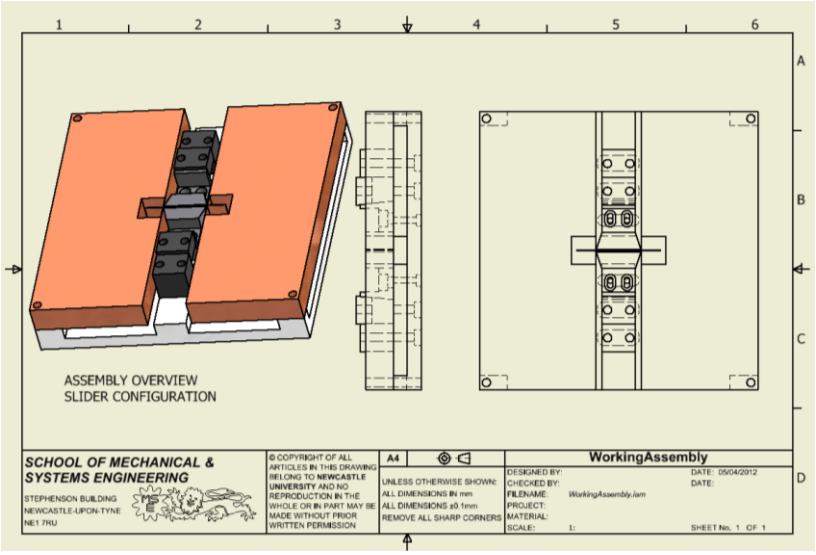

Figure 6.31 CAD drawing of the complete P3B assembly, as fabricated. Bolted fastenings are omitted for clarity.

Attention is now given to the expected response of the resonator system seen at the output of the preamplifier for a given applied field. The generalised response to an applied Lorentz force is given by (5.19); the corresponding generalised Lorentz force and stiffness, as well as the Q factor, as defined by (2.45) are given by the methods of Chapter 3. Evaluating the generalised response by calculating these quantities gives a prediction for the deflection of the XBR in terms of the generalised modal coordinate $\hat{T}$. Normalising the mode shapes and corresponding coordinates such that the central displacement of the sense beam is 1 metre for $\hat{T} = 1$, the average displacement in metres of the sense beam over the capacitor area $\bar{X}$ is given by

$$\bar{X} = \frac{\hat{T}}{\ell_2} \int_0^{\ell_2} X_2 \; dx_2 \tag{6.8}$$

The displacement-to-voltage sensitivity of the pickoff electronics is given by

$$V_{\substack{OUTPUT \\ PREAMP}} = G_{PREAMP} \times 2\bar{X} \frac{\omega_n \varepsilon_0 b \ell_2}{h_0^2} V_{BIAS}^2 \tag{6.9}$$

Combining (5.19), (6.8) and (6.9), one has

$$V_{\substack{OUTPUT \\ PREAMP}} = \frac{|\mathrm{F}|\mathrm{Q}_P \omega_n \varepsilon_0 b \cos(\omega_n \hat{t} + \Phi_P)}{2h_0^2 \mathrm{K}_0} V_{BIAS}^2 G_{PREAMP} \int_0^{\ell_2} X_2 \; dx_2$$

(6.10)

Evaluating (6.10) by assuming $\mathrm{Q}_P = O(10^2)$ and a generalised Lorentz force corresponding to 1 amp sense current and a field strength $B = 1 \times 10^{-3} T$ along with the specified geometries leads to an estimate for the order of magnitude of the observed harmonic voltage response as

$$V_{\substack{OUTPUT \\ PREAMP}}^{P3A} \cong 1.0 \times 10^{-7} G_{PREAMP} \; ; V_{\substack{OUTPUT \\ PREAMP}}^{P3B} = \cong 1.0 \times 10^{-6} G_{PREAMP} \quad (6.11)$$

6.6 XBM results

In this section, experimental results are presented for the P3 series of prototypes using the presented experimental method. For each resonator, after assembly of the test rig, measurements were undertaken by driving the XBM via the HF2LI and the Lorentz drive amplifier, and the voltage output from the output preamplifier was recorded. For each measurement, the Maxwell coil was excited using a current-regulated supply to generate a fixed, uniform magnetic field transverse to the device. The synchronous demodulation procedure used a 8th order low-pass filter. An initial frequency sweep was performed in a 500 Hz band centred on the analytically predicted value in 0.5 Hz increments. At each frequency, 128 averages were performed. The total time taken was 21 hours.

Having located the resonant peaks, a detailed sweep was then undertaken, obtaining 1000 measurements over a 100 Hz bandwidth centred thereupon, with the same sample rate and filter settings. The results are discussed in what follows in the context of the predictions made by the model developed in the previous chapters.

6.6.1 Response to magnetic field

In this subsection, operation of the test setup as an XBM is demonstrated. The raw response data sampled by the HF2LI is presented first.

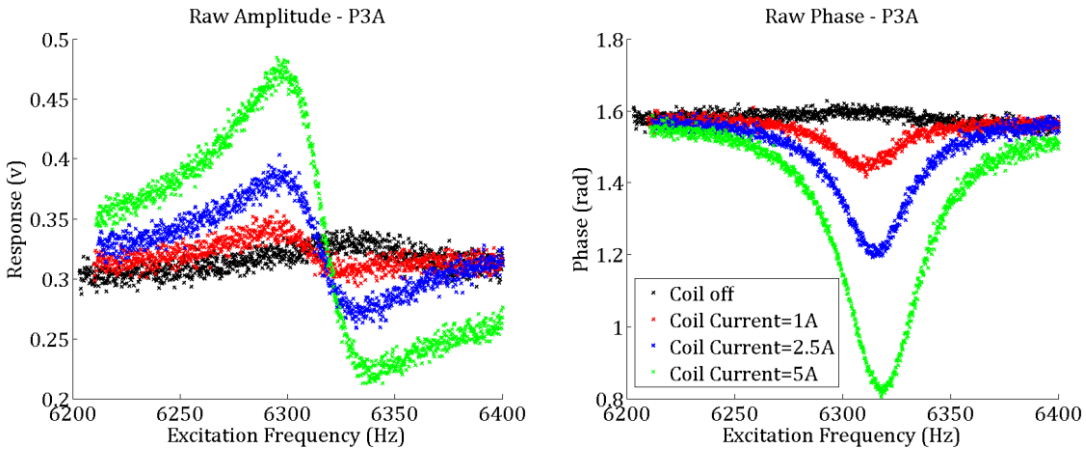

Figure 6.32 Left to right, measured output amplitude and phase vs. frequency for P3A, using a fixed sense current of 1 Amp, for some values of applied magnetic field.

The response of P3A to an applied magnetic field is displayed in Figure 6.32. In both plots, a distinct response to an applied field is observed. The magnitude appears to be related in a linear fashion to the coil current. However, despite the measures taken to minimise the sense current path resistance and to use differential mode amplification to minimise parasitics, a nonzero signal and correlated phase are still evident in the left-hand and right hand plots respectively, even when the coil is not energised. From the right hand plot, the zero field signal leads the sense current (which provides the phase reference) by roughly $\frac{\pi}{2}$ radians, suggesting its source is voltage fluctuation of the sense beam induced by source resistance and driving a current through the pickoff capacitors.

By evaluating and subtracting the complex feedthrough obtained from the measurement taken at zero applied field, it is possible to recover a cleaner signal corresponding to the XBR response.

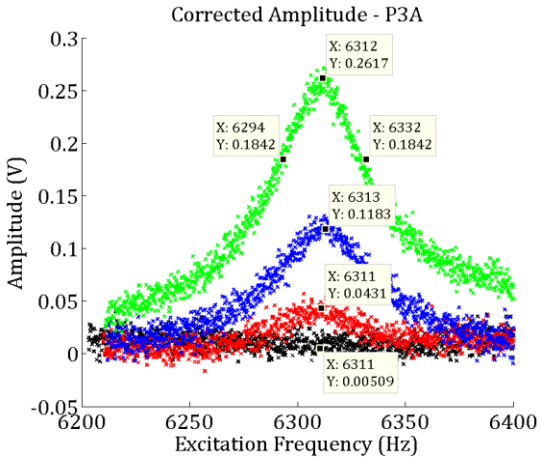

Figure 6.33 Response of P3B, corrected by subtracting feedthrough. Datatips are included indicating the amplitude and frequency of the peak response for each level of applied field, and also at the -3dB points for the largest applied field.

The response is more recognisable as a resonance peak in this form. The Q factor can now be estimated by taking the quotient of the -3dB bandwidth by the peak frequency; for the data displayed in Figure 6.33, a rough calculation yields $Q = 166$. To obtain an objective measurement, a Gaussian was least-squares best fit to the data, and the fitted parameters used to extract an objective statistic for the Q factor and natural frequencies. The data is presented in Section 6.6.2.

The same measurement scheme was employed for P3B. The response was considerably larger for an equivalent sense current, owing to the reduced generalised stiffness of the thinner sense beam; to prevent the output of the amplifier from clamping at the Zener voltage, the coil excitation was reduced by an order of magnitude.

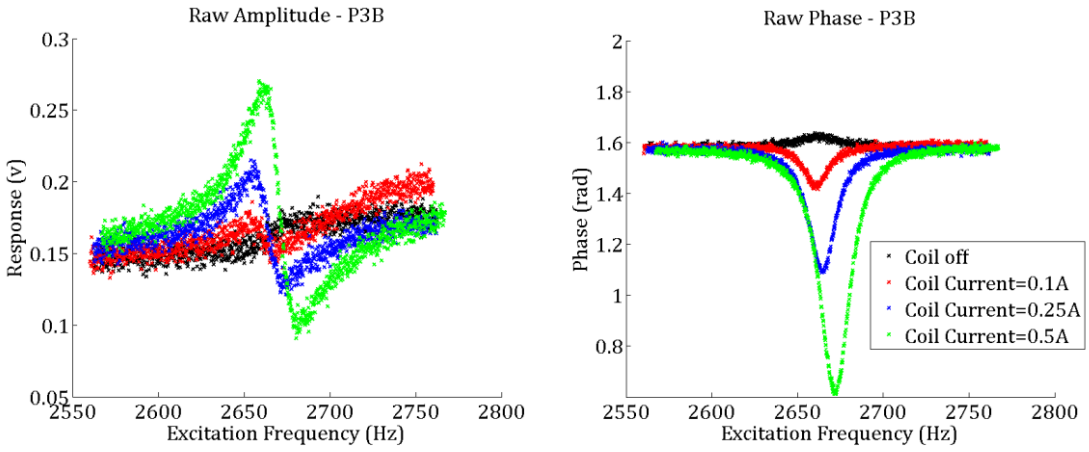

Figure 6.34 From left to right, measured output amplitude and phase vs. frequency for P3B, again using a fixed sense current of 1 Amp and varying the applied field.

As before, current feedthrough is present; in this case, it is attenuated by the lower operating frequency of P3B. Subtracting the complex components of the feedthrough from the total signal, the corrected response is obtained:

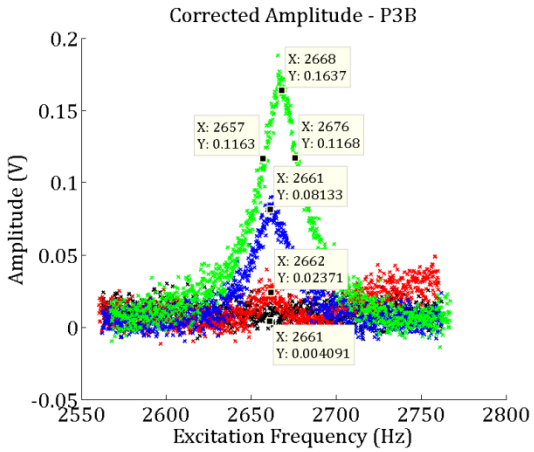

Figure 6.35 Corrected response obtained for P3B. Again, peak values and -3dB points are indicated via data tips.

The response to a coil excitation of $100mA$, given in red, corresponds to a field of $112\mu T$, and is just distinguishable from the feedthrough at the observed noise level. The noise voltage was not observed to change if the XBR circuit path was shorted, suggesting that electronic noise is the sensitivity-limiting factor for the XBM, as expected. Using the Gaussian fits on the corrected response data as the coil energising current was varied over 100 values and the characterisation of the coil from Section 4.3.2 it was possible to obtain the response of the magnetometer to applied field; the data is presented below.

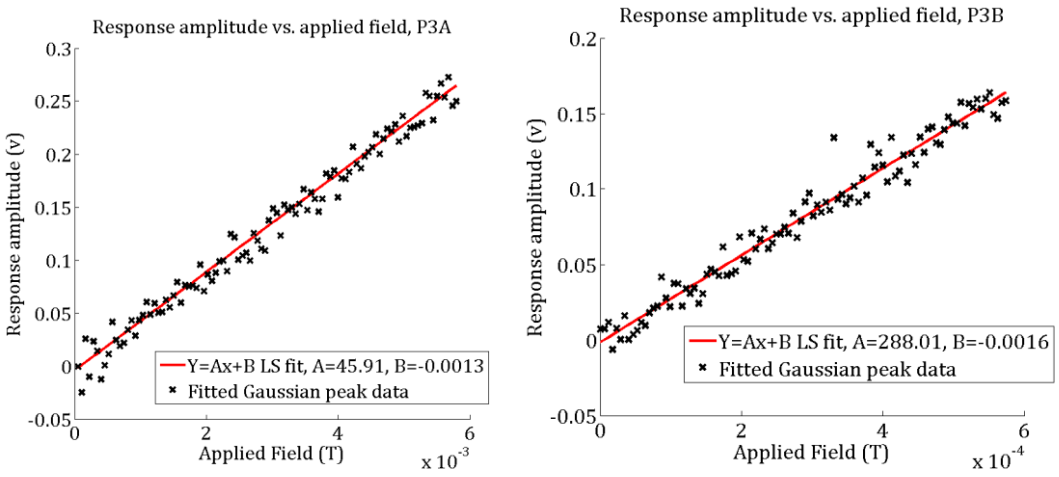

Figure 6.36 Left to right, response linearity for P3A and P3B respectively. The data points correspond to the peak values of the fitted Gaussians; the red line represents the least squares linear best fit to the dataset. The corresponding slopes and intercepts are given in the legend.

Figure 6.36 shows that the response is broadly linear, with some noise scatter. The sensitivities are on the order of those expected from (6.11). The uncertainty range of the intercept includes zero in both cases, suggesting that the vertical component of Earth field in the vicinity of the test was beneath the noise floor. The RMS voltage noise was $0.0106\,V$ for P3A and $0.0115\,V$ for P3B. The value of field strength for which the fitted response is equal to the noise using this electronic configuration was $2.309 \times 10^{-4}T$ for P3A and $3.99 \times 10^{-5}T$ for P3B.

6.6.2 Natural Frequencies and Q factors

The natural frequencies and Q factors predicted by the loss and dynamics model are compared to the experimental model in this subsection. These parameters were obtained by least-squares iterative fitting of a Gaussian in amplitude, centre frequency, and spread to the raw data.

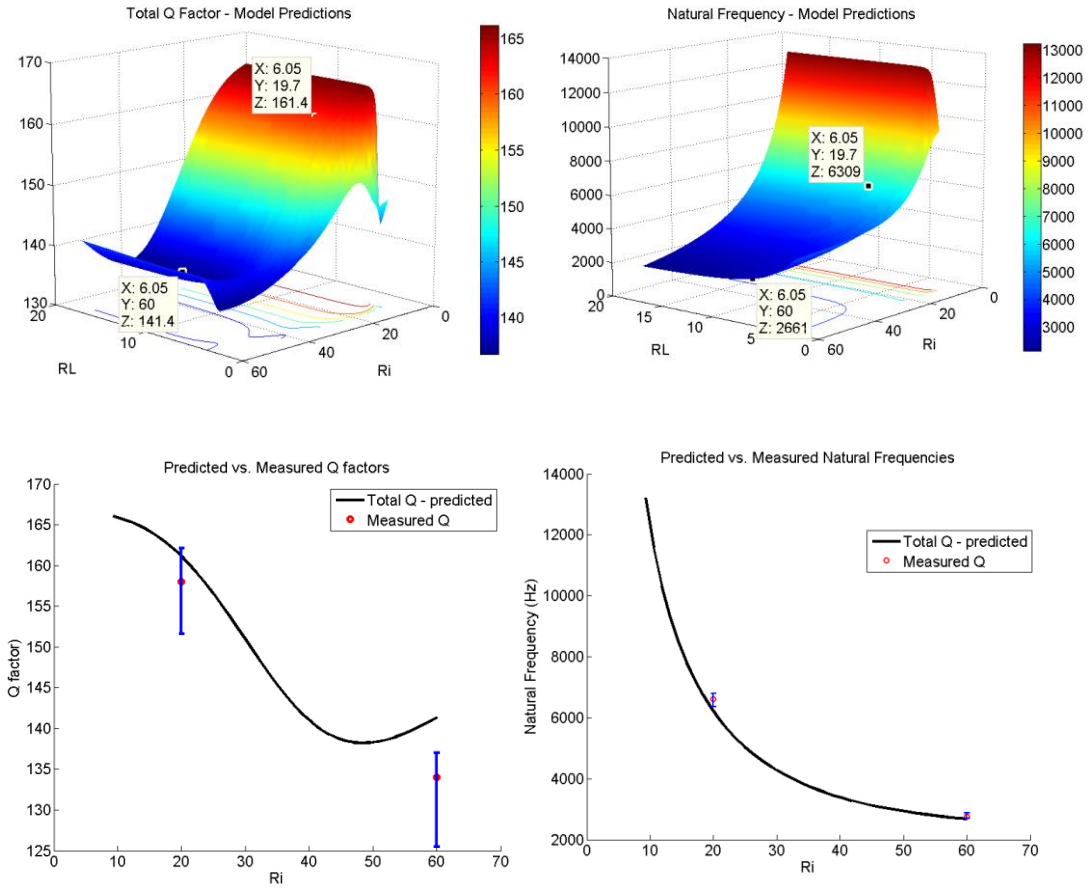

Figure 6.37 Top left to bottom right, Q factors and natural frequencies, as measured for P3A and P3B, compared to the model predictions.

The natural frequencies agree to within the margin of experimental error for both devices. The Q factors are slightly lower than predicted by the model; however, the trend in the data is in line with the predictions. The agreement overall can be considered good, in that the predictions are very close to the range of measured values. Indeed, the predicted value falls within the range of measured values in both Q and natural frequency for P3A. The small discrepancies observed in prediction and experiment for P3B could be due to variation in the material properties and hence the bulk loss, variations in the temperature leading to increased TED; or manufacturing variation. Other loss mechanisms were shown in Chapter 5 to be orders of magnitude smaller, and can be safely neglected here.

6.6.3 Summary

The chief experimentally measured characteristics of the P3A and P3B magnetometers are exhibited and compared to the corresponding predicted values in Table 6.8.

Quantity	P3A Predicted	P3B Predicted	P3A Measured	P3B Measured
Natural frequency	6.309×10^3	2.661×10^3	$6.299 - 6.32 \times 10^3$	$2.659 - 2.681 \times 10^3$
Q factor	1.41×10^2	1.61×10^2	$1.26 - 1.37 \times 10^2$	$1.53 - 1.63 \times 10^2$
Field sensitivity	$9.7 \times 10^2\ V/T$	$9.8 \times 10^3\ V/T$	$4.59 \times 10^2\ V/T$	$2.88 \times 10^3\ V/T$
Field resolution	–	–	$2.309 \times 10^{-4} T$	$3.990 \times 10^{-5} T$

Table 6.8 Predicted vs. measured natural frequencies, Q factors, field sensitivities, and attained resolutions of the P3 prototype family.

Agreement is very pleasing for the mechanical parameters. The field sensitivities are lower than the predictions by a factor of two to four, but are within an order of magnitude of the expected values. Finally, the field resolutions for each sensor are given.

6.7 Conclusions

A series of macroscale XBM prototypes have been fabricated. The P3 series of two prototypes were demonstrated in operation as magnetometers – the first time a

functioning flexural XBM fabricated using macroscopic machining has been reported. This also constitutes the first flexural XBM to be demonstrated in metal. The Q factors reported are in satisfactory agreement with the Chapter 5 model.

6.8 References

[1] "HF2LI Datasheet," *Zurich Instruments*, 2010. [Online]. Available: http://www.zhinst.com/products/hf2li. [Accessed: 24-Jun-2013].

[2] "Quick scope," *Mitutoyo Bulletin 2018*, 2011. [Online]. Available: http://www.mitutoyo.com/pdf/2018_QuickScope.pdf.

[3] "Facts about plasma technology and plasma cutting," *Linde AG Technical Report*, 2011. [Online]. Available: http://www.boc-gas.com.au/internet.lg.lg.aus/en/images/BOC Facts about plasma technology351_68107.pdf. [Accessed: 01-May-2012].

[4] P. S. Sheng and V. S. Joshi, "Analysis of heat-affected zone formation for laser cutting of stainless steel," *Journal of Materials Processing Technology*, vol. 53, no. 3–4, pp. 879–892, Sep. 1995.

[5] C. Sommer and S. Sommer, "Profiting With Wire EDM," in *Complete EDM Handbook*, Advance, 2005, pp. 45–60.

[6] "LM675 Op Amp Datasheet," *Texas Instruments*, 1999. [Online]. Available: http://www.ti.com/lit/ds/symlink/lm675.pdf. [Accessed: 16-Sep-2012].

[7] J. Clerk-Maxwell, *Treatise on Electricity and Magnetism*. Oxford: The Clarendon Press, 1873, p. 319.

[8] Trifield, "DC Milligauss Meter Model MGM," *Web Site*, 2013. [Online]. Available: http://www.trifield.com/content/dc-milligauss-meter/. [Accessed: 22-Jun-2013].

Chapter 7. Conclusions

In this chapter, the accrued knowledge gained in the course of the theoretical and experimental investigations constituting the project is drawn together and summarised. Conclusions are drawn with regards to the potential for XBRs and XBMs. The domain over which knowledge has been obtained and its limits are discussed, and areas in which further research would be advantageous are identified. Finally, the success of the project as a whole is evaluated relative to the goals given in the introduction.

7.1 Introduction

The present chapter draws the thesis to a close. Its aim is to form a grand synthesis of the knowledge accrued through the component investigations of the project documented in the previous chapters.

7.2 Conclusions

7.2.1 Review of outcomes

In the following subsections, the most important outcomes from each analytical chapter of the thesis are recapitulated and summarised.

7.2.2 Chapter 2

The dynamics of an XBR under Lorentz and classical forcing, as well as parametric drive, were studied in this chapter using a multiple scales singular perturbation method. The response was derived as being of the form of (2.69). It was shown that the response is a function of the applied control voltages, the magnetic field, and the modal stiffness, mass, and Q factor. The effect of nonlinearity was considered; the response for the mechanically nonlinear case including damping effect was shown to be of the form described by (2.91) and (2.92); including parametric effects, as well as electrostatic and mechanical nonlinearity yielded (2.98) and (2.99). A method of mitigating undesirable nonlinear effects was proposed; the condition for mitigating cubic nonlinearity was given by (2.100). Taken together, the results yield insight into

the behaviour of an XBR (or other resonator) under the action of a control system, developing work previously presented by Gallacher et al. for ring gyroscopes.

7.2.3 Chapter 3

In order to apply the methods of Chapter 2 to a real system, the modal quantities are required. Motivated by this consideration, as well as previous reports in the literature of XBR behaviour deviating strongly from that expected from a free-free model, and in the absence of any reported attempts to study the phenomenology of XBR modal dynamics, an approach based on the Rayleigh-Ritz method was proposed and developed. Physical insight into how the interaction between the substructures comprising the XBR yields the modal properties was obtained; cf. Figures 2.2 and 2.3. and Section 2.2. Based on a priori intuitive and analytical understanding of the substructure modal interactions, an efficient modal analysis procedure suitable for implementation and iteration using modern computational resources was proposed. The results of the method were shown to agree with COMSOL Multiphysics® Finite Element code very well, with far more rapid convergence and shorter solve times, demonstrating the ability of the approach to offer fast searches of the parameter space of the problem over and above that offered by off-the-shelf methods.

7.2.4 Chapter 4

After the third chapter, the final missing piece required to close the control model and thereby form a self-consistent and self-contained paradigm for the study of XBRs was a quantification of the Q factor of the resonator. Furthermore, the very purpose of the XBR geometry is to mitigate support loss by geometric impedance tuning; somewhat surprisingly, no attempt to study the efficacy of this strategy has ever been reported previously in the literature.

Building from previous work on elastic waves by Miller and Pursey adapted by Jimbo and Itao in the 1960s to model support loss from cantilevers, a series of original integral-form expressions were derived relating the forces of constraint at the interface between the supports of an XBR (or other beam-supported resonator type) and the resulting power flow into the substrate were derived as (4.50b), (4.51), (4.61a) and (4.61b). A numerical scheme for evaluating the integrals was proposed, and the

results evaluated as the force distribution parameters were varied. It was shown that the power flow is quadratic in the forces of constraint, and that interactions between the displacements generated by multiple supports modulate the power flows, suggesting that, if multiple supports are spaced such that their spacing is an odd half-integral multiple of the surface wave length, then destructive interference effects can appreciably reduce support loss beyond what is obtained by nodal supports. This principle is applicable to high-frequency supported resonators. New insight into support loss was thus derived.

7.2.5 Chapter 5

In Chapter 5, a review is made of the anticipated loss mechanisms in the XBR system. In addition to the support loss considered in Chapter 4, gas damping, intrinsic loss, surface loss, and thermoelastic damping were identified. Existing results giving closed form expressions quantifying these phenomena for beams were generalised to the XBR case. Next, a system level model for the performance of the sensor in the presence of noise was derived, using results from chapters 2,3, and 4 along with the XBR loss expressions. This model provides insight into the performance of an XBR system, accounting for the effects of geometry, materials, and electronics. Results were presented illustrating the variation of the device performance, as well as modal characteristics of the XBR including Q factors and natural frequencies, as a variety of geometric, material, environmental and control parameters were varied over ranges relevant to practical XBR design. The subtle and contingent manner of the variations demonstrated the utility and necessity of a detailed system-level picture of how output performance arises from the interaction of the subsystems for optimal design.

7.2.6 Chapter 6

In chapter 6, the development of an XBR system and test rig from basic components was presented. A drive amplifier and sense preamplifier appropriate to the design were developed, with care and attention devoted to achieving optimal system performance through the delivery of a large high-frequency sense current and achieving low input-referred electrical noise at the preamplifier output. A series of XBR designs were proposed, analysed using the models of the preceding chapters, and

fabricated. Based on system performance considerations, a method for accurate and repeatable location of the sense electrodes so as to create a controlled, high aspect ratio capacitive gap was demonstrated, utilising inclined-plane force multiplication to provide mechanical actuation. The system was demonstrated in operation as a magnetometer, proving the concept of a macroscopic flexural XBM for the first time.

7.2.7 Scope, Limitations and Further Work

In the next subsections, the limitations of the work presented in each chapter are briefly outlined, along with the author's suggestions for profitable directions in which further progress can be made. The models of this work are idealisations, omitting some detail of the physical problem, as is true of all mathematical descriptions of reality. Those omissions worthy of further investigation, in the opinion of the author, are the focus here.

7.2.8 Chapter 2

The most important omission in the chapter is a lack of experimental validation of the predictions, and in particular of the parametric excitation scheme. If the nonlinearity-mitigation scheme can be demonstrated in operation, then the impact of the model would be greatly augmented. Also necessary to fully exploit the work is a detailed proposal for a practical implementation of the controls, perhaps employing a phase-lock loop and a phase tracking strategy to establish the required phased signals.

7.2.9 Chapter 3

The methods of Chapter 3 are based entirely on linear theory; as presented, they make no account of nonlinear phenomena. On the other hand, it is well known that, for large excursions, clamped beams such as the XBR supports experience a coupling between displacement and axial tension due to geometric nonlinearity, breaking the Euler-Bernoulli assumptions radically. The "mode shapes" no longer possess the qualities associated with linear eigenfunctions; the invariant subspaces are no longer linear manifolds, but rather general Riemannian manifolds (invariant manifolds). A nonlinear structural model of XBRs would yield rich information on the behaviour of these structures under large amplitude deflection. It would be expected that, as the modal participation of the supports is shown in this chapter to be small, that the

overall effect of the nonlinearity would be weaker than in the case of a clamped-clamped beam undergoing comparable deflections; nevertheless, intuitive generalisations of this sort are often contradicted by nonlinear theory. Furthermore, small nonlinearities in terms of natural frequency and mode shapes may have comparatively large effects on the support and dissipation behaviour associated with the application of the methods of Chapters 4 and 5 to the results of the dynamical model.

In terms of the linear model, expanding the quasicomparison function selection technique to encompass more general resonator geometries, such as bulk cavities, discs, plates, shells, thick beams, and other types would allow the benefits of the approach to be extended to optimisation of more general resonators. An extension of the Rayleigh-Ritz principle to include nonautonomous action is possible and has been reported several times in the literature; such a modification would allow quantification of the effects of parametric drive, dissipation, and control strategies on the mode shapes and the ramifications for XBR response, loss mechanisms, and ultimately XBM performance.

7.2.10 Chapter 4

Two limitations of the formulation given in this chapter are immediately apparent: the assumption of a semi-infinite, conservative substrate; and the assumption of uniform stress distribution at the support-substrate interface.

The Helmholtz potentials approach is easily extended to any stress distribution for which an analytical expression or approximation is available. This would permit the consideration of supported resonators for which the elastic wavelength is comparable to the support thickness, as with bulk resonators at high mode orders and other high-frequency geometries. As for the substrate, several approaches are possible. One is to apply an analytical method to finite geometries to capture the effects of boundary reflection and mode conversion, and of dissipation from sources such as dry or internal friction, anelastic scattering, and the like. An alternative method would employ numerical methods such as Finite Elements, which have the advantage of ease and directness, at the cost of analytical insight. Combining both approaches to develop more realistic models of loss in supported resonators would further enhance our

ability to design optimal high-Q resonators and to fully exploit and generalise the principle of operation of the XBR.

7.2.11 Chapter 5

Chapter 5 constitutes the system level optimisation work undertaken during this project. A framework for analysis is established, based on a simple idealisation of system plus conditioning elements. There remain many open questions in this area worthy of pursuit. One would be a more detailed analysis of the noise behaviour of the system, considering other noise sources in the XBR besides thermal noise, such as Lorentz force noise induced by current fluctuations, $\frac{1}{f}$ noise, $\frac{1}{f^3}$ noise referred to the operating frequency by nonlinear effects, etc. A detailed noise analysis of the conditioning electronics, including the op amps and circuit elements, as well as the influence of environmental EMI, would also contribute to XBR systems optimisation.

A more detailed loss model, accounting for the frequency and perhaps temperature dependence of the bulk and surface loss mechanisms in different materials, drawing on the extant internal friction literature rather than using a constant value would broaden the scope and improve the quantitative accuracy of the modelling.

Perhaps the best ratio of time invested to return in terms of design improvement in the whole thesis would be obtained by implementing a constrained nonlinear optimisation routine utilising the consolidated performance model of Chapter 5 as a profit function to be optimised by a technique such as simulated annealing. This would lead to a robust approach to designing the best possible XBR or XBM within given constraints on overall dimensions and the feature size and capabilities of the chosen manufacturing route.

7.2.12 Chapter 6

Chapter 6 demonstrates the feasibility of a macroscopic XBM system. A substantial portion of the overall resources of the project, in terms of time and effort, was put into obtaining a functional set of conditioning electronics with reasonable performance; however, the author feels that further optimisation from an electrical engineering perspective is possible. Furthermore, implementing and characterising the designs as

part of an integrated microsystem, rather than using separate circuit elements and hand assembly, is a prerequisite for commercial development and real-world delivery of a useable MEMS XBM that merits and commands ongoing research effort.

7.2.13 Answers to open questions

A list of open questions to be addressed in the thesis was given in Section 1.4. They are recapitulated here and addressed in order, using the knowledge generated by the work and contained in the thesis.

- *Is parametric amplification a useful technique to apply to XBMs?*

Parametric amplification has several benefits for an XBM. Firstly, the phase-sensitive nature of the technique suppresses out of phase noise, lowering the noise floor by a factor approaching $\sqrt{2}$. Secondly, the amplified response to a small signal, although it leaves the squeezed intrinsic noise floor of the device unchanged, increases the corresponding output current by a factor equal to the parametric gain while leaving the sense electronics noise floor unchanged. Thus, a factor of at least 10^2 improvement in sensitivity can be made, if the operating conditions and configuration are such that electronic noise predominates. Cf. Chapter 5.

Additionally, it may be possible to use parametric effects to mitigate nonlinearities arising in an XBR or other resonator system, by the techniques outlined in Chapter 2, which will extend the effective dynamic range of the device and increase linearity. Further work is necessary to investigate this concept.

- *Can it be done?*

The author was not able, within the constraints of this project, to demonstrate the operation of an XBM with parametric drive. However, the method has been demonstrated for capacitively actuated beam and ring resonators previously in the literature. Although the implementation would not be trivial, it can be concluded that a parametrically driven XBR is both feasible and capable of extending the performance envelope of XBMs.

- *What are the limits of, and limiting factors on, the force sensitivity of XBRs and field sensitivity of XBMs?*

The intrinsic limit on the resolution of small signals in a resonant sensor comes from noise. In chapter 5, a performance metric is derived for the XBR, based on the assumption that the dominant noise source is thermal noise, along with a knowledge of the system dynamics obtained in Chapters 2-4 and the Fluctuation-Dissipation and Equipartition theorems. For a force sensor, the units are $N/\sqrt{Hz}$; for a magnetometer, sensitivity has units of $T/\sqrt{Hz}$ and s ubdivisions thereof.

Resonator and measurement Q factor, generalised stiffness, and the Lorentz coupling all enter into the metric expression. In general, to minimise the thermal noise floor, the Q should be made as high as possible, while the generalised stiffness should be minimised. This is borne out by the results for P3A and P3B: the Q factors are comparable, but the more compliant resonator P3B resolved a field almost a factor of ten smaller than its counterpart and is therefore almost ten times more sensitive, in concordance with the model.

It is further shown in Chapters 5 and 6 that often, and in particular for the cases considered in this work, electrical noise predominates over mechanical noise. In this regime, a larger electrical response will dilute the electronic noise, leading to improved resolution. It is therefore critical to optimise the conditioning electronics – in particular the preamplifier – in order to maximise performance.

- *How do the associated sensitivities change as the parameters are varied?*

A concise and detailed answer to this question is not available. Indeed, it has been shown that, even within the limited domain of this thesis, the sense and amplitude of the changes in sensitivity are contingent on the material, the length scale, the actuation and sensing mechanisms, and the conditioning electronics, among other factors. However, the techniques developed herein are applicable to XBRs of many material and geometric configurations, and could be generalised readily to encompass other sense/actuation strategies, such as laser vibrometry, interferometric, or piezoelectric transduction, provided that the designer has sufficient understanding of the corresponding dynamical behaviours and noise characteristics.

- *Are there general optimality conditions, or is it necessary to evaluate each material and geometric case separately?*

Again, the optimality conditions for the geometry, transduction etc. are clearly dependent on the particular case being considered. It is therefore necessary to consider each case in some detail; the reader is referred to Chapters 2-5.

- *How do these effects vary with scale?*

It can be said that, in general, the force sensitivity of well-designed XBRs tends to decrease with downscaling at the smallest scales. This is not true for all geometric choices or initial scales (Cf. Figure 5.15); rather, the complicated interaction of noise sources, Q factors, natural frequencies, and compliances that gives rise to the thermal limit on force sensitivity is not characterised by a single relation between sensitivity and scale.

- *How can we model these phenomena in an efficient, flexible way suited to design optimisation?*

Three ingredients are required for an XBR theory: a resonator-level dynamics model, a system-level control and noise model, and dissipative constitutive relations to close the problem. It has been demonstrated that a Rayleigh-Ritz model for the dynamics, Multiple Scales techniques for the control system, and the theory developed herein are capable of constituting such a theory, in a flexible and efficient manner, at least by comparison to commercial, general purpose FE code. It should be noted that there are many alternative methods of analysis that could be substituted for one or another of the ingredients; for example, the method of harmonic balance can produce closely analogous results when applied to control modelling; wave–based methods are available for the XBR dynamics; and so forth. The author can state that no other systematic method of analysis or theory has been reported on in the literature for systems-level XBM optimisation.

- *In terms of mechanical engineering, is it possible to realise a flexural XBM using planar macromachining techniques, such as Wire EDM?*

In Chapter 6, the converse proposition has been disproved by counterexample. The analysis suggests that, with appropriate and practical electronics, it is indeed possible

to produce small XBMs using these techniques capable of supplying sub-nanotesla resolution.

- *If so, how can the resulting magnetometers be expected to perform?*

The body of work, in particular Chapters 5 and 6, indicate that the fundamental physical limitations on the performance of XBMs are orders of magnitude in advance of that which has available commercially, and indeed what has been reported in the research literature. Given the noise constraints, realising the promise of precision MEMS magnetometers is critically dependent on developing low-noise, high-gain electronics to extract the tiny currents generated by capacitive sensing, and on the development of improved micromachining technologies that permit the creation of high aspect ratio capacitive gaps to maximise the current response to a given field and ultimately the field resolution at the output.

- *From a systems engineering perspective, how do the drive and sense processing electronics affect performance?*

The effect of the ancillaries on operational performance is decisive. The results of Chapter 6 make plain the fact that, in order to produce a practical, functional device with high performance characteristics, a systems-level approach is needed to draw together lower-level understanding of the subsystems (the resonator, the transducers, the control system, the drive and conditioning electronics, and readout). On the other hand, an integrated and optimised system of suboptimal components will not achieve the inherent performance possibilities of the XBM concept.

- What needs to be done in order to get the most from these ancillaries?

The primary determinant of the ability of an XBM system to resolve small signals as quickly as possible is the signal-to-noise ratio at the output. In Chapter 6, equation relating the system variables to the minimum detectable field was derived.

7.2.14 Achievement of goals

The overarching goals of the thesis were defined in Section 1.1. The degree to which each has been achieved is evaluated in this subsection.

i. Figures for the field sensitivities and Q factors of Lorentz magnetometers reported in the literature have been presented, and the major application fields for these devices have been determined and discussed, in Chapter 1. The major findings can be summarised as:

- Current MEMS resonant magnetic field sensors are capable of sensitivities on the order of tens to hundreds of $nT/\sqrt{Hz}$.
- The most sensitive current MEMS XBRs to have been reported upon display a sensitivity on the order of 100 $nT/\sqrt{Hz}$. The work was undertaken by the Johns Hopkins research group who originally formulated the XBM concept.
- A precision MEMS IMU, as defined in the introduction, has not been reported on to date in the literature. If a MEMS magnetometer with $1nT/\sqrt{Hz}$ sensitivity or better could be realised at reasonable cost and power consumption, under achievable packaging and environmental constraints, this class of device would be made feasible.

Goal i, as defined in the introduction, is therefore fulfilled, in the judgment of the author.

ii. In the course of the thesis, a general theory of XBM performance was developed. It can be decomposed into two components. The first is constituted by the work of Chapter 2, which accounted for the effects of capacitive transduction, dissipation, parametric amplification, and nonlinearity, from a theoretical perspective. An approach to developing a control model for XBM operation was also proposed therein. This model *assumed* the modal characteristics and damping behaviour of the system as a priori known. The second is the dynamical RRM approach of Chapter 3, which provided an efficient and flexible way to obtain the modal characteristics, and was extended in Chapters 4 and 5 to encompass the effects of dissipation in such a way as to account for the detailed variation in these effects with the geometric and material properties defining the system. It therefore *closes* the control model.

The modelling was further extended to consider the effects of thermomechanical and electrical noise in Chapter 5. With this augmentation, the theory is able to give meaningful predictions about the force sensitivity of an XBR, and the closely related field sensitivity of an XBM.

These developments, taken together, constitute an original theory of the performance of the Xylophone Bar Resonator as a force sensor and of the Xylophone Bar Magnetometer, fulfilling Goal ii.

iii. In Chapter 6, a functional macroscopic flexural XBM was reported, under open-loop control and readout. The measured results agreed to within a satisfactory margin of error with the XBR theory, providing quantitative validation. Therefore, Goal iii has been fulfilled.

iv. The intrinsic limits to the sensitivity of XBMs have been shown in Chapter 5 to be sufficient to herald the arrival of precision MEMS XBRs. The major challenges to manifesting this capability are systems level, associated with the development of sufficiently high-performance signal conditioning electronics and achieving sufficiently precise micromachining to surpass current designs.

7.3 Dissemination of results

In order for the knowledge and expertise gained in the course of this work to be translated into real-world impact, both within the MEMS and broader research community and in society in general, dissemination is a critical process. The author has, to date, undertaken the following steps to promote the broad dissemination of the body of work:

- Presented early work on control, thermal, and support loss modeling at the IMAPS DPC conference in 2012, in Scottsdale, Arizona. The work won a “Best Student Paper” award and $1000 cash. The paper was published in the conference proceedings and is listed on SCOPUS.
- Presented an outline of the RRM model at the IOP conference “Modern Practice in Stress and Vibration Analysis”, in Glasgow, UK. The paper attracted

interest from the keynote speakers, among others, and was published in the IOP Journal of Physics: Conference Series, which is also indexed on SCOPUS.

- The RRM model in detail, along with some results, has been accepted for publication in the Elsevier "Journal of Sound and Vibration" (JSV), which has a Thomson Reuters impact factor of 1.613, a SJR of 1.359 and an SNIP of 2.721, indicating the status of the journal as a leader in the field of sound and vibration and ensuring broad dissemination and wide uptake of the results.

In the future, the author plans to present the remainder of the work as follows:

- Chapter 4 will be submitted for consideration to a high impact sound and vibration journal such as JSV.
- The work presented in Chapter 5 will be applied to consider particular cases pertaining to practicable MEMS implementations and submitted to a MEMS journal, such as JMEMS.
- Chapter 2 will be submitted to a signal processing journal such as IEEE Transactions on Control Systems.
- The findings of Chapter 6 will be submitted as a short communication to a systems engineering journal, such as Systems and Control Letters.

7.4 Closing remarks

In this thesis, a theoretical framework for analysis of an XBM system has been proposed, developed, and used to develop a functional magnetometer under open-loop control. It has been shown that the ideal performance of the resonant component is capable of providing performance beyond that offered commercially or in the lab today for comparable devices. The developments necessary from a systems perspective to realise this potential have been enunciated. With further work, it is hoped that progress can be made towards bringing the putative benefits of low cost inertial navigation to fruition by development of an integrated nanotesla-sensitive MEMS XBM.